The study of the correlation between the microstructural properties and the electrochemical performance of the Li-ion battery high-energy-density positive electrode

Tuan-Tu Nguyen

Thèse de Doctorat

Mention: Chimie
Spécialité: Chimie et Electrochimie des Solides

présentée à ***l'Ecole Doctorale en Sciences Technologie et Santé (ED 585)***

de l'Université de Picardie Jules Verne

par

Tuan-Tu Nguyen

pour obtenir le grade de Docteur de l'Université de Picardie Jules Verne

The study of the correlation between the microstructural properties and the electrochemical performance of the Li-ion battery high-energy-density positive electrode

Soutenue le 9 Décembre 2021, après avis des rapporteurs, devant le jury d'examen :

M. P. ALBERTUS, Professeur, University of Maryland	**Rapporteur**
M. S. ROBERTS, Directeur de Recherches, Sandia National Lab	**Rapporteur**
M. A. FRANCO, Professeur, UPJV	**Rapporteur**
M. S. COOPER, Professeur, Imperial College London	**Examinateur**
M. B. DELOBEL, Ingénieur, Verkor	**Examinateur**
M. P. TRAN-VAN, Ingénieur R&D, Renault	**Examinateur**
M. C. DELACOURT, Chargé de Recherches HDR, UPJV	**Directeur de thèse**
M. A. DEMORTIERE, Chargé de Recherches HDR, UPJV	**Co-Directeur de thèse**

Acknowledgement

First and foremost, I am very grateful to the jury members, Dr. Paul Albertus, Dr. Scott Roberts, Dr. Samuel Cooper, Dr. Bruno Delobel, and Dr. Pierre Tran-Van for accepting the invitation for my PhD defense. Thank you all for your interest in this work and for providing examination and advice on this work. Having you all as part of my PhD defense committee is such pressure but also a great honour for me.

Then, I have to say that I would not be here today to write this thesis without knowing Bruno Delobel, who was somehow my counterpart at Renault back then and became my tutor then now my colleague. Thank you for giving me the opportunity back to that day, waiting for me to handle the administrative issues. And of course, thank you for bothering me with tons of questions and ideas, which keep pushing me to reach a higher level.

Honestly, I cannot say that I have had much success during my years of study in France. I have been satisfied being a moderate student with few achievements. In particular, I have thought that I would never know the feeling to be surrounded by talented people. But this PhD definitely gave me the chance to meet with brilliant people around the globe, which I still cannot believe.

Thanks are due to Charles Delacourt for his patience, his commitment, his kindness and his meticulousness. Although I had heard about Charles before my PhD regarding his brilliant mind and his kindness, I have to say that I was surprised. He is such a modest person, and I felt so lucky to have him as a tutor. He is the person who questioned me about the word I have used when describing physics phenomena, which shows how rigorous he is when it goes to science. Thank you for spending time correcting my paperwork despite my broken English and, most of the time, my carelessness.

Thanks are due to Arnaud Demortière for his time and his kindness as my PhD supervisor. He is the type of supervisor with whom you can share your thoughts without any hesitation. He always believes in his students, which is critical, I think, to build confidence in the students, which turns them into autonomous scientists.

Benoit Fleutot has also supported me as my supervisor at the beginning of my PhD. Even though he left after, I could still learn many things from him.

I have also had the great privilege to collaborate with Sam Cooper on the third chapter of this thesis. Sam is a brilliant senior lecturer from Imperial College London, who is always enthusiastic about science. He has inspired me greatly by his confidence, energy, way of thinking, and especially his meticulousness, which is very similar to Charles's. Thank you for everything.

Without forgetting Vincent De Andrade, Julie Villanova, Imène Estève. From whom, I have received precious advice and expertise in their domains on this work.

The LRCS has also supported me through this work. Friends from LRCS has been of great help on many occasions, and I look forward to continued collaboration with many of them well

into the future. Emiliano always helped me to make the best slurry and electrode in the lab. He showed me how you could live in style but still deliver brilliant results at work. Thank Laura, Ronan, Ulas, Sorina, Ana Christina, Abbos, Scott to make my time in Amiens much less tedious with many good memories. I have also a very good friendship with Arash Jamali, the kindest people I have ever met, thank you.

I am also very grateful to attend lectures from Prof. Christian Masquelier, Jean-Noel Chotard and Prof. Alejandro Franco. I have also had the great privilege to discuss with Prof. Dominique Larcher, who proves that you do not need to go too far to be innovative; innovation can be everywhere when we see things from different perspectives.

Thanks are due to Dolares, with whom I have talked so often when staying late in the lab. After a long day at work, chatting with Dolares is somehow so joyful and relaxing.

I want to say thank you to my old colleague in the Innovation team at Renault. I had a great time working with them as an intern and then as a junior engineer. Their support and guidance throughout my first steps into the battery world was hugely motivating, and I do not feel as if I was sufficiently grateful at the time.

Last but not least, I am grateful to have Zeliang Su as my flat-mate during my PhD, with whom I have enjoyed discussing everything, from scientific topics to geopolitics, games, and life. He supported me through many challenging moments during my PhD by any possible means. I cannot even count the number of times we stayed late working at the lab, ordered pizza, then returned to work until midnight. Two time spending together at the APS to perform night and day experiments were unforgettable memory in my life. It is my honour to know him.

To my lovely family, and my darling.

"Success is not a destination, it is a journey"

- Zig Ziglar

Abstract

Although “post” Li-ion battery is arising as an inevitable solution for sustainable energy transition, it would be unwise to assume ‘conventional’ Li-ion battery is approaching the end of their era; as many strategies are still available to improve their performance. While progress has been continuously achieved to get even better active materials, engineers and academic researchers have kept improving on the electrode scale. The most direct way can be done through the microstructure design. In light of this, this PhD work attempts to understand the interplay between the electrode microstructure and its performance, which plays a vital role in achieving high-performance Li-ion battery electrodes. This work relies on three major pillars, which are electrochemical measurements, X-ray tomography and numerical modeling. The $LiNi_{0.5}Mn_{0.3}Co_{0.2}O_2$ industry-grade electrodes are investigated.

The first part of this work focuses on the first two pillars that allow a complete characterization of porous electrodes, comprising both electrochemical performance and microstructural properties. Appropriate experimental methods are carried out to determine the transport properties of the electrodes, such as electrode tortuosity factor and effective electronic conductivity. Thin electrodes are made for the determination of active-material intrinsic properties. The electrochemical performance of industry-grade electrodes is then assessed through discharge rate capability. A complete quantitative analysis of the 3D microstructures using the X-ray holotomography technique is performed. The microstructural heterogeneities are quantified for each phase separately (active materials, carbon binder domain, pore space), along with the statistical quantification of their inter-connectivity at the particle scale. Besides, *Operando* X-ray Absorption Near Edge Structure coupled with transmission X-ray nano computed tomography are done, offering a direct correlation between electrode microstructure and local electrochemical performance. Also, an image quality assessment method is investigated, which utilizes convolutional neural networks. It can be a direct tool to produce reliable segmentation results and guide the image pre-processing step (*e.g.* denoise, contrast enhancement) for quality enhancement.

The second part relies on the numerical approach to further understand the underlying physics of the electrode during operation. One starts with introducing a new concept of the tortuosity factor, which is demonstrated through a numerical approach to be more appropriate for porous electrodes. A model representing the symmetric cell method is implemented in an open-source application called *TauFactor* for the electrode tortuosity factor determination using tomographic data. Then, the performance of four industry-grade electrodes is investigated through mathematical models. As the Newman pseudo-2D model fails to capture the behavior of the set of electrodes, the formation of porous agglomerates due to the calendering process to achieve high-energy density is identified to be responsible for this discrepancy. Thus, porous agglomerates are included in the Newman pseudo-2D model. The validation of the electrodes with different electrolytes is done. As a result, the porous agglomerate effects are identified as a dominant limiting factor at high C-rates for high-energy-density electrodes.

Keywords: Li-ion battery, electrode microstructure, electrochemical performance, tomography, mathematical modeling.

Résumé

Bien que les batteries "post" Li-ion apparaissent comme une solution inévitable pour la transition énergétique durable, il serait peu sage de penser que les batteries Li-ion approchent de la fin de leur ère, car de nombreuses stratégies sont encore disponibles pour améliorer leurs performances. Alors que des progrès ont été réalisés en permanence pour obtenir des matériaux actifs encore meilleurs, les ingénieurs et les chercheurs ont continué à améliorer l'échelle des électrodes. Le moyen le plus direct est le design de la microstructure. Dans cette optique, ce travail de thèse tente de comprendre l'interaction entre la microstructure de l'électrode et sa performance, qui joue un rôle vital dans l'obtention d'électrodes de haute performance. Ce travail s'appuie sur trois piliers majeurs, qui sont les mesures électrochimiques, la tomographie aux rayons X et la modélisation numérique. Les électrodes de qualité industrielle $LiNi_{0.5}Mn_{0.3}Co_{0.2}O_2$ sont étudiées.

La première partie de ce travail se concentre sur la caractérisation complète des électrodes poreuses, comprenant les performances électrochimiques et les propriétés de la microstructure. Des méthodes expérimentales appropriées sont mises en œuvre pour déterminer les propriétés de transport des électrodes. Des électrodes fines sont fabriquées pour la détermination des propriétés intrinsèques des matériaux actifs. Les performances électrochimiques des électrodes sont ensuite évaluées en fonction de leur capacité de décharge. Une analyse quantitative complète des microstructures 3D des électrodes est réalisée à l'aide de la technique de l'holotomographie aux rayons X. Les hétérogénéités liées à la microstructure sont analysées. Elles sont quantifiées pour chaque phase séparément, ainsi que la quantification statistique de leur inter-connectivité à l'échelle de la particule. En outre, la structure de l'absorption *Operando* XANES couplée à la nano-tomographie aux rayons X sont réalisées, offrant une corrélation directe entre la microstructure de l'électrode et sa performance électrochimique locale. En outre, un outil direct, qui utilise des réseaux neuronaux convolutifs pour produire des résultats de segmentation fiables et guider l'étape de prétraitement de l'image pour en améliorer la qualité, est développé.

La deuxième partie s'appuie sur l'approche numérique pour mieux comprendre la physique liée au comportement de l'électrode pendant son fonctionnement. On commence par introduire un nouveau concept de facteur de tortuosité, dont on démontre par une approche numérique qu'il est plus approprié pour les électrodes poreuses. Un modèle représentant la méthode de la cellule symétrique est mis en œuvre dans une application open-source appelée *TauFactor*. Ensuite, les performances de quatre électrodes de qualité industrielle sont étudiées à l'aide de modèles mathématiques. Comme le modèle pseudo-2D de Newman ne parvient pas à capturer le comportement de l'ensemble des électrodes, la formation d'agglomérats poreux due au processus de calandrage pour atteindre une densité énergétique élevée est identifiée comme responsable de cette divergence. Ainsi, les agglomérats poreux sont inclus dans le modèle pseudo-2D de Newman. En conséquence, les effets des agglomérats poreux sont identifiés comme un facteur limitant dominant à des régimes élevés pour des électrodes à haute densité énergétique.

Mots-clés : Batterie Li-ion, microstructure d'électrode, performance électrochimique, tomographie, modélisation mathématique.

Table of Contents

List of Figures

the electrode. Each point was obtained by calculating the fraction of the phase in a 2D slice across the Z-axis. **a.** State I (Pristine electrode). **b.** State II (CCCV charge to 4.3 V). **c-d.** Discharge 1C to 50% DoD captured at position 1 and 2, respectively. **e.** State III (CCCV discharge to 2.5 V). 202

List of Tables

List of Abbreviations

AM	Active Materials
APS	Advanced Photon Source
ASA	Active Surface Area
BET	Brunauer-Emmett-Teller
CBD	Carbon Binder domain
CC	Constant Current or Current Collector
CNN	Convolutional neural network
CPE	Constant Phase Element
CT	Computed Tomography
CV	Constant Voltage
CV	Control Volume
DoD	Depth of Discharge
EIS	Electrochemical Impedance Spectroscopy
ESRF	European Synchrotron Radiation Facility
EV	Electric Vehicle
FBP	Filtered Back Projection

FIB-SEM	Focus Ion Beam – Scanning Electron Microscopy
FSW	Finite-Space Warburg
HVS	Human Vision System
ICE	Internal Combustion Engine
IQA	Image Quality Assessment
LiB	Li-ion Battery
MSE	Mean Square Error
NMC	$LiNi_xMn_yCo_{(1-x-y)}O_2$
P2D	Pseudo-two dimensions
PA	Porous Agglomerate
PApa	Porous Agglomerate model with polynomial approximation
PE	Porous Electrode
PVdF	Polyvinylidene Fluoride
RDM	Restricted Diffusion Method
RVA	Representative Volume Analysis
SCM	Symmetric Cell Method
SoC	State-of-Charge

TLM	Transmission Line Model
TPB	Triple Point Boundary
XCT	X-ray Computed Tomography
XRD	X-ray Diffraction
VGG	Visual Geometry Group

Chapter I . General Introduction

I.2 Motivation

Nowadays, given the growth of worldwide population and the exponential development of technology, the energy demands still do not seem to reach the peak. To fulfill these demands, humanity keeps wiping out the resources from nature. Over 60% of the world's energy is still produced through the combustion of fossil fuels or coal, as can be seen in Figure I-1. Different alternatives for energy demands have been proposed so far. However, only in a minority of cases, they can compete with fossil fuels and coal in terms of cost and energy density. Consequently, humanity is facing a real problem regarding climate change arising from the insulating "greenhouse effect" caused by the release of CO_2 (majority) and other gasses into the atmosphere. Climate change became a global threat, which requires a global effort to tackle it. In light of this, the Paris climate agreement has been signed to fight global warming, which unites most of the leading countries of the world, who are also the major energy consumers in the world, for a joint action plan in order to reduce the release of "greenhouse gases".

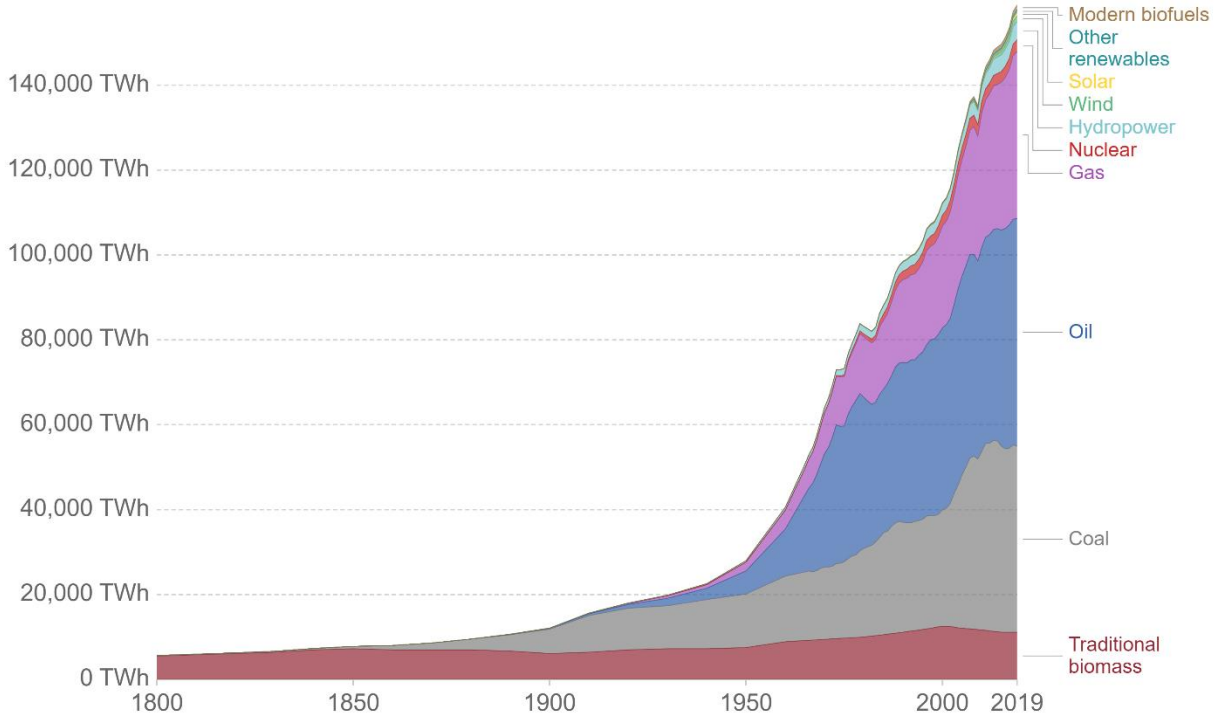

Figure I-1. Global energy consumption by source of energy. Sources : BloombergNEF.

However, to be able to cope with the action plan, the changes have to come from different sectors that are listed in Figure I-2. Among those sectors, the transportation sector is one of the biggest greenhouse gas emission source, where conventional vehicles relying on fossil fuels still offer many advantages compared to the "greener" alternatives.

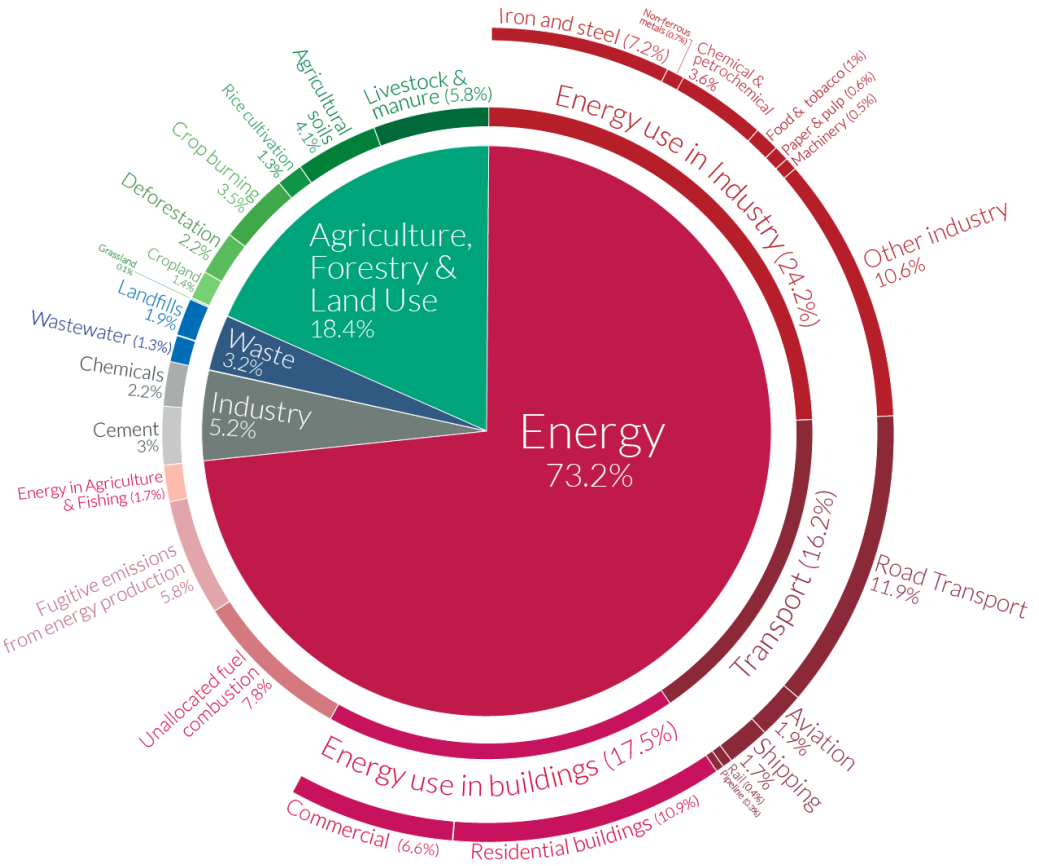

Figure I-2. Greenhouse gas emissions by sector. The transport sector contributes up to 16.2% of greenhouse gas emission. Sources: BloombergNEF.

Over the last decade, electric vehicles have been considered as a more sustainable solution for mobility, contributing to reducing the dependence on fossil fuel. Figure I-3 shows all available electric car models through 2020, which reflects the willingness of the automotive industry as a whole toward the EV transition. Although the transition in the automotive industry away from internal-combustion-engine (ICE) vehicles is well underway, there still are challenges and barriers to overcome for meeting the goals, as the electric vehicle fleet only reach 1% or less of the global vehicle fleet up to now with expectation for it to rise up to 31% by 2040.[1]

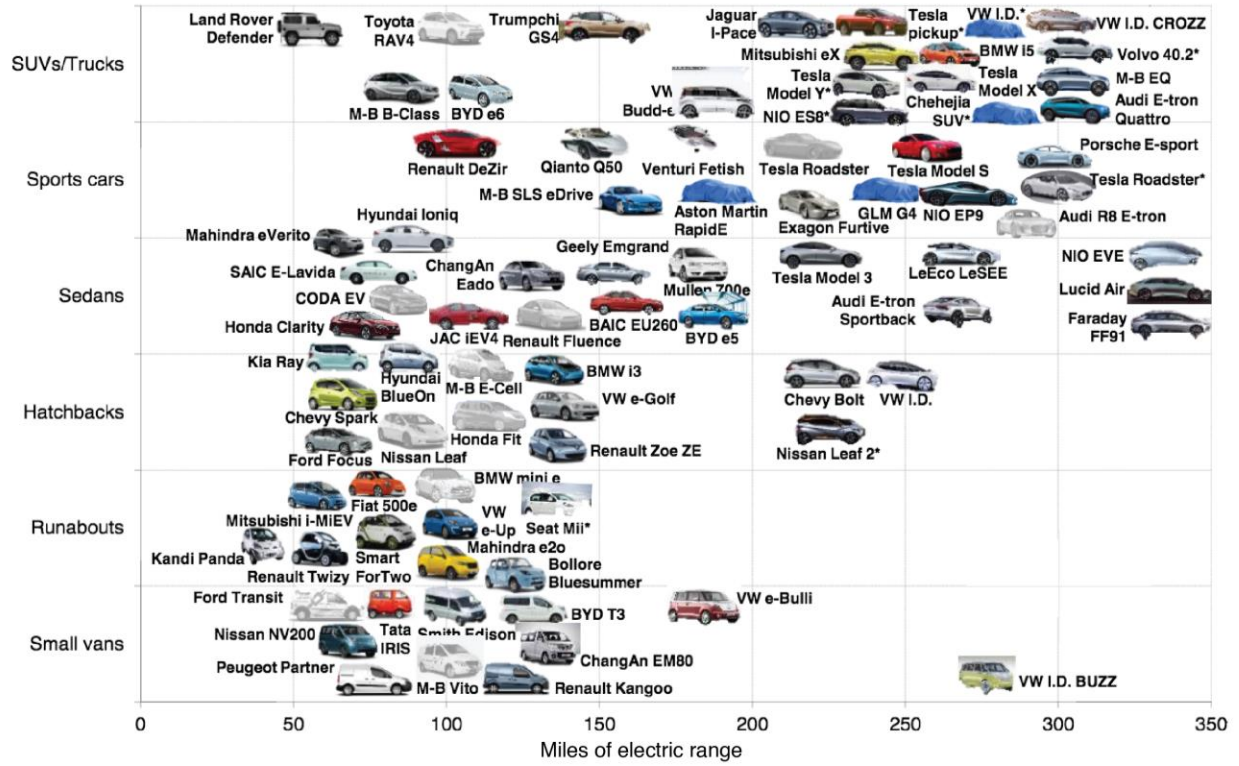

Figure I-3. Electric Vehicle boom. Model by style and range available through 2020. Sources: BloombergNEF.

Compare to conventional vehicles using ICE, the complexity of the mechanical architecture of EVs is significantly less, as the electric powertrain consists of less components with better energy efficiency (Figure I-4a). For instance, the electric machine used as an engine in EVs already reach up to 94% of energy efficiency compared to that of the ICE being anywhere between 10% and 45% (Figure I-4b). Moreover, EVs also use regenerative braking to recapture and reuse energy that normally would be lost in braking and waste no energy idling. As a result, EVs have a better power to the wheels efficiency (77%-90%) when comparing to gasoline-powered vehicles (16%-25%).[2]

Give their high power to the wheels efficiency, there is not much room for that for EVs. Under this situation, among the component on the electric drive system, the energy loss in the electrochemical devices remains somewhat important.

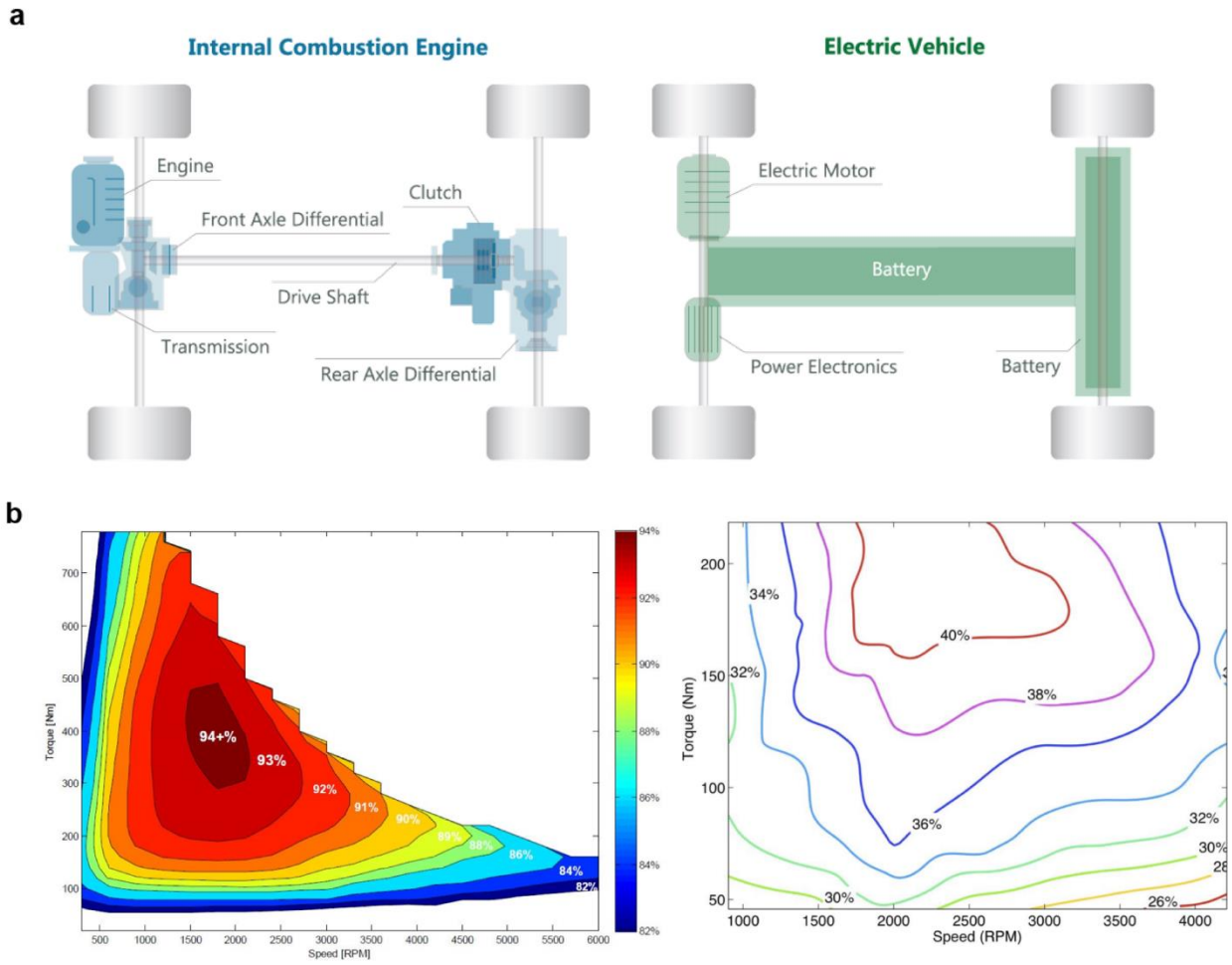

Figure I-4. Comparison between ICE and Electric Vehicles. a. The mechanical architecture of the two types of vehicle. **b.** The efficiency map of the ICE (left) and the Electric motor (right).

That is to say, the electrochemical devices providing energy are the most critical puzzle that needs to be solved before triggering the EV transition. Among different electrochemical devices, Li-ion batteries (LiB) have become an important secondary (rechargeable) battery technology and are widely used in portable electronics and a growing number of electric vehicles. It has shown a high potential to substitute fossil fuel to power the vehicles, as they possess a high energy density with an ability to be scaled-up for mass production, while there is still room for cost reduction. With the rapid growth of the use of LiB, the battery cost will be less than $100/kWh by 2030 (Figure I-5) that makes the cost competitive with that of ICE vehicles.

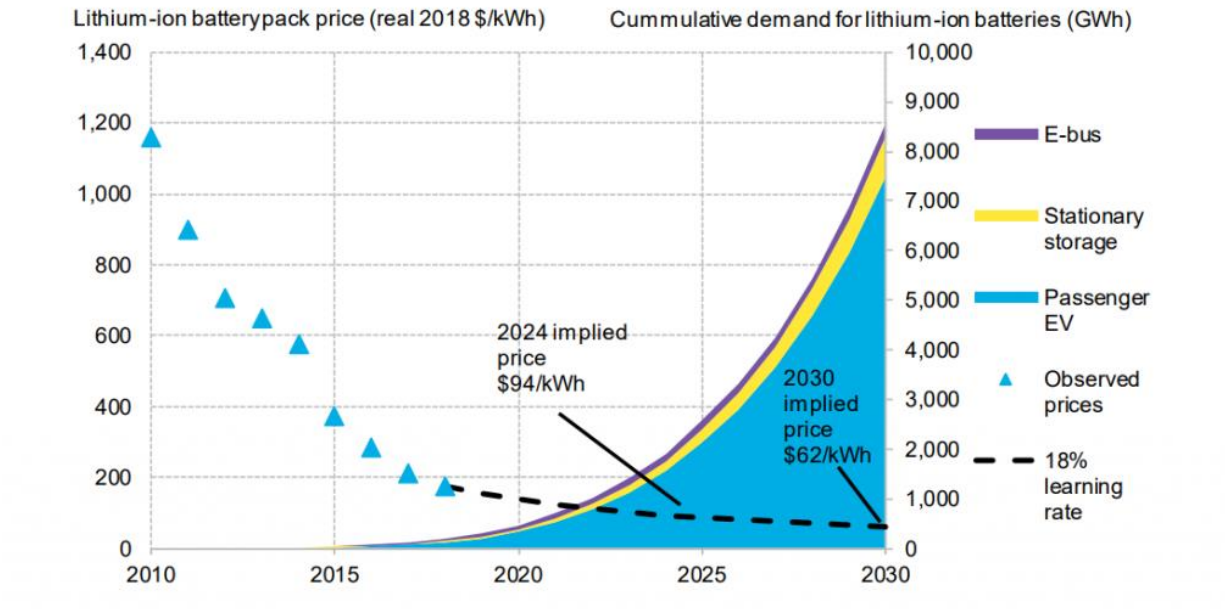

Figure I-5. LiB cost and demand roadmap. The cost of the LiB pack is projected to be lower than 100$/kWh with the increase of its demand for e-mobility. Sources: Bloomberg NEF.

Therefore, the significant remaining challenges are: driving range and charging time without compromising safety. In light of this, not only the academic researchers but also industry sectors such as battery suppliers as well as car manufacturers, have put huge efforts into solving these two challenges. Align with this global interest, this work is carried out to contribute to a deeper understanding of the LiB in order to get closer to the target.

I.3 Scope of the work

Although scientists from academia and industry are already exploring new technologies that could provide higher energy density, referred to as "Post LiB", one should not underestimate the time it takes for technology adoption, as every new technology has to go through "hype cycles" as they go from initial scientific breakthroughs to widespread use. Sapunkov *et al.*[3] developed a qualitative version of the hype cycle chart placing the various battery technologies, as shown in Figure I-6. Moreover, it has historically taken 4-5 years to develop a new vehicle model in the automotive industry. The move to electrification is shortening these timelines, but safely getting below 3 years is difficult, and that is only after the battery has already passed a rigorous test cycle.

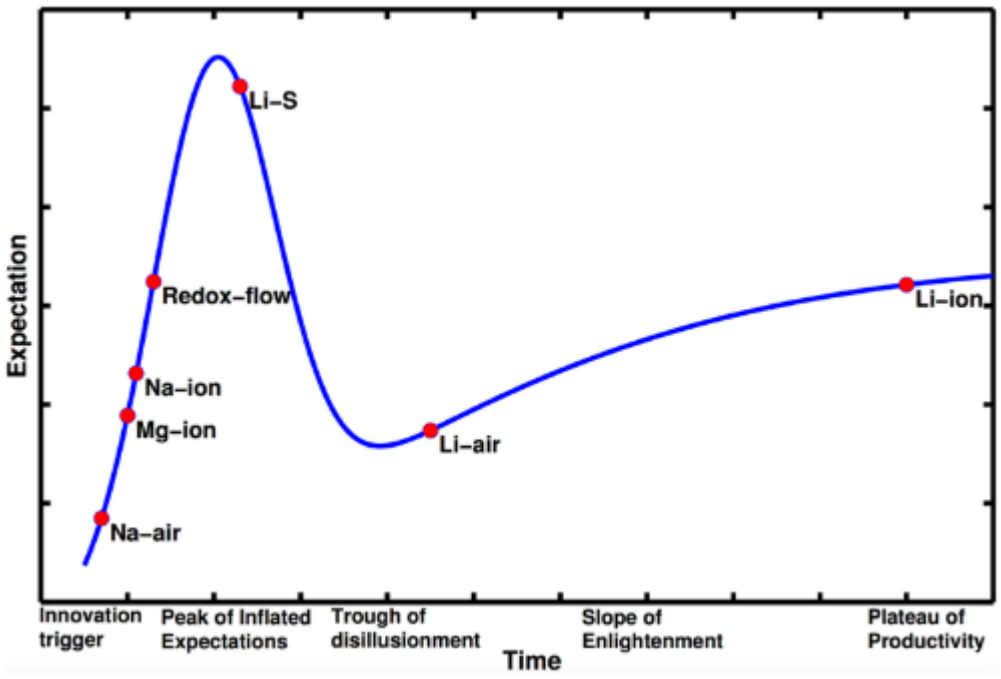

Figure I-6. The « hype cycle » of the battery technologies. A typical technology goes through five phases: (i) innovation trigger, (ii) peak of inflated expectations, (iii) trough of disillusionment, (iv) slope of enlightenment and (v) plateau of productivity. Na–air, Mg–ion, Na–ion and redox-flow batteries are still in the innovation trigger phase. Li–S and Li–air have moved past the innovation trigger, and it is still debated which one of the two will emerge as a practical battery. Li–ion batteries are well into the plateau of productivity, with the costs of these cells decreasing substantially over time. Sources: Sapunkov *et al.*[3]

Thus, in a short-term perspective, one has to keep relying on LiB technology, especially when there is still room for improvement of LiB. This is the main reason for what our focus aims to enhance the LiB performance with today's materials from an engineering aspect. Figure I-7 shows the evolution of the energy density that decreases with AM weight fraction when going from the level of the materials to the final application. Different initiatives can be considered at different levels to improve battery performance across the manufacturing process.

For instance, Tesla suggested a new cell design with the "tabless" concept in a recent patent.[4] This solution is set to reduce the Ohmic's loss due to the electronic transport in the current collector along with the reduction of heat generation. On the other hand, CATL introduced a new process that allows the fabrication of pack directly from the cell without the need of a module system (Cell to Pack, no module technology). The manufacturer claims that it allows increasing the energy density of the pack by 10%-15% while ensuring the functionality to be the same as the old design with modules.

Alternatively, this work seeks to optimize high-energy-density electrodes' performance through improvements at the electrode level, *i.e.* electrode design.

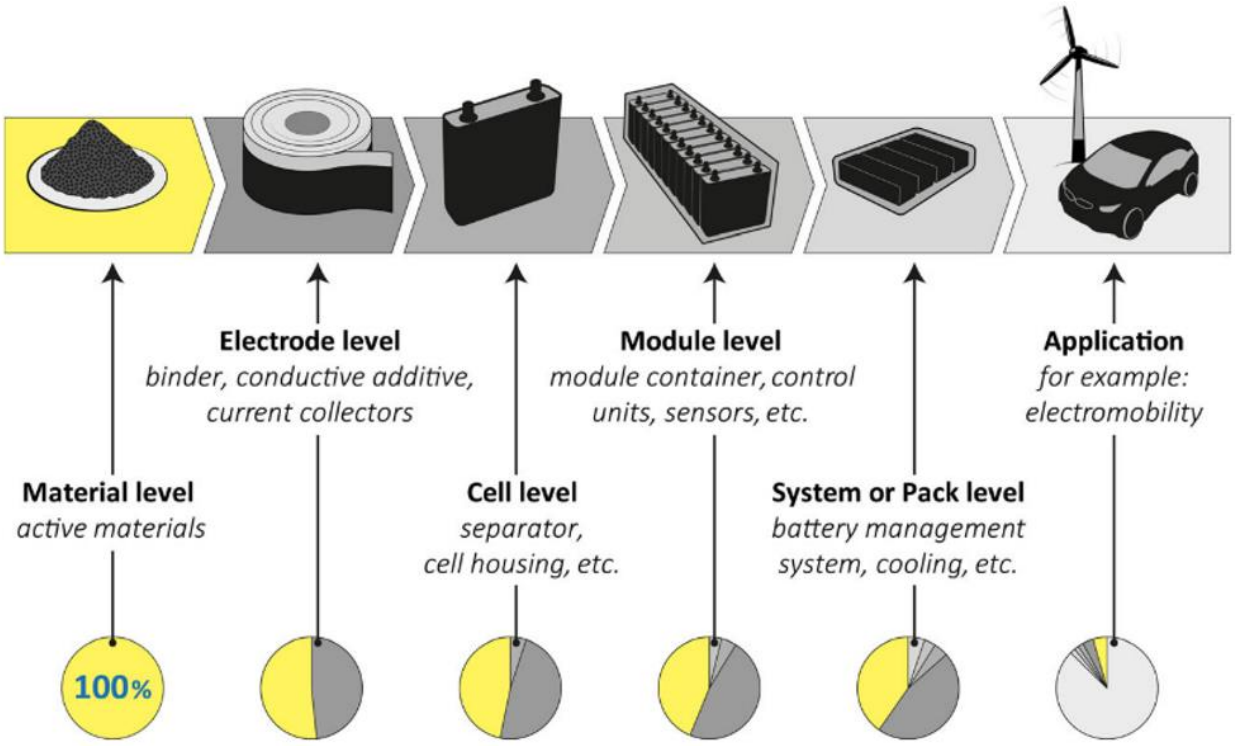

Figure I-7. The evolution of active material weight fraction across the product development process. The active material weight fraction decreases as we get closer to the final product due to the increase of inactive materials such as cell housing, sensors, control unit, cooling system. Source: European Commission.

I.4 Enhanced Li-ion Battery - from electrode microstructural design aspect

At the electrode level, it turns out that two different factors contribute to the electrode performance, namely intrinsic materials properties and electrode microstructural design. Several works highlighted the vital role of the electrode microstructure towards electrochemical kinetics, mechanical, and transport properties, which significantly impacts the electrode performance in terms of energy density, power capability, and lifetime.[5–13] The electrode microstructure optimization should be independent from the selection of active materials and can be applied to both electrodes. In light of these concepts, this work attempts to improve the performance of high energy density electrodes through electrode design optimization rather than improving with the characteristics of the materials.

For this purpose, it is crucial to understand how the electrode microstructural properties affect its electrochemical performance, so as to establish a microstructure-performance relationship. This can shed light on the research for an optimal electrode microstructure suitable for electric vehicles. But first, it requires the ability to accurately determine the microstructural properties over a wide range of scales as well as the electrochemical properties. Even after getting those information, the interplay between these two aspects is not straightforward to unravel, as the effects from the electrode microstructure can strongly overlap within an operational cell and together affect the

battery performance. To understand this interplay, physics-based numerical models stand as a powerful tool to quantify the effects of different limitation sources on the performance.

Since the target application for this work is high energy density battery for the automotive industry, industry-grade electrodes with high energy density are studied in this work.

I.5 Overview

The rest of the dissertation is organized as follows :

Background. Chapter II gives an overview of the fundamentals of the LiB studied in this work. It includes an explanation of the operating principle and a brief review of different limitations found within a cell. This is followed by a brief review of the microstructural design of the electrode. The remainder of this chapter is dedicated to different approaches used in this work. It includes tomographic-based methods to access the electrode microstructure and LiB physics-based models to get further insights into the interplay between microstructure and performance.

Electrode tortuosity factor. Chapter III introduces the electrode tortuosity factor concept, which exhibits conceptual differences from the conventional tortuosity factor. Therefore, several key issues with the conventional "flow-through" type tortuosity factor are highlighted when used to characterize electrodes. This chapter presents a numerical approach based on simulations performed on numerically-generated microstructural images, demonstrating that the new concept of electrode tortuosity factor captures the transport processes relevant to porous electrodes (PE) better than the "flow-through" type tortuosity factor.

Heterogeneity quantification by image-based approach (X-ray nano-holotomography). In chapter IV, a quantitative phase-contrast X-ray nano-holotomography technique is used as a straightforward approach to capture the 3D electrode microstructure. A complete characterization of microstructural properties from tomographic data is carried out. The microstructural heterogeneities are quantified, and a comparison between different electrodes is made. Based on the analysis, different scenarios are also discussed to better understand the microstructure's impact on the electrochemical performance.

Image Quality Assessment for tomographic images. In this chapter, we tackle the uncertainty issue when using the image-based approach to determine microstructural properties. This chapter presents a method based on convolutional neural networks that can guide the image enhancement process and conduct reliable segmentation results with respect to subjective human opinion. The uncertainties relating to the raw image processing step can, therefore, be reduced. As a result, image processing can turn into a very robust, observer-independent process.

The use of physics-based battery model to validate the experiments. In chapter VI, a physics-based model is developed to analyze the discharge behavior of industry-grade $LiNi_{0.5}Mn_{0.3}Co_{0.2}O_2$ (NMC532) electrodes. A parametrization process relying on appropriate experimental

measurements is performed for the active material and each electrode. The model allows quantifying the effects of different limitation sources on the electrode performance. Thus, it is possible to unveil the rate-limiting processes in a given situation, facilitating the rational design of electrodes and cell optimization.

Operando 3D XANES for Visualization of State-Of-Charge Heterogeneity within High-Energy-Density NMC Electrodes. In chapter VII, we perform X-ray Absorption Near Edge Structure (XANES) coupled with transmission X-ray computed tomography (XCT) at the nanoscale in *Operando* mode to capture the electrode microstructure and chemical information during high-rate electrochemical operation. The goal is to propose a more efficient approach to directly unveil the effects of the microstructural heterogeneities on local electrochemical performance. For the first time to the best of the author's knowledge, there is an attempt to work with electrodes similar to real-life designs (%v AM > 60%) and a high operating current density.

Conclusions and Perspectives. Chapter VIII summarizes the main lessons from this work and some suggestions for additional microstructure characterizations and cell modeling in the future. It helps for improved manufacturing process, microstructure, and performance.

References

[1] BloombergNEF, “Electric Vehicle Outlook 2020,” can be found under https://about.bnef.com/electric-vehicle-outlook/, **2020**.

[2] “Compare Cars,” can be found under https://fueleconomy.gov/, **n.d.**

[3] O. Sapunkov, V. Pande, A. Khetan, C. Choomwattana, V. Viswanathan, *Transl. Mater. Res.* **2015**, *2*, 045002.

[4] Tesla Motors, *A Cell with a Tabless Electrode*, **n.d.**

[5] R. Xu, Y. Yang, F. Yin, P. Liu, P. Cloetens, Y. Liu, F. Lin, K. Zhao, *J. Mech. Phys. Solids* **2019**, *129*, 160.

[6] M. M. Forouzan, B. A. Mazzeo, D. R. Wheeler, *J. Electrochem. Soc.* **2018**, *165*, DOI 10.1149/2.1281809jes.

[7] G. Gaiselmann, M. Neumann, V. Schmidt, O. Pecho, T. Hocker, L. Holzer, *AIChE J.* **2014**, *60*, 1983.

[8] A. H. Wiedemann, G. M. Goldin, S. A. Barnett, H. Zhu, R. J. Kee, *Electrochim. Acta* **2013**, *88*, 580.

[9] J. Eller, M. Ebner, C. Burns, J. Dahn, V. Wood, *J. Electrochem. Soc.* **2018**, *165*, 339.

[10] M. M. Sebdani, M. Baniassadi, J. Jamali, M. Ahadiparast, K. Abrinia, M. Safdari, *Int. J. Hydrogen Energy* **2015**, *40*, 15585.

[11] X. Lu, A. Bertei, D. P. Finegan, C. Tan, S. R. Daemi, J. S. Weaving, K. B. O. Regan, T. M. M. Heenan, G. Hinds, E. Kendrick, D. J. L. Brett, P. R. Shearing, *Nat. Commun.* **2020**, *11*, 1.

[12] S. Wen Peterson, The Effect of Microstructure On Transport Properties of Porous Electrodes, **2015**.

[13] S. L. Morelly, N. J. Alvarez, M. H. Tang, *J. Power Sources* **2018**, *387*, 49.

Chapter II . Background

II.1 Li-ion Battery Fundamentals

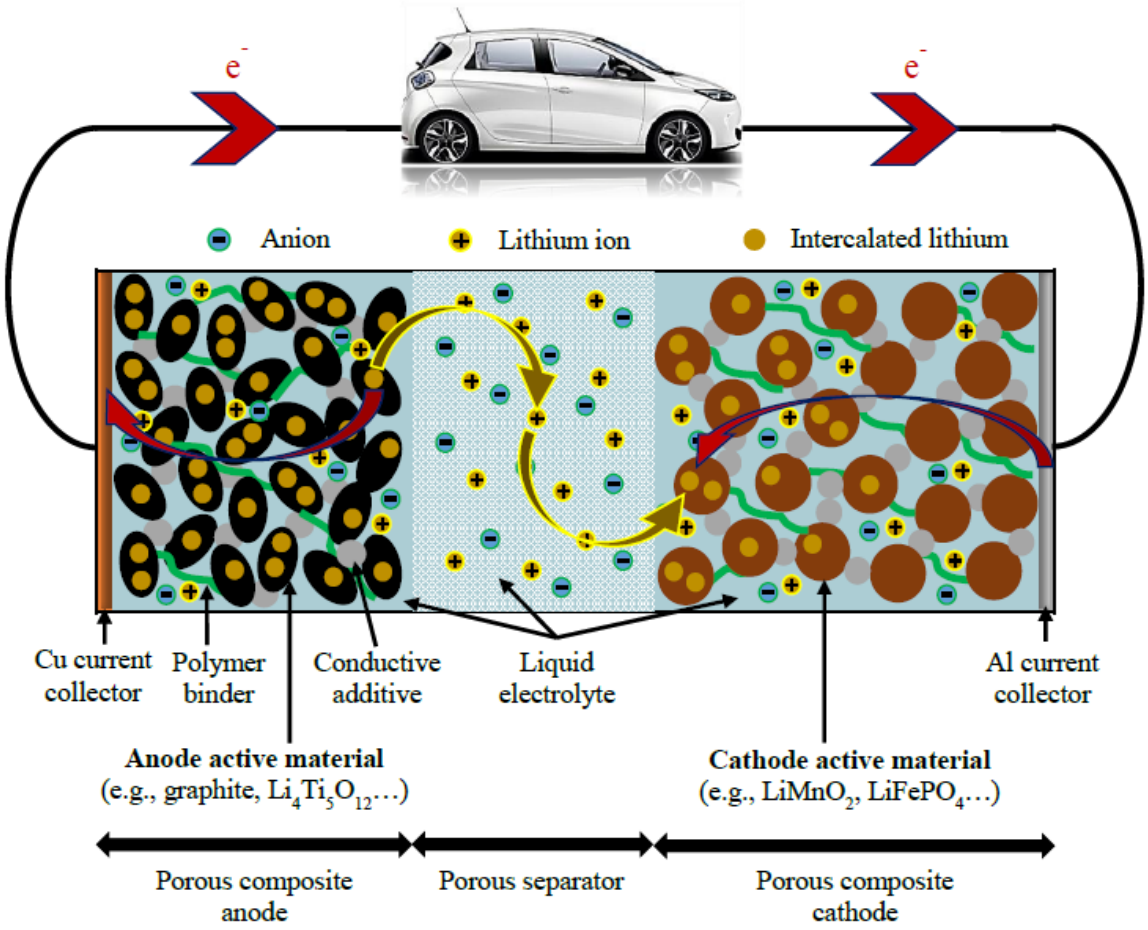

Figure II-1. Overview of the Li-ion Battery system that operates the Electric Vehicle. Source: Malifarge, PhD Thesis.[1]

The LiB was first commercialized by Sony in 1991. A typical LiB is composed of a positive electrode (cathode), a negative electrode (anode), a separator and an electrolyte. This so-called "rocking chair" secondary battery, is based on the reversible exchange of lithium between two insertion materials that operate at different potentials. Commonly, the electrode microstructure is a mixture of different phases: active materials (AM), additives such as a mixture of conductive carbon (*e.g.*, C65) and binder (*e.g.*, Polyvinylidene Fluoride (PVdF)), and pores, which are eventually filled with an electrolyte. The conductive carbon is added to improve the effective electronic conductivity of the electrode, whereas the polymeric binder increases the mechanical stability of the electrode. The composite mixture is coated onto a current collector consisting of a copper foil at the anode and an aluminum foil at the cathode. A porous polymer membrane (*e.g.*, polypropylene) is inserted between the two electrodes. Both electrodes and the separator are filled with a liquid electrolyte generally made up of a mixture of linear and cyclic carbonates (*e.g.*, diethyl carbonate (DEC), dimethyl carbonate (DMC) and ethylene carbonate (EC)) and a lithium salt (*e.g.*, lithium hexafluorophosphate ($LiPF_6$)).

A schematic diagram of a LiB discharge is represented in Figure II-1. Upon discharge, the AM at the anode de-inserts lithium while releasing electrons, whereas that at the cathode inserts lithium. Electrons generated by the oxidation at the anode are collected and pass through an external circuit to the cathode while ions move across the electrolyte to the same direction. The process is reversed during the charge. Meanwhile, during charge and discharge, cathode and anode potentials vary depending on the degree of Li insertion. The resulting cell potential is controlled to remain between two cut-off potentials above and below, which help to prevent irreversible reactions that could deteriorate cell performance and may lead to safety issues.

In the final application, this safe potential window is usually further shortened to ensure battery operation at constant performance over the battery life.

At equilibrium, the LiB electrode behavior represents the inherent properties of the AM present inside. However, the experimental potential responses under current show a deviation from that at equilibrium, due to polarizations arising from electrochemical processes.

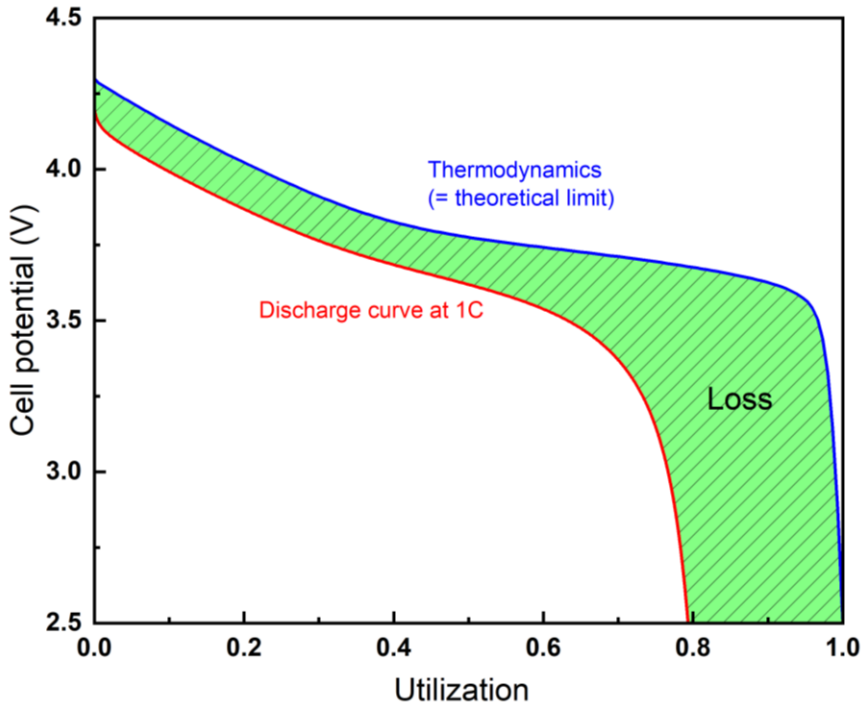

Figure II-2. Losses of a half-cell LiB system (Li foil | Separator | Working Electrode). Equilibrium potential curve vs Discharge curve at 1C. Different contributions to the polarization that induces the overall loss.

Figure II-2 shows the equilibrium potential curve (versus Li foil) of a NMC electrode used in this work along with its lithiation response (versus Li foil) at current 1C, in which the dashed region represents the overall loss. The overall loss, in turn, depicts the polarizations arising from different processes occurring during the operation. Let aside the contribution from the separator properties and from the Li foil, the magnitudes of these polarizations depend upon either the

intrinsic properties of the composite materials or the electrode microstructure. In essence, they can be resolved into four different mechanisms as follows:[2–4]

- Loss by solid diffusion inside the AM particles
- Loss by mass transport in liquid phase
- Loss by electrochemical reaction kinetics at solid/liquid interface
- Loss by electronic transport in solid phase (including inadequate contacts between different phases).

II.1.1 Loss by solid diffusion inside the AM particles

The AM is a host accommodating Li-ions during the (dis)charge process through an intercalation mechanism. Since the AM is generally a good electronic conductor, one assumes that all current is carried by electrons in the solid phase after the intercalation. An electron will move along with a Li-ion inside the AM (*i.e.*, ambipolar motion), such that there is no migration term in the flux density expression, as the diffusing species is neutral $<Li^+,e^->$, not Li^+.

The solid-state diffusivity of an AM can be represented by the Fickian or chemical diffusion coefficient, D_s. This coefficient is related to the thermodynamic diffusion coefficient, D, derived from the Stefan-Maxwell equations, by the relationship for concentrated solutions:

$$D_s = D\,\frac{\frac{c_{s,T}}{c_{s,max}}\left(1+\frac{d\ln f_{\pm}}{d\ln c_s}\right)}{1-\frac{d\ln c_{s,max}}{d\ln c_s}} \qquad \text{(Eq. II-1)}$$

where $c_{s,T}$ is the total concentration of the active materials, $f_{\pm}$ is the mean molar activity coefficient of the electrolyte, $c_{s,max}$ is the maximum concentration of intercalated Li in active materials particle, c_s is the intercalated Li concentration within active materials particle.

D may vary with the Li concentration inside the particles, as the available vacancies in the lattice to accommodate Li-ions varies. It also depends on the materials crystallographic structure, that can change during operation.[5] Therefore, Fickian diffusion coefficient can also vary significantly with Li concentration via Eq. II-1. Approaching the full lithiation state, the available vacancy concentration decreases significantly, resulting in a significant drop in the thermodynamic diffusivity of the AM, so does the Fickian diffusion coefficient.[5]

The solid diffusion limitation can be characterized through the characteristic time, T_{AM} (s):

$$T_{AM} = \frac{R_p^2}{D_s} \qquad \text{(Eq. II-2)}$$

where R_p is particle radius, which is also the diffusion length in the AM particles.

Notably, the diffusion path length appears with a square exponent. Thus, the loss by solid

diffusion can be significantly reduced with the particle size.[6]

II.1.2 Loss by mass transport in the electrolyte

This loss arises from the mass transport in the electrolyte (liquid phase) filling in pore space in order to access the reaction sites. Porous structure obstructs the mass transport of liquid phase, resulting in effective transport properties, which differ from the bulk properties. Thus, this loss contributes to the porous electrode effects along with the loss by electronic transport across the solid phase.

The mass transport limitation can be characterized through the characteristic time, T_{elyte} (s):

$$T_{\mathrm{elyte}} = \frac{L_{\mathrm{elyte}}^2}{D_{\mathrm{eff}}} \qquad \text{(Eq. II-3)}$$

where L_{elyte} is the diffusion length in the electrolyte filled in pore space and D_{eff} the effective Fickian diffusion coefficient of the binary electrolyte.

Moving towards high-energy-density electrodes (either by increasing the electrode thickness and/or decreasing the porosity), one will have to deal with the power limitations which mainly arise from mass transport limitations in the liquid phase within the porous electrode.[4,5,7–9]

II.1.3 Loss by electrochemical reactions at solid/liquid interface

The loss is related to the charge transfer process occurring at the AM/electrolyte interface due to the electrochemical reactions. It represents the kinetics of electrochemical reactions, which vary as a function of the intrinsic reaction rate of AM. Particle radius can have an impact on this loss as it is connected to the active surface area. Lowering the particle size enables a high AM/electrolyte interfacial area within a given geometric dimension of the electrode. It reduces the local current density per active surface area for a given total operating current.

II.1.4 Loss by electronic transport across the solid phase (including inadequate contacts between different phases)

The loss is attributed to the electronic transport in the solid phase (mixture of AM and additives) to access the reaction sites. It results in an Ohmic loss contributing to the overall polarization. Furthermore, additional Ohmic loss can appear due to the contact resistances that might take place at the interface of different phases. The contact resistance between the current collector and the porous film has also been reported in previous works.[10,11] The contact resistance between the conducting matrix (carbon binder domain) with the AM phase might also result in overpotential.[12]

II.2 Li-ion Battery Microstructure Design

As mentioned above, porous structures are widely used for making electrodes since they can massively increase the specific interfacial area between phases, which increases the accessible capacity of the AM at high C-rates. However, the trade-off is the complexity of the electrode microstructure, as it adopts a hierarchical architecture.[10,13,14] The microstructure has been reported to play a crucial role in the performance of lithium-ion battery electrodes, as it affects the effective electronic/ionic transport properties through the morphology of the pore network and the conducting matrix;[15–19] the electrochemical kinetics via the interfacial area between phases;[20,21] as well as the mechanical properties.[22]

Therefore, the research for an optimal electrode microstructure needs to consider simultaneously different aspects, making it a non-trivial issue. For instance, an "ideal" CBD morphology does not only need to ensure good electronic conductivity, *i.e.* simply increase the %v of CBD would not be an obvious solution to improve the overall performance. The microstructures of the electrodes used in this work are investigated in detail in Chapter IV, in which we demonstrated that the excess of conductive carbon could negatively affect the active surface accessibility for ions. Furthermore, the CBD has been shown to be porous, which can locally increase the tortuosity of the ionic conducting pathway reducing the ionic transport properties.[18]

Several works reported different approaches to optimize the electrode design for better performance.[23–30] Lu *et al.*[23] demonstrated numerically that graded-porosity designs (with the higher porosity layer at the separator side) could be used to increase the accessible capacity of an electrode. Other works have employed ultra-fast laser ablation to create structured electrodes (NMC and Graphite) to improve the ionic transport within the porous electrodes, which results in higher areal specific capacities at higher current rates, especially for the thick and low-porosity electrodes.[27–30]

In light of this, our work in Chapter III also highlights the vital role of "dead-end" pores within the region near the separator to improve the power capability of high energy density electrodes.

II.2.1 Macro-homogeneous Parameters For Porous Structure Characterization

To reflect the microstructural properties of porous electrodes for battery modeling, most models apply a macroscopic treatment in which the electrode geometry is considered homogenous, and the exact geometric details are disregarded. In such a way, the electrode complex microstructure is reduced into a few macro-homogenous parameters such as porosity, ε; macroscopic specific active surface area (ASA), a_{ASA} ($\mathrm{m}^2_{\mathrm{ASA}}/\mathrm{m}^3_{\mathrm{PE}}$) ; and an electrode tortuosity factor, τ_{e}. These metrics represent the effective properties (volume-averaged) of the electrode structure.

Porosity ε is defined as the ratio of void volume over the total volume of the porous electrode and is mainly controlled by the slurry formulation and the calendering steps. For LiB porous

electrodes, pore space will be filled with electrolyte providing ionic conducting network. Porosity can be readily calculated by knowing the composition, densities, weight, and volume of the porous electrode:

$$\varepsilon\ (\%) = 1 - \frac{m_{\mathrm{PE}} \sum_{\mathrm{i}} \frac{\%w_{\mathrm{i}}}{\rho_{\mathrm{i}}}}{A_{\mathrm{CC}} L_{\mathrm{PE}}} \qquad \text{(Eq. II-4)}$$

where $\%w_{\mathrm{i}}$, ρ_{i} are weight fraction and density of phase i presented in the PE, A_{CC}, L_{PE}, and m_{PE} are the macroscopic current collector surface area, thickness and weight of the porous electrode.

However, Eq. II-3 provides the total porosity, which comprises open and connected pores that contribute to ionic transport as well as closed and isolated pores that are strictly not filled with electrolyte. More specific methods for probing the "open" porosity can be used, such as intrusion mercury porosimetry or Helium pycnometry. To get the pore size distribution of all open pores, a combination of different methods might be required since each method cannot cover the entire range of pore size that exist in the porous electrode. In the battery industry, porosity is controlled by the composition of a slurry, its drying, and subsequent compressing of the electrode, so-called calendering.

Macroscopic specific active surface area a_{ASA} represents the available surface area on the AM particles for electrochemical reactions. It can, in principle, be explored using imaging techniques, although resolution constraints can be a challenge. Adsorption techniques like Brunauer-Emmett-Teller (BET) method are typically preferred. Nevertheless, there can be a difference between the surface area measured with the BET method and the active surface area used in a macro-homogenous model such as the Newman P2D model, since BET area is a measure of the entire area available for gas adsorption, such as the basal plane of the graphite for instance, the CBD, and will penetrate nanopores that are not accessed by electrolyte, and not only the electrochemically active surface area. Thus, being able to resolve the CBD distribution within the electrode can allow to determine the active surface area parameter accurately.

Compared to the two microstructural properties mentioned above, the tortuosity factor, in turn, bears different definitions, which depends on the different methods for its determination. Since it is an important parameter for correlating electrode microstructure with performance through numerical modeling, it is critical to have an appropriate method for its accurate determination.

In this work, we use the standard definition for the electrode tortuosity factor, τ_{e}, as stated in the following equation:[31–37]

$$\frac{\tau_{\mathrm{e}}}{\varepsilon} = \frac{\rho_{\mathrm{eff}}}{\rho} = \frac{\kappa}{\kappa_{\mathrm{eff}}} = \frac{D}{D_{\mathrm{eff}}} = N_{\mathrm{M,e}} \qquad \text{(Eq. II-5)}$$

Where $N_{\mathrm{M,e}}$ is the MacMullin number; ρ, κ and D are, respectively, the "intrinsic" electrical resistivity ($\Omega.\,\mathrm{m}$), conductivity ($\mathrm{S.\,m^{-1}}$) and diffusion coefficient ($\mathrm{m^2.\,s^{-1}}$) of the bulk electrolyte;

and ρ_{eff}, κ_{eff} and D_{eff} are the observed "effective" values resulting from the transport constraints imposed by a porous (and likely tortuous) microstructure.

This definition for electrode tortuosity factor τ_{e} bears a more physical meaning since it represents the change of transport properties within the porous structure with regard to the bulk, which is intrinsic of the materials.

The MacMullin number in Eq. II-4 is also reported here since it describes the effect of a porous microstructure on the behavior of the liquid phase within the pore network, and as such it also appears in the Newman P2D model through the mass balance in the liquid phase and the Mac-Innes equation for ionic transport.

Geometric tortuosity can also be found in the literature[38,39] that accounts for both the additional path length and its effect on the velocity of a species when going through a porous structure. By definition, the tortuosity factor can be calculated with the square of the ratio between two distances: the shortest pathway (geodesic distance) travelled by a species L_{p} and the straight distance between those two points L_{cv}. However, as Epstein has clarified,[40] this definition does not consider the effect of the non-uniform cross-sectional area of the pathway, which is rarely the case in the highly complex electrode microstructures encountered in porous electrodes (Figure II-3). As such, this definition is not well suited for characterizing 3D pore networks.

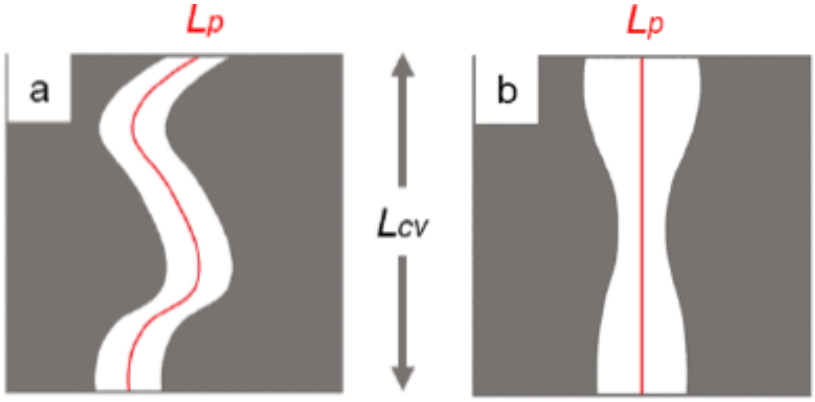

Figure II-3. Geometrical tortuosity factor illustration. a. Pathway with the uniform cross-sectional area. **b.** Pathway with the non-uniform cross-sectional area. The definition of geometrical tortuosity suffers from key conceptual limitations as it ignores constriction in flow paths.

Lastly, the tortuosity factor can also be estimated using the correlation of Bruggeman.[41] However, various assumptions are required to boil down into a simple correlation between tortuosity factor and porosity. Therefore, this correlation, in turn, has some key limitations for the use in the framework of porous electrodes that are reported in detail by Tjaden *et al.* in.[42]

$$\tau_{\text{Bruggeman}} = \begin{cases} \varepsilon^{-0.5} & (spheres) \\ \varepsilon^{-1} & (cylinders) \end{cases} \qquad \text{(Eq. II-6)}$$

For instance, the Bruggeman model assumes that the obstructions to transport consist of either spheres or cylinders. Nonetheless, Figure II-4 shows the particle geometry of Graphite and NMC materials; both are far from these standard morphologies.

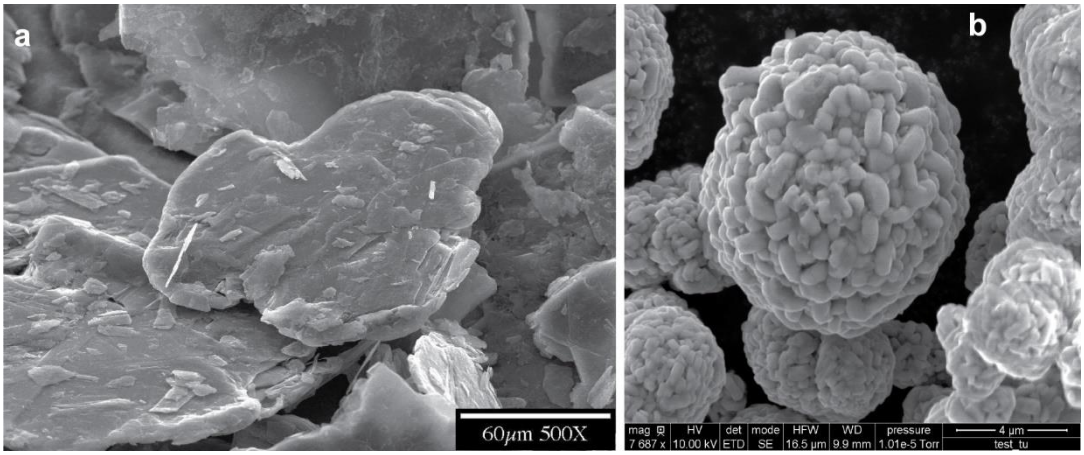

Figure II-4. The geometry of the AM particles. a. Natural crystalline flake Graphite particle. **b.** NMC secondary particles used in this work.

II.2.2 Microstructural Heterogeneities

As we demonstrate later in this dissertation, microstructural properties of porous electrodes are frequently non-uniformly distributed. Non-optimized manufacturing process, non-optimized electrode compositions, and degradation over time can cause non-uniform agglomeration of carbon and binder fillers, or sedimentation of big particles, leading to non-uniform distribution of phases. Consequently, at the microscale, microstructural properties such as tortuosity factor, the volume fraction of phases, inter-connectivity between phases can vary between different regions across the electrodes (in-plane and through-plane).[43–45]

Nevertheless, capturing the non-uniformities requires a multi-scale investigation, as the electrode adopts a hierarchical architecture. In essence, characterization techniques performed at the macroscopic scale (*i.e.* electrode level) allows only macro-homogenous parameters determination.

Non-uniform distribution of phases herein referred to as microstructural heterogeneities, are part of our focus in this dissertation. They have been demonstrated to induce a non-uniform electrochemical behavior, which can deteriorate the final performance and cause macroscopic failures.[22,46–49] In order to quantify the effects of microstructural heterogeneities on electrochemical performance, appropriate physics-based models along with accurate microstructural properties are required. Chapter IV addresses the challenge of microstructural properties determination using the holotomography XCT technique. A physics-based model that can take these outputs into account still needs further investigations.

II.3 3D Imaging Techniques

Since it is of particular importance to access the complex microstructure of a porous electrode to understand its effects on electrochemical performance, over the last decades, tomography techniques have been emerged as a powerful tool to this end.

Tomography, from the Greek words *tome* meaning “slice” and *graphos* meaning “to write”, describes a family of methods that allow objects to be imaged in the three dimensions. More generally, tomography techniques involved using hundreds or thousands of 2D images to reconstruct the 3D volume.

These techniques provide interesting quantitative and/or qualitative metrics that shed light on the effects of the microstructure on the final performance.[50,51] In particular, they allow for spatial analysis of the distribution of the different phases within the electrode, which is not accessible from regular electrochemical measurements.[31,47]

Focused ion beam - Scanning electron microscopy (FIB-SEM),[20,50,52,53] and XCT including µCT[54–57], and nanoCT[46,58–63] are the most commonly used 3D techniques to study the microstructure of batteries.

The FIB-SEM technique usually offers a higher spatial resolution (*ca.* 5-10 nm pixel size) than XCT, but only a small volume (*ca.* 10x10x10 μm^3) can be acquired under reasonable time and labor. It uses a focused Gallium-ion beam to mill the sample sequentially, the ion beam pauses after each milling to allow capturing the 2D cross-sectional image by SEM. Then, the ion beam is moved with resolution up to 10 nm step by step relative to a reference mark milled on the sample. The 3D volume is simply obtained by combining the series of cross-sectional images through the sample depth. However, the technique is inherently destructive, preventing all subsequent studies of the microstructure if needed.

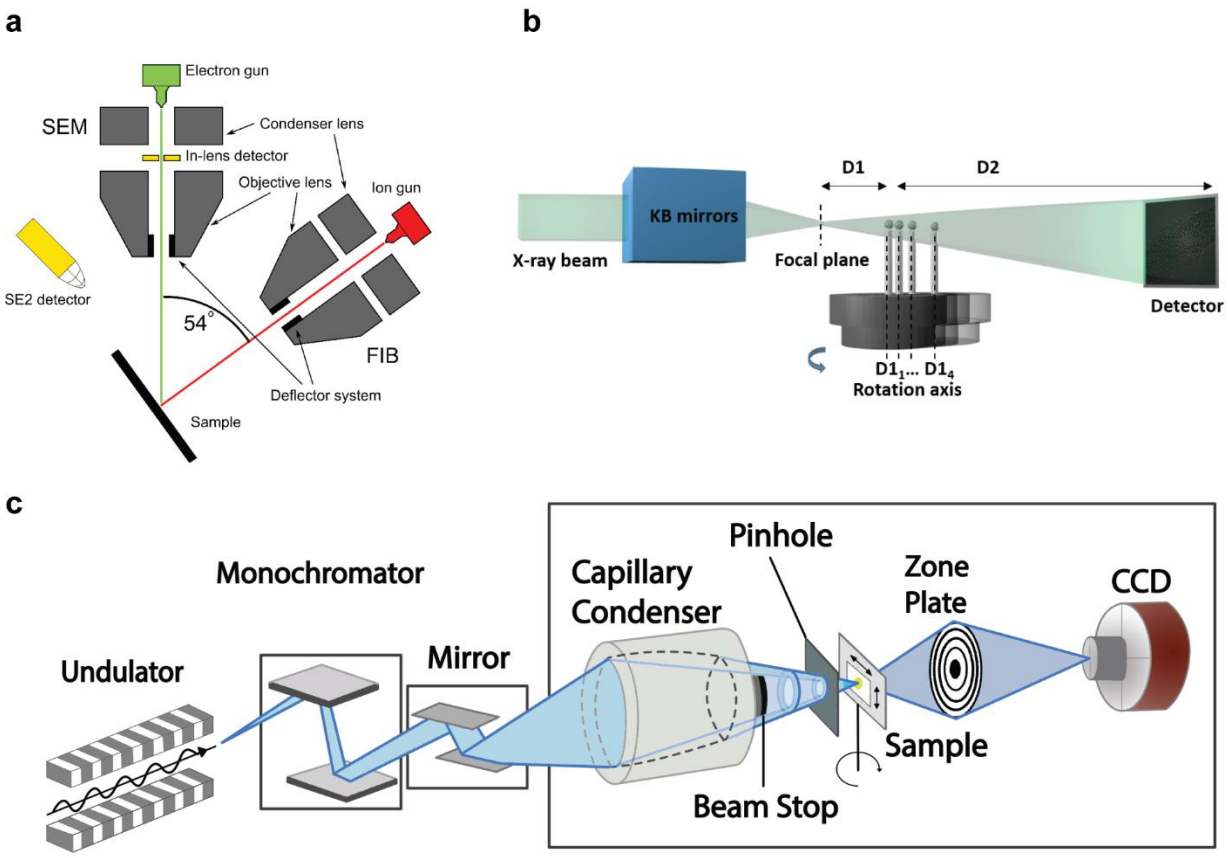

Figure II-5. 3D Imaging techniques. a. Schematic of a dual-beam FIB-SEM setup. **b.** Schematic representation of the hard X-ray nano-holotomography experimental setup at ID16B (ESRF). **c.** Schematic representation of nano-XCT setup at 32ID-C (APS).

An alternative to FIB-SEM, XCT offers a non-destructive approach, relying on the interactions between materials in the sample and the incident X-ray beam. The interaction of X-ray with every material can be described through the refractive index n, such as: $n = 1 - \delta - j\beta$, where β is the absorption coefficient and δ is the decrement of the refractive index and refer, respectively, to the change of amplitude and the phase shift of the X-ray, as it passes through the materials. Tomography datasets are collected at different angles by acquiring 2D projection data as the object is rotated about an axis normal to the beam source, and are then reconstructed into the 3D volume using numerical algorithms. Different iterative and noniterative algorithms have been developed to efficiently and accurately perform the task of tomographic reconstruction for different measuring geometries.[64,65] In the vast majority of cases these datasets are reconstructed to form an image using filtered back projection (FBP).

Most XCT experiments rely on attenuation contrast. Materials have different β values, leading to variations in the transmitted X-ray amplitude as a function of material density and thickness in a particular beam direction. Thus, the intensities of the transmitted beam with respect to each material in the sample can be measured and used to reconstruct the distribution of the related material within the sample. Nevertheless, since low-density materials such as the mixture of carbon

conductive and polymeric binder, have low attenuation, their contrast compared to pores in final images is weak. Consequently, image analysis, especially the segmentation step, is challenging, and in most studies, CBD and pores cannot be resolved.

Besides the attenuation contrast information, XCT also probes the phase contrast information, which relates to the decrement of the refractive index, δ. Since it can be a thousand times greater than its absorption factor, phase-contrast between weakly attenuating materials is enhanced. A variety of phase retrieval techniques have been developed. Among the most widely used are Holotomography,[59,60] and Zernike phase contrast.[63,66] However, as the mapping of δ relies on the measurement of interference effects, at least spatially coherent X-ray sources are required for phase-contrast tomography.

The holotomography technique used in Chapter IV and developed by Cloetens *et al.*[60] at European Synchrotron Radiation Facility (ESRF) allows to retrieve the phase quantitatively and get back to absorption-like images. Practically, it consists in acquiring four data sets at four focuses to sample distances ($D1_1$, $D1_2$, $D1_3$, $D1_4$ in Figure II-5b). This four distance scheme is justified by the fact that a spatially coherent X-ray beam illuminating a phase object will extinct some spatial frequencies in the projections, depending on the effective propagation distance.[67] Based on these four data sets, a numerical scheme allows the optical phase to be retrieved giving a single absorption-like image at the highest magnification, corresponding to the distance $D1_1$.

Zernike phase contrast originally proposed by Zernike[66] in 1935 introduces a phase shift between scattered and non-scattered X-rays by inserting a phase ring located after the zone plate. The interaction of the phase-shifted non-scattered and scattered X-rays from the sample produces an image in the detector plane that has the appearance varying with the phase shift of the sample structures. As a result, the contrast between low attenuating materials having different phase shifts can be improved and enhance the appearance of edges and interfaces within the sample.

While µ-XCT offers the capability of analyzing large volumes such as the visualization of an entire device,[57] nano-XCT provides a spatial resolution below 100 nm allowing to access properties at a micro-scale with high reliability.[46,59] Depending on the materials, the trade-off between an appropriate resolution and a large volume (*i.e.*, the representativeness) needs to be considered to obtain reliable results. The principles and applications of modern X-ray tomography are discussed in great detail in [64] [65].

II.4 Li-ion Battery Modeling

In this section, the battery modeling is introduced. Numerical modeling to understand battery performance has a history of more than 50 years. The battery model categories vary widely depending on the applications of interest, they can be classified by either physics-based models or empirical models, but also by their length-scale/time-scale, *e.g.*, from quantum chemical calculations of material properties, through continuum performance models, and to techno-economic analysis of markets.[68,69]

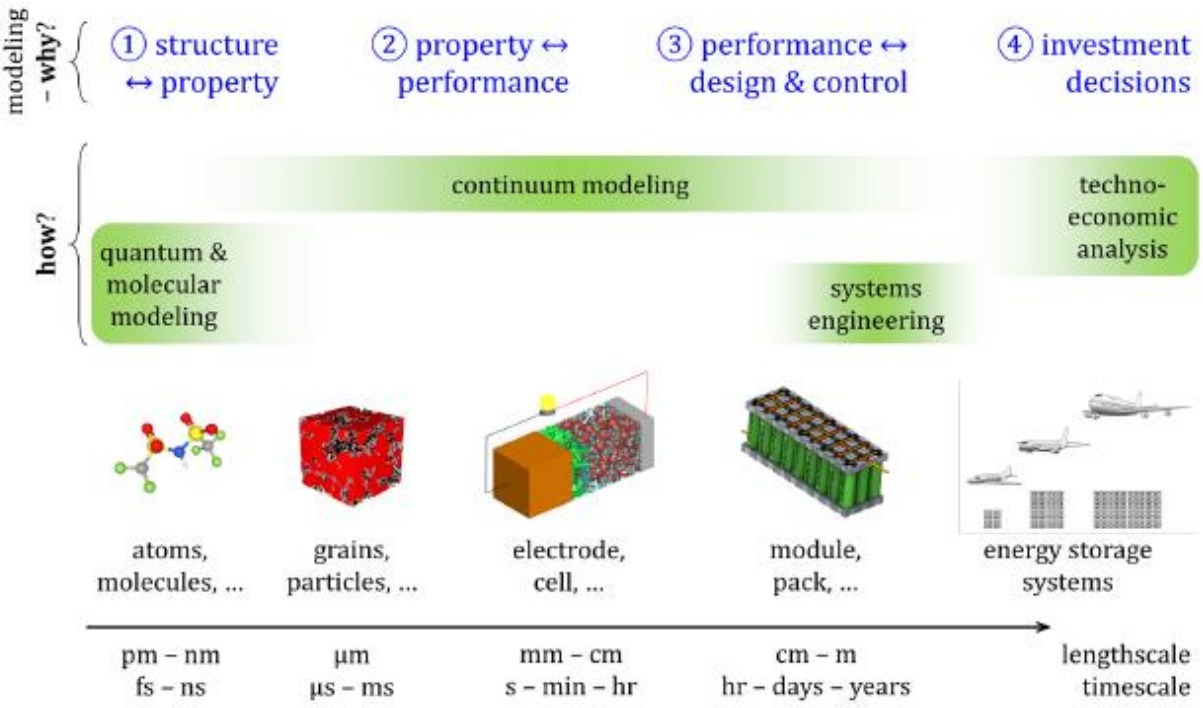

Figure II-6. The spectrum of battery modeling. Models address one of four "why" questions using appropriate paradigms—the "how." Length and timescales of interest are associated with each corresponding paradigm; sometimes, these are (somewhat subjectively) also categorized into micro, meso, and macroscale. Each of these paradigms can be implemented using physics-based and/or data-driven technique. Source: Howey et al.[68]

In general, the model-based approach can be performed cheaply and quickly, which provides a straightforward tool to explore wide new hypothesis or usage scenarios. The insights obtained from the models can be subsequently validated with well-defined experiments. In contrast, for the same achievements, the experimental approach requires a new experiment to be run for every use case of a battery; which, in turn, costs significant time and resources.

In addition, physics-based models allow for a detailed interpretation of the experimental results, as they are able to quantify the contributions of different phenomena involved during the battery operation. They provide further understanding on material behavior and performance-limiting processes (*e.g.*, transport or kinetics), which allows the optimization of the electrode design to improve the performance.

However, one crucial part of the numerical model in general, and physics-based models in particular, is parameterization. To get relevant quantitative conclusions about the contribution of different processes to the electrode performance, it is of particular importance to have an accurate set of parameters for the system under investigation. In most works dealing with physics-based models, values from supplementary literature sources are frequently used for some parameters; while some other parameters are fitted or even guessed. Without a well-determined set of parameters, the investigation using a model-based approach can quickly end up being a fitting

exercise. It can lead to repeated mistakes and the propagation of inappropriate assumptions. Consequently, the potential insights of identifying performance-limiting factors may be compromised.

Nevertheless, performing experiments in which the intended parameters can be accurately identified is a non-trivial issue. In chapter III, we highlight the fact that an appropriate method needs to be used to determine the right parameter that matches the reality used in the model, through the case of the tortuosity factor.

In this dissertation, a parametrization is carefully carried out to characterize first the NMC materials, then each of four industry-graded electrodes. Then, the experimental discharge capabilities of these electrodes are validated against simulations obtained from physics-based macro-homogenous models. Based on the well-known Newman P2D model, which Newman's research group develops at University of California Berkeley, USA[70], a new model that considers the effects of AM agglomerate formation is developed. It demonstrates to be more suitable to represent the experimental results for the set of electrodes studied in this work.

II.4.1 Newman P2D model

Newman P2D model is a physics-based model of the anode/separator/cathode elementary sandwich. The model equations and various model features are described in detail in [2,71–75]. In this dissertation, only the basic model features are described, for the sake of conciseness. The model is based on the porous electrode theory. That is, the PE is treated as a superposition of two continua that are considered to coexist at every point within the electrode. There is one continuum representing the solid mixture including AM, conductive carbon, and polymeric binder, and another one representing the liquid phase (electrolyte). Moreover, the exact geometry details of all the particles and pores in the electrode is disregarded, as they are considered as small enough compared to the volume element dimensions. Thus, each coexisting phase is ascribed macro-homogenous parameters, as described previously.

The model is a 1D + 1D (or P2D) model, *i.e.*, there is a dimension x across the sandwich ("macro" model), and a radial dimension r along the AM particles that are assumed spherical and isotropic ("micro" model).

In the "macro" model, an electronic current density $\vec{\imath}_1$ flowing across the PE thickness in the solid phase is represented by Ohm's law, while an ionic current density $\vec{\imath}_2$ flows similarly in the liquid phase and is expressed according to a Mac-Innes equation, that depends on both potential and salt concentration gradients in the liquid electrolyte. The mass balance is applied on the anion (*e.g.*, PF_6^-), which has an identical concentration as the cation by virtue of electroneutrality. The anion flux density is treated with concentrated solution theory. The foundation of concentrated solution theory is the Onsager-Stefan-Maxwell multicomponent transport framework. In these equations, R is the ideal gas constant, T is the absolute temperature, t_+^0 is the transference number of lithium ions in the electrolyte with respect to the solvent velocity, and c_2 is the salt concentration

in the electrolyte. These two current densities are linked through the so-called pore-wall flux of Li, j_n, representing the rates of the electrochemical reactions at solid/liquid interface, expressed with Butler-Volmer kinetics.

In the "micro" model, given AM is a good electronic conductor, the Li concentration distribution within the AM particles is obtained by solving for a mass balance on "neutral" Li, *i.e.* the <Li^+,e^-> neutral combination. If volume changes in the solid are negligible, and the thermodynamic factor is taken as unity as a first approximation, the material balance boils down to Fick's second law.

The "macro" model connects with the "micro" model through the pore-wall flux of Li^+. The "micro" model represents the particle scale, while the "macro" model relates to the microstructural properties of the electrode. Thus, if the "micro" model can accurately represent the particle behavior, one may want to study the "macro" model to optimize the electrode design.

Figure II-7 summarizes all the equations and the boundary conditions of the Newman P2D model.

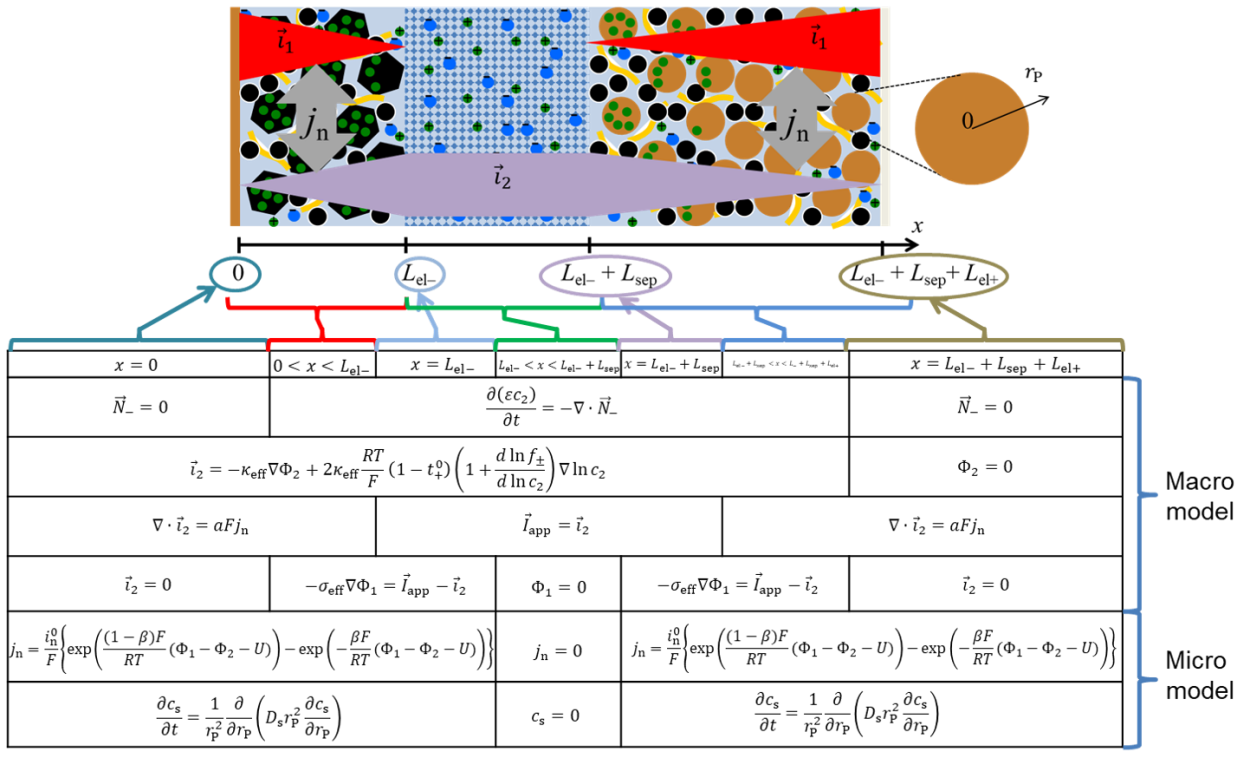

Figure II-7. Elementary sandwich used as the basis for Newman P2D model, which was developed by Newman's research group in the 1990's.[70] Model equations and boundary conditions are provided in the table. Note that boundary conditions for the bottom equation (spherical diffusion in the active particles) are not indicated, for conciseness.

If a lithium foil electrode were used in place of a negative insertion electrode, a half-cell is

modeled with a porous cathode and a porous separator layer. The cathode is in contact with the separator on one end and with the current collector on the other end. Electric current is applied at the interface of the cathode and the current collector.

In the Newman P2D model, a total of *ca*. 20 parameters is required to compute the simulations. Overall, there are six independent variables, namely the salt concentration in a binary electrolyte, c_2; the solid-phase Li concentration within the AM particle, c_s; the pore-wall flux, j_n; the ionic current density, i_2; the electric potential of solid phase, Φ_1; the electric potential of liquid phase, Φ_2; which are defined at each node along the elementary sandwich at each time.

Whenever a constant solid diffusion coefficient is used, methods like the Duhamel superposition[72] or the polynomial approximation[77] are frequently implemented to solve for solid diffusion and obtain the solid Li concentration at the particle surface. With a variable diffusion coefficient, the full solid concentration profile along the radial dimension of the active particle is solved numerically at each node of the sandwich, which makes the calculation more computationally intensive. A control volume formulation is used to solve the set of ordinary and differential equations across the sandwich. More details on the solution procedure may be found in.[2,71,75]

Nomenclature

a_i	$\mathrm{m}_i^2/\mathrm{m}_{\mathrm{PE}}^3$	Interfacial surface area between phase i and the liquid phase at porous electrode scale
$c_{\mathrm{s,surf}}$	$\mathrm{mol}/\mathrm{m}_{\mathrm{AM}}^3$	Concentration of intercalated Li at the surface of the AM particle within porous agglomerate
$c_{\mathrm{s,T}}$	$\mathrm{mol}/\mathrm{m}_{\mathrm{AM}}^3$	Total concentration of active materials
$c_{\mathrm{s,max}}$	$\mathrm{mol}/\mathrm{m}_{\mathrm{AM}}^3$	Maximum concentration of intercalated Li in active materials particle
c_{s}	$\mathrm{mol}/\mathrm{m}_{\mathrm{AM}}^3$	Intercalated Li concentration within active materials particle
$c_{i,0}$	$\mathrm{mol}/\mathrm{m}^3$	Solvent concentration in phase i
c_i	$\mathrm{mol}/\mathrm{m}^3$	Salt concentration in a binary electrolyte in phase i
D1	m	Focus to sample distances
D	m^2/s	Thermodynamics diffusion coefficient of a binary electrolyte
D	m^2/s	Measured diffusion coefficient of a bulk binary electrolyte
$D_{\mathrm{eff},i}$	m^2/s	Effective salt diffusion coefficient of the liquid phase in phase i
D_{s}	m^2/s	Diffusion coefficient of Li in active materials particles
F	C/mol	Faraday's constant
$f_{\pm}$		Mean molar activity coefficient of a binary electrolyte
$\vec{\imath}_i$	$\mathrm{A}/\mathrm{m}_{\mathrm{CC}}^2$	Current density in phase i in the Newman P2D model or at porous agglomerate scale in the PApa model
i_{n}^0	$\mathrm{A}/\mathrm{m}_{\mathrm{ASA}}^2$	Exchange current density at the active surface area across porous electrode
I_{app}	$\mathrm{A}/\mathrm{m}_{\mathrm{CC}}^2$	Discharge current density
j		Imaginary unit

j_{n}	$\mathrm{mol}/(\mathrm{m}_{\mathrm{AM}}^{2} \cdot \mathrm{s})$	Pore-wall flux between active material particles and liquid phase in the Newman model
k_0	$\mathrm{mol}/[\mathrm{m}^2 \cdot \mathrm{s} \cdot (\mathrm{mol}/\mathrm{m}^3)^{1.5}]$	Reaction rate constant of the active materials
L_{PE}	µm	Porous electrode thickness
L_{sep}	µm	Separator thickness
L_{elyte}	m	Diffusion length in electrolyte
L_{p}	m	Shortest pathway (geodesic distance) travelled by a species
L_{cv}	m	Straight distance between two points
L_{s}	m	Diffusion length in solid phase
m	kg	Mass
M	kg/mol	Molar weight of salt in a binary electrolyte
n		Refractive index
$\vec{N}_i$	$\mathrm{mol}/(\mathrm{m}^2 \cdot \mathrm{s})$	Flux density of species i in the Newman P2D model
R	$\mathrm{J}/(\mathrm{mol} \cdot \mathrm{K})$	Ideal gas constant
R	Ω	Sample resistance determined by the µ4-probe experiment
r	m	Radial dimension along the active materials particle
r_{P}	µm	Radius of an active materials secondary particle
T	K	Absolute temperature

T_{AM}	s	Characteristic time of solid diffusion
T_{elyte}	s	Characteristic time of ionic transport in the electrolyte
t	s	Time
t_+^0		Transference number of Li^+ in the electrolyte with respect to the solvent velocity
U	V	Equilibrium potential of the AM vs Li
$\vec{v}_0$	$\mathrm{m/s}$	The solvent velocity
w_i		Weight fraction of phase i
x	µm	Dimension across the sandwich
x_0		Initial Li stoichiometry

Greek symbols

Φ_i	V	Electric Potential of phase i
μ_i	J/mol	Electrochemical potential of species i
ρ_{i}	$\mathrm{kg/m^3}$	Density of phase i
$\tau_{\mathrm{Bruggeman}}$		Tortuosity Factor by Bruggeman
τ_{e}		Electrode tortuosity factor
β		Absorption coefficient
δ		Decrement of the refractive index
ε		Porosity

κ	$\mathrm{S/m}$	Ionic Conductivity of the electrolyte
σ	$\mathrm{S/m}$	Electronic Conductivity of the solid phase
τ		Tortuosity factor

Subscripts

0	Solvent
1	Solid Matrix (Active Materials + Additives)
2	Liquid Phase (Electrolyte) in the pore space (Newman model) or in macro-pores (PApa model)
$+$	Cation of the Salt
$-$	Anion of the Salt
AM	Related to the Active Materials
eff	Effective properties
PE	Belong to the Porous Electrode
el	Electronic in the solid phase

References

[1] S. Malifarge, PhD Thesis, **2017**.

[2] J. Newman, K. E. Thomas-Alyea, *Electrochemical Systems*, Wiley-Blackwell, **2012**.

[3] A. Nyman, T. G. Zavalis, R. Elger, M. Behm, G. Lindbergh, *J. Electrochem. Soc.* **2010**, *157*, A1236.

[4] S. Malifarge, B. Delobel, C. Delacourt, *J. Electrochem. Soc.* **2018**, *165*, A1275.

[5] K. Märker, P. J. Reeves, C. Xu, K. J. Griffith, C. P. Grey, *Chemistry of Materials* **2019** *31* (7), 2545-2554.

[6] T. V. S. L. Satyavani, B. Ramya Kiran, V. Rajesh Kumar, A. Srinivas Kumar, S. V. Naidu, *Eng. Sci. Technol. an Int. J.* **2016**, *19*, 40.

[7] H. Gao, Q. Wu, Y. Hu, J. P. Zheng, K. Amine, Z. Chen, *J. Phys. Chem. Lett* **2018**, *9*, 5100.

[8] N. Ogihara, Y. Itou, T. Sasaki, Y. Takeuchi, *J. Phys. Chem. C* **2015**, *119*, 4612.

[9] H. Zheng, J. Li, X. Song, G. Liu, V. S. Battaglia, *Electrochim. Acta* **2012**, *71*, 258.

[10] J.-C. Badot, É. Ligneel, O. Dubrunfaut, D. Guyomard, B. Lestriez, *Adv. Funct. Mater.* **2009**, *19*, 2749.

[11] M. Ender, A. Weber, E. Ivers-Tiffée, *Electrochem. commun.* **2013**, *34*, 130.

[12] M. Doyle, J. Newman, A. S. Gozdz, C. N. Schmutz, J. Tarascon, *J. Electrochem. Soc.* **1996**, *143*, 1890.

[13] X. Zhang, Z. Ju, Y. Zhu, K. J. Takeuchi, E. S. Takeuchi, A. C. Marschilok, G. Yu, *Adv. Energy Mater.* **2020**, 2000808.

[14] A. A. Franco, *RSC Adv.* **2013**, *3*, 13027.

[15] F. Cadiou, T. Douillard, N. Besnard, B. Lestriez, E. Maire, *J. Electrochem. Soc.* , **2020**, 167(10), 100521.

[16] S. L. Morelly, N. J. Alvarez, M. H. Tang, *J. Power Sources* **2018**, *387*, 49.

[17] J. E. Vogel, M. M. Forouzan, E. E. Hardy, S. T. Crawford, D. R. Wheeler, B. A. Mazzeo, *Electrochim. Acta* **2018**, *297*, 820.

[18] J. Landesfeind, M. Ebner, A. Eldiven, V. Wood, H. A. Gasteiger, *J. Electrochem. Soc.* **2018**, *165*, A469.

[19] D. E. Stephenson, B. C. Walker, C. B. Skelton, E. P. Gorzkowski, D. J. Rowenhorst, D. R. Wheeler, *J. Electrochem. Soc.* **2011**, *158*, A781.

[20] J. Joos, T. Carraro, M. Ender, B. Rüger, A. Weber, E. Ivers-Tiffée, *ECS Transactions*, **2011**, 35(1), 2357.

[21] H. Zheng, L. Tan, G. Liu, X. Song, V. S. Battaglia, *J. Power Sources* **2012**, *208*, 52.

[22] R. Xu, Y. Yang, F. Yin, P. Liu, P. Cloetens, Y. Liu, F. Lin, K. Zhao, *J. Mech. Phys. Solids* **2019**, *129*, 160.

[23] X. Lu, A. Bertei, D. P. Finegan, C. Tan, S. R. Daemi, J. S. Weaving, K. B. O. Regan, T. M. M. Heenan, G. Hinds, E. Kendrick, D. J. L. Brett, P. R. Shearing, *Nat. Commun.* **2020**, *11*, 1.

[24] J. Billaud, F. Bouville, T. Magrini, C. Villevieille, A. R. Studart, *Nat. Energy* **2016**, *1*, 16097.

[25] J. S. Sander, R. M. Erb, L. Li, A. Gurijala, Y. M. Chiang, *Nat. Energy* **2016**, *1*, 1.

[26] J. Newman, *J. Electrochem. Soc.*, 1995, 142(1), 97.

[27] J.-H. Rakebrandt, P. Smyrek, Y. Zheng, H. J. Seifert, W. Pfleging, in *Laser-Based Micro-Nanoprocessing XI* (Eds.: U. Klotzbach, K. Washio, R. Kling), SPIE, **2017**, p. 100920M.

[28] J. B. Habedank, L. Kraft, A. Rheinfeld, C. Krezdorn, A. Jossen, M. F. Zaeh, *J. Electrochem. Soc.* **2018**, *165*, A1563.

[29] J. Park, C. Jeon, W. Kim, S. J. Bong, S. Jeong, H. J. Kim, *J. Power Sources* **2021**, *482*, 228948.

[30] L. Kraft, J. B. Habedank, A. Frank, A. Rheinfeld, A. Jossen, *J. Electrochem. Soc.*, **2020**, 167(1), 013506.

[31] S. J. Cooper, D. S. Eastwood, J. Gelb, G. Damblanc, D. J. L. Brett, R. S. Bradley, P. J. Withers, P. D. Lee, A. J. Marquis, N. P. Brandon, P. R. Shearing, *J. Power Sources* **2014**, *247*, 1033.

[32] D. Kehrwald, P. R. Shearing, N. P. Brandon, P. K. Sinha, S. J. Harris, *J. Electrochem. Soc.* **2011**, *158*, A1393.

[33] I. V. Thorat, D. E. Stephenson, N. A. Zacharias, K. Zaghib, J. N. Harb, D. R. Wheeler, *J. Power Sources* **2009**, *188*, 592.

[34] N. A. Zacharias, D. R. Nevers, C. Skelton, K. Knackstedt, D. E. Stephenson, D. R. Wheeler, *J. Electrochem. Soc.* **2013**, *160*, A306.

[35] J. Landesfeind, J. Hattendorff, A. Ehrl, W. A. Wall, H. A. Gasteiger, *J. Electrochem. Soc.* **2016**, *163*, A1373.

[36] S. Malifarge, B. Delobel, C. Delacourt, *J. Electrochem. Soc.* **2017**, *164*, E3329.

[37] M. Ebner, D. W. Chung, R. E. García, V. Wood, *Adv. Energy Mater.* **2014**, *4*, DOI 10.1002/aenm.201301278.

[38] L. Shen, Z. Chen, *Chem. Eng. Sci.* **2007**, *62*, 3748.

[39] Y. C. K. Chen-Wiegart, R. Demike, C. Erdonmez, K. Thornton, S. A. Barnett, J. Wang, *J. Power Sources* **2014**, *249*, 349.

[40] N. Epstein, *Chem. Eng. Sci.* **1989**, *44*, 777.

[41] D. A. G. Bruggeman, *Ann. Phys.* **1935**, *416*, 636.

[42] B. Tjaden, S. J. Cooper, D. J. Brett, D. Kramer, P. R. Shearing, *Curr. Opin. Chem. Eng.* **2016**, *12*, 44.

[43] B. J. Lanterman, A. A. Riet, N. S. Gates, J. D. Flygare, A. D. Cutler, J. E. Vogel, D. R. Wheeler, B. A. Mazzeo, *J. Electrochem. Soc.* **2015**, *162*, 2145.

[44] T. Nguyen, J. Villanova, Z. Su, R. Tucoulou, B. Fleutot, B. Delobel, C. Delacourt, A. Demortière, *Adv. Energy Mater.* **2021**, *11*, 2003529.

[45] B. L. Trembacki, D. R. Noble, M. E. Ferraro, S. A. Roberts, *J. Electrochem. Energy Convers. Storage* **2020**, DOI 10.1115/1.4045973.

[46] Y. Yang, R. Xu, K. Zhang, S. Lee, L. Mu, P. Liu, C. K. Waters, S. Spence, Z. Xu, C. Wei, D. J. Kautz, Q. Yuan, Y. Dong, Y. Yu, X. Xiao, H. Lee, P. Pianetta, P. Cloetens, J. Lee, K. Zhao, F. Lin, Y. Liu, *Adv. Energy Mater.* **2019**, *9*, 1900674.

[47] J. Eller, M. Ebner, C. Burns, J. Dahn, V. Wood, *J. Electrochem. Soc.* **2018**, *165*, 339.

[48] S. J. Harris, P. Lu, *J. Phys. Chem. C* **2013**, *117*, 6481.

[49] E. Sahraei, E. Bosco, B. Dixon, B. Lai, *J. Power Sources* **2016**, *319*, 56.

[50] L. Almar, J. Joos, A. Weber, E. Ivers-Tiffée, *J. Power Sources* **2019**, *427*, 1.

[51] P. Pietsch, M. Ebner, F. Marone, M. Stampanoni, V. Wood, *Sustain. Energy Fuels* **2018**, *2*, 598.

[52] T. Hutzenlaub, A. Asthana, J. Becker, D. R. Wheeler, R. Zengerle, S. Thiele, *Electrochem. commun.* **2013**, *27*, 77.

[53] L. Zielke, T. Hutzenlaub, D. R. Wheeler, C.-W. Chao, I. Manke, A. Hilger, N. Paust, R. Zengerle, S. Thiele, *Adv. Energy Mater.* **2015**, *5*, 1401612.

[54] P. R. Shearing, D. S. Eastwood, R. S. Bradley, J. Gelb, S. J. Cooper, F. Tariq, D. J. L. Brett, N. P. Brandon, P. J. Withers, P. D. Lee, *Microsc. Anal*, ***2013***, *27(2), 19-22.*

[55] Z. Liu, J. Scott Cronin, Y. C. K. Chen-Wiegart, J. R. Wilson, K. J. Yakal-Kremski, J. Wang, K. T. Faber, S. A. Barnett, *J. Power Sources* **2013**, *227*, 267.

[56] M. Ebner, F. Geldmacher, F. Marone, M. Stampanoni, V. Wood, *Adv. Energy Mater.* **2013**, *3*, 845.

[57] D. P. Finegan, M. Scheel, J. B. Robinson, B. Tjaden, I. Hunt, T. J. Mason, J. Millichamp, M. Di Michiel, G. J. Offer, G. Hinds, D. J. L. Brett, P. R. Shearing, *Nat. Commun.* **2015**, *6*, 1.

[58] D. S. Eastwood, R. S. Bradley, F. Tariq, S. J. Cooper, O. O. Taiwo, J. Gelb, A. Merkle, D. J. L. Brett, N. P. Brandon, P. J. Withers, P. D. Lee, P. R. Shearing, *Nucl. Instruments Methods Phys. Res. Sect. B Beam Interact. with Mater. Atoms* **2014**, *324*, 118.

[59] V. Julie, L. Jérôme, C. Peter, B. Pierre, D. Gérard, S. Heikki, U. V. François, *J. Power Sources* **2013**, *243*, 841.

[60] P. Cloetens, W. Ludwig, J. Baruchel, D. Van Dyck, J. Van Landuyt, J. P. Guigay, M. Schlenker, *Cit. Appl. Phys. Lett* **1999**, *75*, 5486.

[61] Z. Su, V. De Andrade, S. Cretu, Y. Yin, M. J. Wojcik, A. A. Franco, A. Demortière, *ACS Appl. Energy Mater.* **2020**, acsaem.9b02236.

[62] A. Tkachuk, F. Duewer, H. Cui, M. Feser, S. Wang, W. Yun, *Zeitschrift für Kristallographie-Crystalline Materials*, **2007**, 222(11), 650-655.

[63] C. Holzner, M. Feser, S. Vogt, B. Hornberger, S. B. Baines, C. Jacobsen, *Nat. Phys.* **2010**, *6*, 883.

[64] P. Pietsch, V. Wood, *Annu. Rev. Mater. Res.* **2017**, *47*, 451.

[65] E. Maire, P. J. Withers, *Int. Mater. Rev.* **2014**, *59*, 1.

[66] F. Zernike, *Phys. Zeitschr.* **1935**, 848.

[67] H. F. Talbot, *London, Edinburgh, Dublin Philos. Mag. J. Sci.* **1836**, *9*, 401.

[68] D. A. Howey, S. A. Roberts, V. Viswanathan, A. Mistry, M. Beuse, E. Khoo, S. C. Decaluwe, V. Sulzer, *Electrochem. Soc. Interface* **2020**, *29*, 30.

[69] A. A. Franco, *RSC Adv.* **2013**, *3*, 13027.

[70] “The Newman Research Group,” can be found under http://www.cchem.berkeley.edu/jsngrp/, **n.d.**

[71] K. E. Thomas, J. Newman, R. M. Darling, *Advances in lithium-ion batteries*, **2002**.

[72] M. Doyle, Design and Simulation of Lithium Rechargeable Batteries, University of California Berkeley, **1995**.

[73] J. Newman, K. E. Thomas, H. Hafezi, D. R. Wheeler, in *J. Power Sources*, Elsevier, **2003**, pp. 838–843.

[74] J. Newman, W. Tiedemann, *AIChE J.* **1975**, *21*, 25.

[75] M. Doyle, *J. Electrochem. Soc.* **1993**, *140*, 1526.

[76] D. K. Karthikeyan, G. Sikha, R. E. White, *J. Power Sources* **2008**, *185*, 1398.

[77] V. R. Subramanian, V. D. Diwakar, D. Tapriyal, *J. Electrochem. Soc.* **2005**, *152*, A2002.

Chapter III . Electrode tortuosity factor for quantifying transport in porous Li-ion battery electrodes

III.1 Introduction

Among all the macro-homogenous parameters, the tortuosity factor determination presents a great challenge as they are an emergent global property of the microstructures' interaction with a particular transport process and, as such, require either a transport experiment or a simulation. The focus of this chapter is on the determination of tortuosity factors relevant to LiB electrodes. For this purpose, we choose to work with the standard definition for the tortuosity factor, τ_e, as stated in the Eq. II-5.

The following two experimental techniques are used in the field of electrochemistry to determine the tortuosity factor of electronically insulating porous materials, such as battery separators. Both techniques require the porous medium to be infiltrated with an ionically conductive salt (of known bulk conductivity (κ) and diffusivity (D)), and then placed between two electronically conductive plates to form a cell.

The first technique is known as the "restricted-diffusion method" (RDM)[1–3] and is based on measuring diffusion in the time domain. For this technique, the plates on either side of the cell must be electroactive with respect to one of the ions in the electrolyte. A bias is applied between the plates, establishing a constant current, which in turn generates a linear salt concentration gradient across the cell. When the bias is removed, the salt gradually diffuses back to a uniform distribution, which is known as the relaxation step. By monitoring the salt diffusion during the relaxation step at sufficiently long times,[2] which can be done by following the decay of the electrochemical potential at each plate, using reference electrodes, one can determine the effective salt diffusion coefficient, D_{eff}, within the porous medium. The experimental measurement of a cell potential can also be compared to a simulation with a numerical transport model to determine the effective salt diffusion coefficient within porous medium. In the case of an infinite dilute solution, the relation between the flux and the gradient concentration can be described by Fick's law.

The second technique utilizes the frequency-domain, where the high frequency impedance response of this symmetrical cell is measured (referred to as SCM for convenience in this chapter). By making the assumption that this impedance is caused entirely by the migration flux passing through the electrolyte filled pores, the effective ionic conductivity of the electrolyte filled pore network, κ_{eff}, can then be calculated using Ohm's law.

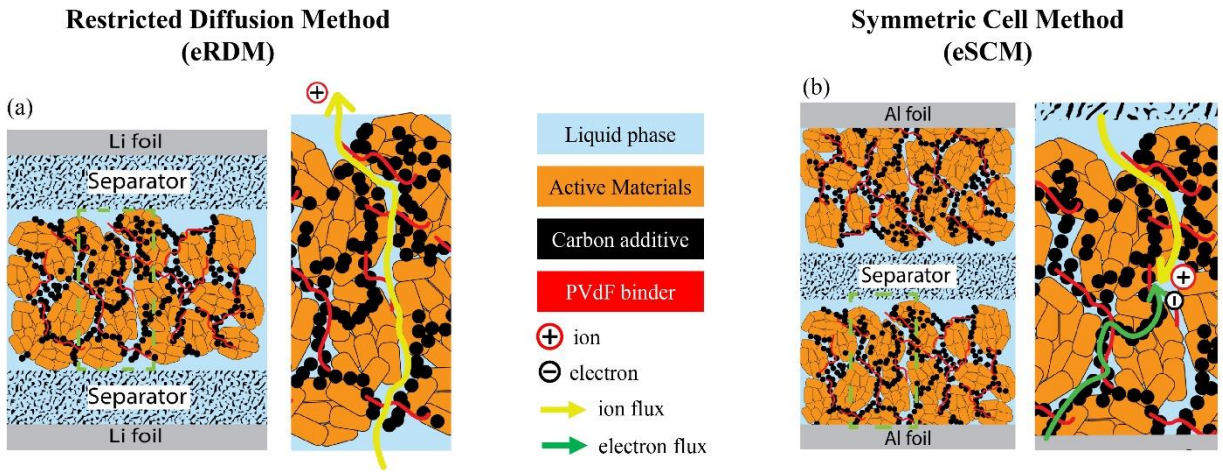

Figure III-1. Schematics of experimental setup and the physics underlying the two methods for determining tortuosity factors of porous electrodes: a. eRDM[4] , and **b.** eSCM[5,6]. The arrows show different conducting pathways travelled by charged particles(ions/electrons).

Crucially, the two commonly used methods described above cannot be applied directly to electronically-conducting porous materials, such as battery electrodes. This is in part because the material would provide an electronic short-circuit path between the two plates, but also because the presence of the electronic conductor would interact with the potential field, which undermines the simplified assumptions in the analysis. However, the following two adapted version of these methods have been proposed:

The first method was developed by Thorat *et al.*[4] and is a time-domain approach based on RDM, but with two key differences. The cell used for this experiment requires a "free-standing" electrode, which is typically obtained by simply peeling the porous electrode material off the current collector foil. This electrode is then placed between two separators (*i.e.* electronically insulating and permeable materials) to electronically isolate it, before sandwiching these three layers between two lithium foils, as shown in Figure III-1a. Similar to RDM, a bias is applied causing a steady-state current in order to establish a salt concentration distribution across the cell. The use of the transport model is preferred, as it facilitates the decorrelation of the contribution of the porous electrodes layer to the overall transport from other porous layers (two separator layers). The experimental measurement of a cell potential is compared to a simulation with a numerical transport model to determine the effective salt diffusion coefficient within porous electrodes. Here, we refer to this variant of the RDM for electronic conductors as eRDM.

The second approach was developed by Landesfeind *et al.*[5] and Malifarge *et al.*[6] and, similar to SCM, it is a frequency-domain technique. It employs a conventional symmetrical cell setup, as shown in Figure III-1b, where pair of identical electrodes (backed by CC foil) are placed either side of a separator. In order to extract information about the pore phase only, a blocking condition is imposed at the electrode surface, preventing insertion of the mobile ions. This can be achieved through either the use of a non-intercalating electrolyte salt and/or by using electrodes in a non-

intercalating state (*e.g.* fully lithiated/delithiated). EIS is then used to extract an impedance spectrum[7], from which information about the processes inside this cell can be extracted. A more involved analysis is required than for the simple SCM method and is described in more detail later in this article. We refer to this symmetrical cell method for characterizing transport in porous electronic conductors as eSCM.

A recent comparison of these two methods for commercial battery electrodes was made by Pouraghajan *et al.*[8], which showed a reasonable agreement between these two approaches in cases where both of them can be implemented. Nevertheless, in many cases[8], the eSCM seems to be faster and more convenient to implement than the eRDM, which requires a current-collector-free electrode along with precise determination of the bulk diffusion coefficient of the liquid electrolyte.

Besides electrochemical methods for quantifying the tortuosity factor mentioned above, 3D imaging techniques (*e.g.*, FIB-SEM, µ-XCT or nano-XCT) can be used to capture the geometry of these porous electrodes at the nanoscale. Although the imaged volume is generally very small in comparison to the cell, if it is large in comparison to the pore features, then this data may still be used to extract average morphological metrics that are representative of the whole electrode. However, the lack of capability in capturing either the fine features (due to the resolution) or different phases (carbon-binder domain is rarely well captured with XCT based on attenuation contrast) in the tomographic data can be a source of errors that impacts the quantification of microstructural properties, in particular interfacial area.[17,18]

Among various tools for analysing tomographic data, *TauFactor*, developed by Cooper *et al.*[19], is an open-source MATLAB application that calculates tortuosity factors directly from segmented image stacks, as well as volume fractions, surface areas and other microstructural properties. To calculate the tortuosity factor, *TauFactor* uses an over-relaxed iterative approach to solve the steady-state diffusion equation of species in an infinitely dilute solution between two fixed value boundaries in a porous medium. However, it is worth stating that this simple definition of the tortuosity factor does not account for the multi-physics processes occurring in a real electrochemical system; so, for example, there are no contributions to ionic transport from electric migration or convection and no double-layer formation at solid/liquid interface.[20] It is the simplicity of this approach which allows for the system to be solved quickly, and this, in turn, has made this method of tortuosity factor determination the standard when using tomographic data.

In this chapter, we develop a new frequency domain solver within the *TauFactor* framework in order to replicate the eSCM approach and understand why it can give different results to those derived through eRDM. Specific cases of 2D and 3D microstructures are studied to showcase the crucial difference between the two methods and highlight cases where one approach might be preferred.

III.2 Results

Tortuosities calculated by the two approaches are denoted: τ for a tortuosity factor derived from the conventional eRDM approach and τ_{e} for "electrode tortuosity factor" determined using the eSCM. Furthermore, MacMullin Numbers N_{M} and $N_{\mathrm{M,e}}$ are defined similarly.

The conventional definition of tortuosity factor, τ, considers the steady-state flux of species from one side of the control volume (CV), through the pore network and out the opposite side. In this work, we describe pathways connecting between these two sides as "through-pores". Pores that start from the separator side and reach the current collector side would count as through-pores (*i.e.* the current collector is not counted as part of the porous electrode). Those pores that either do not connect across the full thickness or have negligible contribution to the steady-state diffusive flux (see Figure III-2) are denoted as "dead-end pores" and their presence would cause an increase in the value of τ.

However, in the case of battery porous electrodes, "dead-end" pores may make a significant contribution to the transport. This is because battery electrodes do not require transport all the way through the pore structure, but rather the combination of ion transport from the separator (through the liquid) to the solid/liquid interface and electron transport from the current collector (through the solid) to the solid/liquid interface. This suggests that the conventional tortuosity factor, τ, may be a misleading metric when trying to predict battery performance.

By simulating the eRDM and eSCM concepts to extract both τ and τ_{e} from a variety of microstructures, we will demonstrate that τ_{e} is more relevant to predicting the performance of battery electrodes.

III.2.1 Simulations of 2D microstructures

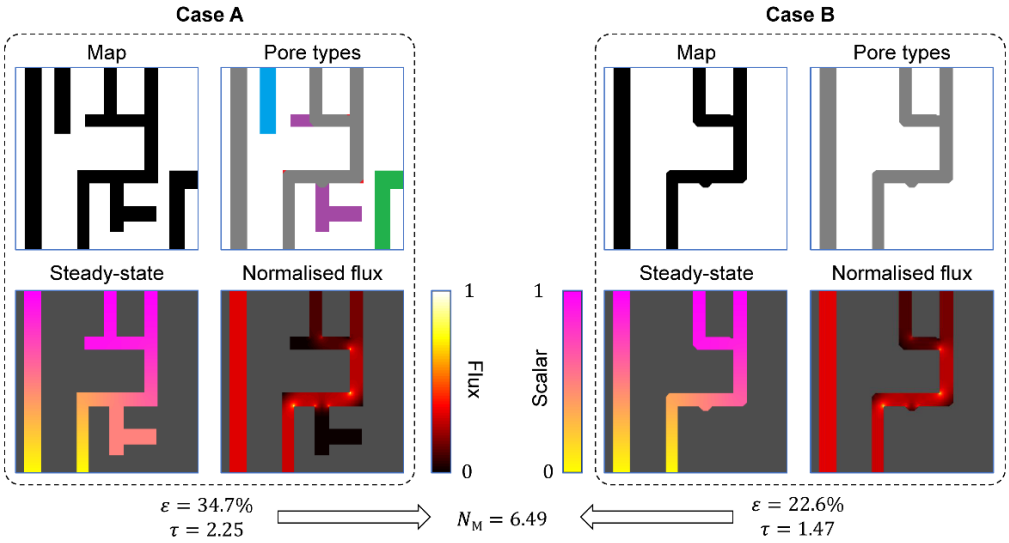

Figure III-2. Illustration of different types of pores that can be present within porous electrodes and their effects on the tortuosity factor τ and McMullin number N_M determination. The simulated steady-state scalar distributions are shown as well as the normalised flux maps. Case A: microstructure with five different pores types: Gray - through pores; Blue - dead-end pores for eRDM, that may or may not be available for eSCM, depending on the orientation of the CV; Purple - dead-end pores for eRDM that branch from the through pores; Green - dead-end pores like Blue but could become through pores if the CV was larger as it extends out the side of the CV; and Red – small corner regions having low flux. Case B: microstructure with only through-pores (gray) based on low flux threshold. The microstructure size is 256x256 pixels.

In Figure III-2, we first consider an example to clearly showcase different types of pores that are investigated throughout this work. Based on the diffusive flux through the porous structure at steady-state (simulated with *TauFactor*), two main types of pores, as mentioned above, through pores and dead-end pores can be identified along with the quantification of their volume fraction respectively. Case A consists of both through and dead-end pores. At steady-state, only percolated pores are shown, in which there are pore regions that have a uniform concentration. Thus, these regions of pores contribute negligibly to the diffusive flux, as can be seen in the flux density map with almost no flux there. Since the diffusive flux is expected to penetrate through the porous microstructure principally by through-pores rather than dead-end pores, we apply an arbitrary threshold value (2% of maximum) to the flux density map at steady-state to label pores as "through" or "dead-end". Then, among the dead-end pores, we divided them into subclasses of pores (differentiated by color). Once every pore is labeled, case B shows a microstructure that contains only the through pores (in gray) previously presented in case A. It's interesting to note that the value of N_M is the same for cases A and B, since the transport through these two systems would be essentially the same, as the pores that were removed make a minimal contribution to transport through the system.

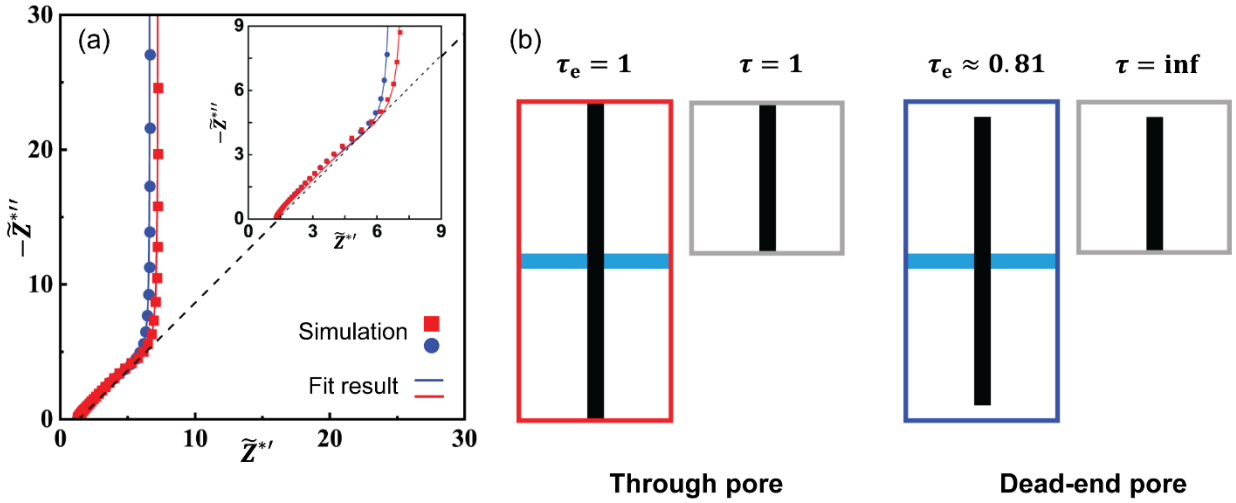

Figure III-3. Comparison of the two approaches applied to the simplest cases. a. Simulated EIS of eSCM of the two 2D microstructures containing either only straight through-pores (red) or only straight dead-end pores (blue) along with the corresponding fits with Eq. III-3. The inset image displays the zoom at the mid-frequency region. The 45° slope in dashed line is used to guide the eyes; **b.** The geometry of two microstructures with τ_e and τ derived from the eSCM and eRDM simulations. Box colour corresponds to the colours in the Nyquist plot. The light blue band in the middle of the SCM geometries represents a separator with a direct pore connecting the two sides. The microstructure size is 100x100 pixels, the pixel size equals to 1 µm.

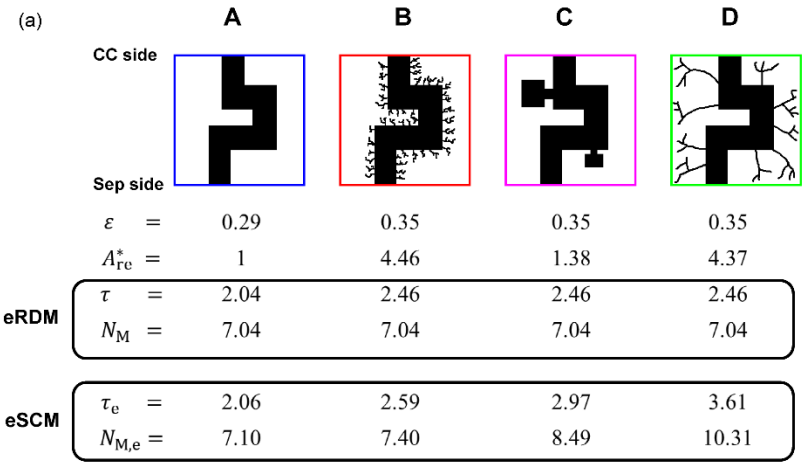

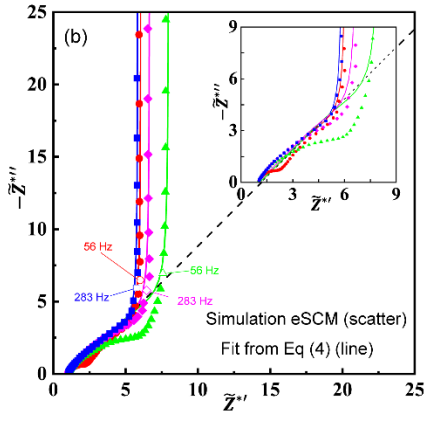

Figure III-4. Comparison of two approaches with 2D microstructures. a. the four 2D microstructures are presented along with τ, N_M given by eRDM and τ_e, $N_{M,e}$ given by eSCM in each case; the current collector "CC side" and the separator "Sep side" are labelled; **b.** simulated EIS of eSCM of the four microstructures along with the fit using Eq. III-3, the inset graph shows a zoom on the mid-frequency region to highlight the deviation of the simulated EIS shape from the conventional TLM response. The 45° slope in dashed line is used to guide the eyes. The microstructure size is 300x300 pixels, the pixel size equals to 1 µm.

The difference in terms of concept and physics between the two methods, eRDM and eSCM, is first illustrated through a very simple 2D example, as shown in Figure III-3b, in which the microstructure has either only straight through-pores or only straight dead-end pores.

With only through-pores, the two approaches give the same value of 1 for the tortuosity factor, as expected for straight pores. Furthermore, this result helps to cross-check the symmetric cell model implemented in *TauFactor*. On the other hand, for a 2D structure based on a dead-end pore, the tortuosity factor values found by the two methods strongly contrast with each other: an infinite tortuosity factor results from the eRDM, whereas the eSCM yields an electrode tortuosity factor value less than 1.

Microstructures made of simple pore networks containing both through and dead-end pores are studied next, as shown in Figure III-4. The MacMullin number N_{M} in Eq. II-4 is also reported here since it describes the effect of a porous microstructure on the behavior of the liquid phase within the pore network[5,21,22] and as such it also appears in the Newman P2D model through the mass balance in the liquid phase and the Mac-Innes equation for ionic transport.[23]

A template geometry is created in which there is only one through pore (case A in Figure III-4). Then, three other geometry (cases B, C, D) are derivatives of geometry A through adding a constant volume fraction of dead-end pores ($\varepsilon_{\mathrm{dead}} = 6\%$). The dead-end pores are all branched from the through pore. They are intentionally made to be different in terms of morphology from one structure to another, which leads to different value of A^*. The following four structures are investigated:

1. Only one main through pore and no dead-end pore (A).
2. Many short dead-end branches in addition to the main through pore (B).
3. Dead-end branches with low microstructural active surface area in addition to the main through pore (C).
4. A few long dead-end branches in addition to the main through pore (D).

The four microstructures are intentionally designed to have the same value of the conventional MacMullin number, N_{M}. In addition, the three derivative microstructures each have the same conventional tortuosity factor, τ, as each other. The microscopic active surface area A^* is represented as a relative value A^*_{re} to that of microstructure A for ease of comparison. The electrode tortuosity factor, τ_{e}, is then expected to be impacted only by the dead-end pores in different ways in each situation according to their morphology. It can lead to more pronounced discrepancies between the two methods, so that we can unveil the fundamental difference between them.

As shown in Figure III-4a, the three geometries B, C and D have the same tortuosity factor value (higher than for geometry A), despite having quite different morphologies of added dead-end pores. This result highlights that the dead-end pores have no impact on the regular tortuosity value given by eRDM, which is consistent with the fact they do not contribute to the transport through the structure at steady state. In fact, it should be noted that the diffusional flux (from which

conventional tortuosity is calculated) is inversely proportional to the MacMullin number (*i.e.* the same in each case). So even though the dead-end pores do not contribute to species transport at steady-state, their presence does have an effect on the determination of tortuosity, via their additional volume fraction. The identical values for the MacMullin number found by eRDM would imply that the effect of these porous microstructures (mostly the dead-end pores), on the behavior of transport through the pores, is the same, regardless of their different pore network morphologies. However, this interpretation would be misleading when modelling battery electrodes, as will be discussed below.

Let us now compare the tortuosities from the eSCM to those of the eRDM described above. In geometry A, when there is only a main through-pore and no dead-end pores added, the tortuosities found by both methods have a good agreement (<1% for relative difference), despite measuring quite different concepts (*i.e.* flux between parallel boundaries and flux from one boundary to the solid/liquid interface).

As expected, for cases B, C and D, we find differences in the tortuosities and MacMullin numbers found by the two methods. As discussed, eSCM is a relative measure of how difficult it is to access the solid/liquid interface from one of the boundaries. Firstly, microstructure A has the lowest value of τ_e, so we can think of its surface area as being easy to access, although it does not actually have much surface area available. Microstructure B has a highest interfacial surface area, originating from many short dead-end pores. This surface area is slightly harder to access when compared to microstructure A, which is reflecting in the value of τ_e; however, it does have over 4 times as much area available. Microstructure C also has fairly short dead-end pores, but they are much bulkier and there are only two of them. Half of all the additional new surface area is far from the separator, hence a high value of τ_e is observed, and only a modest additional surface area was added anyway. Lastly, microstructure D has a similarly large increase in surface area to case B, but now very long pores must be travelled to access it, so it has the highest tortuosity factor. Importantly, the value of A^* can be observed in the characteristic frequencies of each microstructure through Eq. III-5. The microstructure B and D have the highest values of A^* among all the microstructures, meaning that more time is required to saturate their capacitive surface and hence lower characteristic frequencies are observed.

Figure III-4b also contains an inset showing a detailed view of the medium-to-low frequency region (NB. The high frequency offset on the real axis results from a separator spacer between the two electrodes as illustrated in Figure III-3). As can be seen, for cases B and D, the simulated impedance spectra strongly deviate from the expected shape for the TLM in this region (*i.e.* 45° slope). The shape of this region is a function of the accessible surface area per unit penetration depth, which explains why A and C are initially identical. Such a signature on the impedance spectra, although being only related to the microstructure, could be misinterpreted for an additional electronic/electrochemical process (*e.g.*, contact resistance between electrode film and current collector or between particles) in experimental symmetric cell impedance measurements.

The discrepancy between τ and τ_e in the results above should not be surprising as the two methods are measuring distinct (but in some cases related) properties of the microstructure. Nevertheless, a key conclusion from the results reported here is that in the case of porous electrodes (*i.e.*, where the pores are pathway for charged species to reach the electrochemical surface area), the more conventional eRDM approach suffers from some key conceptual issues compared to the eSCM approach. In particular, the fact that through-pores and dead-end pores both do participate in the ionic transport during electrode operation, because electrochemical reactions occur at the interfacial area of these pores contrary to only through-pores in the case of eRDM. Stated more plainly, a battery electrode does not need any pores to percolate all the way from the separator to the current collector in order to function, although this non-percolating scenario would give a value of $\tau = \infty$ if measured with eRDM. Hence, the electrode tortuosity factor, τ_e, obtained from the eSCM seems to be a more appropriate metric to characterize porous electrodes than the tortuosity factor, τ, as eSCM more closely resembles how an actual battery electrode works. However, in the case of an electrode whose particle/feature size was much smaller than the electrode thickness and therefore where the conventional tortuosity factor could be extracted from a subvolume, the eRDM approach may still have some relevance, though it would still suffer from incorrectly accounting for the impact of dead-end pores. Thus, for battery macroscopic models such as Newman P2D model, the electrode tortuosity factor τ_e should be preferred over the conventional tortuosity factor τ during the parametrization step.

Interestingly, the present results can also reveal information about the likely effect of certain pore morphologies on power performance. For example, if we consider geometries A and B, even though both microstructures show a similar N_M and R_{ion}, the accessible interfacial surface area of pores is not the same, since microstructure B has also the dead-end pores in addition to the through pore. This means that the specific electrochemical active surface area of the microstructure can be increased while keeping a low N_M, which may improve power performance.

III.2.2 Simulations of 3D microstructures

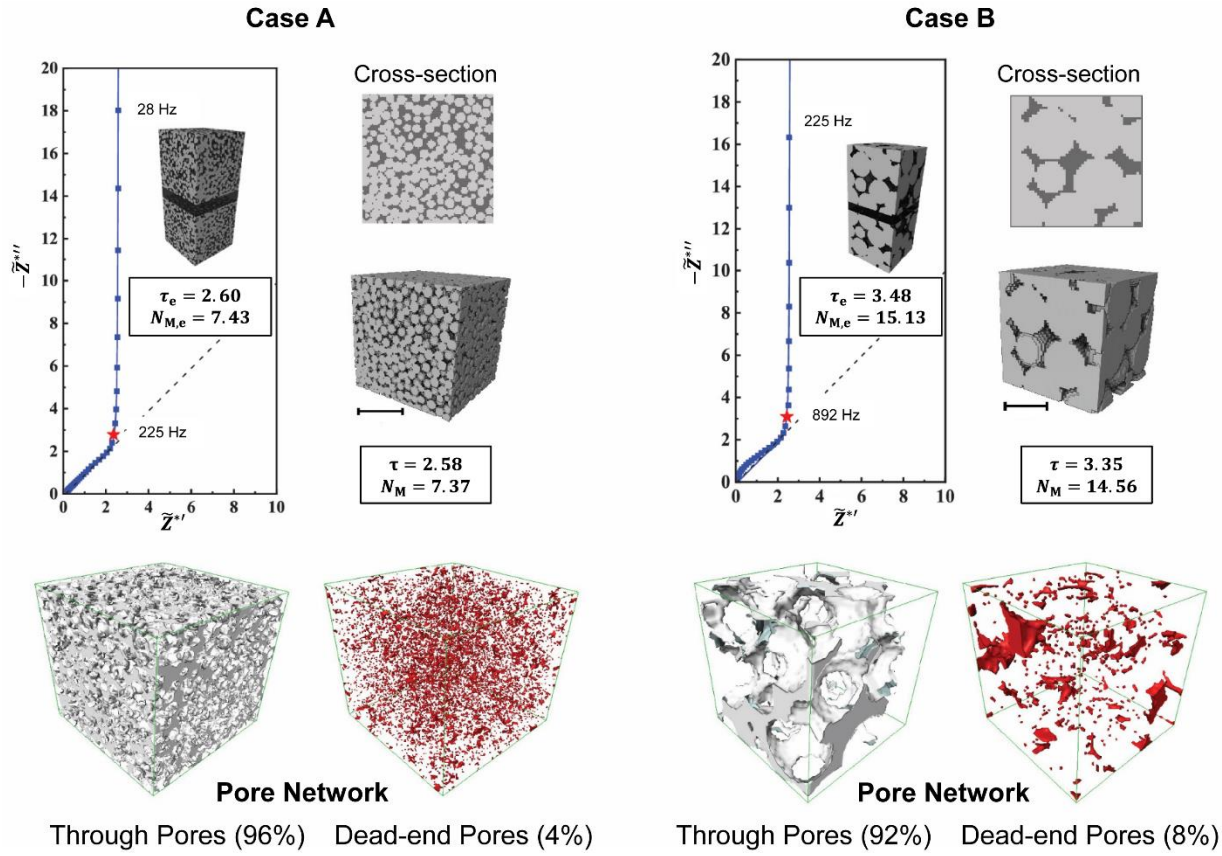

Figure III-5. Comparison of two approaches using two numerically generated 3D microstructures. Case A: microstructure with 2 µm particle size and $\varepsilon = 35\%$. **Case B:** microstructure with 5 µm particle size and $\varepsilon = 20\%$. For each case, a plot shows simulated EIS of eSCM along with the fit using Eq. III-3. Each plot contains an inset showing the resulting electrode tortuosity factor τ_e and the corresponding symmetric cell configuration. The cross-section and the tortuosity factor τ of these microstructures given by the eRDM are also presented. The pore networks separated into through-pores and dead-end pores are shown. Here, only open pores (connected pores) that possess less than 2% (arbitrary threshold value) of the total flux density are considered as dead-end pores. The threshold value was set to take into account the dead-end pores having either no flux or low flux. The microstructure size in case A is 100x100x100 voxels, in case B is 50x50x50 voxels, and the voxel size is 250 nm.

In this section, we examine 3D microstructures in order to investigate more realistic electrode geometries. Figure III-5 shows simulations performed on two 3D microstructures that have small and larger particle size with porosity $\varepsilon = 35\%$ (case A) and $\varepsilon = 20\%$ (case B), respectively. For both cases, the tortuosity values were calculated using the two methods and do not show a substantial difference.

Regarding case B, Figure III-5 shows that there is a deviation of the impedance response from the idealized response of the TLM. As mentioned in the previous section, this deviation results from variations in the available surface area per unit penetration depth and as such can be used to

indicate one of two relevant concepts. Either the volume being simulated is too small (compared to its characteristic features) to be considered representative of the electrode as a whole; or the microstructure itself is simply not homogenisable (*e.g.* a graded electrode) and standard porous electrode theory cannot be applied[23,24]. Compared to case A, the particle size in case B is larger, thus the pore details in case B are no longer at a size negligible compared to that of the control volume, suggesting it may not be representative. Even if the full thickness of the electrode is already captured, increasing just the area (*i.e.* dimensions parallel to the current collector) will also allow for a greater degree of averaging to occur. For example, both the volume fraction and surface area at each distance increment from the current collector may approach a constant value if a large enough area was observed, at which point the simulated EIS response is expected to get closer to the idealized impedance response given by TLM or Newman P2D model.

This work clearly illustrates how the simulated EIS spectrum for a symmetric cell in blocking conditions could be used as a quantitative tool to assess deviation from the porous electrode theory for a particular electrode microstructure. Moreover, when symmetric cell impedance measurements deviate from the expected TLM spectra (as reported in ref. [5] [7]), this model can help us understand why.

Figure III-5 shows two specific cases where there is a good agreement in the tortuosity values between the two approaches. The pore networks are highly percolated in both cases (>99%, as expected for packed spheres) and low flux dead-end pores only occupy a minority of the pore networks (4% and 8%, value given by *TauFactor*, for microstructures A and B, resp.), as illustrated in Figure III-5. Hence, the presence of dead-end pores has a minor effect on the tortuosity of the pore networks when eSCM is considered, allowing good agreement with eRDM. Importantly, a significant proportion of the dead-end pores are on the boundaries of the control volumes, suggesting that the dead-end fraction would have decreased further if a larger control volume were considered.

These results show that in case of more realistic 3D microstructures, a reasonable agreement may be obtained between the two approaches. It might also shed light on the work of Pouraghajan *et al.*[8], since for commercial electrodes of typical porosity, the pore network might contain mostly through-pores with only small fraction of dead-end pores.

Here, to contrast with the above example, one can imagine a microstructure that has very low porosity, which typically leads to a decrease in the percolation of the pore network and therefore a greater fraction of dead-end pores. In order to showcase this concept, a new 3D microstructure was generated having two adjacent layers with two different porosities. For 90% of the thickness, the porosity is set to 35%, but for the last 10% of its thickness, the porosity is abruptly reduced to 20%, as shown in the cyan box in Figure III-6. The purpose of this is to close most of the pores in order to create an otherwise well-percolated network of long dead-end pores. As a result, some dead-end pores travel almost the entire thickness of the microstructure, thereby increasing the impact of dead-end pores, depending on its orientation relative to the separator/current collector. As such, a substantial difference between the tortuosities measure using the two methods is

expected. It is worth mentioning that the microstructure in this example is potentially an informative and relevant model for some real electrodes, where sub-optimal manufacturing processes can yield a larger electrode density in the region close to the current collector (excess of binder) or the separator (drying too quickly).

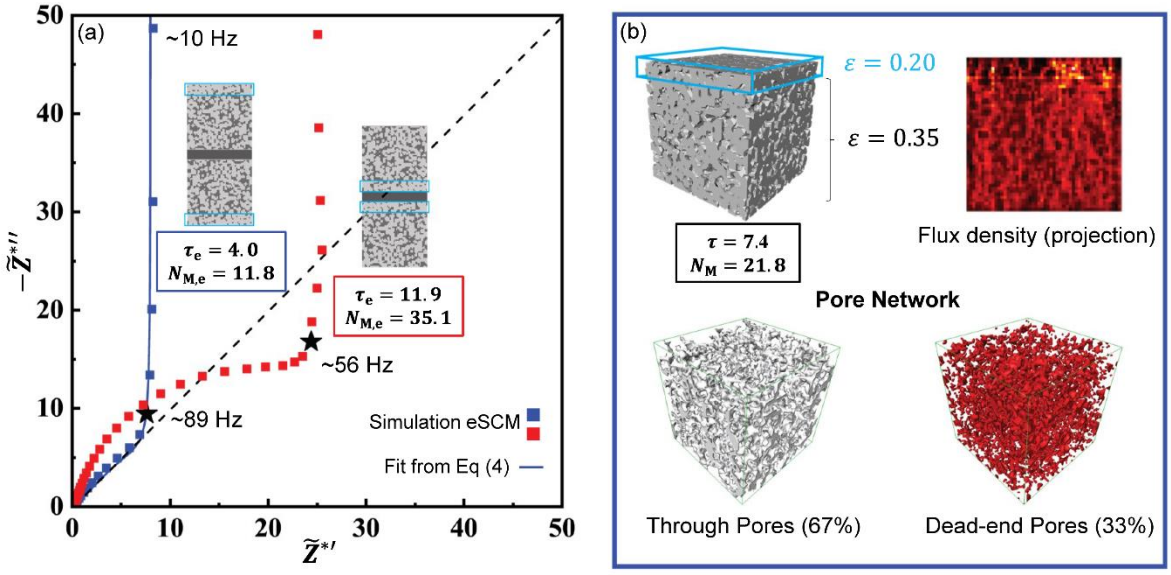

Figure III-6. Illustration of a numerically generated 3D microstructure having two adjacent layers with two different porosities. 90% of volume has $\varepsilon = 35\%$, while 10% (cyan box) of volume has $\varepsilon = 20\%$. **a.** The plot shows the simulated EIS of eSCM along with the fit using Eq. III-3. The plot contains an inset showing the cross-section of the two microstructures, that have either the lower porosity region at the current collector side (blue square) or at the separator side (red square), in symmetric cell configuration with the associated electrode tortuosity factor τ_e; **b.** The 3D microstructure that has lower porosity at the top is shown in detail along with the associated tortuosity factor τ given by eRDM simulation. The simulated flux density shows a lower density on the top corresponding with the lower porosity region. The pore network separated in through-pores and dead-end pores is also presented. The microstructure size is 50x50x50 voxels, the voxel size equals to 1 µm.

In Figure III-6, the volume fraction of dead-end pores in the microstructure (33%) is significantly larger than the microstructure in Figure III-5. These dead-end pores are also larger and better connected across the entire CV. Notably, at the top of the microstructure where the porosity decreases, there are less available through-pores allowing the flux of species all the way through (as measured in eRDM). This effect is illustrated in the the projection of simulated flux density from *TauFactor*, also shown in Figure III-6.

Despite having a high conventional tortuosity factor, this pore network, with its relatively large fraction of long, well-percolated, dead-end pores, has most of its surface area easily accessible, when the dense region is next to the current collector. This is reflected in the fitted value of $\tau_e = 4.0$, which is much lower than the value of $\tau = 7.4$ calcuated for eRDM. However, when the microstructre is reversed $\tau_e = 11.9$, which is even higher than the eRDM value, highlighting the

importance of directional microstructural information absent from conventional electrode models. As mentioned above, electrodes that are dried too quickly during manufacture can have a fairly dense layer of binder near the top, resembling this configuration, and they show poor rate performance.

With the dense layer next to the current collector, the impedance spectrum closely matches the TLM response; however, this is not the case when the dense layer is next to the separator. As already noted, deviations in the medium frequency region of the spectrum are caused by variations in the available surface area per unit penetration depth into the sample. Thus, the spectrum shows more information about these variations the closer they are to the separator, which is also where they would make a greater difference to cell performance. Furthermore, following on from a discussion earlier in the paper, Figure III-6 demonstrates that the homogenisablity of an electrode also depends on the analysis direction, which reinforces the conclusions from the simple case of open or closed straight pores in Figure III-3. This directional dependence of the eSCM approach is very informative and clearly reflected in real battery performance data. As such, the electrode tortuosity factor given by the eSCM should be a more appropriate metric for exploring the interplay between the electrode microstructure and cell performance, as it is able to highlight considerations critically lacking from the conventional tortuosity factor as well as various geometric tortuosity definitions. The result in Figure III-6 suggests that graded-porosity designs (with the higher porosity layer at the separator side) could be used to increase the accessible capacity of an electrode. This design concept was also explored by Lu *et al.*;[25] however, their analysis was based on geometric tortuosities, which make many simplifications including ignoring path constrictions.

Finally, to understand why τ_e should be used in conventional P2D Newman models instead of τ, it should be understood that single values of the volume fractions, specific surface area and tortuosity factor are typically used to describe a whole electrode. Although it is possible to make each of these values vary as a function of depth (producing a visible effect on the Nyquist plot), the conventional tortuosity factor used to quantify the "obstruction to transport caused by microstructure" refers only to the "flow through" scenario and so is not able to represent anything about how accessible the surface area is. The tortuosity is the only term used to encode microstructural complexity in the P2D model and as such τ_e should be used instead of τ as it more closely represents the scenario in question.

III.3 Discussion

Effective transport properties are critical for understand and modelling battery electrodes. Two main experimental methods exist for determining tortuosity factors (eRDM and eSCM), but they do not always agree. In this study, conceptual flaws are exposed in the use of the conventional tortuosity factor, τ, derived from eRDM for characterising porous battery electrode materials. In particular, the fact that τ is based on steady-state flow all the way through a system, whereas in a real electrode, ions migrate into the electrode and then on to the active surface area of the electrode itself. A new frequency domain solver was written to simulate the more realistic transport scenario

of distributed surface capacitance. This solver (eSCM) has been integrated into the open-source *TauFactor* platform, which already contains a solver for the conventional tortuosity factor (eRDM), and both can be applied directly to segmented tomographic data.

Various synthetic microstructures were generated and then analysed using both tortuosity paradigms to highlight the distinction between the two. Like τ, the electrode tortuosity factor, denoted τ_e, may depend on both the orientation of the microstructure (*i.e.* for anisotropic materials); however, unlike τ, the direction of the analysis can also impact τ_e, which is a concept of particular relevance to graded battery electrode microstructures.

The simulation results from this work unambiguously reveal that dead-end pores are the principal cause of discrepancies between the two approaches. Unlike the conventional "flow through" tortuosity factor where direct pores are optimal ($\tau = 1$), it is demonstrated that τ_e can be less than one, suggesting systems where the interfacial surface area is even easier to access than that of straight pores. As such, eSCM should be preferred over eRDM to be used in Newman P2D model and/or a TLM to model porous electrodes. Electrochemical modelers should consider this important result at the stage of precise P2D model parametrization.

Finally, this work demonstrates that the impedance spectra simulated from 3D microstructures may deviate from the conventional behavior simulated by a TLM or Newman P2D model in one of two scenarios: Either the control volume is not large enough to be representative of the material, or the system is not conventionally homogeneous, *e.g.* the accessible interfacial area varies significantly with depth. As well as a qualitative comparison, it is possible to conceive of various metrics that could be used to quantify the degree of agreement between simulated EIS spectrum of the symmetric cell and TLM fit, thus providing a direct way to assess the degree to which porous electrode theory applies to a particular electrode microstructure.

All of these concepts are to be applied to real electrode microstructural data in a follow-up study exploring optimal electrode design.

III.4 Methods

As mentioned above, this work focuses specifically on tortuosity factor determination methods applied to battery porous electrodes. Two methods, eRDM by Thorat *et al.*[4] and eSCM by Landesfeind *et al.*[5] and Malifarge *et al.*[6] are further described and compared in the following sections.

III.4.1 Restricted diffusion method for porous electrodes (eRDM)

Figure III-1a shows a schematic of the experimental setup. The cell is first polarized to generate a constant current. Under the applied current, cations are released at one electrode and diffuse/migrate through the three porous layers (separator/free-standing electrode/separator) before finally being consumed at the other electrode. The electric field also causes the electrolyte

anions to migrate; however, since the electrodes are blocking with respect to the anions, they accumulate at the positive electrode. This results in a salt concentration gradient across the cell, which in turn results in a concentration overpotential, and a cell potential gradient between two plates. The current is then interrupted and reference electrodes at each side monitor the cell-potential decay during the so-called relaxation step.

During the relaxation process, the migration/diffusion of the ions is obstructed by the porous microstructure of the electrode and separators. A numerical model can then be used to fit the cell-potential decay behavior in order to extract the effective salt diffusion coefficient of the porous layers. For instance, a transport model based on the Mac-Innes equation in a concentrated solution, including migration and diffusion in the liquid phase, can be used.[4] The cell-potential behavior during the polarization step can also be simulated if the model takes into account the charge transfer process at anode and cathode. Hence, it requires knowledge of several intrinsic electrolyte properties rather than just its ionic conductivity, *e.g.* the transference number and the diffusion coefficient, and also the parameters related to the kinetic reactions at the Li foil interfaces. Finally, using the porosity and tortuosity factors of the separators (which must already be known), it is then possible to isolate the effect of the free-standing electrode and extract its tortuosity factor by numerical fitting.

III.4.2 Symmetric cell method for porous electrodes (eSCM)

The experimental setup for eSCM significantly differs from the eRDM approach and consists of a symmetrical cell with two identical electrodes facing each other with a separator in between, as shown in Figure III-1b. The method is based on electrochemical impedance measurement of a symmetric cell in order to determine the effective ionic conductivity of the electrolyte across the porous electrode, which is related to the tortuosity factor of the structure through Eq. II-4.

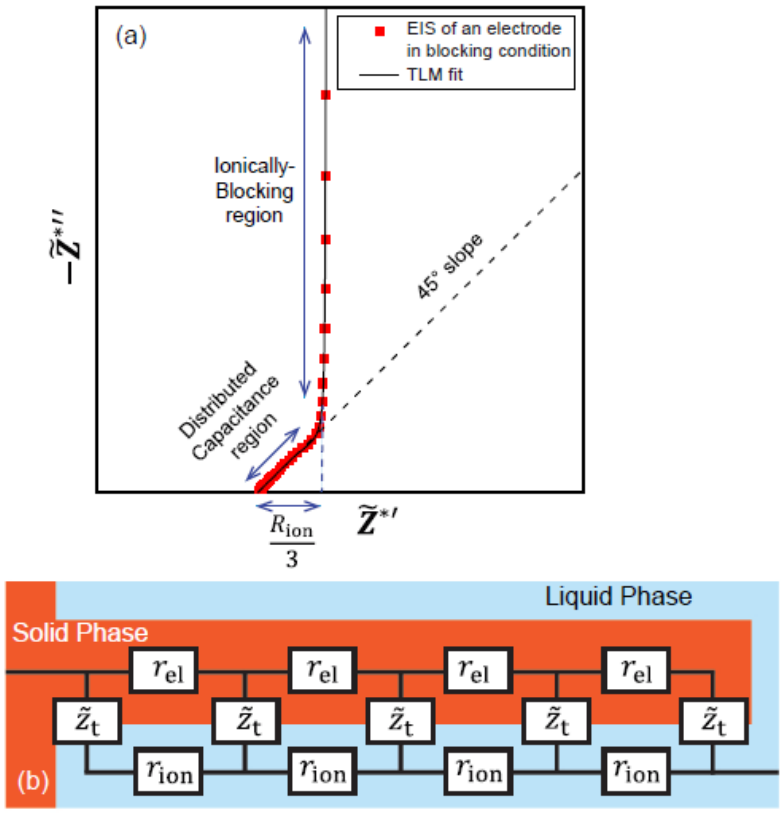

Figure III-7. Impedance theory of the eSCM method. a. An ideal impedance response of a symmetric cell in blocking condition (no faradaic process so $\tilde{z}_t$ becomes c_{dl} which is pure capacitance of the double layer) along with the fit using the TLM represented in **b.**, which allows the determination of τ_e. The dashed line is used to highlight the 45° slope of the medium frequency region.

For tortuosity factor determination using eSCM, a so-called blocking (*i.e.* zero flux) condition is applied at the pore-wall, as no faradaic processes are occurring. In this manner, there is no contribution from charge transfer, or diffusion in either the liquid or solid phases. Another simplifying assumption is that the transport within the separator alone determines the high frequency intercept on EIS spectrum. This means that only processes within the porous electrodes themselves are the cause of the medium and lower frequency EIS data and the effective ionic resistance within the porous electrodes can be determined using a simpler model. The Nyquist plot in Figure III-7a shows an idealized impedance response of a symmetric cell in blocking condition. In the medium frequencies, a linear region with a nearly 45° slope results from the distributed capacitance of the double-layer throughout the porous electrode in combination with the ion migration required to access each region of the solid/liquid interface.[26–28] In the low frequencies, the impedance response tends towards a vertical line, typical of ionically-blocking behavior.

A porous electrode can be represented by a structure with essentially straight-cylindrical pores of uniform diameter, which are homogeneously filled with electrolyte and have a uniformly distributed ionic resistance and double-layer capacitance per unit length. The electrode material is also considered to have uniformly distributed electronic resistance. This porous electrode can then

be macroscopically described by a uniform RC transmission line model (TLM), see Figure III-7b.[29–31] The electronic resistance of the solid matrix of the electrode and the ionic resistance of the liquid phase are expressed by a serial connection of ohmic resistors, r_{el} and r_{ion}, respectively. In addition, there can be a faradaic and/or capacitive process taking place at the solid/liquid interface, which are described by the surface impedance elements $\tilde{z}_{\mathrm{t}}$.

Hence, a TLM can be used to fit the symmetric cell impedance response, allowing for the determination of the effective ionic conductivity which is expressed through the effective resistance of the electrolyte R_{ion} across the electrode[5,7]. This quantity can be further used to determine the tortuosity of the electrodes according to the following equation:

$$\frac{\tau_{\mathrm{e}}}{\varepsilon} = \frac{R_{\mathrm{ion}} A_{\mathrm{CC}} \kappa}{2 L_{\mathrm{PE}}} = N_{\mathrm{M,e}} \qquad \text{(Eq. III-1)}$$

where $R_{\mathrm{ion}} = \sum r_{\mathrm{ion}}$; L_{PE} is the electrode thickness (m); A_{CC} is the macroscopic current collector area (m^2); τ_{e} is the electrode tortuosity factor, which, as will be discussed later in the paper, is distinct from the conventional tortuosity factor; and $N_{\mathrm{M,e}}$ is the Mullin number calculated with the electrode tortuosity factor instead of the conventional tortuosity factor.

Here, we also introduce the relationship between different types of surface areas that are used throughout this work:

$$A^* = \frac{A_{\mathrm{micro}}}{A_{\mathrm{CC}}} = \frac{a_{\mathrm{ASA}} A_{\mathrm{CC}} L_{\mathrm{PE}}}{A_{\mathrm{CC}}} = a_{\mathrm{ASA}} L_{\mathrm{PE}} \qquad \text{(Eq. III-2)}$$

where the non-dimensional term A^* is the microscopic active surface area of the electrode per unit of current collector area; A_{micro} is the microstructural active surface area (m^2); a_{ASA} is the volume specific active surface area ($\mathrm{m}_{\mathrm{ASA}}^2 \cdot \mathrm{m}_{\mathrm{PE}}^{-3}$).

Landesfeind *et al.*[5] assumed that the effective electronic resistance of the solid electrode material is much lower than the effective ionic resistance of the electrolyte in the pores so that it can be ignored (*i.e.* $r_{\mathrm{ion}} \gg r_{\mathrm{el}} = 0$). In practice, either a highly electronically conductive electrode (such as graphite) must be used, or the experiment should be carried out using an electrolyte with a low enough salt concentration to reduce its ionic conductivity.[5,18] The TLM equation that represents the impedance of a porous electrode can then be simplified to Eq. III-3:[5,31,32]

$$\tilde{Z}_{\mathrm{PE}} = \sqrt{R_{\mathrm{ion}} \cdot \tilde{Z}_{\mathrm{t}}} \coth\left(\sqrt{\frac{R_{\mathrm{ion}}}{\tilde{Z}_{\mathrm{t}}}}\right) = \sqrt{\frac{R_{\mathrm{ion}}}{j\omega A_{\mathrm{CC}} C_{\mathrm{DL}}}} \coth\left(\sqrt{j\omega A_{\mathrm{CC}} C_{\mathrm{DL}} R_{\mathrm{ion}}}\right) \qquad \text{(Eq. III-3)}$$

where $\tilde{Z}_{\mathrm{PE}}$ is the porous electrode impedance (Ω); j is the imaginary unit; ω is the frequency; $\tilde{Z}_{\mathrm{t}} = \frac{1}{j\omega A_{\mathrm{CC}} C_{\mathrm{DL}}}$ is the total interfacial impedance (Ω), which, in blocking condition, becomes $C_{\mathrm{DL}} = \sum c_{\mathrm{dl}} \Delta A^*$, the interfacial double layer capacitance per unit current collector area ($\mathrm{F} \cdot \mathrm{m}_{\mathrm{CC}}^{-2}$); A^* is defined in Eq. III-2, c_{dl} interfacial double layer capacitance per unit microstructural active surface area ($\mathrm{F} \cdot \mathrm{m}_{\mathrm{ASA}}^{-2}$).

Notably, given the assumptions above, one may realise that the mathematical description of TLM (Eq. III-3) reduces to that of a Finite-Space Warburg (FSW) element. Nonetheless, it is worth mentioning that the parameters governing the behaviour are clearly different. The intrinsic capacitances in the two models are not the same, *i.e.* surface scaling in Eq. III-3 instead of volumetric scaling in the case of FSW.

The limiting values of the real and imaginary parts of $\tilde{Z}_{\mathrm{el}}$ as $\omega \to 0$ are shown as follows:[32]

$$\lim_{\omega \to 0}(\tilde{Z}'_{\mathrm{PE}}) = \frac{R_{\mathrm{ion}}}{3} \qquad \text{(Eq. III-4)}$$

$$\lim_{\omega \to 0}\left(\tilde{Z}''_{\mathrm{PE}}\right) = \frac{-1}{\omega A_{\mathrm{CC}} C_{\mathrm{DL}}} \qquad \text{(Eq. III-5)}$$

From Eq. III-4, R_{ion} can also be determined approximately since the length of the 45° sloped region spans across approximately $R_{\mathrm{ion}}/3$ along the real axis.[7] Likewise, Pouraghajan *et al.*[33] showed different methods to quickly estimate R_{ion} that all provide a reasonable estimate with minor discrepancy as compared to using the fit of Eq. III-3.

The impedance of the electrode is normalised for ease of comparison by using:

$$\tilde{Z}^{*}_{\mathrm{PE}} = \tilde{Z}_{\mathrm{PE}} \frac{A_{\mathrm{CC}} \kappa_{\mathrm{eff}}}{L_{\mathrm{PE}}} \qquad \text{(Eq. III-6)}$$

Malifarge *et al.*[6] developed a more general analytical expression of the symmetric cell impedance that takes into account an arbitrary electronic resistance of the conductive matrix. More recently, Pouraghajan *et al.*[33] developed a generalized TLM that takes into account additional possible sources of impedance, such as a contact resistance with the current collector, the charge-transfer resistance and the electronic resistance of the electrode solid phase.

To better fit the experimental results, the pure capacitance that represents the double layer charging/discharging at the solid/liquid interface can be replaced by the Q_{S} ($\mathrm{F} \cdot \mathrm{m}_{\mathrm{ASA}}^{-2} \cdot \mathrm{s}^{-(1-\gamma)}$), which denotes a pseudo-capacitance, accompanied by an exponent γ in the constant-phase element (CPE).

Furthermore, the electrolyte concentration is assumed here to be high enough and the interfacial area not too large such that we may neglect any significant depletion of ions due to the accumulation of charge in the double layer at the electrode/electrolyte interface. Under this assumption, in addition to the fact that no charge transfer is expected to take place, no concentration gradient is assumed to develop across the cell. Hence, the electrolyte concentration remains uniform throughout the cell. Electrolyte diffusion can thus be safely neglected with the present experimental setup.

It is worth noting that when charge transfer is blocked in Newman P2D model, it simplifies down to the TLM[23,24,29,34], which is why the P2D model can also be used to fit the impedance

response of the symmetric cell in blocking condition.[6] However, it is restricted to the limiting case where the double layer is a pure capacitance (CPE exponent $\gamma = 1$ in the TLM).

III.4.3 Numerical Methods – Simulation

TauFactor is an open-source MATLAB application developed by Cooper *et al.*[20] for characterizing microstructure based on image data; including determining the tortuosity factors. In line with the conventional definition of the tortuosity factor, only simple Fickian diffusion is currently solved in *TauFactor*, which is only valid in certain cases, *e.g.* diffusion of species in an infinitely dilute solution within pores having electrically insulating walls (no double-layer formation). *TauFactor* uses an over-relaxed iterative approach to numerically solve Fick's diffusion equation at steady-state in order to calculate the flux and hence the associated tortuosity factor.

A diffusion simulation can be used to model effective steady-state electronic or thermal conductivity instead, by conceptually replacing the concentration gradient with a potential or temperature gradient respectively, as the mathematics is identical.

To the authors' knowledge, there is currently no numerical tool specifically for modelling the eSCM directly from 3D microstructural data. As such, this critical functionality has now been added to *TauFactor* as a tool for the battery community to highlight the fundamental differences between tortuosities determined by eRDM and eSCM.

While an eRDM model must capture the diffusion of species all the way through a pore network between two parallel boundaries, eSCM considers the migration of a species from the walls of one porous electrode's surface onto the surface of the other electrode (both having a double-layer capacitance). Consequently, there is an extra term that represents the double-layer charging/discharging at the solid/liquid interface within the porous electrodes. Furthermore, the geometry for the simulation now comprises a porous separator layer in between two identical electrode structures to be accounted for, instead of simply a passive (three-layers) porous structure as in the case of eRDM (see Figure III-8). The solid phase of the porous separator is considered to be inert, meaning there is no interaction with either the electrode solid phase or the liquid phase. In a future work, the 3D model of this symmetric cell structure may be simplified to just a "half-cell", which would be computationally less expensive.

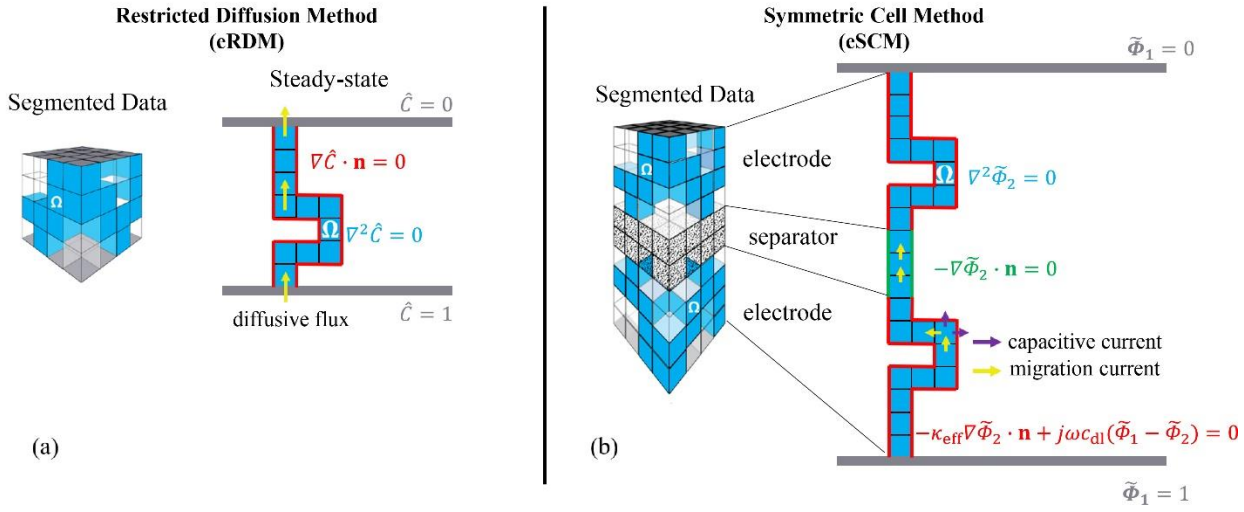

Figure III-8. Illustration of the use of segmented tomographic data as input along with the governing equation and boundary conditions for: a. eRDM and **b.** eSCM simulation implemented in TauFactor. Voxels in blue represent the pore network, transparent voxels represent the solid phase. For eRDM, $\hat{C}$ is the complex concentration of the diffusing species. For eSCM, there is a domain in between the two electrodes that represents the porous separator. Since there is no electrochemical reaction occurring in the system, $\tilde{\Phi}_1$ and $\tilde{\Phi}_2$ are simply the electron-conducting phase (solid) and ionic-conducting phase (liquid) electric potentials respectively; ω is the pulsation of the boundary stimulation; j is the imaginary unit; c_{dl} is interfacial double layer capacitance per unit microstructural active surface area. For both methods, Ω is the pore network domain in the system (in both electrodes and separator); **n** is the outward pointing unit normal to each voxel face. The color of the equations corresponds to the domain where they are applied. Vectors are represented in bold.

Along with tortuosity determination, Cooper *et al*. also implemented in *TauFactor* the option to solve this equation in the frequency domain. As a result, one obtains an impedance spectrum of a diffusing species through the pores of an inert (electronically-insulating) porous medium, which can capture the effect of pore structural features that leads to deviations from the conventional Warburg diffusion model.[35] It's worth noting that the time constants in the diffusion impedance are a volumetric phenomenon, whereas in the eSCM method, they originate from the interfacial capacitance instead. The mathematics correspondence of these two scenarios is described in the appendix of. [35]

In this work, the governing equation of eSCM and its boundary conditions are also Fourier transformed to their frequency domain representation, where sinusoidal stimulation of electric potential typical of EIS becomes a constant value imposed at the boundary, as shown in Figure III-8. As with the other solvers in *TauFactor*, the solver is pre-compiled into C++ and an iterative over-relaxation approach is used to accelerate convergence at each frequency.

We use the symmetric cell model proposed by Landesfeind *et al.*[5] in which the solid phase of the porous electrode is assumed to have a negligible electronic resistivity, such that its electronic potential is uniform within each electrode. For each frequency, the simulated impedance $\tilde{Z}_{\text{PE-sim}}$

is calculated as the ratio of the potential difference between the solid phases of the two electrodes ($\Delta\widetilde{\Phi}_1 = 1$ V is arbitrary selected) and the total ionic current density (expressed per geometric cross-sectional area of the cell). Since the physical problem is linear, the value of $\Delta\widetilde{\Phi}_1$ has no effect on the simulated impedance and so it is arbitrarily set to unity throughout.

As for the experimental data analysis in ref. [6], the electrode tortuosity is determined from a least-mean square fit of the simulated impedance response to the TLM model using Eq. III-3. Practically, the *fminsearch* function in MATLAB is used as the non-linear fitting function to minimize the objective functions shown below:

$$F = \sum_{n=1} \frac{(|\tilde{Z}^*_{\mathrm{PE-sim}} - \tilde{Z}^*_{\mathrm{PE}}|)^2}{|\tilde{Z}^*_{\mathrm{PE-sim}}|^p} \qquad \text{(Eq. III-7)}$$

where $\tilde{Z}^*_{\mathrm{PE-sim}}$ is the normalised-simulated impedance given by eSCM from *TauFactor*; $\tilde{Z}^*_{\mathrm{PE}}$ is the normalised-fitting impedance given by Eq. III-3, p is a weighing factor.[33] However, it should be noted that the value of τ_e can be extract from just the values of $\tilde{Z}^*_{\mathrm{PE}}$ at $\omega \to 0$ and $\omega \to \infty$.

III.4.4 Set of studied microstructures

Simulations are run on both 2D and 3D numerically-generated microstructures. The parameters used to simulate the eSCM are given in Table III-1. "Model" 2D microstructures (generated in MS paint) containing simple pore networks are investigated to demonstrate the fundamental difference in terms of the physics and the concept behind the two methods, eRDM and eSCM. Furthermore, 2D microstructures are modified to investigate some specific cases that help unveil the effects of microstructural features such as different morphology of pore networks or different types of pore, on the simulated impedance spectra and/or derived tortuosity value.

Table III-1. Parameters used in eSCM simulation

Parameters	Value
κ	0.046 [1] $\mathrm{S \cdot m^{-1}}$
c_{dl} (per unit active surface area)	0.01 [2] $\mathrm{F \cdot m^{-2}}$
f	$10^7 - 10^{-1}$ [a]
Voxel size	$1 \times 1 \times 1$[a] $\mu\mathrm{m}^3$

[1] The electrolyte conductivity is chosen from ref. [5] for 10mM blocking electrolyte of salt $TBAClO_4$. [2] The interfacial double layer capacitance per unit microstructural electrode active surface area is chosen from ref. [5]. [a] Assumed values.

For 2D microstructures, we first consider the case where there is a porous separator in which there are only straight pores that perfectly align with those of porous electrodes on both side. For 3D microstructure, to facilitate the data preparation step, we use a free-standing electrolyte layer

where only liquid electrolyte is present between the two electrodes with no porous separator. The investigation can also be extended to include the pore network within the separator between the two electrodes in the symmetric cell simulations in future work, since tomographic data of several types of separators are already available in open-access literature.[36]

For the 3D structures, random-packing of spheres is generated using GrainGeo module by GeoDict[40] to imitate a battery porous electrode microstructure. Simulations using 3D microstructures allow us to gain insight into the likely behavior of real-life electrodes, given the tomographic data is reliable enough in capturing the real electrode microstructure, and help us shed light on the appropriate method for the determination of tortuosity for battery applications.

Nomenclature

A^*	$\mathrm{m}^2_{\mathrm{ASA}}/\mathrm{m}^2_{\mathrm{CC}}$	Microscopic active surface area of the electrode per unit of current collector area
A_{CC}	$\mathrm{m}^2_{\mathrm{CC}}$	Current collector surface area
A_{micro}	$\mathrm{m}^2_{\mathrm{ASA}}$	Microstructural active surface area
a_i^*	$\mathrm{m}_i^2/\mathrm{m}^3_{\mathrm{CV}}$	Volume-specific surface area of phase i within the control volume captured by tomography
a_i	$\mathrm{m}_i^2/\mathrm{m}^3_{\mathrm{PE}}$	Interfacial surface area between phase i and the liquid phase at porous electrode scale
c_{dl}	$\mathrm{F}.\mathrm{m}^{-2}_{\mathrm{ASA}}$	Interfacial double layer capacitance per unit microstructural active surface area
$\hat{\mathrm{C}}$	$\mathrm{mol}/\mathrm{m}^3$	Complex concentration of the diffusing species when solving Fick's 2nd law of diffusion at frequency domain
C_{DL}	$\mathrm{F}/\mathrm{m}^2_{\mathrm{CC}}$	Interfacial double layer capacitance per unit current collector area
f	Hz	Frequency
j		Imaginary unit
$\vec{n}$		Outward pointing unit normal to a plane or each voxel face
p		Weighing factor
Q_{s}	$\mathrm{F}/(\mathrm{m}^2_{\mathrm{ASA}} \cdot \mathrm{s}^{1-\gamma})$	Pseudo-capacitance at the solid/liquid interface expressed per porous electrode active surface area
R_{ion}	Ω	Effective ionic resistance of the electrolyte
r_{el}	Ω	Electronic resistance in a differential segment of the electrode
r_{ion}	Ω	Ionic resistance in a differential segment of the electrolyte
$\tilde{Z}_{\mathrm{PE}}$	Ω	Complex porous electrode impedance

$\tilde{Z}_{\mathrm{t}}$	Ω	Complex total interface impedance
$\tilde{Z}_{\mathrm{PE}}^{*}$		Complex normalised porous electrode impedance
$\tilde{z}_{\mathrm{t}}$	$\Omega \cdot \mathrm{m}^2$	Complex surface impedance elements

Greek symbols

Φ_i	V	Electric Potential of phase i
$\tau_{\mathrm{Bruggeman}}$		Tortuosity Factor by Bruggeman
τ_{e}		Electrode tortuosity factor
γ		Constant Phase Element exponent
ε		Porosity
κ	S/m	Ionic Conductivity of the electrolyte
σ	S/m	Electronic Conductivity of the solid phase
τ		Tortuosity factor
ω	rad/s	Pulsation
Ω		Pore network domain in the system

Subscripts

1	Solid Matrix (Active Materials + Additives)

2	Liquid Phase (Electrolyte) in the pore space
eff	Effective properties
re	relative
PE	Belong to the Porous Electrode
el	Electronic in the solid phase

References

[1] J. Newman, T. W. Chapman, *AIChE J.* **1973**, *19*, 343.

[2] S. D. Thompson, J. Newman, *J. Electrochem. Soc.*, **1989**, 136, 3362.

[3] H. S. Harned, D. M. French, *Ann. N. Y. Acad. Sci.* **1945**, *46*, 267.

[4] I. V. Thorat, D. E. Stephenson, N. A. Zacharias, K. Zaghib, J. N. Harb, D. R. Wheeler, *J. Power Sources* **2009**, *188*, 592.

[5] J. Landesfeind, J. Hattendorff, A. Ehrl, W. A. Wall, H. A. Gasteiger, *J. Electrochem. Soc.* **2016**, *163*, A1373.

[6] S. Malifarge, B. Delobel, C. Delacourt, *J. Electrochem. Soc.* **2017**, *164*, E3329.

[7] N. Ogihara, S. Kawauchi, C. Okuda, Y. Itou, Y. Takeuchi, Y. Ukyo, *J. Electrochem. Soc.* **2012**, *159*, 1034.

[8] F. Pouraghajan, H. Knight, M. Wray, B. Mazzeo, R. Subbaraman, J. Christensen, D. Wheeler, *J. Electrochem. Soc.* **2018**, *165*, 2644.

[9] D. S. Eastwood, R. S. Bradley, F. Tariq, S. J. Cooper, O. O. Taiwo, J. Gelb, A. Merkle, D. J. L. Brett, N. P. Brandon, P. J. Withers, P. D. Lee, P. R. Shearing, *Nucl. Instruments Methods Phys. Res. Sect. B Beam Interact. with Mater. Atoms* **2014**, *324*, 118.

[10] P. R. Shearing, D. S. Eastwood, R. S. Bradley, J. Gelb, S. J. Cooper, F. Tariq, D. J. L. Brett, N. P. Brandon, P. J. Withers, P. D. Lee, *Microsc. Anal*, ***2013***, *27(2), 19-22.*

[11] V. Julie, L. Jérôme, C. Peter, B. Pierre, D. Gérard, S. Heikki, U. V. François, *J. Power Sources* **2013**, *243*, 841.

[12] P. Pietsch, V. Wood, *Annu. Rev. Mater. Res.* **2017**, *47*, 451.

[13] R. Elango, A. Demortière, V. De Andrade, M. Morcrette, V. Seznec, *Adv. Energy Mater.* **2018**, *8*, 1703031.

[14] Z. Su, V. De Andrade, S. Cretu, Y. Yin, M. J. Wojcik, A. A. Franco, A. Demortière, *ACS Appl. Energy Mater.* **2020**, acsaem.9b02236.

[15] L. Zielke, T. Hutzenlaub, D. R. Wheeler, C.-W. Chao, I. Manke, A. Hilger, N. Paust, R. Zengerle, S. Thiele, *Adv. Energy Mater.* **2015**, *5*, 1401612.

[16] T. Hutzenlaub, A. Asthana, J. Becker, D. R. Wheeler, R. Zengerle, S. Thiele, *Electrochem. commun.* **2013**, *27*, 77.

[17] F. L. E. Usseglio-Viretta, A. Colclasure, A. N. Mistry, K. P. Y. Claver, F. Pouraghajan, D. P. Finegan, T. M. M. Heenan, D. Abraham, P. P. Mukherjee, D. Wheeler, P. Shearing, S. J. Cooper, K. Smith, *J. Electrochem. Soc.* **2018**, *165*, A3403.

[18] J. Landesfeind, M. Ebner, A. Eldiven, V. Wood, H. A. Gasteiger, *J. Electrochem. Soc.* **2018**, *165*, A469.

[19] D. J. Miller, C. Proff, J. G. Wen, D. P. Abraham, J. Bareño, *Adv. Energy Mater.* **2013**, *3*, 1098.

[20] S. J. Cooper, A. Bertei, P. R. Shearing, J. A. Kilner, N. P. Brandon, *SoftwareX* **2016**, *5*, 203.

[21] K. K. Patel, J. M. Paulsen, J. Desilvestro, *J. Power Sources* **2003**, *122*, 144.

[22] R. B. MacMullin, G. A. Muccini, *AIChE J.* **1956**, *2*, 393.

[23] J. Newman, K. E. Thomas-Alyea, *Electrochemical Systems*, Wiley-Blackwell, **2012**.

[24] J. Newman, W. Tiedemann, *AIChE J.* **1975**, *21*, 25.

[25] X. Lu, A. Bertei, D. P. Finegan, C. Tan, S. R. Daemi, J. S. Weaving, K. B. O. Regan, T. M. M. Heenan, G. Hinds, E. Kendrick, D. J. L. Brett, P. R. Shearing, *Nat. Commun.* **2020**, *11*, 1.

[26] R. de Levie, *Electrochim. Acta* **1963**, *8*, 751.

[27] A. Lasia, *J. Electroanal. Chem.* **1995**, *397*, 27.

[28] J. P. Meyers, M. Doyle, R. M. Darling, J. Newman, *J. Electrochem. Soc.* **1988**, *147*, 2930.

[29] R. de Levie, *Electrochim. Acta* **1963**, *8*, 751.

[30] H. Keiser, K. D. Beccu, M. A. Gutjahr, *Electrochim. Acta* **1976**, *21*, 539.

[31] U. Tröltzsch, O. Kanoun, *Electrochim. Acta* **2012**, *75*, 347.

[32] M. Itagaki, S. Suzuki, I. Shitanda, K. Watanabe, *Electrochemistry*, 2007, 75(8), 649-655.

[33] F. Pouraghajan, H. Knight, M. Wray, B. Mazzeo, R. Subbaraman, J. Christensen, D. Wheeler, *J. Electrochem. Soc.* **2018**, *165*, 2644.

[34] R. de Levie, *Electrochim. Acta* **1964**, *9*, 1231.

[35] S. J. Cooper, A. Bertei, D. P. Finegan, N. P. Brandon, *Electrochim. Acta* **2017**, *251*, 681.

[36] M. F. Lagadec, *ETH Zurich* **2018**, DOI 10.3929/ethz-b-000265085.

Chapter IV . 3D Quantification Of Microstructural Properties Of NMC High-Energy Density Electrodes By X-Ray Holographic Nano-Tomography

IV.1 Introduction

As discussed in Chapter II, due to the low attenuation of the CBD, the X-ray contrast of the CBD compared to pores in final images is weak. Therefore, the CBD and pores in the majority of the studies cannot be resolved, which prevents the complete characterization of the electrode microstructure. Few studies based on nano-XCT have attempted to capture the three phases separately: AM, CBD, and pores. The common approach is to add a synthetic structure of CBD[1,2] to the AM framework obtained from the tomographic data. Although this approach offers the ability of adjustment of the CBD morphology,[3–5] the results stay somehow "fictive". A more realistic approach is from Daemi *et al.*,[6] in which they combined the information from the FIB-SEM analysis of a stand-alone CBD electrode (*i.e.* prepared with no NMC particles). The use of a stand-alone CBD electrode was also used by Lu *et al.*[7] to capture features of the CBD using a novel nano-XCT dual-scan superimposition technique. The validity of the stand-alone CBD electrode might be questioned since the behavior of the CBD slurry during the manufacturing process might not be the same as when considering the presence of AM in the slurry. Recently, Müller *et al.*[8] proposed the multimodal approach combining nano-XCT data with data obtained using ptychographic X-ray CT. Impressively, this approach enables CBD to be clearly visualized, as the ptychographic technique offers higher spatial resolution (40 nm) along with a pixel size of 20 nm. However, combining different imaging techniques requires significant effort for the sample preparation step, the imaging process and the post-processing data. As an innovative solution, Morelly *et al.*[9] proposed to replace the conventional carbon black by carbon-coated iron nanoparticles as contrast-enhancing particles, which allows resolving the CBD from the remaining. However, this approach cannot be applied for a wide range of industry-graded electrodes, as it still requires a supplementary step for making electrodes with specific additives.

In this chapter, the hard X-ray nano-holotomography technique illustrated in Figure IV-1a and available at the ID16B beamline of the ESRF is used[10,11] to extract microstructural properties of three different NMC porous electrodes. This phase contrast technique allows the reconstruction of large 3D volumes (for those, the size can be up to 100x100x100 μm^3, see Figure IV-1b, c), while keeping a small pixel size (50 nm) for an adequate high spatial resolution and intensity contrast to distinguish the three domains: AM, CBD and pores. It is worth noting that the resolution of the holotomography technique might not be enough to capture the nano-porosity that can exist in the CBD clusters and that can only be captured by FIB-SEM technique (Figure IV-2). Given that this porosity can reach up to 47% within the CBD,[2] it can contribute significantly to electrochemical performance, as discussed by Trembacki *et al.*[5] and Ferraro *et al.*[12] using synthetic CBD morphology. Nevertheless, the holotomography technique still provides a persistent and high-throughput workflow to capture other microstructural details. Furthermore, the volumes examined with holotomography are relatively large, in respect to the most prominent component within the electrodes, *i.e.* NMC particles ($d_{50} = 4.7$ µm). The representativeness can therefore be validated.

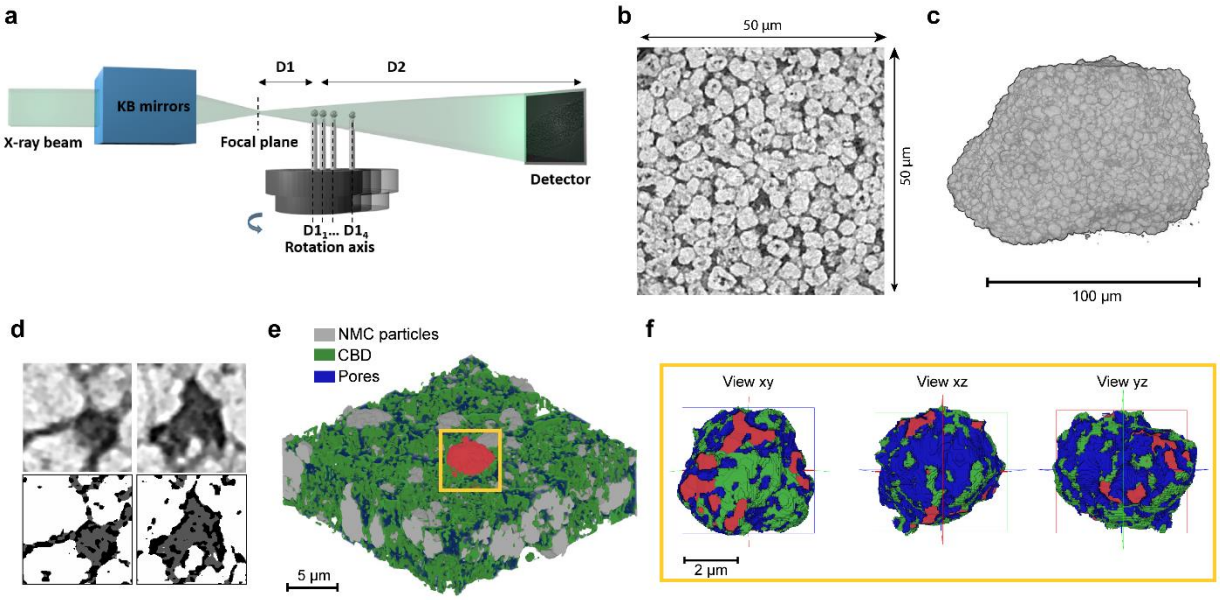

Figure IV-1. Illustration of the workflow used for this study. a. Schematic representation of the hard X-ray nano-holotomography experimental setup at ID16B [62] **b, c.** Raw data filtered with Non-local Mean and Unsharp Mask in 2D and 3D. **d, e.** Examples of the segmentation results in 2D and 3D using the machine learning segmentation plugin, Trainable Weka[13], in ImageJ. **f.** Visualization of the individual NMC particle colored in red in e along with the interfacial area with the other phases.

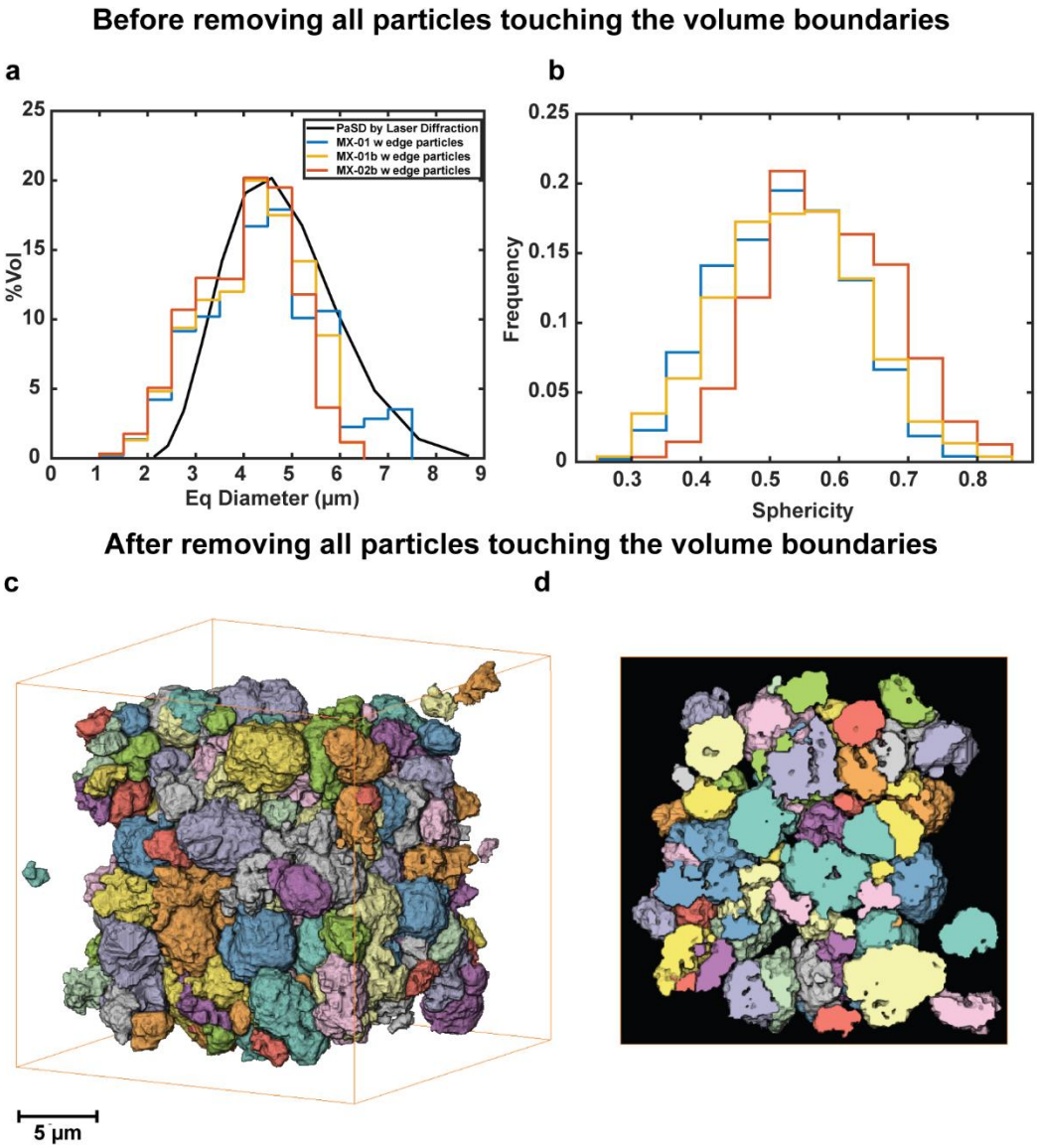

Figure IV-2. Analysis of Active Materials phase. **a, b.** The particle size distribution and the sphericity of all particles presented within the control volume. **c, d.** The MX-02b after removing all particles touching the control volume boundaries along with the 2D slice showing the cracking parts of the AM particles.

The discrimination of the morphology of the different phases within the electrode using a machine-learning segmentation method (Figure IV-1d, e) allows for a complete image-based analysis in order to investigate the effects of the microstructure on the electrode electrochemical performance. A statistical approach is frequently employed to determine microstructure inhomogeneities. It can be done by studying variations of different sub-volumes at different locations. In this study, beside the global analysis of the control volume, a statistical analysis at the particle scale (Figure IV-1f) including more than 500 individual NMC particles for each sample is proposed instead. It has been chosen because certain metrics are more relevant at particle scale, since they are related to the kinetics of the electrochemical reaction, which occurs at the interface between the AM particles and the electrolyte. This approach provides statistically-significant

results that offer an insight into the distribution of the microstructural properties at particle scale. Finally, a scenario to comprehend the impact of the microstructure on the electrochemical performance (via discharge rate-capability measurements) of the three electrodes is proposed.

IV.2 Results & Discussion

The results presented here after are based on a careful image processing of the 3D volumes obtained by X-ray nano-holotomography. All the steps of the image processing and data analysis are detailed in the 'Methods' section of this chapter. It is worth noting: (i) that the representativeness of the control volumes used for the data analysis has been validated (Figure IV-3), (ii) that a machine learning algorithm (Random Forest via Trainable Weka plugin in ImageJ) has been used for the segmentation and (iii) that a global analysis of the control volume along with a statistical quantification of the inter-connectivity between phases at the particle scale are performed for the complete characterization of the microstructures.

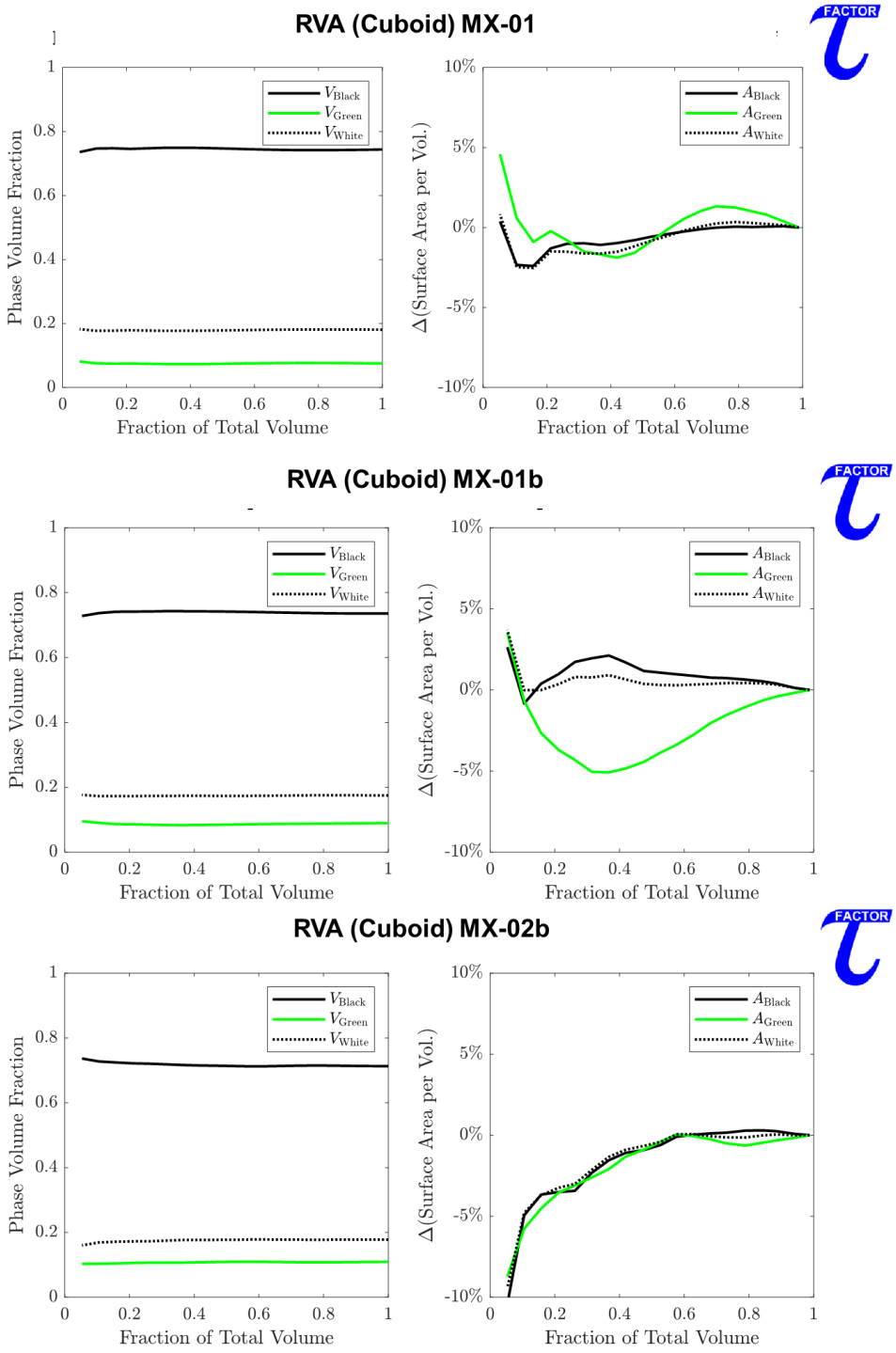

Figure IV-3. Representative Volume Analysis. The analysis shows the evolution of the variation of %v and surface area of different phases by the size of the control volume, which is approximately incremented 5% in the three directions at each iteration. It is denoted as Cuboid method in *TauFactor*. It can be seen that in all cases, the %v of the three phases rapidly converges to representative values as the fraction of total volume increases. In contrast, the surface area in turn are more sensitive to the control volume size. However, the results show that by getting closer to 100% of the total volume, which equals to the control volume studied in the text, the variation of the surface area of the three phases converge to 0%.

Thus, the three control volumes can be considered as representative. In this figure, the AM phase is represented in black, the CBD phase is represented in green and the Pores phase is represented in dashed black line.

IV.2.1 Active material phase

As illustrated in Figure IV-1b-d, the NMC particles of the AM phase can be well-identified based on either the grey level (brightest region) or their morphology (*e.g.* "spherical"-type secondary particles). The volume fraction (%v) of AM phase for the three samples are given in Table IV-1. It shows that the obtained values are slightly higher (2-5%) than expected ones. While the expected value can contain itself an inherit error due to either the fabrication process or the measurement of the volume, the difference is also due to the fact that the voxels at the phases interfaces may belong to more than a single phase due to the partial volume effect (detailed in the "Methods" section). As such, there is always some uncertainty in segmenting the interfacial regions between phases. To evaluate the sensitivity of the uncertainty in this region, from the segmentation results, a dilatation and an erosion of a single pixel layer at the AM phase boundary have been done. This step induces a variation of ±6% on the obtained %v AM. Thus, this discrepancy is considered within the uncertainty range due to the method limitation (*i.e.* image resolution). It is worth noting that the overestimation of %v of AM will lead to the underestimation of the %v of either CBD or pores.

Table IV-1. Volume fraction of the active materials in the three electrodes. Expectation (Exp) values provided by the supplier are reported along with the values extracted from the 3D tomographic data (Data).

Sample	**MX-01**		**MX-01b**		**MX-02b**	
%v AM	Data	Exp.	Data	Exp.	Data	Exp.
	74.4	70.92	74.1	69.6	71.7	69.6

Figure IV-4a shows the AM phase in MX-01 after being separated into more than 500 individual NMC particles (using Avizo software). It is worth noting that the electrodes studied in this work are for high energy applications, that require high density of AM. This can be seen through the highly packed of NMC particles within the control volume. After the separation of the NMC particles, image-based particle size distribution can be calculated for each sample. Yet, the edge effect of the cropped volume can cause a decrease in particle size. It refers to particles that are at the boundaries of the cropped volume. As such, only a part of them is taken into account for the volume calculation, which under-estimates their exact size. Thus, to better quantify the particle size, all particles touching the volume boundaries have been removed (see Figure IV-2). Figure IV-4b shows the particle size distribution of three samples along with the distribution obtained by the laser diffraction measurement on raw material powder. All three sample exhibit the highest peak corresponding to the d_{50} of the materials, despite a slightly lower-than-expected particle size, when comparing to the laser diffraction's result. Here, we assume that this is due to the calendaring

process, which is known to cause fractures of AM particles under the high pressure.[14] This assumption is supported by the visualization of cracked particles in the SEM image of the MX-02b cross-section in Figure IV-4d. The cracking parts are also presented in our segmented volume as single AM particles (Figure IV-2), as we also accounted the internal fissures during the segmentation step. Also, internal pores are observed for NMC secondary particles. Interestingly, we can observe the occasional presence of the CBD inside these internal pores (see purple arrows in Figure IV-4d), which shows that these pores can be opened to the electrolyte. This observation is in line with the work done by Miller *et al.*,[15] who revealed the penetration of electrolyte through the AM grain boundaries. Thus, the (de)lithiation process can theoretically occur from the inside of the NMC secondary particles, reducing the diffusion length, thereby easing the solid-diffusion process. The broad sphericity distribution (and lower than 1) observed in Figure IV-4c challenges the assumption on the sphericity of the NMC particles that is made in many simulations.

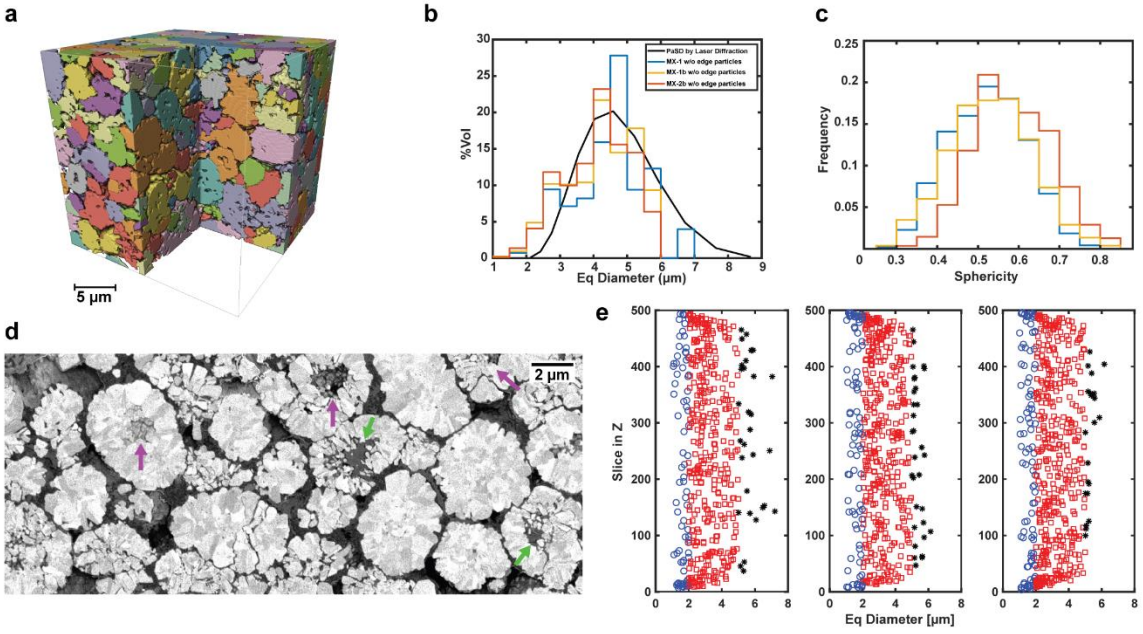

Figure IV-4. Morphology of the AM phase in three different samples. **a.** The AM phase of MX-01 sample is separated into individual particles that allow the statistical analysis of the microstructural properties by particles. **b.** Particle size distribution is given by tomographic data without removing the edge particles and by laser diffraction. **c.** The distribution of the sphericity of the NMC particles in the three samples. **d.** FIB-SEM image of the sample MX-02b shows cracked NMC particles. Purple arrows: internal pore without CBD, Green arrows: internal pore with CBD **e.** Spatial repartition of the NMC particles in the three samples in the direction normal to the current collector. Blue circles: Small particles, Red squares: Average particles and Black stars: Big particles.

Image-based approach allows the access to the spatial distribution of the AM particles. Since our sample preparation protocol (see details in 'Methods' section) allows to keep the through-plane direction aligned with the Z-axis during the acquisition step, we can visualize the distribution of the AM particles in the direction normal to the current collector (Figure IV-4e) (the coordinates of the particle are based on the coordinates of its centroid in space). Our results clearly point out

that the big particles tend to move into the bulk of the electrode rather than be in the electrode boundaries (either separator side or current collector side), which is consistent with the work from Ebner *et al.*.[16] For the remaining, most of the particles are well-distributed along the electrode thickness, which can be confirmed with the minor variation of the %v of AM phase with the fraction of total volume in Figure IV-3. The small particles are found to be more at the boundary of the control volume, which can due to the edge effect mentioned above.

IV.2.2 Carbon Binder Domain

The CBD refers to the additives that do not contribute to the capacity of the electrode (inactive materials) but rather to the rate performance of the electrode. It consists of a mixture of good electronically-conducting materials (*e.g.* carbon black, carbon fiber) and a polymeric binder. The CBD provides the mechanical stability of the electrode and establish the electronic conducting pathways within the electrode for most active materials. Thus, it is expected to be well-percolated and uniformly-distributed throughout the electrode volume. Otherwise, electrons cannot be transported uniformly to all reaction-sites (at the AM particle surface in contact with electrolyte) across the electrode.

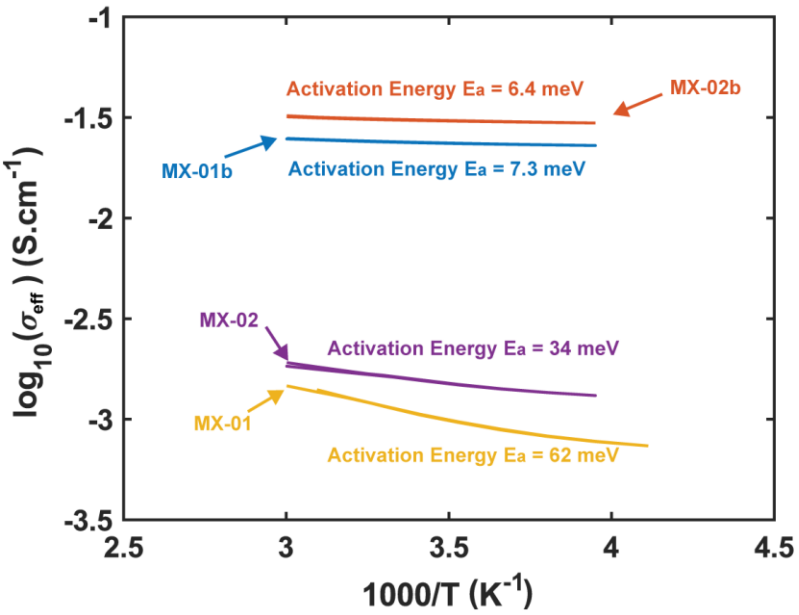

Figure IV-5. Electronic conductivity measured by the 4-line method. The electronic conductivities of four different electrodes are measured in function of temperature, which give the corresponding activation energy for each electrode. Noting that the MX-02 is not in the scope of the study in this chapter.

Table IV-2 shows the microstructural properties of the CBD extracted from the 3D microstructure data along with the electronic conductivities measured by the 4-line method (see Figure IV-5). Figure IV-7a shows the 3D CBD distribution and morphology (green) in the three different samples. It can be seen that the CBD tends to form clusters that locate in between neighboring particles rather than a film-like morphology. The presence of CBD clusters observed

in this work is consistent with other work [19] [42] [43] based on different approaches. As it is observed in the 2D slices of the Figure IV-7b, the CBD clusters present a porous morphology, which has been also confirmed by high resolution FIB-SEM data of MX-02b presented in Figure IV-6, as well as in [19] [42]. Looking at Table IV-2, the extracted %v of CBD from MX-01 and MX-02b volumes are consistent with the expected values, while in MX-01b, the obtained %v of CBD yields a lower value. Despite a lower %v compared to MX-02b and MX-01b, the CBD network in MX-01 has a larger volume-specific surface area a^*_{CBD} (Table IV-2), which refers to the sum of interfacial area CBD/AM, and CBD/pores normalized to the control volume. The decrease of a^*_{CBD} at higher %v, as it is the case for MX-02b, indicates a more important formation of CBD agglomerates. It is important to note that the formation of CBD agglomerates will negatively impact the inter-connectivity between CBD and the other phases, as it will be discussed later in the paper. The percolation of the CBD is quantified for the three samples (Table IV-2). As expected, higher %v coupled with a lower a^*_{CBD} in MX-01b and MX-02b results in a better percolation compared to MX-01.

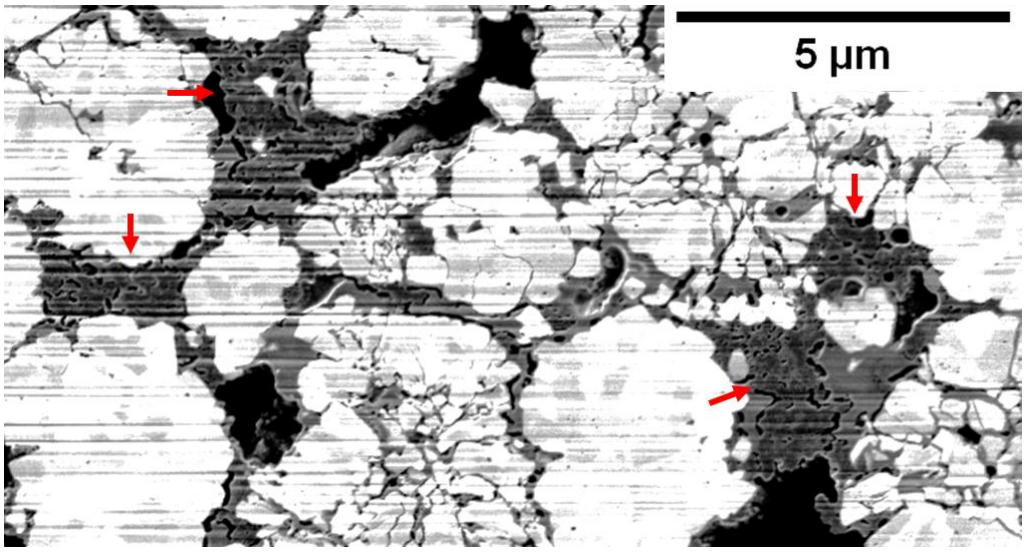

Figure IV-6. FIB-SEM data of MX-02b. The image shows the porous morphology of the CBD clusters (marked with red arrows).

Table IV-2. Microstructural properties of the CBD phase. Expected (Exp.) values are presented along with the values extracted from the 3D tomographic data (Data).

Sample	**MX-01**		**MX-01b**		**MX-02b**	
Percolation [%]	88.2		91.4		93.2	
%v CBD	Data	Exp.	Data	Exp.	Data	Exp.

	7.5	7.8	8.8	11.3	10.5	11.3
a^{*}_{CBD} $(\mu m^{2}_{\mathrm{CBD}} \cdot \mu m^{-3}_{\mathrm{CV}})$	1.12		1.08		1.00	
σ_{eff} $(S \cdot cm^{-1})$	0.0025		0.0250		0.0300	
E_a (eV)	0.030		0.007		0.006	

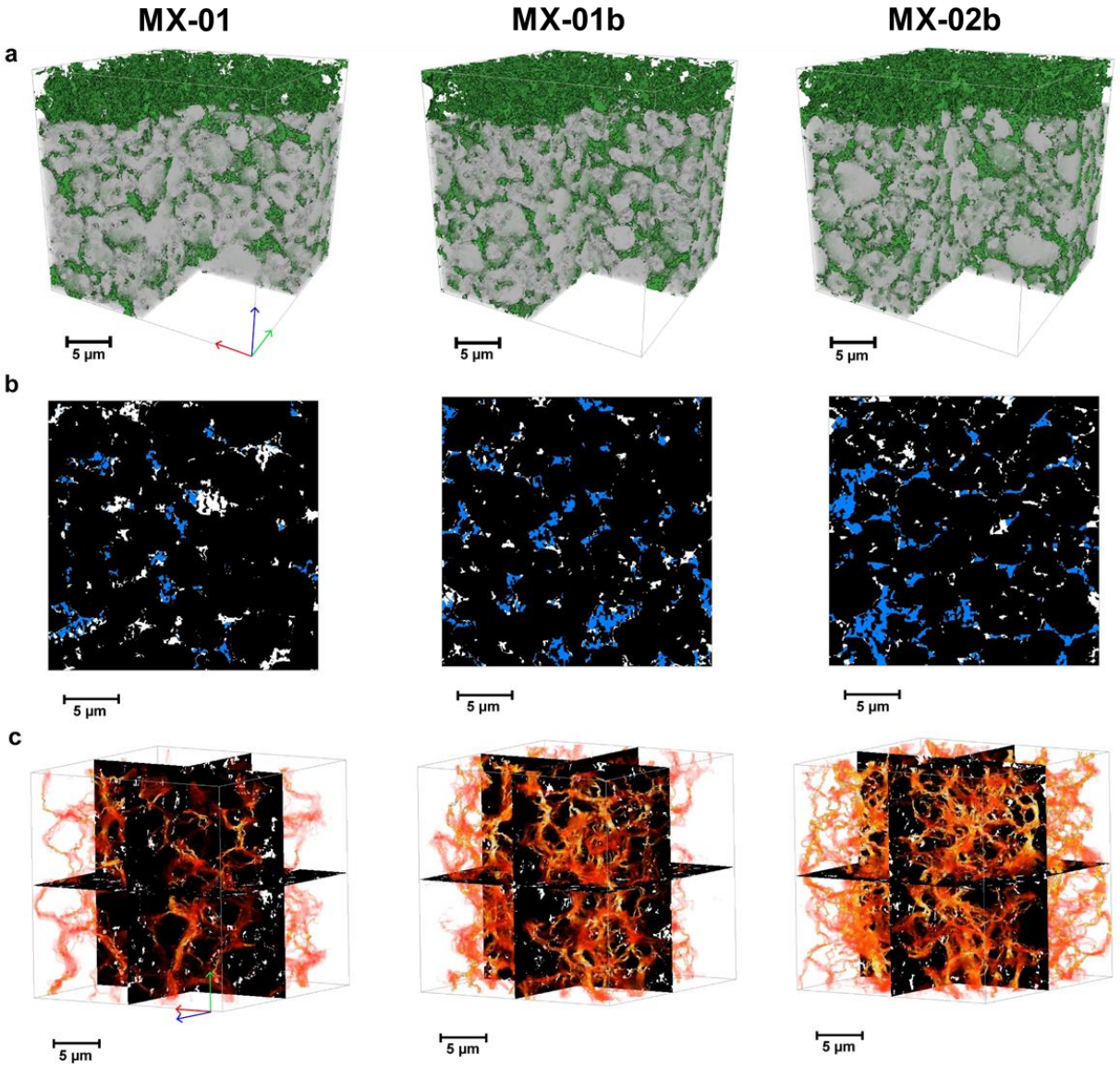

Figure IV-7. 3D microstructure of the CBD and simulations from diffusion-based method (with *TauFactor*) in the three different electrodes. a. The CBD network (green) within the control volume (25x25x25 µm^3). For the ease of visualization, the rest is represented as a transparent grey phase. **b.** For the

ease of the observation of the porous morphology of the CBD, 2D slices are chosen to be shown, in which dead-end paths (white) and flux-through paths (blue) are both presented. One can observe the porous morphology of the CBD in various clusters (either in blue or white). **c.** The normalized flux density within the flux-through paths was colored for the three volumes. Dead-end pathways are represented in the three ortho slices as the white phase. Through-plane: Z-axis (green arrow), In-plane: X-axis (red arrow), Y-axis (blue arrow).

Figure IV-7c shows the simulation results of the normalized electronic current density through the control volume in the direction normal to the current collector in the three samples using a diffusion-based method (see details in 'Methods' section). It is worth to mention that, the flux density maps include only the pathways that allow moving from one side to the other side of the microstructures, so-called flux-through paths.[17] No or low flux regions were detected by applying an arbitrary threshold value (2% of maximum) to the flux density map at steady-state, denoted as dead-end paths. They are represented in white in Figure IV-7b, c.

In MX-01b and MX-02b, a considerable amount of flux-through paths are presented compared to MX-01. These pathways can be considered as long-range connections presented in the CBD network. They are essential for establishing a good inter-connectivity between different regions of the electrode at larger scale, which, along with a better percolation, enhances the electronic conductivity of the electrode.[18–20] This hypothesis is supported by the electronic conductivity measurements, shown in Table IV-2, on the three samples using the four lines method.[21,22] As expected, MX-02b and MX-01b exhibit a higher conductivity along with a lower activation energy compared to MX-01.

While flux-through paths can be considered as long-range contacts that rapidly transport electrons between different regions of the electrode, dead-end paths rather play a role of short-range contacts, which uniformly distribute the electrons to the reaction-sites throughout the electrode. As a result, the synergistic effect which provides both long-range and short-range contacts can be crucial to the electrode performance, especially at high C-rates, as highlighted by several authors.[18–20,23]

IV.2.3 Pore Network

The pore network is responsible for the ionic transport when filled with the electrolyte. Its microstructure governs the effective ionic conductivity of the electrolyte within the porous structure, which is critical for the electrode performance at high C-rates, especially for high loading electrodes.[24] As expected for high energy density electrodes, the segmentation of the three volumes results in porosities that are unusually low (<20%), as it can be seen in Table IV-3. Although the porosities are slightly lower than the expected values, they are consistent with the electrode specifications. Despite their low porosities, all three samples exhibit a percolation of the pore network greater than 94%. MX-01b has a lowest porosity but presents a highest volume specific surface area a^*_{pores}, which is defined in the same way as a^*_{CBD}. The morphology of the pore network (segmented in blue) in the three different samples is illustrated in Figure IV-8a.

Table IV-3. Microstructural properties of the pore network. Expected (Exp.) values are presented along with the values extracted from the 3D tomographic data (Data).

Sample	**MX-01**		**MX-01b**		**MX-02b**	
Percolation [%]	95.5		94.6		94.6	
Porosity	Data	Exp.	Data	Exp.	Data	Exp.
	18.1	21.2	17.1	19.1	17.8	19.1
a^*_{pores} $(\mu m^2_{\mathrm{pores}} \cdot \mu m^{-3}_{\mathrm{CV}})$	1.05		1.07		1	
τ (N_M)	X-axis	Z-axis	X-axis	Z-axis	X-axis	Z-axis
	8.13 (45.17)	4.12 (22.88)	9.31 (54.44)	4.15 (24.15)	7.31 (41.07)	3.74 (21.05)
τ_e $(N_{M,e})$	X-axis	Z-axis	X-axis	Z-axis	X-axis	Z-axis
	8.51 (47.28)	3.78 (20.87)	8.57 (50.12)	3.95 (22.99)	6.97 (39.16)	3.56 (20.00)

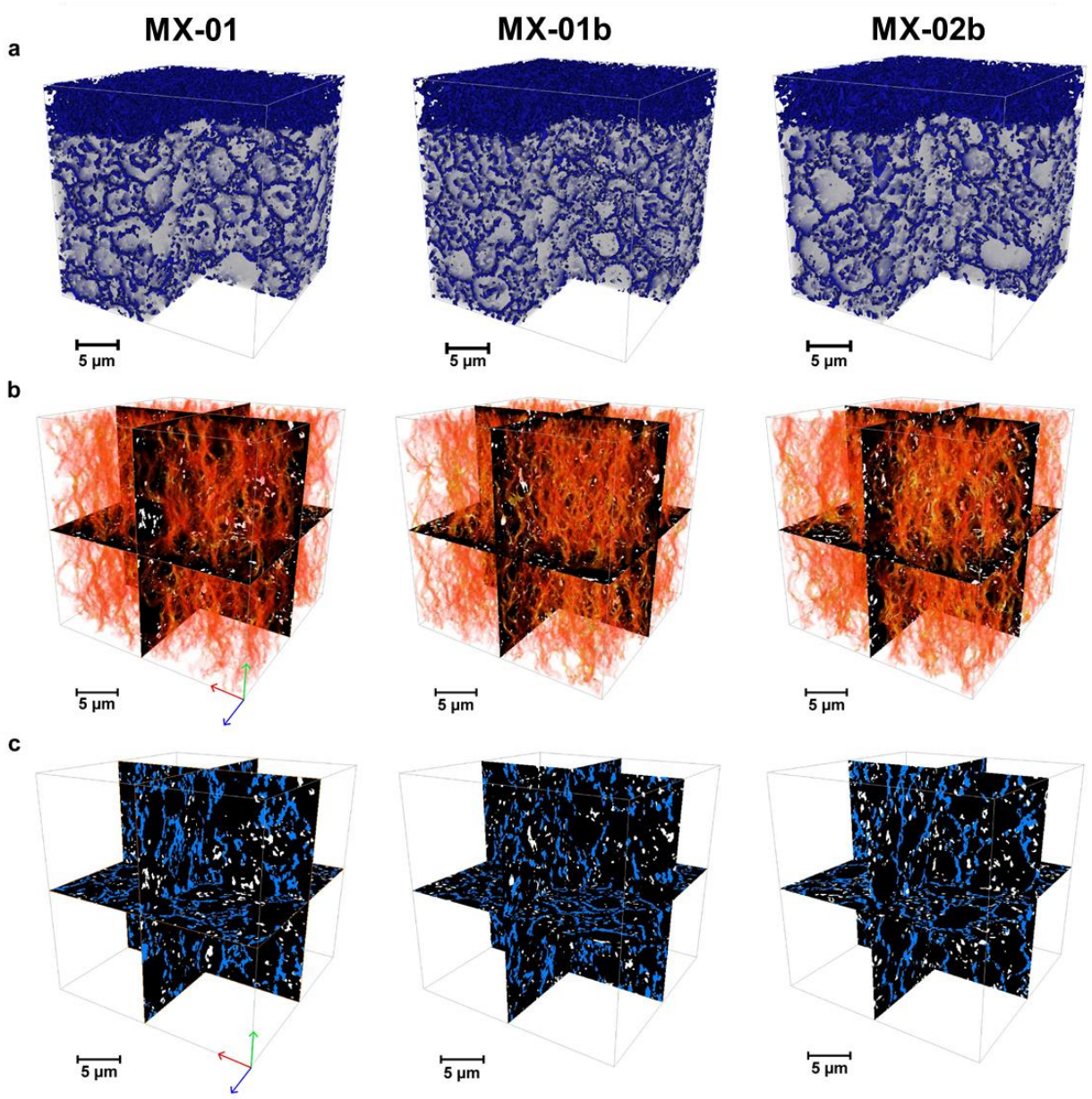

Figure IV-8. 3D microstructure of the pore network and simulations from diffusion-based method in the three different electrodes. a. Morphology of the pore network (blue) within the control volume, the AM & CBD phases are represented in transparent grey for the ease of visualization. **b.** The normalized flux density map of the pore network. The flux only passes by the through-pores in red, dead-end pores are represented in white on the ortho slices. **c.** The 2D ortho-slices of the pore network separated into through-pores (blue) and dead-end pores (white). Through-plane: Z-axis (green arrow), In-plane: X-axis (red arrow), Y-axis (blue arrow).

To investigate the impacts of the pore network on the ionic transport properties, the tortuosity factor and the McMullin number of the pore network are quantified using simulations. However, compared to other microstructural properties such as porosity or volume-specific surface area, the determination of the tortuosity factor is still not standardized in the literature. Our previous work[17]

showed that there is a theoretical difference between the tortuosity factors calculated by the two methods: the diffusion-based method (regular method),[25] and the symmetric cell method (SCM).[26,27] The diffusion-based method considers the transport through the porous microstructure whereas the symmetric cell method considers the transport to the AM surfaces within the porous microstructure. As demonstrated in [48], the electrode tortuosity factor, obtained from the SCM, is more suitable to characterize porous electrodes than the commonly-used tortuosity factor. Still, both tortuosity factors are calculated in this work for comparison. Furthermore, the tortuosity factors (in-plane and through-plane) were also quantified allowing the investigation of tortuosity anisotropy. The tortuosity anisotropy has been widely reported in the literature. It has been demonstrated by tomography-based approach as well as experimental measurements (for the case of MCMB active materials) to increase with either the non-spherical AM particles or the calendaring process.[28–31] A minor tortuosity anisotropy ($\tau_{\mathrm{through-plane}} > \tau_{\mathrm{in-plane}}$) is reported for NMC electrodes in [61] [62] via simulations using 3D microstructures with numerically-generated CBD. The results can be attributed to the roughly spherical geometry of the raw NMC particle. However, for both methods used for the tortuosity factor determination, the through-plane tortuosity factor is noticed to be significantly lower than the in-plane for all electrodes. Given the low level of porosity ($\varepsilon < 20\%$) studied here, the electrodes might suffer of a high applied pressure during the calendaring step. Thus, it can result in a reduction of the gap between particles in the direction normal to the current collector (Z-axis). The solid phase (NMC particles + CBD) in the three electrodes can, therefore, form agglomerates with their longest axes normal to the current collector. This can prevent the ionic transport in the liquid phase in the direction parallel to the current collector (in-plane), which causes the higher tortuosity in this direction compared to the through-plane direction. To qualitatively verify our hypothesis, we calculated the two-point correlation of the three volume. This metric is commonly used to characterize a microstructure, as it calculates the probability that two points x and $x + r$ separated by a vector r belong to the same phase i. Thus, it is valuable for analyzing the anisotropy of the microstructure, as any anisotropy on the characteristic distance (the size where the two-point correlation reaches an asymptotic value) implies an anisotropy on the analyzed phase geometry.

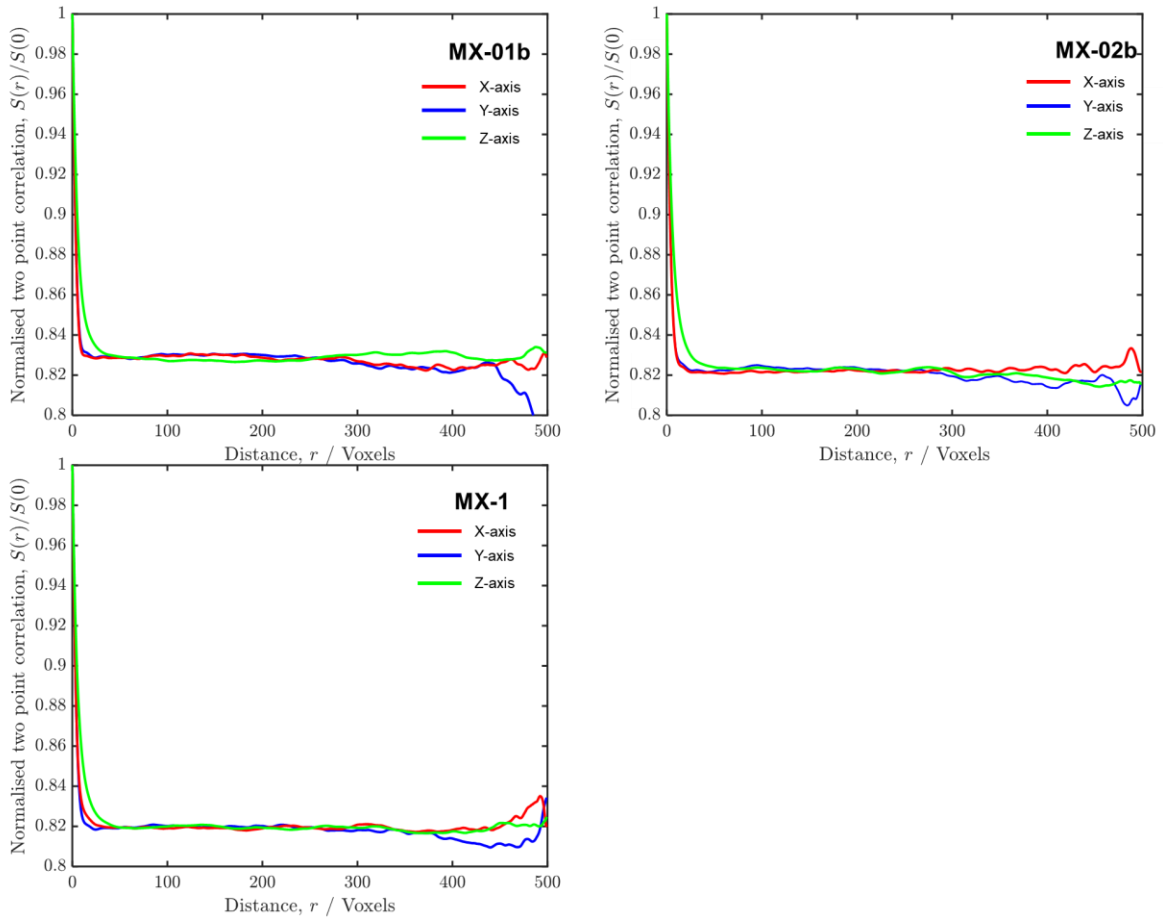

Figure IV-9. Two-point correlation of the solid phase in the three volumes (here, the solid phase: AM + CBD, is considered, as both phases are ionically-blocking). The data in Z-axis shows a delay compared to X and Y-axis to reach the asymptotic behavior, which represents the anisotropic of the considered phase in Z-axis.

The two-point correlation reveals that the solid phase sizes in the through-plane direction (Z-axis) are significantly larger compared with the in-plane sizes (X and Y-axis) (see Figure IV-9), as the Z-axis line reach the asymptotic values after the in-plane lines. The through-plane direction should be preferred over the in-plane directions in terms of ionic transport properties in order to improve the electrode performance, since the porous electrode limitations rather develop across the electrode thickness. For the rest of the article, tortuosity will refer to the through-plane tortuosity factor unless otherwise specified.

The results of conventional tortuosity factors (McMullin numbers) show the highest value for MX-01b and the lowest value for MX-02b. Figure IV-8b shows the simulation results using the diffusion-based method, in which we can see the flux density passing through the three volumes (via flux-through pores). The flux density map reveals a uniform distribution of flux for MX-01. In contrast, MX-01b and MX-02b both show locally higher flux density regions pointing out to a heterogeneous flux-through porosity. The high flux density regions may represent the

restriction/constriction effects (bottlenecks) in the pore network, which may be useful for understanding localized degradation mechanisms. Besides, the simulation of diffusion flux passing through the volumes allows the identification of the flux-through and dead-end pores, as can be observed in Figure IV-8c.

Using the SCM, we can see a decreasing trend of the electrode tortuosity factors and McMullin numbers compared to the previous values for all electrodes in all directions (Table IV-3). The MX-01b still has the most tortuous pore network compared to the other two in terms of electrode tortuosity factor. In both approaches, the lowest tortuosity factor is found for MX-02b, even though it does not have the highest porosity. Although the differences between two methods are not apparent, it is worth to restate that the SCM relies on the (dis)charging of double-layer capacitance at the solid/liquid interface throughout the electrode instead of the diffusional flux through the porous structure as for diffusion-based method. Thus, it takes into account both flux-through and dead-end pores contributions to the overall ionic transport of the pore network.[17] In Figure IV-8c, the dead-end pores presented in the ortho-slices (colored in white) are mainly small sections and disconnected (%v < 5% and without percolation), which results in slight effects on the tortuosity of the pore networks when the SCM is considered.[17]

IV.2.4 Inter-connectivity between phases

The inter-connectivity between the different phases within the electrode is investigated in the following section, as it constitutes an important parameter for the electrode to achieve a good electrochemical performance. For this purpose, we adopted a statistical approach in which more than 500 individual particles within each volume were separately studied. It is worth noting that, in this section, all the volume-specific interfacial areas and the triple-phase boundary (TPB) density, *i.e.* the boundary where the three different phases (AM, CBD, pores) meet, are normalized by each AM particle volume and not by the control volume as in the previous sections. The subscript p is added to these metrics (a_{p}^{*}, $\mathrm{TBP_p}$ density) to avoid confusion.

For fuel cell electrodes, TPB is the exact location that electrochemical reactions take place during the operation, since it is the meeting point of three components that are required for the electrochemical process. In contrast, for lithium-ion battery, the electrochemical reactions are not necessary take place unique at the TPB but rather at the AM/electrolyte interface, as will be discussed later in the text. Yet, the TPB for lithium-ion battery remains the reaction-site that costs a lowest polarization related to the electrochemical reaction.

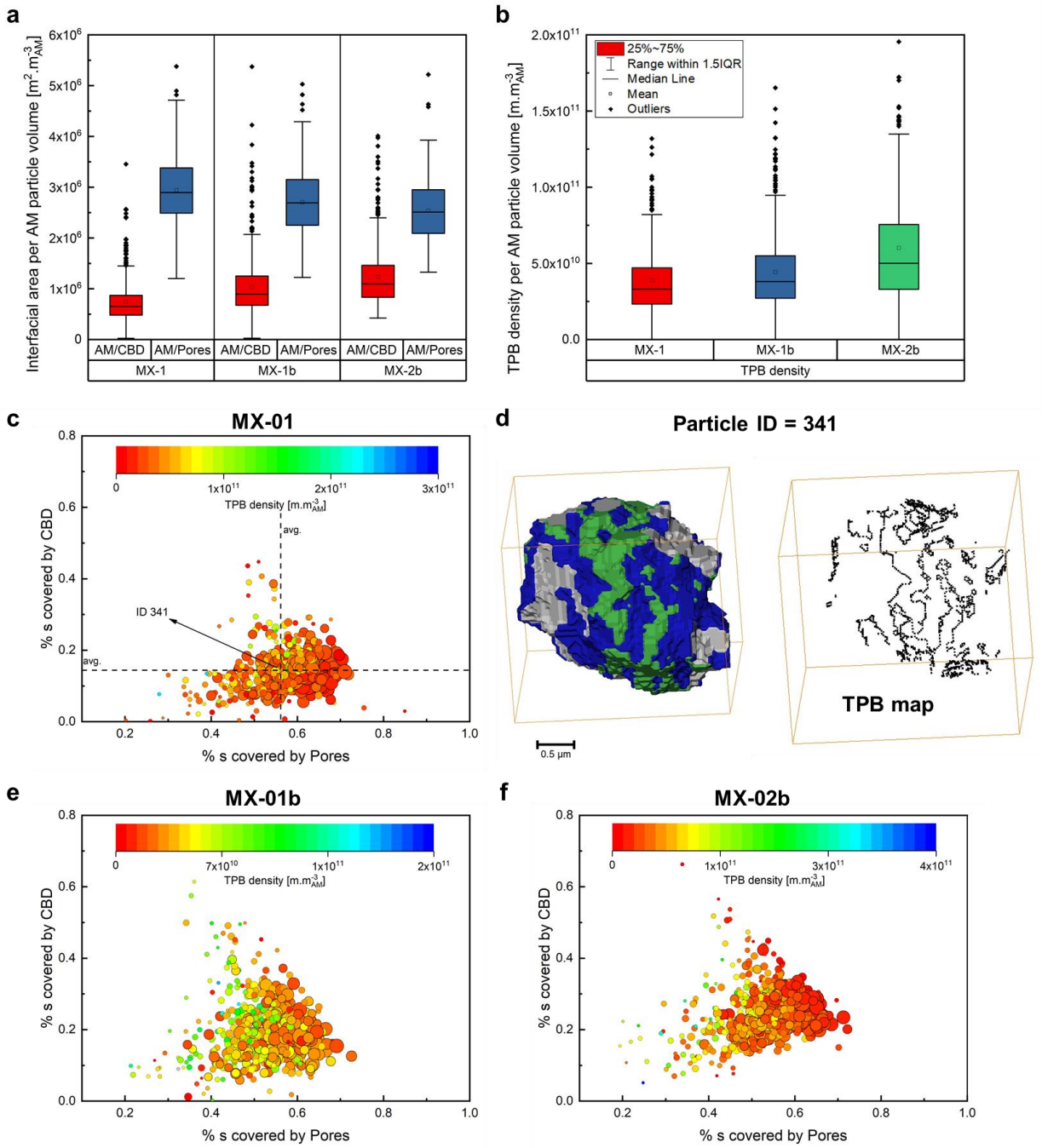

Figure IV-10. Inter-connectivity between phases in three samples. a. Interfacial area per AM particle volume between AM/CBD ($a^*_{P(AM/CBD)}$) and AM/pores ($a^*_{P(AM/pores)}$) are presented for each sample. **b.** TPB_p density per AM particle volume for each sample. **c, e, f.** Comparison of the distribution of different microstructural properties in three samples. The size of the dot corresponds to the particle size. The color corresponds to the TPB_p density of the particle, which is represented on the color bar. **d.** Visualization of the AM/CBD (green) and AM/pores (blue) interfacial area along with the TPB map of the representative particle of sample MX-01 (ID=341). The dashed line to guide eyes cut each other at the representative particle.

Figure IV-10a shows the distribution of the interfacial area between the AM particles and the CBD of the three samples, $a^*_{\mathrm{P(AM/CBD)}}$. MX-02b has the highest inter-connectivity between NMC and CBD among the samples along with a large dispersion. Despite a lower %v of CBD, MX-01 possesses a lower dispersion of $a^*_{\mathrm{P(AM/CBD)}}$, which represents a more uniform distribution of the CBD. However, the lower average interfacial area with CBD found in MX-01 might introduce an additional contact resistance due to the poor AM particle-CBD contacts.

The interfacial area between the AM and the pores, $a^*_{\mathrm{P(AM/pores)}}$, is also determined and shown in Figure IV-10a. This interfacial area corresponds to the electrochemical active surface area, where the charge transfer process occurs. It is worth noting that although the CBD can eventually be ionically-conducting by considering either the ability to absorb electrolyte the PVdF[32–34] or the porous morphology showed above, one might expect it to have lower ionic transport properties at high C-rates than the electrolyte filling in the pores. The presence of CBD at the AM surface can, therefore, negatively impact the kinetics of charge transfer at the interface AM/CBD. Hence, the interfacial area between AM/pores will mainly determine the exchange current density (A/m^2_{ASA}) within the porous electrode. Consequently, assuming all the AM surface are in contact with electrolyte only (*i.e.* ignoring the CB coverage of the AM particles) can potentially lead to errors in the evaluation of electrode properties used for the simulation of the electrode behavior.[35] MX-01 yields a higher AM/pores interfacial area compared to MX-01b and MX-02b, which can be explained by its highest porosity and its lower AM/CBD interfacial area.

Figure IV-10b shows the distribution of TPB_p density at each particle in the three samples. The TPB_p density per particle volume was found to be the highest in the sample MX-02b, in average. This sample also presents the largest dispersion of the TPB_p density values. In contrast, sample MX-01 presents a lower average for the TPB_p density values but with a more uniform distribution. The results from $a^*_{\mathrm{P(AM/CBD)}}$ and TPB_p density unveil the impact of %v of CBD on the three microstructures considered in this study. Even though the CBDs in MX-01b and MX-02b have a smaller volume-specific surface area (a^*_{CBD}) than in MX-01, both are still able to provide a larger interfacial area $a^*_{\mathrm{P(AM/CBD)}}$ and a higher TPBs density throughout the microstructures due to a higher amount of CBD. This means that the CBD is still well-dispersed throughout the volume in the samples with high %v of CBD that have been used in this work. The mechanism of lacking short-range contacts for a higher %v CBD, as mentioned above, is therefore not valid for samples MX-01b and MX-02b. This can be confirmed further with the visualization of the CBD in Figure IV-7a, in which one can see that the CBD distributes well over the entire volume of MX-01b and MX-02b (very few spaces without the CBD).

Figure IV-10c, e, f show the percentage of particles surface covered by the CBD and the pores by particles for MX-01b, MX-02b and MX-01 respectively. The TPB_p density of each particle is also represented with a color scale bar. A broader distribution can be seen for the MX-02b and MX-01b as discussed previously. Furthermore, smaller particles tend to have a higher cover ratio

of CBD as well as TPB_p density. On the other hand, larger particles show a higher cover ratio of pores. A "representative" particle having an effective %s. covered by CBD (~14%) and pores (~56%) is showed for sample MX-01 in Figure IV-10d along with its TPB_p map. This particle can be relevant for macroscopic modelling approach.

In summary, the sample MX-01 shows a higher degree of uniformity than MX-01b and MX-02b in terms of inter-connectivity between phases at particle scale. As a result, one might expect lower microstructural heterogeneities effects during operation for MX-01 compared to the others, which can be detrimental for the performance. This is in line with what has been reported by Müller *et al.*[36] and Forouzan *et al.*[37] through numerical modeling.

The Figure IV-11a displays the results of the rate capability of the three electrodes measured in a coin-cell setup at 25°C (see Methods section). The rate capability allows assess the performance of an electrode under different currents density. It shows that MX-01 outperforms the MX-01b (same loading), especially at high current density region (I>I*), whereas MX-01b presents a higher TPB_p density and a higher %v of CBD. It is worth mentioning that MX-02b also underperforms when comparing to an electrode having the same loading with lower %v of CBD (this electrode, however, is not studied in this work). It is worth noting that for the battery porous electrodes such as graphite or some oxide materials, the charge transfer does not occur only at the TPB_p, since the AM phase can have an appreciable electronic conductivity. For NMC material, this is particularly true once it is partially delithiated.[38] Thus, the lack of AM/CBD interfacial area, as well as a low TPB_p density, can be compensated by the electronic transport through the NMC particles to join the reaction-sites, as discussed in [11] [45]. In addition, the brutal drop of the rate capability in the high current density region is commonly attributed to the porous electrode effects, *i.e.* through the McMullin number as the main limitation is considered to be in the liquid phase. Nevertheless, by using a 3D particle-resolved, mesoscale model to investigate the electrochemical behaviors on a per-particle and per-surface basis, Ferraro *et al.*[12] demonstrated a significant capacity loss coming from the reaction rate at the surface of AM particles. The latter is directly related to both interfacial surface area: AM/Pores and AM/CBD of each particle. In light with this, based on the analysis results in our work (Figure IV-10), the excess of CBD (MX-01b, MX-02b) might cause an additional issue for the electrode performance at high C-rates. Indeed, it can lead to the reduction of electrochemical active surface area at the particle scale, due to the ionically-blocking properties of the interface AM/CBD, as illustrated in Figure IV-11b. This consequence of the CBD excess has been reported by several authors.[3,5,12,35,39] Consequently, the solid-diffusion limitation can be exacerbated due to the lower electrochemical surface area, because of longer diffusive pathways for lithium to travel from the surface to the bulk of the NMC particles. This results in an underutilization of AM. However, this scenario is only valid when the AM has a good electronic conductivity, which can compensate for the lack of the AM/CBD interface and/or the TPB_p density, as discussed above. For an AM with high electronic resistance, the TPB_p density can be vital for the performance of the electrode at high C-rates, as reaction-sites mainly sit at the TPB. For instance, since NMC exhibits a reduction of electronic conductivity at the vicinity of the full lithiation state, Ferraro *et al.*[12] observed a higher reactivity at the interfacial

area between AM and porous CBD (*i.e.*, there is electrolyte within the pores of CBD), which consists of multi TPB_p. Here, as NMC exhibits a good electronic conductivity,[38] the performance at high C-rate seems to be negatively impacted by the excess of CBD, as observed for MX-01b and MX-02b. Thus, to improve the power rate of the Li-ion battery electrodes having a good electronic conductivity AM, one should go for high values of interfacial area between AM and pores rather than between AM and CBD. A porous CBD phase can also create positive impacts as it allow the electrolyte to impregnate, so that increases the AM/Pore interface.

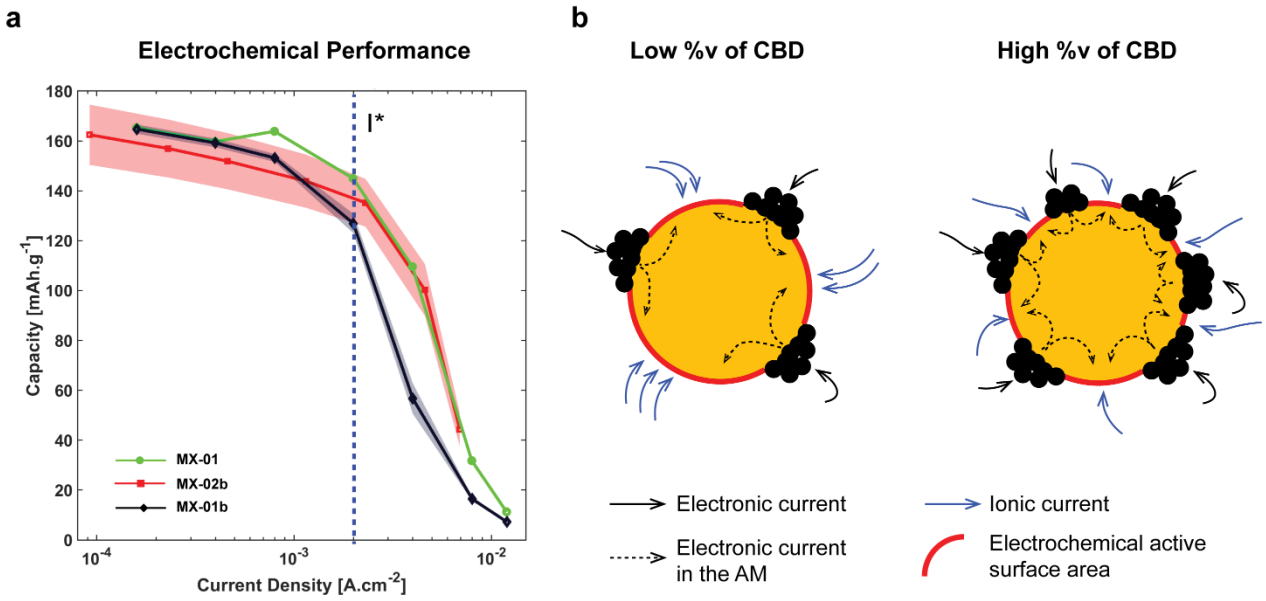

Figure IV-11. Correlation to the electrode performance. a. The lithiation performance of the three electrodes measured in a coin-cell setup at 25°C. The current density I^* indicated the boundary between high and low current density regions. **b.** Our proposed scenario to explain the impact of the microstructure on the final performance. The electrochemical active surface area are highlighted in red. The excess of CBD increases the coverage by CBD over the AM particle surface as well as the TPB_p density but reduces significantly the interfacial area between AM and electrolyte filled in pores at which charge transfer takes place.

Besides, microstructural heterogeneities can also significantly impact the electrode performance. Here, a higher degree of uniformity observed in MX-01 compared to MX-01b could help minimize the electrochemical heterogeneities, improve material utilization, and reduce polarization losses during operation. All result in a better rate capability.

IV.3 Conclusion

In this work, we demonstrated that the X-ray holotomography-based approach is an efficient way to reveal valuable insights about the microstructural properties and the electrode heterogeneity that is not straightforward to quantify using regular electrochemical-based approaches.

We show that with higher %v of CBD, the CBD provides a higher interfacial area with the AM

phase, along with the tendency to form agglomerates. The formation of agglomerates promotes the formation of long-range contacts within the porous electrode, which provides a good electronic conductivity. However, electrode performance is observed to be deteriorated at high C-rates, with higher %v of CBD, when comparing two electrodes with the same loading but with different ratios. Based on the analysis, we suggested herein that increase the %v of CBD causes a decrease of the electrochemical active surface area (surface area AM/pores). For an electronically-conducting AM, the TPB density and the AM/CBD interfacial area are thought to have minor effects on the performance at high C-rates. Thus, to improve the power rate of the Li-ion battery high-energy electrodes, engineering of electrode design should aim for high values of interfacial area between AM/pores instead. Also, the research for an "ideal" CBD morphology needs to consider simultaneously different aspects and not only the electrical conductivity, *i.e.* simply increase the %v of CBD would not be an obvious solution to improve the overall performance.

Regarding the pore network, we compared the two methods for tortuosity factor determination: the diffusion-based method (regular tortuosity factor) and the SCM (electrode tortuosity factor). A decrease trend was observed when comparing the electrode tortuosity factor to the regular tortuosity factor, which highlights a positive contribution of the dead-end pores to the overall ionic transport, albeit it is small compared to that of through pores, at least with the electrodes studied here. The tortuosity anisotropy of the pore network has been observed for through-plane and in-plane directions for both methods. The tortuosity factor in the direction normal to the current collector was found to be substantially lower than the in-plane direction (about half). Although the cause of the anisotropy stays uncertain, a hypothesis that is related to the calendaring process used in this work to achieve electrodes with a high energy density was proposed.

Finally, a higher heterogeneity in terms of inter-connectivity between phases at particle scale was also found for the electrodes with higher %v of CBD, which can lead to higher risk of performance deterioration during battery operation. All of these results are to be included in a numerical model to a quantitative investigation of their effects on the performance in a follow-up study.

IV.4 Methods

IV.4.1 Analyzed samples

Three different positive electrodes are investigated in this work and labelled as MX-01, MX-01b, MX-02b. Each electrode is a mixture of NMC532, conductive carbon black and PVdF with different composition. Their specifications are shown in Table IV-1, 2 and 3, where expected values of AM, CBD and pores are reported respectively.

The particle size distribution of the raw NMC532 particles is determined with the laser diffraction method. This method is a widely used particle sizing technique for materials ranging from hundreds of nanometers up to several millimeters in size. It measures particle size distribution by measuring the angular variation in intensity of light scattered as a laser beam passes through a

dispersed particulate sample. Large particles scatter light at small angles relative to the laser beam and small particles scatter light at large angles. The angular scattering intensity data is then analyzed to calculate the size of the particles responsible for creating the scattering pattern, using the Mie theory of light scattering. The particle size is reported as a volume equivalent sphere diameter. As for output, laser diffraction will give a volume-weighted distribution. That is, the contribution of each particle in the distribution relates to the volume of that particle, *i.e.*, the relative contribution will be proportional to size.

IV.4.2 Sample preparation

The sample preparation is a crucial step to get a high-quality result and to avoid artefacts during the acquisition process. Then, a careful preparation of the sample is needed to have the sample size required for X-ray nano-tomography. When performing X-ray tomography, the size of the sample is of importance. The first obvious reason is linked to the absorption of the X-rays. Indeed, because it is a transmission technique, it is necessary to have enough X-rays going out of the sample to have enough signal on the detector. The second reason is linked to the field of view of the detector. The 3D resolution will be better if the sample lateral size fits into this field of view. Local X-ray tomography, *i.e.* into samples that are bigger than the field of view, are possible but usually results in a compromise on the final resolution. As the field of view is equal to the number of pixel on the camera times the pixel size, it is usually quite large for micro-scale X-ray tomography. Then, appropriate sizing of ex-situ samples (from 0.5 to few mm) is typically not a problem. In this study the pixel size used was 50 nm and corresponds to a field of view of 130 µm. Moreover, because of the absorption of the NMC particles at the used energy, an optimal size of 50 µm diameter has been calculated.

For this, a “free-standing” electrode was first required, which was typically obtained by simply peeling the porous electrode material off the current collector foil. A laser cutter built in-house at IMPMC laboratory was used to precisely cut a pillar of *ca.* 50 µm in diameter from the bulk electrode. It is worth mentioning that to avoid any damage of the laser beam on the region of interest, the pulse mode was used for laser beam instead of permanent mode. Then, the electrode pillar was mounted on the tip of a quartz capillary, which is mounted on the sample holder, using cyanoacrylate glue (see Figure IV-12).

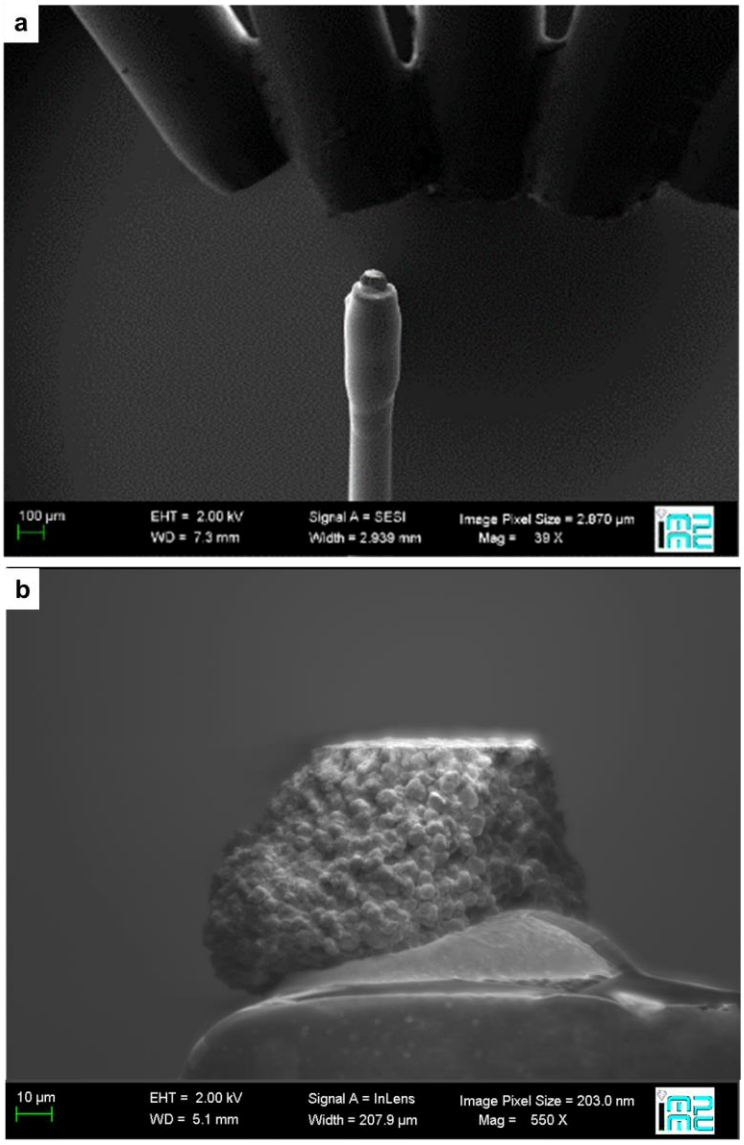

Figure IV-12. Sample preparation for X-rays nano-tomography experiments. a. The SEM image of the tip of a quartz capillary with the sample. **b.** Zoom on the sample.

IV.4.3 Electrochemical measurements

All measurements are carried out in a controlled temperature chamber at 25°C. The cycling test were performed with a multipotentiostat (Biologic, France). The operational range for the NMC materials in this work is chosen between 2.5 and 4.3 V versus Li/Li^+.

All coin cells first undergo a formation process in which they are cycled four times with constant-current (CC) discharge/charge cycles at C/10 to form a stable passive layer the particle surface. For the fifth cycle, a constant voltage (CV) is held at the end of the discharge until the current gets down to C/50. This extra steps before further charging were to ensure that the electrode completely lithiated (pristine state) after removing all possible limitations (for example: solid-

diffusion limitation). Finally, a CCCV charge followed by a CC discharge are carried out, both at C/25, for capacity determination. The available capacity is determined at the end of the CC discharge.

Rate-capability tests are performed on either a VMP3 or a BCS (Bio-Logic, France). The rate experiments were conducted on two separate electrodes of the same composition for the reproducibility. We assume that there is no electrode degradation during the measurements. The cells are cycled with different currents following by a CV at the end of each cycle to reach a stable stoichiometry until the current gets lower than C/50. In the rate capability test, the cells were charged with a CC phase followed by a CV phase, which remained unaltered, independent of the applied discharge current. Between each charge and discharge cycle a pause of 1 h was kept to allow for relaxation of the cells. In the discharge procedure, the cells were discharged with C/25, C/10, C/5, C/2, 1C, 2C.

For effective electronic conductivity determination, EIS were carried out using ITS system with the 4 lines configuration, and MTZ device from Biologic, France. The 4 lines configuration (see the experiment setup in Figure IV-5) is known to minimize the impact from the contact resistances between the probes and the sample, which can vary along with the applied pressure on the sample. The temperature was set to vary within a range [-20°C,60°C] allowing to extract the activation energy of the electronic conductivity. Activation energy close to zero refers to a metallic behavior of the materials, which provides good electronic conducting pathways.

IV.4.4 Holographic X-ray nanoCT technique for Li-ion battery

The holotomography technique used in this study and developed by Cloetens *et al.*[10] is based on phase contrast imaging. It gives high contrast images for low atomic number samples. The setup at the ID16B beamline of the ESRF[40] is described in Figure IV-1a. The high flux ($8X10^{10}$) nano-beam (50x50 nm^2) is used as a secondary source. Thanks to the diverging beam of 29.6keV, four tomographies at four different distances from the focal plane are performed by acquiring 2515 projections over 360° with an exposure time of 0.4s per 2D image recorded on a PCO edge 5.5 camera. The 3D reconstructions with a pixel size of 50 nm are achieved in two steps: (1) recursive phase retrieval calculation[41,42] using an in-house developed octave script based on a Paganin-like[43] approach with a delta/beta of 137 and (2) filtered back projection reconstruction using ESRF software PyHST2.[44]

IV.4.4.1 Data processing

Pre-processing

Due to shortcomings in the image acquisition process, the base signal of an X-ray scan is often superimposed by different kind of image artefacts, that can be observed in the reconstructed image most frequently as noise, and blur effects.[45,46] For multi-phases microstructures, these effects can be very disturbed for the segmentation step. Therefore, pre-processing of the reconstructed 2D

images might be needed to improve the image quality, allowing a good result in the segmentation process.[45,46]

In this work, we applied a non-local mean filter subsequently following by an unsharp mask for edge enhancement systematically to all the tomographic data. Non-local means filter has been reported to be an excellent candidate to efficiently remove noise and at the same time conserve edges between objects. In addition, an unsharp mask is for edge enhancement after denoising process. It reduces the partial volume effect, as shown in Figure IV-13, due to image blur and/or low resolution.

At the boundary between two phases (highlighted in red in Figure IV-13), gradual grey level changes spanning several voxels due to the image blur and/or low resolution, as referred to as partial volume effect. As a result, voxels near the phases interface can be misleading as a "third phase", which can be a source of errors. Consequently, this can lead to a morphology completely unreal. Figure IV-13 illustrates a scenario in which, after applying a thresholding corresponding to a theoretical value of %v of NMC, almost every NMC particles is covered by a thin film of CBD which are far to be correct, as CBD tends to form porous clusters instead of thin film. A detailed study of pre-processing methods is beyond the scope of this work. For more details information, we direct the reader to ref [41].

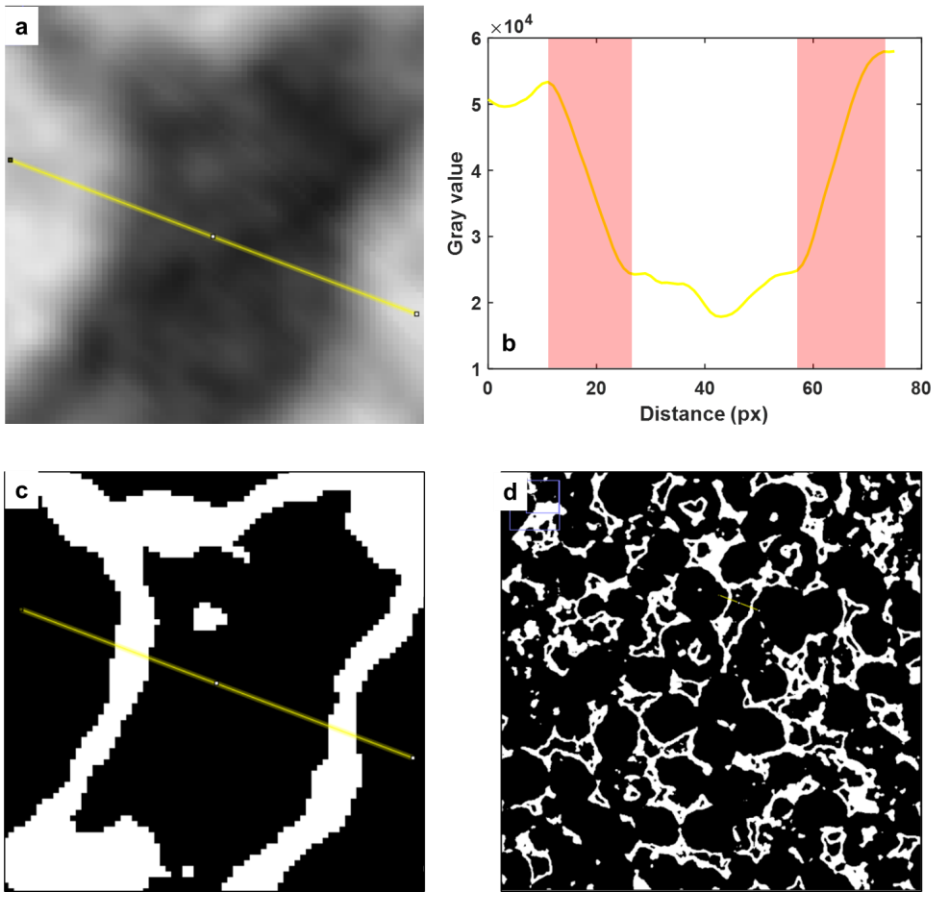

Figure IV-13. The partial volume effect can significantly affect the segmentation based on image

histogram, that lead to unreliable results. a. 2D zoom of raw data on a region where there are three phases (AM, CBD, Pores) presented. **b.** The profile of gray value of the straight line that pass through the three phases, with the partial volume effect region highlighted in red. **c.** The binary thresholding result of this region using traditional method based only on the histogram of the image. The black phase represented the AM and pores, whereas the white phase is for the CBD. **d.** The binary thresholding result of the entire image. The NMC particles can be recognized through their spherical-type shape. Thus, it can be seen that all of the NMC particles are covered by white phase which is the CBD.

As it can be seen in Figure IV-14, the contrast between the CBD and the pore space was enhanced after filtering. Figure IV-13 illustrates the partial volume effect, when the boundaries between two phases do not manifest themselves as crisp intensity steps (type Dirac signal), but rather as gradual grey level changes spanning several voxels. The contrasts between phases are improved while preventing details loss, as shown in the histogram (global) and line profile (local) of the image (Figure IV-14).

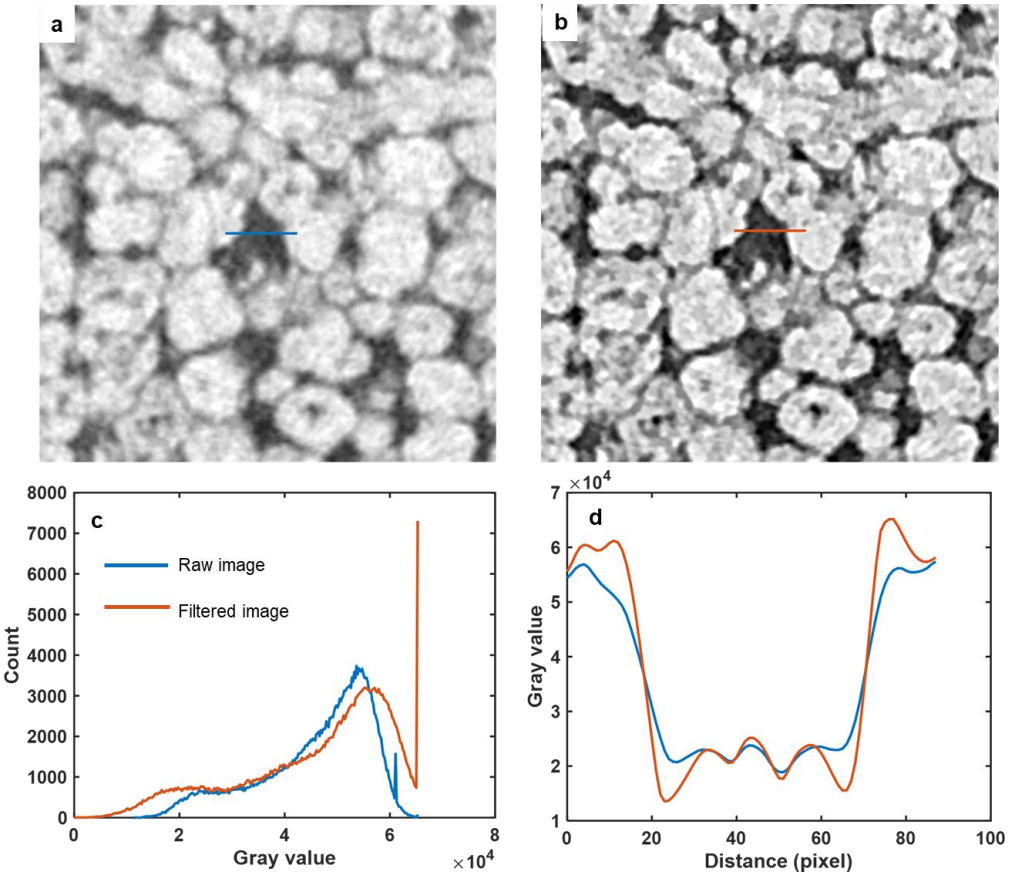

Figure IV-14. Pre-processing Data. a. Zoom on a 2D cross section extracted from a 3D reconstruction of the sample (Raw data). **b**. Resulted image after filtering with non-local mean filter and unsharp mask of the image a. **c**. Comparison of the histograms of two datasets in **a** and **b**. **d**. Comparison of the gray level at the line in the two images in **a** and **b**.

Pietsch *et al.*[47] have reported that the uncertainty of the segmented data is well correlated with the Otsu inter-class variance. Here, we evaluated this metric on our dataset before and after the

filtering process. The filtering process allows to get a better inter-class variance, hence reduces the uncertainty of the segmentation process.

Image segmentation

Image segmentation is a crucial step in image processing and affects all subsequent image analyses. It is commonly done by histogram evaluation, which considers only voxel's grey level (global thresholding). This approach can be very efficient in terms of computational time and efforts if high contrast between phases is presented, *i.e.* separate peaks appear in the histogram. However, for a multi-phases microstructure, each phase is frequently represented by a distribution of grey level that can be partially overlapped with others, or even completely hidden in the histogram. Hence, the threshold uncertainty range can be significant when using a global approach. Moreover, it is worth to note that since this approach is based only on voxel's grey level, it can be susceptible to the partial volume effect. Local segmentation methods such as watershed, converging active contours, show a better performance on the multiphase segmentation of tomographic images, as reported by Schlüter *et al.*.[45] However, they always rely on grey's level and/or gradient of grey values of pixels for the classification.

In this work, the segmentation was performed with an ImageJ's plugin named Weka,[13] which involved machine learning in performing the segmentation. This approach is based on features extracted from the image through a set of different filters. It is based on microstructural information captured from the image (2D) or volume (3D) to train a machine learning model rather than the only grey level for the classification of voxels. The model uses a random forest algorithm, which has been reported to be relevant for classification task without the need for substantial computational resources. This tool is part of the machine learning field, so-called "supervised learning", that needs a label data to train the model. Regarding the label data, the users have to carefully classify the pixels (taken from different slices located throughout the volume depth) into different classes (three in this work) based on various criteria: the pixel's grey value, the pixel's neighborhood, the morphology of each phase (*e.g.,* the AM particle frequently takes a roughly spherical geometry, while the CBD tends to form clusters in between AM particles). The pixels that were classified by the users are then considered as "reference label". They are used for the training step to get the best model that minimizes the errors. The model is applied to segment the rest of the volume automatically. We repeat this process for each sample in this work. The label data, therefore, needs to be carefully selected by users. The labelling step is mainly based on the subjective human opinion about the difference of grey value and can vary upon people. Thus, having a pre-processing step to improve the quality of the image can be helpful to reduce the segmentation error. We compared the segmentation results of the AM phase in MX-02b with the segmentation result of the same phase using binary threshold technique on the high resolution FIB-SEM data to validate our segmentation, see Figure IV-15.

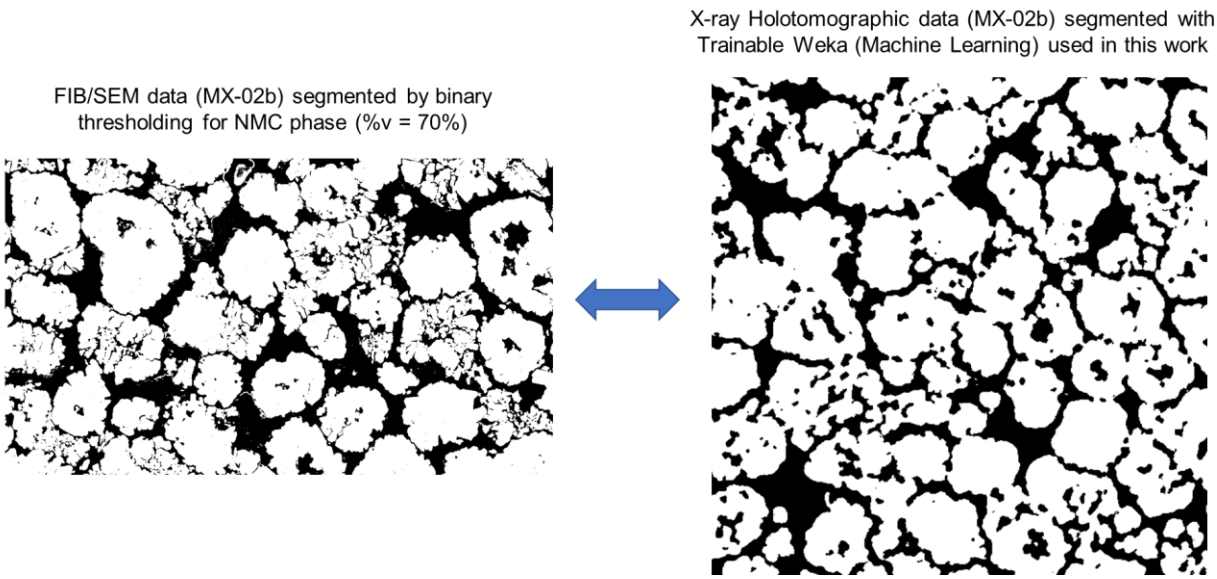

Figure IV-15. Validation of the Segmentation Results. Comparison of the AM phase morphology between the segmentation results of FIB-SEM data (using binary thresholding of the image histogram) and the segmentation results from X-ray Holotomographic data (using Machine Learning algorithm). One can find a good similarity of the AM phase morphology between the two results (cracks inside particles, gaps between particles).

IV.4.4.2 Microstructural analysis

Once images are segmented into three separated phases, the reconstructed 3D volumes of the electrodes were imported into the commercial software package Avizo V9.4 (Avizo, Thermo Fisher Scientific, Waltham, Massachusetts, USA) for 3D visualization and NMC particles separation. The particle size distribution is used as reference to adjust parameters of the separation object algorithm in Avizo.

The phase volume fraction is defined by the ratio: $\frac{V_i}{V_{\mathrm{cv}}}$, where V_i refers to the volume of phase i, calculated as the percentage of voxels corresponding to this phase, and V_{cv} to the total volume of the control volume.

The percolation represents the intra-connectivity of the phase i. It is quantified by the ratio between all connected voxels of phase *i* to the total voxels of this phase (connected and isolated voxels) within the control volume. Voxels that share a common face are considered as connected.

The sphericity is a measure of how closely the shape of an object resembles that of a perfect sphere. It is defined by the ratio of the surface area of a sphere with the same volume as the given particle to the surface area of the particle: $\psi_{\mathrm{p}} = \frac{\pi^{\frac{1}{3}} V_{\mathrm{p}}^{\frac{2}{3}}}{A_{\mathrm{p}}}$, where ψ_{p}, V_{p} and A_{p} are the sphericity, the volume and the surface area of the individual particle respectively. The sphericity is calculated for each individual AM particle.

The specific surface area quantifies the surface area of phase i per unit electrode volume. On the other hand, the specific interfacial surface area refers to the total surface area of the interface between two phases i, j per unit electrode volume.

It is worth to note that our analysis is based on voxelized data for convenience such that a meshing process is not necessary. This approach is relevant for volume quantification as it shows comparable results to other approaches. However, for surface area, this approach tends to overestimate the value of the surface area, even though with a high value of resolution. The marching cube (MC) algorithm[48] is shown to give the highest accuracy for the surface area calculation.[49] This algorithm polishes the originally derived voxel-based surface mesh as described in [75]. The ratio a_{voxel}, a_{MC} of the three volumes analyzed here varies from 1.2 to 1.3. Nevertheless, we may have of particular interest to the relative values rather than the absolute one since the comparison between samples can still give us insight about the effects of microstructures.

The TPB density is defined as the length of the intersection among three phases i, j, and k, normalized by the total volume of the microstructure domain. For voxelized data used in this work, a TPB is defined as the length of the edges where three of the four connecting voxels contain different phases.

Most of the parameters studied throughout this work are straightforward to quantify using either *TauFactor* and/or built-in tools or plugins in Fiji or Avizo. The visualization of the TPBs required adding work.[50] *TauFactor* is an open-source MATLAB application developed by Cooper *et al.*[51] allowing a complete characterization of the microstructure based on image data. The analysis were proceeded first on separated phases (AM, CBD, pores), then on the correlation between phases to capture the microstructural characteristics of the electrodes as a whole. Furthermore, based on the *TauFactor* framework, an in-house code was developed. It allows extracting different microstructural properties when the AM phase was separated into individual particles.

For tortuosity factor determination, our previous work in [17] unambiguously demonstrated that the electrode tortuosity factor given by the symmetric cell method is a more appropriate metric to characterize porous electrodes than the conventional tortuosity factor determined with the diffusion-based method. Hence, in this work, we quantified both tortuosity factors using two approaches for comparison.

Recently, Gayon-Lombardo *et al.*[52] proposed to use periodic boundaries instead of Dirichlet boundaries for the diffusion-based method for the conventional tortuosity factor determination. They suggested that this approach allows representing better the bulk behavior of the microstructure. Thus, it might be interesting for future works to evaluate the electrode tortuosity factor under the same conditions and to compare the two methods as what has been done by Nguyen *et al.*.[17]

To study the morphology of the CBD, the diffusion-based method was also used for the simulation of a flux of electrons passing through the control volume via the CBD. Although this simulation relies on the Fick's law, the governing equation is mathematically homologue to the Ohm's law, which governs the electronic transport in CBD.

Despite the large acquisition volume given by the X-ray holotomography technique, there is one sample that suffered from crack, which reduces significantly the exploitable data. Consequently, to be consistent in the comparison, we considered an adequate sub-volume of 25x25x25 μm^3 in each of the three samples and defined as the control volume. In addition, a representative volume analysis had been done to study the representativeness of this control volume. As can be seen in Figure IV-3, all three volumes can be considered as homogeneous and representative. The two-point correlation calculation also showed in Figure IV-9 that the asymptotic behavior is reached for all the three volumes justifying the representativeness of the control volume.

Nomenclature

A_{CC}	$\mathrm{m}_{\mathrm{CC}}^2$	Current collector surface area
a_i^*	$\mathrm{m}_i^2/\mathrm{m}_{\mathrm{CV}}^3$	Volume-specific surface area of phase i within the control volume captured by tomography
D1	m	Focus to sample distances
d_{50}	µm	Median diameter of active materials particles
E_{a}	eV	Activation energy
F	$\mathrm{C/mol}$	Faraday's constant
I^*	$\mathrm{A}/\mathrm{m}_{\mathrm{CC}}^2$	Value separating the high and low current density regions
m	kg	Mass
n		Refractive index
w_i		Weight fraction of phase i

Greek symbols

Φ_i	V	Electric Potential of phase i
ρ_{i}	$\mathrm{kg/m}^3$	Density of phase i
τ_{e}		Electrode tortuosity factor
τ		Tortuosity factor
β		Absorption coefficient

δ		Decrement of the refractive index
ε		Porosity
κ	S/m	Ionic Conductivity of the electrolyte
σ	S/m	Electronic Conductivity of the solid phase
ψ_{p}		Particle sphericity

Subscripts

AM	Related to the Active Materials
eff	Effective properties
re	relative
p	variable relative to an AM particle
PE	Belong to the Porous Electrode
el	Electronic in the solid phase

References

[1] M. Chouchane, A. Rucci, T. Lombardo, A. C. Ngandjong, A. A. Franco, *J. Power Sources*, **2019**, *444*, 227285.

[2] L. Zielke, T. Hutzenlaub, D. R. Wheeler, C.-W. Chao, I. Manke, A. Hilger, N. Paust, R. Zengerle, S. Thiele, *Adv. Energy Mater.* **2015**, *5*, 1401612.

[3] A. N. Mistry, K. Smith, P. P. Mukherjee, *ACS applied materials & interfaces*, **2018**, 10(7), 6317-6326.

[4] G. Inoue, M. Kawase, *J. Power Sources* **2017**, *342*, 476.

[5] M. E. F. Bradley L. Trembacki, Aashutosh N. Mistry, David R. Noble, and S. A. R. Partha P. Mukherjee, *J. ofThe Electrochem. Soc.* **2018**, *165*, E725.

[6] S. R. Daemi, C. Tan, T. Volkenandt, S. J. Cooper, A. Palacios-Padros, J. Cookson, D. J. L. Brett, P. R. Shearing, **2018**, DOI 10.1021/acsaem.8b00501.

[7] X. Lu, A. Bertei, D. P. Finegan, C. Tan, S. R. Daemi, J. S. Weaving, K. B. O. Regan, T. M. M. Heenan, G. Hinds, E. Kendrick, D. J. L. Brett, P. R. Shearing, *Nat. Commun.* **2020**, *11*, 1.

[8] S. Müller, M. Lippuner, M. Verezhak, V. De Andrade, F. De Carlo, V. Wood, *Adv. Energy Mater.* **2020**, 1904119.

[9] S. L. Morelly, J. Gelb, F. Iacoviello, P. R. Shearing, S. J. Harris, N. J. Alvarez, M. H. Tang, **2020**, *7*, 32.

[10] P. Cloetens, W. Ludwig, J. Baruchel, D. Van Dyck, J. Van Landuyt, J. P. Guigay, M. Schlenker, *Cit. Appl. Phys. Lett* **1999**, *75*, 5486.

[11] V. Julie, L. Jérôme, C. Peter, B. Pierre, D. Gérard, S. Heikki, U. V. François, *J. Power Sources* **2013**, *243*, 841.

[12] M. E. Ferraro, B. L. Trembacki, V. E. Brunini, D. R. Noble, S. A. Roberts, *J. Electrochem. Soc.* **2020**, *167*, 013543.

[13] I. Arganda-Carreras, V. Kaynig, C. Rueden, K. W. Eliceiri, J. Schindelin, A. Cardona, H. S. Seung, *Bioinformatics* **2017**, *33*, 2424.

[14] R. Xu, Y. Yang, F. Yin, P. Liu, P. Cloetens, Y. Liu, F. Lin, K. Zhao, *J. Mech. Phys. Solids* **2019**, *129*, 160.

[15] D. J. Miller, C. Proff, J. G. Wen, D. P. Abraham, J. Bareño, *Adv. Energy Mater.* **2013**, *3*, 1098.

[16] M. Ebner, F. Geldmacher, F. Marone, M. Stampanoni, V. Wood, *Adv. Energy Mater.* **2013**, *3*, 845.

[17] T. T. Nguyen, A. Demortière, B. Fleutot, B. Delobel, C. Delacourt, S. J. Cooper, *npj Comput. Mater.* **2020**, *6*, 1.

[18] S. L. Morelly, N. J. Alvarez, M. H. Tang, *J. Power Sources* **2018**, *387*, 49.

[19] H. Bockholt, M. Indrikova, A. Netz, F. Golks, A. Kwade, *J. Power Sources* **2016**, *325*, 140.

[20] R. Tang, Q. Yun, W. Lv, Y. B. He, C. You, F. Su, L. Ke, B. Li, F. Kang, Q. H. Yang, *Carbon N. Y.* **2016**, *103*, 356.

[21] B. J. Lanterman, A. A. Riet, N. S. Gates, J. D. Flygare, A. D. Cutler, J. E. Vogel, D. R. Wheeler, B. A. Mazzeo, *J. Electrochem. Soc.* **2015**, *162*, 2145.

[22] S. W. Peterson, D. R. Wheeler, *J. Electrochem. Soc.* **2014**, *161*, A2175.

[23] Y. Shi, L. Wen, S. Pei, M. Wu, F. Li, *J. Energy Chem.* **2019**, 19.

[24] S. Malifarge, B. Delobel, C. Delacourt, *J. Electrochem. Soc.* **2018**, *165*, A1275.

[25] I. V. Thorat, D. E. Stephenson, N. A. Zacharias, K. Zaghib, J. N. Harb, D. R. Wheeler, *J. Power Sources* **2009**, *188*, 592.

[26] S. Malifarge, B. Delobel, C. Delacourt, *J. Electrochem. Soc.* **2017**, *164*, E3329.

[27] J. Landesfeind, J. Hattendorff, A. Ehrl, W. A. Wall, H. A. Gasteiger, *J. Electrochem. Soc.* **2016**, *163*, A1373.

[28] M. Ebner, D. W. Chung, R. E. García, V. Wood, *Adv. Energy Mater.* **2014**, *4*, DOI 10.1002/aenm.201301278.

[29] B. Suthar, J. Landesfeind, A. Eldiven, H. A. Gasteiger, *J. Electrochem. Soc.* **2018**, *165*, 2008.

[30] B. L. Trembacki, D. R. Noble, M. E. Ferraro, S. A. Roberts, *J. Electrochem. Energy Convers. Storage* **2020**, DOI 10.1115/1.4045973.

[31] K. S. F.L.E. Usseglio-Viretta, A. Colclasure, A.N. Mistry, K.P.Y. Claver, F. Pouraghajan, D.P. Finegan, T.M.M. Heenan, D. Abraham, P.P. Mukherjee, D. Wheeler, P. Shearing, S.J. Cooper, *J. Electrochem. Soc.* **2018**, *165*, A3403.

[32] G. Liu, H. Zheng, S. Kim, Y. Deng, A. M. Minor, X. Song, V. S. Battaglia, *J. Electrochem. Soc.* **2008**, *155*, A887.

[33] M. Doyle, J. Newman, A. S. Gozdz, C. N. Schmutz, J. Tarascon, *J. Electrochem. Soc.* **1996**, *143*, 1890.

[34] J. Li, L. Christensen, M. N. Obrovac, K. C. Hewitt, J. R. Dahn, *J. Electrochem. Soc.* **2008**, *155*, A234.

[35] L. Almar, J. Joos, A. Weber, E. Ivers-Tiffée, *J. Power Sources* **2019**, *427*, 1.

[36] J. Eller, M. Ebner, C. Burns, J. Dahn, V. Wood, *J. Electrochem. Soc.* **2018**, *165*, 339.

[37] M. M. Forouzan, B. A. Mazzeo, D. R. Wheeler, *J. Electrochem. Soc.* **2018**, *165*, DOI 10.1149/2.1281809jes.

[38] R. Amin, Y.-M. Chiang, *J. Electrochem. Soc.* **2016**, *163*, A1512.

[39] H. Zheng, L. Tan, G. Liu, X. Song, V. S. Battaglia, *J. Power Sources* **2012**, *208*, 52.

[40] G. Martinez-Criado, J. Villanova, R. Tucoulou, D. Salomon, J. P. Suuronen, S. Laboure, C. Guilloud, V. Valls, R. Barrett, E. Gagliardini, Y. Dabin, R. Baker, S. Bohic, C. Cohen, J. Morse, in *J. Synchrotron Radiat.*, International Union Of Crystallography, **2016**, pp. 344–352.

[41] M. Langer, A. Pacureanu, H. Suhonen, Q. Grimal, P. Cloetens, F. Peyrin, *PLoS One* **2012**, *7*, e35691.

[42] L. Weber, Iterative Tomographic X-Ray Phase Reconstruction, **2016**.

[43] D. Paganin, *Coherent X-Ray Optics*, **2006**.

[44] A. Mirone, E. Brun, E. Gouillart, P. Tafforeau, J. Kieffer, *Nucl. Instruments Methods Phys. Res. Sect. B Beam Interact. with Mater. Atoms* **2014**, *324*, 41.

[45] S. Schlüter, A. Sheppard, K. Brown, D. Wildenschild, *Water Resour. Res.* **2014**, *50*, 3615.

[46] A. P. Sheppard, R. M. Sok, H. Averdunk, in *Phys. A Stat. Mech. Its Appl.*, **2004**, pp. 145–151.

[47] P. Pietsch, M. Ebner, F. Marone, M. Stampanoni, V. Wood, *Sustain. Energy Fuels* **2018**, *2*, 598.

[48] W. E. Lorensen, H. E. Cline, *Comput. Graph.* **1987**, *21*, 163.

[49] J. Joos, T. Carraro, M. Ender, B. Rüger, A. Weber, E. Ivers-Tiffée, *ECS Transactions*, **2011**, 35(1), 2357.

[50] X. Lu, T. M. M. Heenan, J. J. Bailey, T. Li, K. Li, D. J. L. Brett, P. R. Shearing, *J. Power Sources* **2017**, *365*, 210.

[51] S. J. Cooper, A. Bertei, P. R. Shearing, J. A. Kilner, N. P. Brandon, *SoftwareX* **2016**, *5*, 203.

[52] A. Gayon-Lombardo, L. Mosser, N. P. Brandon, S. J. Cooper, *npj Comput. Mater.* **2020**, DOI 10.1038/s41524-020-0340-7.

Chapter V . Self-supervised image quality assessment for X-ray tomographic images of Li-ion battery materials

V.1 Introduction

XCT is considered as a powerful technique to study LiB, since its nondestructive 3D imaging across multiple length scales provides quantitative and qualitative metrics for characterization of their complex microstructure[1]. The effects of microstructural properties on the electrochemical performance of the battery can therefore be investigated, allowing the optimization of the electrode design. However, extracting reliable microstructural properties from 3D tomographic images is not straightforward, as it requires a reliable image processing methodology, which consists of a pre-processing step and a segmentation process followed by an accurate 3D quantitative analysis[2]. Due to the environmental disturbance, the tomographic images frequently contain distortions, such as noise, blur, ring artefact etc., which affect the determination of microstructural properties using those images (e.g., surface area and volume fraction). Besides, user-to-user variation can be significant when different people process the same images. As a result, the image pre-processing step is frequently applied to improve the image quality and reduce the uncertainty allowing reliable analysis. It involves the image feature enhancement (histogram equalization, normalization, brightness, and contrast adjustment) and distortion suppression such as denoise, deblur and ring artefact removal. Segmentation is supposed to distribute pixels among certain groups based on pixel values, with the aim of assigning various regions of the image to different phases of the material.

In addition to the analysis, the pre-processing and the segmentation procedure are both non-trivial issues that have a significant impact on any subsequent image analyzes, such as the calculation of porosity, tortuosity, and the surface area of a specific phase. Due to the lack of a non-distorted reference image, the quality of the pre-processing is typically assessed by subjective visual inspection. However, image pre-processing has a profound impact on following segmentation performance. Schluter *et al.*[3] presented that, with suitable image enhancement prior to segmentation, segmentation algorithms became more robust and were less prone to operator bias. The authors analyzed the segmentation accuracy of the images before and after pre-processing and pointed out that the distortion leads to poor segmentation. In addition, the absence of ground-truth makes it difficult to assess the quality of the segmentation. Pietsch *et al.*[4] proved that subjective judgement was not a reliable standard for the selection of binarization criteria in the segmentation procedure, leading to uncertainties in the results. Therefore, a numerical metric to assess the quality of images is needed to guide the pre-processing step (setting parameters, selecting filters) so that the next segmentation step can result in further highly reliable quantitative analysis.

Image quality assessment (IQA) aims to predict the perceptual quality of a distorted image. However, the human vision system (HVS)[5] needs a reference to quantify the discrepancy by comparing the distorted image either directly with the original undistorted image or implicitly with a hallucinated scene in mind[6]. It is time-consuming and labor-intensive to assess image quality from a crowd of people. Moreover, due to different culture and living environments, people sometimes give different views on the same picture. Especially for tomographic images,

inexperienced and laymen would like to give totally different scores. Therefore, it is complicated to objectively assess the quality of tomographic images.

To avoid the distinction caused by cognitive bias and to provide robust professional estimation, some machine assisted IQA methods have been proposed in recent decades. They are generally divided into three categories: (a) Full-Reference Image Quality Assessment (FR-IQA) which evaluates the distorted image by comparing it to the reference image and measuring the difference[7,8]; (b) Reduced-Reference Image Quality Assessment (RR-IQA) which measures image quality with part of the reference image[9,10]; (c) No-Reference Image Quality Assessment (NR-IQA), which requires little information about reference images and estimates image quality directly from distorted images [11,12].

The conventional metrics used for FR-IQA and RR-IQA are peak signal-to-noise ratio (PSNR) and root mean square error (MSE) which compare image intensity of distorted images to that of reference images without considering HVS. By considering the luminance, contrast and structural information, SSIM[7] used average pooling to calculate a score from a similarity map. Based on SSIM, MS-SSIM[13] compared distorted image to reference image at multiple scales. F-SIM[14] leveraged phase congruency and gradient magnitude features to derive a quality score while GMSD[15] only considered the image gradient as the criterial features. Besides the gradient, MDSI[16] utilized chromaticity similarity and deviation pooling to imitate the HVS and achieved better results.

Although the above methods can serve as an indicator, reference images are not always available in real-world situations. Hence, NR-IQA methods have attracted extensive attention recently which is also challenging due to lack of reference information. Early NR-IQA methods mainly focused on specific types of distortions, such as noise[17], contrast change[18], blur[19] and ring artifact[20],[21]. Since the types of distortion of the images are unknown in real scenarios, these methods are impractical compared to the general methods [22,23] which require no priori information about the distortion types.

With the development of deep neural network (DNN), the deep learning methods have been exploited for NR-IQA without any prerequisites and have demonstrated superior prediction performance. Le *et al.*[24] firstly proposed a shallow convolutional neural network (CNN) to estimate the quality score for natural images. Ke *et al.*[25] introduced a deep learning-based image quality index for blind image quality assessment, which was more efficient and robust. Instead of the multi-stage methods, Sebastian *et al.*[26] presented an end-to-end neural network to regress the quality score by joint learning of local quality and local weights. Instead of considering the whole image in the network, Simone *et al.*[27] cropped the image into patches, estimated the scores separately and fused them finally, which was more suitable for insufficient training data cases. However, the lack of training data was a crucial obstacle for aforementioned methods. To overcome the limitation of data, Xialei *et al.*[28] implemented data augmentation by generating artificial distorted images and then trained a Siamese network (Rank-IQA) to regress the quality scores. Kwan-Yee *et al.*[6] combined the generative neural network to generate the reference

images and convolutional neural network to regress the quality score from the discrepancy. Hancheng *et al.*[29] developed a meta-learning[30] method to estimate the quality score of images with new distortion, which addressed the generalization problem of IQA.

Although many methods have been provided for IQA and achieved excellent results, most of them focus on natural images and require a huge number of annotated labels, which are not practical for X-ray tomography images. For example, the FR-IQA methods need a reference image for each estimation of a distorted image, which implies a high demand of annotations. The already developed NR-IQA methods requiring less data than the FR-IQA method, but still relatively large (hundreds of annotations) to avoid overfitting. Besides, the existing open-source datasets[31],[32],[33] of battery electrodes tomographic images are not for IQA task, *i.e.* without various distortion-types and corresponding scores. Therefore, a light NR-IQA method, which requires less annotated data and is robust to transfer among different X-ray tomography images, is urgently demanded.

The main contributions of this work are summarized as follows:

- A no reference tomographic image quality assessment (T-IQA) method is proposed for tomographic images which requires only dozens of annotated images for training and achieves outperformed results.

- A data generation method is developed by imitating the human observers to label the distorted images automatically for the purpose of addressing the insufficient data problem. Benefit from data generation, our TIQA method requires only one fifth of the number of images comparing to other NR-IQA methods.

- The correlation of image quality score and segmentation results is studied to guide the pre-processing step.

The remainder of the paper is organized as follows: In section “Results”, we show the results of our data generation method and T-IQA method. Moreover, the segmentation result and the link of quality score and segmentation performance are demonstrated in this section as well. In section “Discussion”, we summarize the results and emphasize the features of our method. We also propose several potential applications and future directions of our method. In section “Methods”, we introduce our dataset and the experiment details.

V.2 Results

V.2.1 Data generation results

As shown in Figure V-1, the first step in our approach is to generate the data required for the subsequent training process of the score prediction network, whose purpose is to address the problem of insufficient data. The detailed workflow of the data generation process is illustrated in Figure V-2.

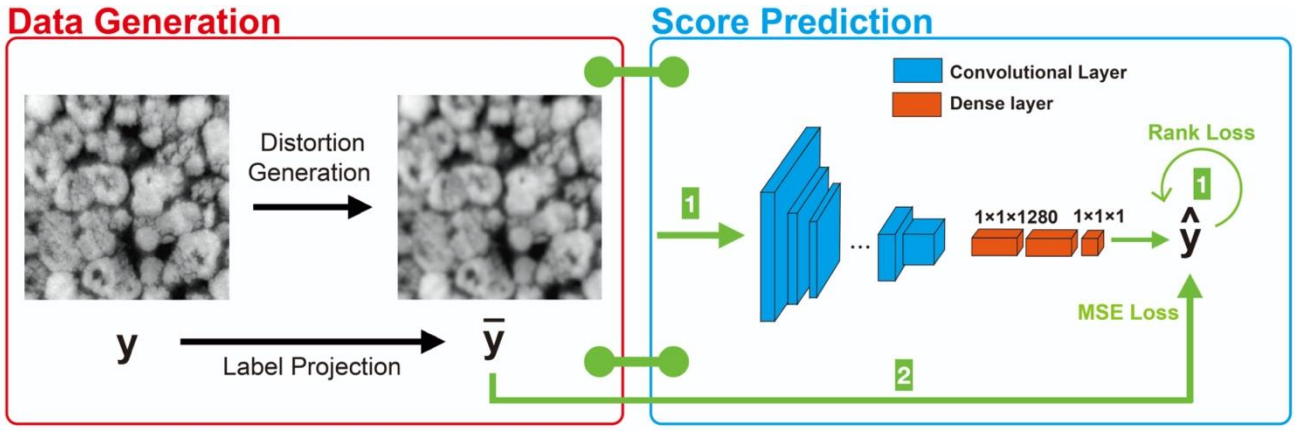

Figure V-1. Pipeline of our T-IQA method. It is composed of two modules: the data generation and score prediction. In score prediction, (1) is the self-supervised learning for ranking the images, (2) is the fine tune procedure for regressing the ranks to a score in fixed range.

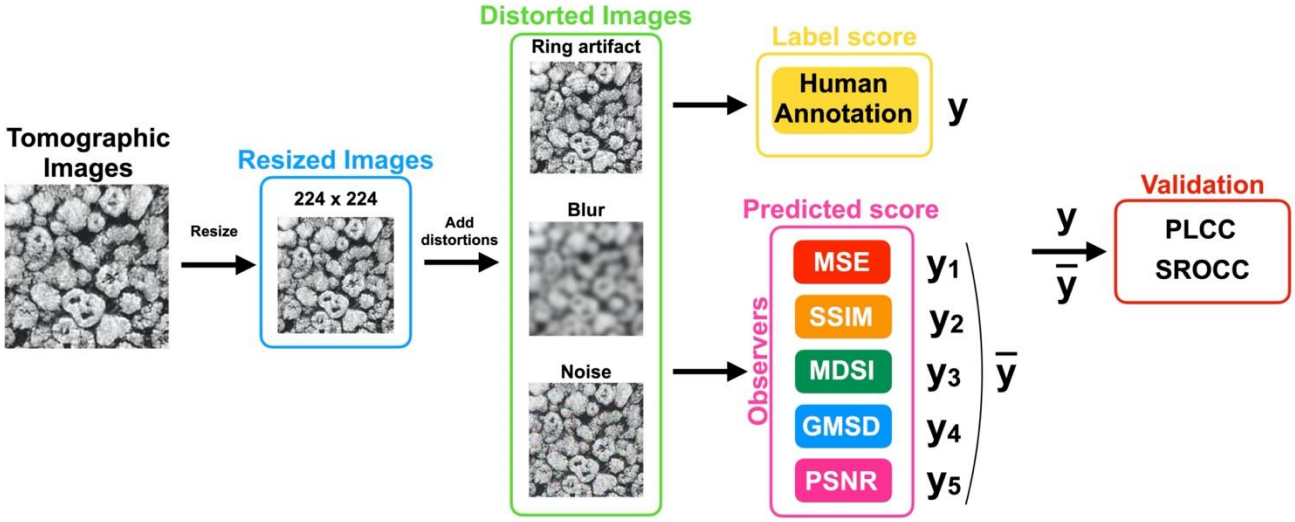

Figure V-2. Detailed structure of data generation. The observers are some FR-IQA methods. y is the human annotation, y_i is the predicted score of the *i-th* observer, $\bar{y}$ is the average score of y_i.

Firstly, the original image is resized and cropped into a fixed size, 224*224 pixels. Notably, to verify whether the resize operation affects the image quality scores, we compare the annotations on the images before and after this operation. The comparison results (Figure V-3) confirm that the pre-processing operations do not affect the image quality. Next, three types of distortion (ring artifact, blur, noise), that are commonly presented in X-ray tomographic images, are added to generate distorted images. (More generated images can be found in Figure V-4). Finally, the label projection step systematically produces the annotations of distorted images by comparing the HVS features of original image and distorted image using different FR-IQA metrics (more details are in Methods section).

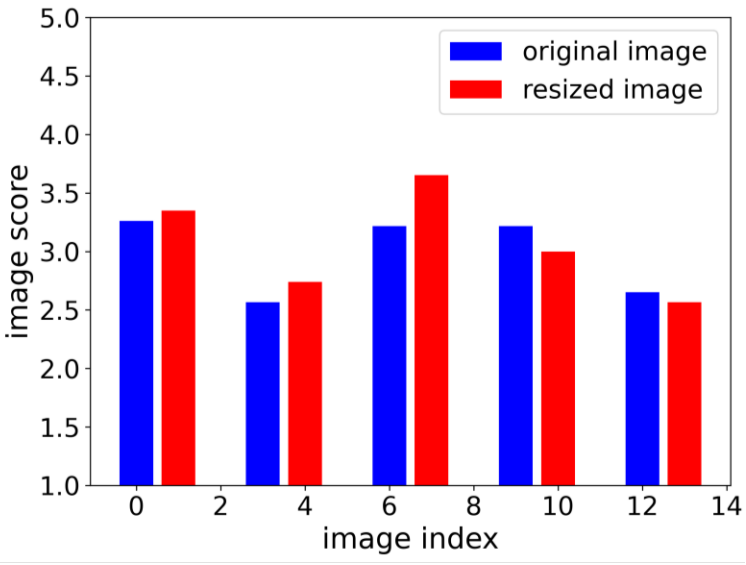

Figure V-3. Comparison of the labels for images before and after down-sampling. Five image pairs are evaluated.

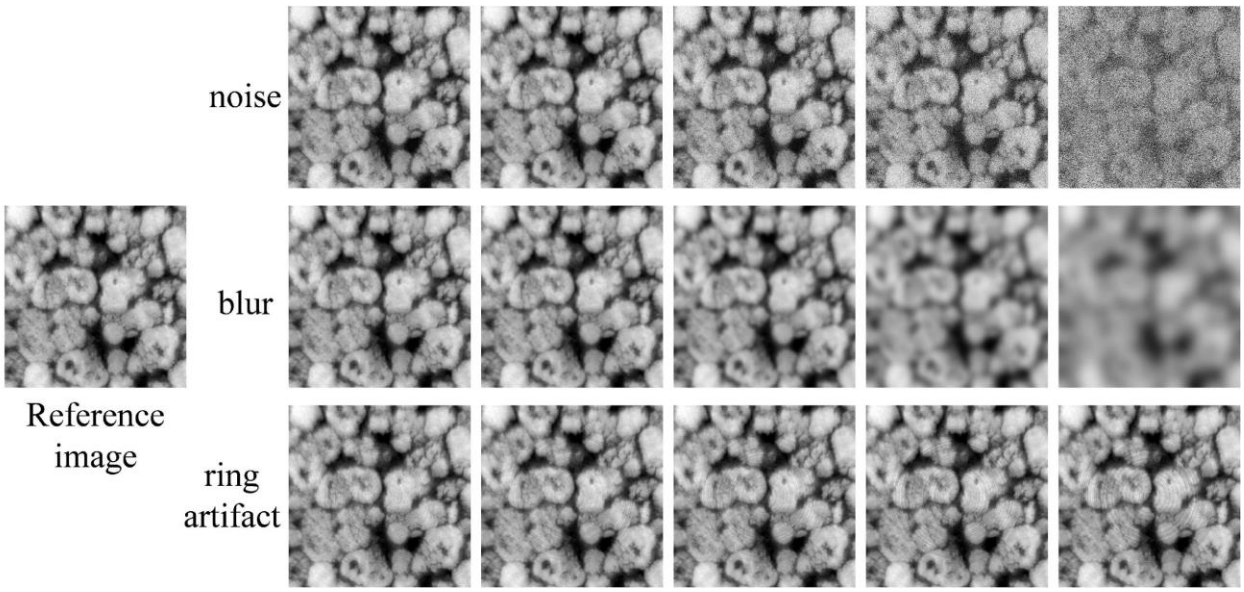

Figure V-4. Results of distorted image generation. These three types of distorted images are produced from the reference image

To validate our method for data generation, we consider two criteria to quantify the correlation between generated results from the label projection step, and corresponding labels from the survey, including the Pearson's linear correlation coefficient (PLCC) and Spearman's rank ordered correlation coefficient (SROCC). As presented in Figure V-5 and Figure V-6, for all types of distortions, the generated scores have positive correlation with the annotations. Especially for the images with noise or blur, the correlation is high. As for the ring artifact, the results demonstrate that the existing general FR-IQA metrics cannot well handle this type of distortion.

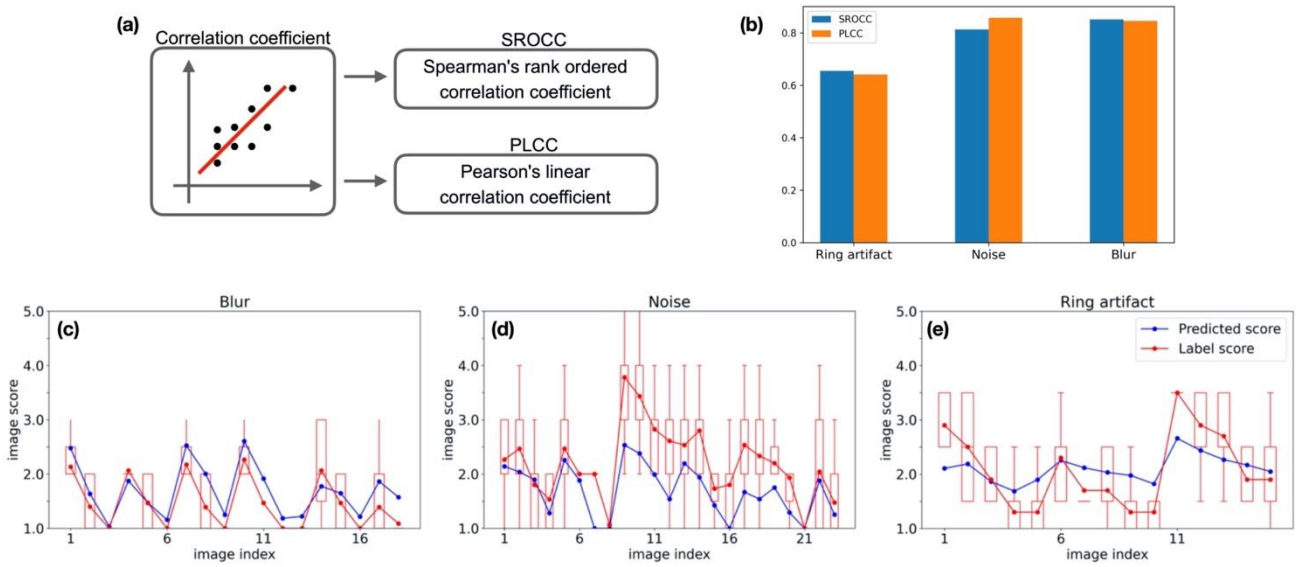

Figure V-5. Evaluation results of label projection module. It shows the data augmentation performance for three types of distortions. **(a)** and **(b)** demonstrate the correlation between predicted scores and human-annotated scores in three types of distorted images. **(c-e)** illustrate the quantitative value of the predicted scores and human labels of images with blur, noise and ring artefact. The red boxes represent the confident human annotations.

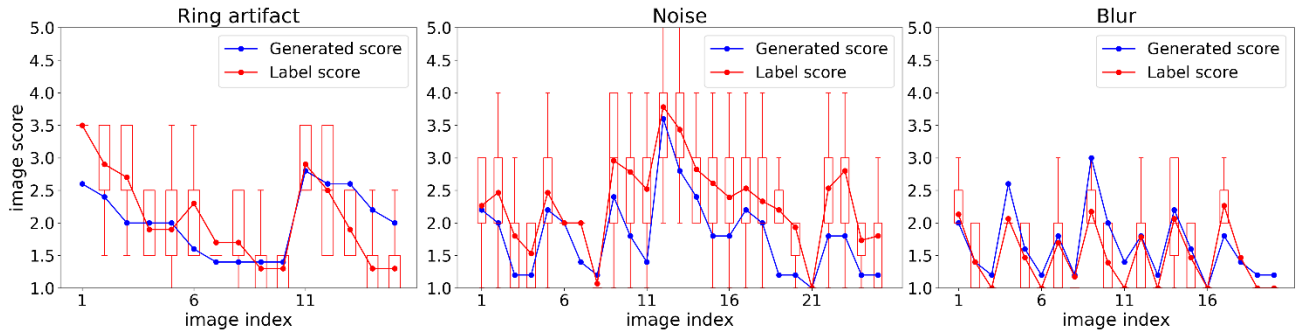

Figure V-6. The qualitative results of label projection. The red box shows the human labels with 95% confidence intervals. The red dot in each line is the average value of the labels. In y axis, the image score ranges from 1 to 5.

V.2.2 Score prediction results

In the procedure of image quality score prediction, as shown in Figure V-1, the network was firstly trained to rank the images according to their distortion levels. Then, based on the prior "ranking" knowledge, it was finetuned to regress the order information to a comprehensive quality score that represents the image quality in the range of 1 (worst) to 5 (best).

In this work, we take the EfficientNet[34] as the feature extractor instead of VGG[35] used in RankIQA[22] because it has less parameters (about 9 million parameters compared to VGG about

138 million trainable parameters), which means easier to converge and less possibility for overfitting.

For the validation of the model, we predict the quality score of 56 images and compared the results with human annotations, as presented in Figure V-7c-f. The results of images with different types of distortions were evaluated separately, which allows to observe the performance of the model towards different distortions. Taken together, these results indicate that there is a correlation between our predicted results and the human labeled scores, which demonstrates our method is able to imitate the HVS for the IQA. Interestingly, for blurred images, it performs excellently on both the relative order and the absolute score.

We also apply our method on two X-ray tomographic volumes to observe the consistence of the results. As demonstrated in Figure V-7a, b, we generate two image volumes with different quality and each of them contains 594 slices with size of 720*720. The images with higher quality are generated by applying filters on the worse images. In the box plot, we can see that the volume (purple) with high quality achieved higher score while the one (cyan) with lower quality had lower score. This comparison results present that our method could guide the pre-processing step and assist in choosing an appropriate filter. Moreover, from the variance of these two boxes, we can conclude that our method has stable performance because the difference among confident scores is small (less than 0.05) comparing to human distinction.

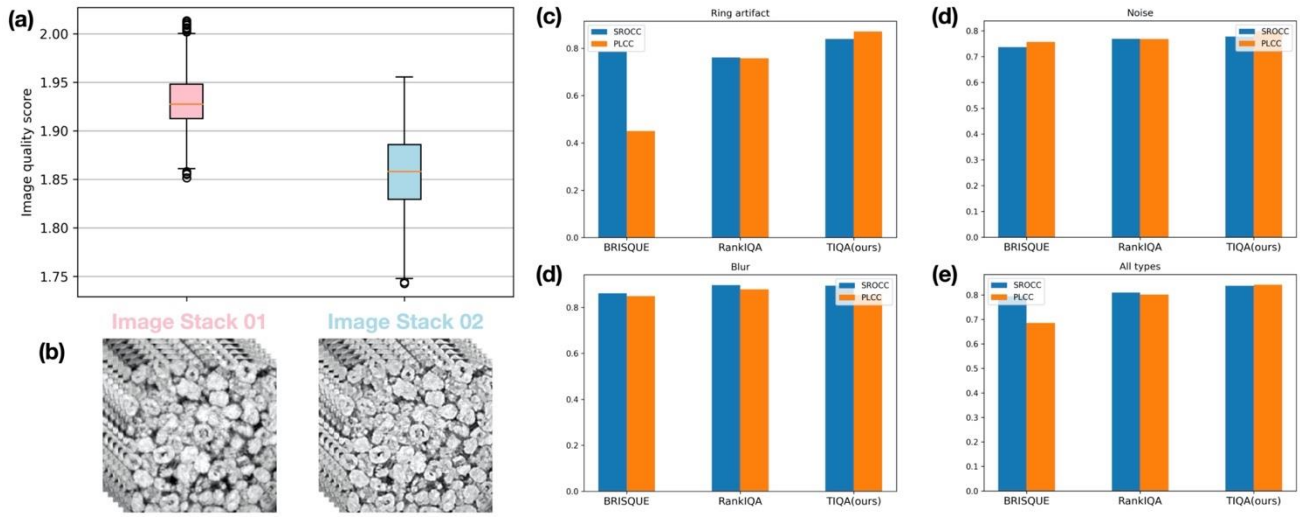

Figure V-7. (a-b) Image quality prediction results of two image volumes. They both are from the same material, but the volume Image Stack 01 has better quality than volume Image Stack 02. The figure on right shows the predicted quality score of the two volumes. The line in the box is the mean value of all scores. (c-e) **Quantitative comparison among different methods**. show the results of assessing the images with ring artifact, noise, and blur distortion, respectively. The last figure (e) illustrates the results of different methods for all types of distortions.

To demonstrate the advantage of our method, we compare it to other outstanding NR-IQA methods through two quantitative metrics (SROCC and PLCC) and the full table is shown in Table

V-1. Here, we represent two of them, BRISQUE[22] and RankIQA[28] in Figure V-7f. Overall, it shows that our method excels at assessing the quality of tomography images since it yields the highest correlation score among these three methods. In terms of the different types of distortion, our method outperforms BRISQUE for all three distortions. When compared with RankIQA, our method achieves better results for images with ring artifact and noise, and on par performance on the images with blur distortion.

Table V-1. Comparison with other deep-learning NR-IQA methods

Method	SROCC	PLCC
dipIQ[24]	0.780	0.782
MEON[25]	0.728	0.716
RankIQA[22]	0.809	0.801
TIQA(ours)	0.837	0.841

V.2.3 Segmentation evaluation method

The T-IQA method provides us with an efficient tool to select the image with best quality among pre-processing process, and the clue of how the distortion affects the segmentation accuracy could suggest the pre-processing step. Therefore, extra experiments were conducted to inspect the relation of the image quality and segmentation accuracy. We implemented a CNN based on D-linkNet[36] to predict the semantic segmentation results and compared them with T-IQA results to explore the influence of the distortions.

As presented in Figure V-8, a CNN network for segmentation is trained on X-ray tomography images and annotated segmentation ground-truth before making predictions. The uncertainty map is generated by calculating the entropy[37] of the possibility of each pixel belonging to different classes. It represents the uncertainty when the network assigns a phase (φ_i) to each pixel. A high uncertainty is represented as a red pixel, while a low certainty is displayed as a white pixel. From the uncertainty map, we can see that a higher uncertainty exists at the interphases, while low uncertainty exists at the bulk, which proves that the network usually produces fuzzy boundary. The segmentation results are obtained by binarizing the probability map. Here, only two classes are considered but the segmentation process can be extended to multiple classes.

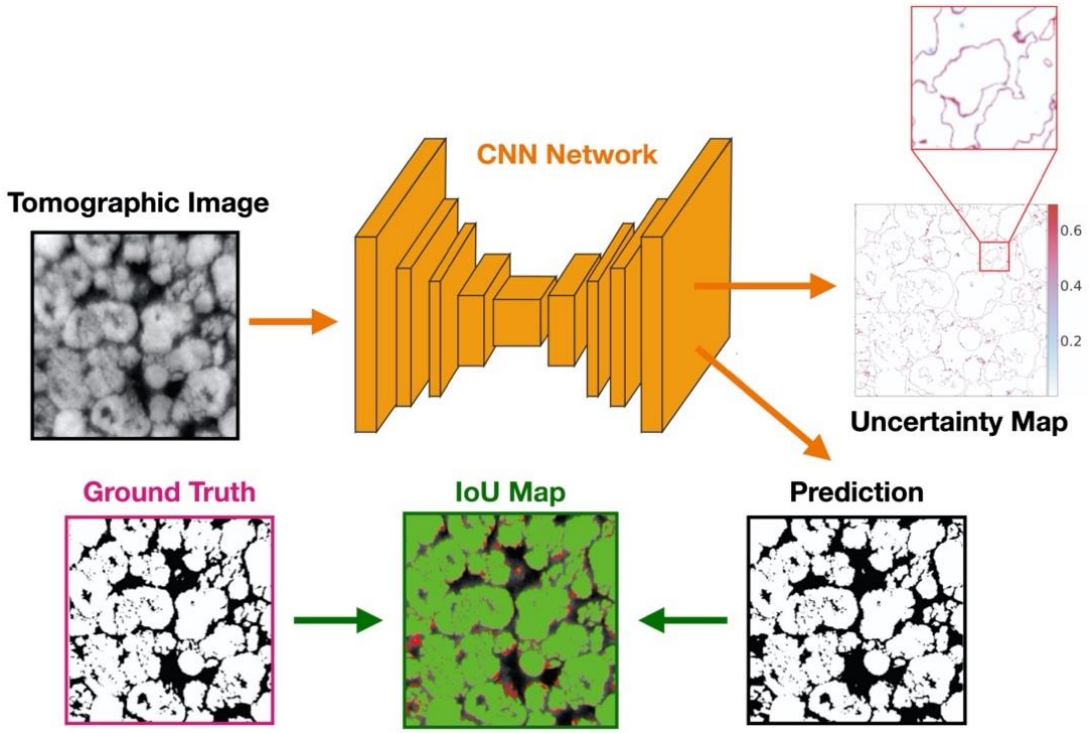

Figure V-8. Pipeline of segmentation evaluation procedure. In uncertainty map, the red area means high uncertainty while the white area means low uncertainty. In IoU map, the red, black, green areas represent true positive, true negative and false negative, respectively.

V.2.4 Relation between IQA results and segmentation accuracy

In addition to the uncertainty map, the $F1$ score, which is calculated from the confusion matrix, is also considered to quantify the segmentation accuracy. The correlation between the T-IQA score and the segmentation accuracy is investigated. We select an original image and its corresponding images with different types of distortions as the data for both IQA and segmentation (see Figure V-9). From the results, we can clearly see that the distortion affects the image quality and the segmentation performance. With distortion, images have lower quality score and $F1$ score which means lower segmentation accuracy. The uncertainty map clearly presents the influence of distortion on final segmentation results. Compared these three types of distortion, the noise causes a large amount of incertitude points in the uncertainty map, shown as the red points in Figure V-9. Although it seems that the blur distortion causes little uncertainty, it leads to vague boundaries and misclassification as well as huge reduction in HVS-based image quality score.

Moreover, the quantitative evaluation results of the T-IQA and segmentation accuracy are shown in Table V-2. From the SROCC and PLCC, we can see that the quality scores predicted by our approach are well correlated to the segmentation accuracy. The T-IQA scores share similar trend with the $F1$ scores, especially for the images with ring artifact and blur distortions.

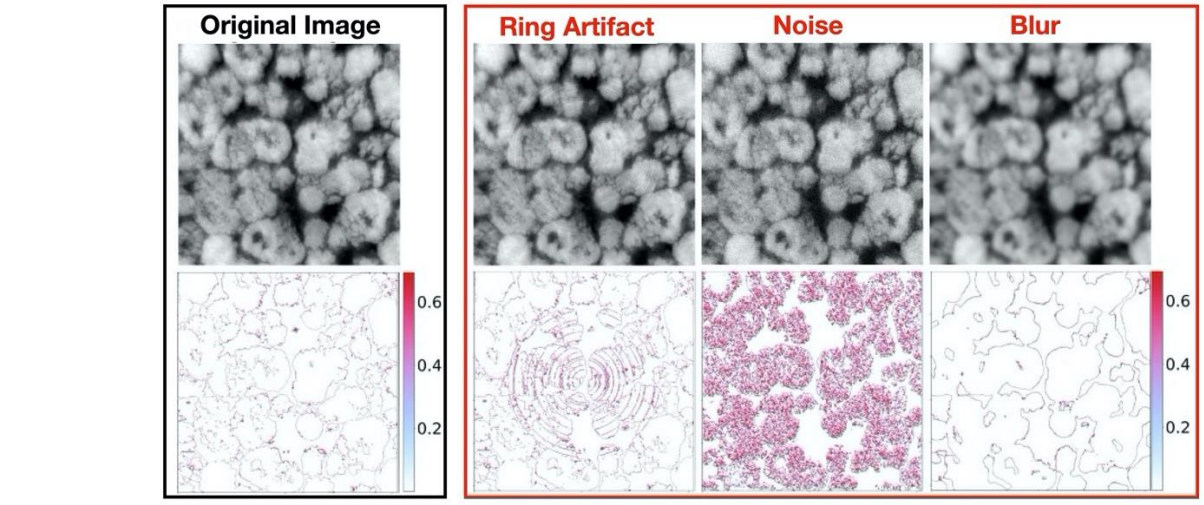

T-IQA score	2.56	2.55	2.30	1.45
IoU score	0.94	0.90	0.74	0.93

Figure V-9. Results of different distorted images evaluated by T-IQA and segmentation. For F1 score, it is in the range of 0 (the worst) and 1 (the best).

Table V-2. Quantitative results of the correlation between predicted quality score and segmentation accuracy. These measurements are calculated between $F1$ score and IQA score.

	SROCC	**PLCC**
Ring Artifact	0.925	0.887
Noise	0.829	0.877
Blur	0.928	0.952

To inspect the impact of distortion on classification result from pixel perspective, we calculate the point correlation pixel by pixel between predicted segmentation masks and ground truth. As shown in Figure V-10, we can observe that the colorful lines (with distortion) have positive correlation with the black line (without distortion). Nevertheless, they may have different sensitivity for specific types of distortion. For example, the point correlation line of the segmentation masks with noise do not converge at the reference line and the fluctuation indicates the serious impact of noise on segmentation results. Additionally, Figure V-10c illustrates that, with the increase of distortion level, the IQA score decreases quickly but the segmentation

accuracy keeps stable, which implies the network can tell very little difference of pixel values in the image and classify the pixels to different categories on the basis of the distinction. Due to the limitation of HVS, people cannot distinguish the little variation of the pixel intensities, as the results of blurred image shown in Figure V-10c.

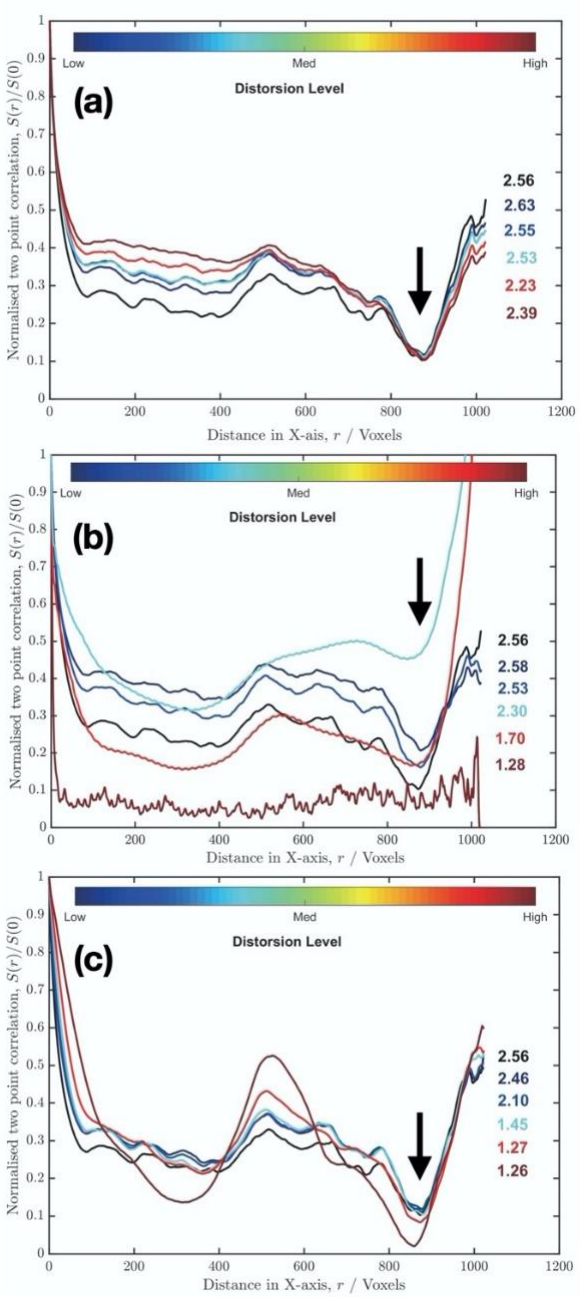

Figure V-10. Point correlation between predicted segmentation mask and ground truth for black phase. The figures (a-c) set out the correlation results from images with ring, noise, and blur. The color bar shows the distortion at different level, from little distortion to severe distortion. The solid line means the point correlation at X direction. The number labeled at the end of each line is the image quality score.

In summary, through the image quality score produced by our method, especially for images

with blur and ring artifact, as described in Table V-2, we can infer the corresponding segmentation performance without implementation. It greatly reduces the time of choosing appropriate pre-processing algorithm to improve the image quality and achieve better segmentation accuracy.

V.3 Discussion

Tomography images are widely used for analyzing the battery microstructure. However, the essential image pre-processing procedure is, mostly, observer-dependent.[38] This observer-dependence can lead to dispersions and uncertainties in the segmentation process. The latter might produce unreliable results that deteriorate the subsequent quantitative analysis, especially when the segmentation involves the supervised training procedure (inaccurate ground-truth). However, we believe that observer dependence can be diminished or eliminated by the appropriate prior pre-processing step, that provides the image with good quality according to HVS. Hence, a trust-worthy metric, which can assess the image quality like human observers, to guide the pre-processing procedure helps with dependable post-processing workflow (segmentation and analysis).

In this chapter, we propose a quantitative metric, denoted as T-IQA, for X-ray tomographic image quality assessment. Moreover, we address the lack of data issue for X-ray tomographic images through the data generation process. Overall, our approach shows a good performance and outperforms the other two IQA methods (BRISQUE & RankIQA) for X-ray tomographic images, given only few annotations for training. It is worth noting that although we try to reduce the demand of training annotations, a small number of labels are still required, so that it cannot be considered as an absolutely blind IQA method.

The correlation of our metric and the segmentation performance has also been explored. The qualitative and quantitative evaluation results prove that the segmentation performance is associated with the predicted quality score, which is also related to subjective human annotations. This correlation gives us tips to reduce the uncertainties and variations of segmentation results by applying pre-processing algorithms to improve the image quality.

For the idea of using neural network to evaluate the results of IQA, we use the similar method as Samuel *et al.*[39], who investigated the effect of image quality on DNN results by applying different distorted images on the same network, but we conducted more types of distortion. Instead of focusing on image classification problem, which classifies an image to one category, we analyzed the impact of distortion on image segmentation problem, that is concerned about pixels classification. Taking advantage of uncertainty map and IoU (Intersection over Union) map, the influence of distortion could be clearly visualized.

In conclusion, this work provides a quantitative IQA metric to guide the pre-processing step based on the subjective human opinion, so that the observer-dependence can be alleviated or removed from the pre-processing and the segmentation step. It greatly reduces the tedious work for selecting the good images and facilitates the automation of analyzing X-ray tomography

images. In addition, it provides more reliable assessment on image pre-processing results, which avoids the conflicts of different human observers, and promises an outperformed segmentation analysis.

However, some limitations remain to be solved. The undistorted images are not well evaluated in our method, due to the lack of images with excellent quality. Although our approach does not need hundreds of images for training, the estimation results of image quality can still be improved with the larger dataset. These limitations can be solved with the contribution from the community by sharing open-sources X-ray tomographic data, such as Tomobank[31] ,[32], [33].

Interestingly, thanks to the demand of automatically analyzing the tomography images, our T-IQA method can be extended to improve the image quality by using different image processing method. For example, by constructing a Teacher-Student model, our method (teacher) can teach a distortion removal network (student) to automatically eliminate the distortions. It will greatly release the burden of human observers and reduce the impact of distortion on segmentation. In addition, the image quality assessment can be extended to object-oriented assessment. For instance, through learning of object information, the network can judge whether the materials inside of the battery are destroyed or not.

V.4 Methods

V.4.1 Dataset creation

We collected 40 8-bit images from 11 different types of batteries with different resolutions. All the images were rescaled to the same resolution 224×224. To avoid deformation, we resized the original image to the width or height equaling 255 while preserving the aspect ratio, then randomly cropped the region with size of 224×224. We also maintained 6 original images for the analysis of the impact of down-sampling operation on image quality score. To expand the dataset, we applied different algorithms with different parameters to generate images with different types of distortion. For example, we generated several rings with different radius and intensities based on original images and add them together to imitate the ring artifact distortion. For blur and noise, we used the methods implemented in scikit-image[40]. Similar to Hanne's method[41], we manually set the parameter values that control the distortion amount such that the visual quality of the distorted images varies, from an expected rating of 1(worst) to 5 (best). The distortion parameter values were chosen based on a small set of images and applied the same for the remaining images in our database.

We performed two surveys for subjective image quality score and conveyed them to different people who included beginners and experts of this field for annotation among five levels: terrible, bad, average, good and excellent. For each image, we collected annotations from 15 people and set the average number as its quality score.

V.4.2 Data generation

As illustrated in Figure V-2, the preprocessed images were regarded as reference images. Then several distortion filters, including noise, blur, and ring artifact, were applied on the reference image to generate the distorted images. The parameter values of the filters were set differently, as shown in Table V-3, to create different distortion masks before adding them to the reference images so as to produce the images at different levels of distortion. For label projection, we used five FR-IQA evaluators, mimicking the human observers, to calculate the difference between reference image and distorted image and pass a score for distorted image. Due to the range of the score from each evaluator varies, we normalized and rescaled them to the same range. Finally, we averaged the produced scores and set it as the generated score.

Table V-3. Parameters to generate distorted images. The parameters in second column are contrast coefficients used to generate ring artifact in images. The third and fourth columns are the variance applied to produce gaussian noise and blur distribution

Level	Ring artifact	Noise	Blur
1	0.10	0.001	1.20
2	0.13	0.006	2.50
3	0.15	0.022	6.50
4	0.18	0.088	15.20
5	0.20	1.000	33.20

V.4.3 Score prediction

As shown in Figure V-1, we took the EfficientNet network as the feature extractor and change the last three layers to output a score for each input image. Among the dense layers, we added dropout[42] to avoid the overfitting. Instead of training the network from scratch, we transferred the weights from the pre-trained model in ImageNet[43] to reduce the time of convergence[44]. The input image size was fixed at 224×224×3 and the corresponding output was a score with shape of 1×1.

We built the image pair by picking an original image, generating the distorted images with distortions at different levels. The image with lower level of distortion was regarded as a better image than the one with higher level of distortion. Taking advantage of the generated ranking information, the network could order the images by quality. The corresponding rank loss[45] function is:

$$L(\hat{y}_i, \hat{y}_j) = \max(0, m + \hat{y}_i - \hat{y}_j) \quad \text{(Eq. V-1)}$$

where $\hat{y}_i, \hat{y}_j$ are the prediction results of a pair of images; m, set at 6 in our experiment, is a margin to control the minimum distance of the positive image pair.

After the image ordering process, the human annotations and the generated machine labels were inputted into the network to regress the output score to a fixed range by leveraging the Minor Square Error (MSE) loss function.

V.4.4 Training and testing parameters

In the score prediction module, we used 32 original images which were expanded to 512 images after data generation but without labels for training the rank. The initial learning rate was set at 3E-5 and decayed after several iterations. The network was trained for 30 epochs and on each epoch, it iterated on the whole dataset. The rate of the dropout was set at 0.5 to avoid overfitting. The Adam[46] optimizer was applied for optimizing the rank loss.

After training the rank, the model was fine tuned in the score regression step. The training dataset contains 29 images with the size of 224*224*3 and their corresponding labels, which are in the range from 1 to 5. The data generation method was also implemented to expand the training dataset to 464 images with generated annotations. Then, they were inputted to the network for regression with the MSE loss. The network iterated 20 epochs with the initial learning rate at 5E-5 which decayed every 4 epochs. The dropout rate was 0.5 in training. For testing procedure, totally 56 images were tested and evaluated with corresponding human annotations.

All the experiments were conducted on python with TensorFlow[47] library. The computing hardware was Tesla K80.

V.4.5 Evaluation metrics

The PLCC is the linear correlation coefficient between the predicted score and human labeled score. It measures the prediction accuracy of an IQA metric, *i.e.*, the capability of the metric to predict the subjective scores with low error. The PLCC is calculated as follows:

$$\mathrm{PLCC} = \frac{\sum_{i=1}^{M_d}(\hat{y}_i - \hat{y}_{\mathrm{avg}})(y_i - y_{\mathrm{avg}})}{(\sum_{i=1}^{M_d}(\hat{y}_i - \hat{y}_{\mathrm{avg}})^2)^{\frac{1}{2}}(\sum_{i=1}^{M_d}(y_i - y_{\mathrm{avg}})^2)^{\frac{1}{2}}} \qquad \text{(Eq. V-2)}$$

where $\hat{y}_i$ and y_i are the predicted score and the human labeled score of the *i-th* image in a dataset of size M_d respectively, , $\hat{y}_{\mathrm{avg}}$ and y_{avg} are the average of the predicted scores and human labeled scores, respectively.

The SROCC is the rank correlation coefficient between predicted score and labeled score and it compares the monotonicity of the prediction performance, *i.e.*, the limit to which the predicted scores agree with the relative magnitude of the labels. The SROCC can be calculated via following equation:

$$\mathrm{SROCC} = 1 - \frac{6\sum_{i=1}^{M_d}(d_i)^2}{M_d(M_d^2-1)} \qquad \text{(Eq. V-3)}$$

where the d_i is the difference between the *i-th* image's rank in prediction results and labels.

V.4.6 Segmentation-based evaluation method

To inspect the effect of distortion on segmentation accuracy, we applied D-LinkNet[36], which is an encoder decoder network connected by dilated convolutions[48], for tomography image segmentation. It segmented the image to 2 classes and produced the probability map which indicated the possibility of each pixel belonging to a class. Finally, the classification result is generated by setting a threshold to binarize the probability map. The network ran for 200 epochs on 110 images with segmentation labels. The size of input image and label was 1024×1024 and they were normalized to range of 0 and 1 before inputting to the network. The initial learning rate was 1E-4 and decayed to one fifth of previous value after fixed steps. The optimizer was Adam and binary cross-entropy loss was used to measure the difference of prediction and ground truth.

In the testing procedure, the output of the network was utilized to generate the uncertainty map. We used the entropy function[37] to calculate the uncertainty, which is described as follows,

$$H[y|x,X,Y] = -\sum_c p(y=c|x,X,Y)\log_p(y=c|x,X,Y) \quad \text{(Eq. V-4)}$$

where x is the test image, y is the predicted class, X and Y are the images and labels in training process, c is the class index.

The IoU (intersection over union) and $F1$ score were utilized to measure the segmentation performance. IoU means the area of overlap between the predicted segmentation and the ground truth divided by the area of union between them. It ranges from 0 to 1 with 0 signifying no overlapping and 1 indicating perfect overlapping. Different from IoU, the $F1$ score can be calculated by:

$$F1 = \frac{2\times overlap}{total\ pixels} \qquad \text{(Eq V-5)}$$

where $total\ pixels$ means the number of pixels in both segmentation results and ground truth, and $overlap$ means the intersection of segmentation results and ground truth.

V.5 Code Availability

The python code for IQA and segmentation evaluation of the project is available at https://github.com/SummerOf15/TomoIQA.

References

[1] T.-T. Nguyen, J. Villanova, Z. Su, R. Tucoulou, B. Fleutot, B. Delobel, C. Delacourt, A. Demortière, *Wiley Online Libr.* **2021**, DOI 10.1002/aenm.202003529.

[2] H. Chan, M. Cherukara, T. D. Loeffler, B. Narayanan, S. K. R. S. Sankaranarayanan, *npj Comput. Mater.* **2020**, *6*, 1.

[3] S. Schlüter, A. Sheppard, K. Brown, D. Wildenschild, *Water Resour. Res.* **2014**, *50*, 3615.

[4] P. Pietsch, M. Ebner, F. Marone, M. Stampanoni, V. Wood, *Sustain. Energy Fuels* **2018**, *2*, 598.

[5] X. Gao, W. Lu, D. Tao, X. Li, in *Vis. Commun. Image Process. 2010* (Eds.: P. Frossard, H. Li, F. Wu, B. Girod, S. Li, G. Wei), SPIE, **2010**, p. 77440Z.

[6] K. Y. Lin, G. Wang, in *Proc. IEEE Comput. Soc. Conf. Comput. Vis. Pattern Recognit.*, IEEE Computer Society, **2018**, pp. 732–741.

[7] Z. Wang, A. C. Bovik, H. R. Sheikh, E. P. Simoncelli, *IEEE Trans. Image Process.* **2004**, *13*, 600.

[8] L. Zhang, Y. Shen, H. Li, *IEEE Trans. Image Process.* **2014**, *23*, 4270.

[9] W. Zhu, G. Zhai, Y. Liu, N. Lin, X. Yang, in *2018 IEEE 20th Int. Work. Multimed. Signal Process. MMSP 2018*, Institute Of Electrical And Electronics Engineers Inc., **2018**.

[10] S. Golestaneh, L. J. Karam, *IEEE Trans. Image Process.* **2016**, *25*, 5293.

[11] W. S. Geisler, *Annu. Rev. Psychol.* **2008**, *59*, 167.

[12] A. Leclaire, L. Moisan, *J. Math. Imaging Vis.* **2015**, *52*, 145.

[13] Z. Wang, E. P. Simoncelli, A. C. Bovik, in *Conf. Rec. Asilomar Conf. Signals, Syst. Comput.*, **2003**, pp. 1398–1402.

[14] L. Zhang, L. Zhang, X. Mou, D. Zhang, *IEEE Trans. Image Process.* **2011**, *20*, 2378.

[15] W. Xue, L. Zhang, X. Mou, A. C. Bovik, *IEEE Trans. Image Process.* **2014**, *23*, 668.

[16] H. Z. Nafchi, A. Shahkolaei, R. Hedjam, M. Cheriet, *IEEE Access* **2016**, *4*, 5579.

[17] M. Liu, G. Zhai, Z. Zhang, Y. Sun, K. Gu, X. Yang, in *IEEE Int. Symp. Broadband Multimed. Syst. Broadcast. BMSB*, IEEE Computer Society, **2014**.

[18] K. Gu, W. Lin, G. Zhai, X. Yang, W. Zhang, C. W. Chen, *IEEE Trans. Cybern.* **2017**, *47*,

4559.

[19] Q. Yan, Y. Xu, X. Yang, in *IEEE Int. Symp. Broadband Multimed. Syst. Broadcast. BMSB*, IEEE Computer Society, **2013**.

[20] H. Liu, N. Klomp, I. Heynderickx, *IEEE Trans. Circuits Syst. Video Technol.* **2010**, *20*, 529.

[21] N. T. Vo, R. C. Atwood, M. Drakopoulos, *Opt. Express* **2018**, *26*, 28396.

[22] A. Mittal, A. K. Moorthy, A. C. Bovik, in *Conf. Rec. - Asilomar Conf. Signals, Syst. Comput.*, **2011**, pp. 723–727.

[23] R. A. Manap, L. Shao, *Inf. Sci. (Ny).* **2015**, *301*, 141.

[24] L. Kang, P. Ye, Y. Li, D. Doermann, in *Proc. IEEE Comput. Soc. Conf. Comput. Vis. Pattern Recognit.*, IEEE Computer Society, **2014**, pp. 1733–1740.

[25] K. Gu, G. Zhai, X. Yang, W. Zhang, in *2014 IEEE Int. Conf. Image Process. ICIP 2014*, Institute Of Electrical And Electronics Engineers Inc., **2014**, pp. 511–515.

[26] S. Bosse, D. Maniry, K. R. Müller, T. Wiegand, W. Samek, *IEEE Trans. Image Process.* **2018**, *27*, 206.

[27] S. Bianco, L. Celona, P. Napoletano, R. Schettini, *Signal, Image Video Process.* **2018**, *12*, 355.

[28] X. Liu, A. D. Bagdanov, *Proceedings of the IEEE International Conference on Computer Vision*, **2017**, 1040-1049.

[29] H. Zhu, L. Li, J. Wu, W. Dong, G. Shi, *Proc. IEEE Int. Conf. Comput. Vis.* **2020**.

[30] Q. Sun, Y. Liu, T. S. Chua, B. Schiele, in *Proc. IEEE Comput. Soc. Conf. Comput. Vis. Pattern Recognit.*, **2019**.

[31] F. De Carlo, D. Gürsoy, D. J. Ching, K. J. Batenburg, W. Ludwig, L. Mancini, F. Marone, R. Mokso, D. M. Pelt, J. Sijbers, M. Rivers, *Meas. Sci. Technol.* **2018**, *29*, 034004.

[32] F. L. E. Usseglio-Viretta, A. Colclasure, A. N. Mistry, K. P. Y. Claver, F. Pouraghajan, D. P. Finegan, T. M. M. Heenan, D. Abraham, P. P. Mukherjee, D. Wheeler, P. Shearing, S. J. Cooper, K. Smith, *J. Electrochem. Soc.* **2018**, *165*, A3403.

[33] M. Ebner, D. W. Chung, R. E. García, V. Wood, *Adv. Energy Mater.* **2014**, *4*.

[34] M. Tan, Q. V. Le, *36th Int. Conf. Mach. Learn. ICML 2019* **2019**, *2019-June*, 10691.

[35] K. Simonyan, A. Zisserman, *3rd Int. Conf. Learn. Represent. ICLR 2015 - Conf. Track Proc.* **2015**.

[36] L. Zhou, C. Zhang, M. Wu, in *IEEE Comput. Soc. Conf. Comput. Vis. Pattern Recognit. Work.*, **2018**.

[37] C. E. Shannon, *Bell Syst. Tech. J.* **1948**, DOI 10.1002/j.1538-7305.1948.tb01338.x.

[38] P. C. Baveye, M. Laba, W. Otten, L. Bouckaert, P. Dello Sterpaio, R. R. Goswami, D. Grinev, A. Houston, Y. Hu, J. Liu, S. Mooney, R. Pajor, S. Sleutel, A. Tarquis, W. Wang, Q. Wei, M. Sezgin, *Geoderma* **2010**, *157*, 51.

[39] S. Dodge, L. Karam, in *2016 8th Int. Conf. Qual. Multimed. Exp. QoMEX 2016*, Institute Of Electrical And Electronics Engineers Inc., **2016**, p. 7498955.

[40] S. Van Der Walt, J. L. Schönberger, J. Nunez-Iglesias, F. Boulogne, J. D. Warner, N. Yager, E. Gouillart, T. Yu, *PeerJ* **2014**, *2014*, e453.

[41] H. Lin, V. Hosu, D. Saupe, in *2019 11th Int. Conf. Qual. Multimed. Exp. QoMEX 2019*, **2019**.

[42] N. Srivastava, G. Hinton, A. Krizhevsky, I. Sutskever, R. Salakhutdinov, *J. Mach. Learn. Res.* **2014**.

[43] Jia Deng, Wei Dong, R. Socher, Li-Jia Li, Kai Li, Li Fei-Fei, **2009**.

[44] K. He, R. Girshick, P. Dollár, **2018**, 1.

[45] W. Chen, T. Y. Liu, Y. Lan, Z. Ma, H. Li, in *Adv. Neural Inf. Process. Syst. 22 - Proc. 2009 Conf.*, **2009**.

[46] D. P. Kingma, J. L. Ba, in *3rd Int. Conf. Learn. Represent. ICLR 2015 - Conf. Track Proc.*, International Conference On Learning Representations, ICLR, **2015**.

[47] M. Abadi, P. Barham, J. Chen, Z. Chen, A. Davis, J. Dean, M. Devin, S. Ghemawat, G. Irving, M. Isard, M. Kudlur, J. Levenberg, R. Monga, S. Moore, D. G. Murray, B. Steiner, P. Tucker, V. Vasudevan, P. Warden, M. Wicke, Y. Yu, X. Zheng, in *Proc. 12th USENIX Symp. Oper. Syst. Des. Implementation, OSDI 2016*, **2016**.

[48] L.-C. Chen, G. Papandreou, F. Schroff, H. Adam, *Proc. IEEE Comput. Soc. Conf. Comput. Vis. Pattern Recognit.* **2017**.

Chapter VI . Numerical Modeling Of Discharge Rate Capability Of Industry-Grade Electrodes

VI.1 Introduction

The $LiNi_xMn_yCo_{(1-x-y)}O_2$ electrode features high theoretical capacity, high energy density, structural stability, and high intrinsic rate capability that offer many potential advantages over existing technologies. While progress has been continuously achieved to get even better active materials,[1–5] industry engineers and academic researchers keep working on making improvement at the electrode scale. This can be done through the microstructure design, which plays a vital role in achieving high-performance LiB electrodes.[6–14]

Obviously, it can be seen that either densification of the electrode and/or increase in thickness significantly improve its volumetric energy density. In addition, the overall AM amount increases with coating thickness as the electrolyte, separator and current collector content decrease relatively, which can be a benefit for gravimetric energy density at the module or pack level. However, the search for optimal design is not straightforward because of the complex interplay between the microstructure and the different processes occurring during battery operation that affect the electrode performance. Understanding this interplay, therefore, is key for the optimization process of the electrode design.

For this purpose, the common approach currently relies on a trials-errors process using experimental testing. The drawback is that it generates little knowledge and understanding of what really happens in a device or during a process. It also requires a considerable amount of measurements with different configurations to be carried out so as to obtain reliable data for investigation. Instead, numerical modeling is promising and potentially a more time-efficient alternative to provide valuable insights for electrode design optimization. Among the different approaches to building a numerical model, physics-based models are based on the use of mathematical equations that represent the underlying physics. Providing the input parameters can be accurately determined, battery physics-based models enable predicting what is actually happening inside a cell in terms of, *e.g.*, local state-of-charge and temperature, electric potentials of solid and liquid phase, electronic and ionic current densities and solid/liquid lithium concentration gradients. Moreover, rate-limiting factors can also be quantified through model analysis.

Among LiB continuum models, the so-called Newman P2D model[15–17] introduced in Chapter II offers the best compromise between computation speed and physical significance. It relies on porous electrode theory and concentrated solution theory.[18] However, such a detailed model requires a number of input parameters, describing each component's morphology, kinetics, transport and thermodynamics, which are not straightforward to determine. Without an exact knowledge of the individual material parameters, statements about internal states are only possible to a minimal extent. Very little literature[14,19–21] has so far dealt with the complete parameterization of a specific LiB. Consequently, in most works dealing with physics-based models, values from supplementary literature sources are used; some key parameters are fitted or even assumed in order to match the experimental results. Still, based on the Newman P2D model, relevant works

demonstrated valuable insights about the performance of porous electrodes (PE).[14,19,20,22–25] Malifarge *et al.*[14] combined experimental measurements with simulations to investigate the effects of Graphite electrode loading and porosity on electrode performance. Similarly, Colclasure *et al.*[25] investigated limitations of extreme fast charging for NMC/Graphite cells with high electrode loading. They demonstrated that electrolyte transport is a major limitation resulting in lithium plating and poor utilization for thick-electrode cells.

Also, many works focus on NMC electrodes since it is a popular class of materials for the cathode. Despite a high extent of the investigation, the interplay between their performance and their microstructure has not been completely unveiled. Several works reported that the somewhat mediocre performance of high-energy density NMC electrodes at high C-rate relates to the transport limitation in electrolyte-filled pores. The tortuosity of the pore network is, therefore, assigned to be the main rate-limiting factor.[24,26]

In contrast, Appiah *et al.*[27] and Xu *et al.*[28] investigated the performance deterioration through the solid-diffusion process, for which an empirical relationship of the solid diffusion coefficient with the electrode thickness and the C-rate was set forth. Although these correlations allow for a good agreement between simulations and experimental results, the approach relies on fitted correlations rather than on a physical foundation.

In this work, we first proceed with a careful parametrization step, in which the majority of the input parameters are determined with appropriate measurements along with the validation on lab-made "model" electrodes. Then, we demonstrate that the conventional Newman P2D model fails at obtaining a good agreement with the experimental results for a set of industry-grade electrodes used in this work. Careful analysis with the Newman P2D model and insights from tomographic data point out that the limitations would arise from the presence of particle agglomerates, which are believed to arise from the electrode calendering for achieving high-energy density. Therefore, a new model is developed in this chapter and shows a good agreement with experimental results. After validation, the performance of different electrode designs is analyzed using the model, *i.e.* the electrode overpotential is decorrelated into each polarization source for a low- and a high-loading electrode design. Results obtained from this model-based analysis are eventually discussed. Finally, as a perspective for optimizing high-energy density electrode design, the performance benefits if agglomerate formation is suppressed are examined with the model.

VI.2 Model Theory

In this chapter, since lithium metal is used in place of a porous negative electrode, a half-cell is modeled. The model consists of one NMC electrode and one separator domains, whereas only the outer surface of the Li foil and the current collector are represented through their boundary with the separator and the electrode, for the sake of simplicity.

VI.2.1 Newman P2D model

The Newman P2D model can be seen as the reference for physics-based modeling of LiB, as described in detail in Chapter II. For this chapter, the Newman P2D model is simulated with DUM*BAT*,[29] a physics-based modeling software for Li-ion cell simulations. Later, we introduce the Newman model using polynomial approximation based on Subramanian *et al.*,[30] which is simulated with COMSOL Multiphysics. For ease of understanding, it is referred to as the "baseline" model, whereas the regular Newman P2D model is denoted as the Newman model here below.

VI.2.2 Porous Agglomerate model

Later in this chapter, we investigate a possible scenario where the calendering process increases the electrode density leading to the formation of porous agglomerates (PA), which is a consequence of groups of individual NMC secondary particles densely packed with CBD and pores. The pores located in these PAs are assumed to be very small and narrow due to the high density of the solid mixture, so that they are denoted as sub-pores. Since the NMC secondary particle diameter is more than thirty times that of the primary particles, the primary particles are not considered, along with grain-boundary effects that might exist.

Thus, we introduce herein a new physics-based model that takes into account the presence of such PAs instead of individual AM particles. The model's mathematical methodology relies on the porous electrode theory in the same manner as the Newman P2D model. Likewise, the electrolyte transport in the electrolyte phase of the electrode is described by concentrated solution theory. The model is implemented and solved with COMSOL Multiphysics.

Regarding the PA model, Dargaville *et al.*[31] proposed a 1D+1D+1D (P3D) model for modeling the $LiFePO_4$ electrode. The three correspond scales are the PE, the PA, and the $LiFePO_4$ particles located inside the PA. Based on this work, several follow-up works[32–34] developed models for electrodes having an agglomerate structure of the AM particles (*e.g.* NMC, $Li(Ni_{0.33}Co_{0.33}Al_{0.33})O_2$) with an inner pore structure. Nevertheless, these works used the PA model to consider the morphology of individual secondary particles, which differs from the concept in this chapter.

Purposely, the model in this work is kept as simple as possible to minimize the number of additional parameters with respect to the Newman model. It is decided to resort to the polynomial approximation to treat the solid diffusion in NMC particles, as proposed by Subramanian *et al.*[30] They developed efficient approximate solutions for the solid diffusion within AM secondary particles by assuming that the Li concentration inside the spherical particle can be expressed as a polynomial across the radial dimension. Therefore, solid diffusion within AM particles is solved by a set of ordinary differential equations and algebraic equations without adding a pseudo-dimension to the model.

In [30], the authors demonstrated that the approximate model using high order (4^{th}-order) polynomial to represent the Li concentration profile within the particles yields a great extent of accuracy that is tantamount to the P2D model. The polynomial is, then, solved in terms volume-average AM-phase Li concentration, surface concentration and volume-average concentration flux.

Since a variable solid diffusion coefficient is considered here instead of a constant coefficient as in [30], it is taken to be a function of the volume-average Li concentration instead of the local Li concentration in the P2D model. The error of this assumption on the simulations are investigated later on when comparing the simulated rate capability upon discharge using Newman model with polynomial approximation against that from the Newman P2D model for the same electrode (see Figure VI-1).

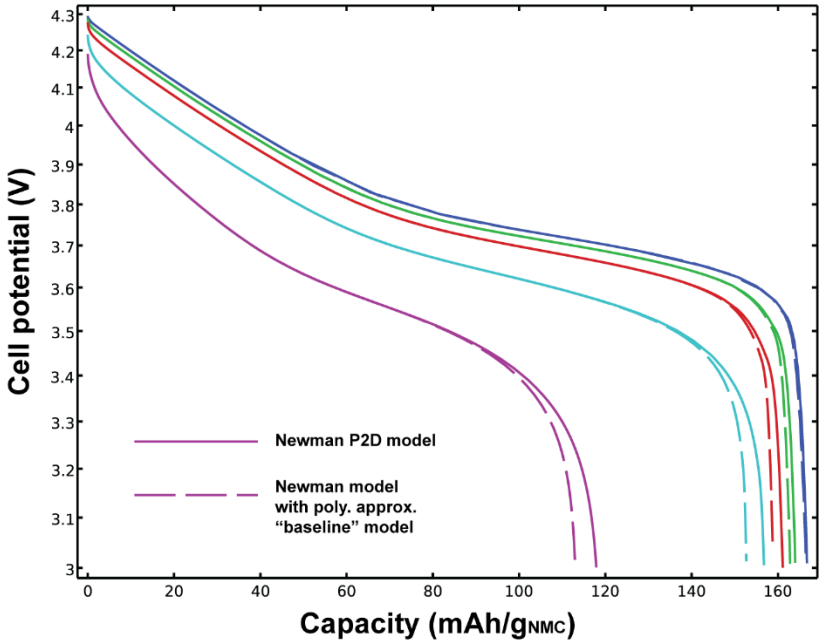

Figure VI-1. Comparison of regular Newman P2D model and "baseline model". Discharge curves at different C-rates obtained by using Newman model with polynomial approximation for the solid phase concentration is compared with those obtained by Newman P2D model.

The PA is assumed to be spherical and radially symmetric. In addition, the interface between secondary particles located at the outer of the PA and electrolyte in macro-pores (*i.e.*, outer surface of the agglomerate) is assumed to be inactive, *i.e.* there is no charge transfer process at the PA/macro-pores interface. Thus, the pore-wall flux occurs only at the interface between AM and sub-pores located inside the PA.

Finally, it is worth mentioning that the effective electronic conductivity of the solid phase in the "macro model" is assumed to be constant. This might not be valid if the conductive pathway is a mixture of CBD and NMC, since the electronic conductivity of the NMC materials has been reported to vary as a function of the Li content.[35]

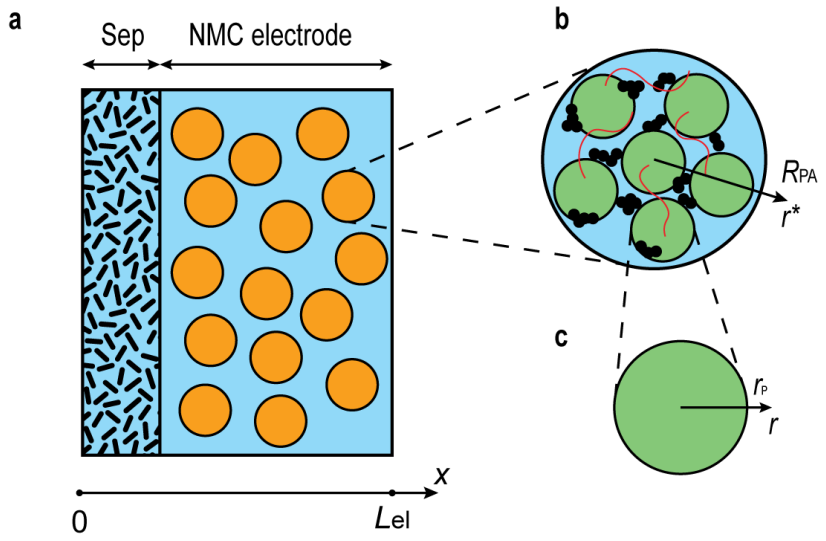

Figure VI-2. Schematic of the two size scales in our proposed model: a. Porous Electrode, **b.** Porous Agglomerate. **c.** Active Material Particle.

A schematic diagram of the model is illustrated in Figure VI-2. The "macro model" refers to the PE scale as in the Newman P2D model. In the PE scale, there is a liquid phase filling in the macro-pore domain and a solid phase, which is made up of PA (referred to as "micro model") instead of a mixture of AM particles and additives. These agglomerates contain the AM, the CBD and a sub-pore domain filled with electrolyte. The total electrode porosity is the sum of that of sub-pores and that of macro-pores.

Within the PA, AM particles are considered spherical with a uniform diameter. It is worth noting that the PA can be extremely dense, which promotes an inter-connectivity between solid particles. Consequently, unlike in the Newman model, the AM particle surface might not be completely exposed to the electrolyte such that the active surface area is reduced. Although the particle/particle interface is not active for electrochemical reaction, it is assumed to allow the inter-particle diffusive flux due to the gradient of concentration between particles in contact. As a result, an additional physics is introduced in the model to represent the mass balance of inserted Li in AM phase at PA scale.

In addition, the CBD is assumed to be well-percolated throughout the PA, so that there is no limitation from electronic transport. Thus, the electric potential is uniformly distributed throughout the PA, *i.e.*, there is no ohmic drop in the solid phase across the radial dimension of the PA.

For the sake of understanding, the solid phase that consists of AM and CBD is referred to as domain 1, the liquid phase in the "macro model" is referred to domain 2, the liquid phase in the sub-pore domain in the "micro model" is referred to domain 3. The AM phase within the PA is subscripted with $_{AM}$. The parameters pertaining to the PE dimensions are denoted with uppercase symbols, whereas lowercase symbols are dedicated to parameters pertaining to the PA scale. The model is also referred to as the PApa model, which comes from **P**orous **A**gglomerate with

polynomial **a**pproximation.

"Macro model"

Regarding the macro model, an electronic current density $\vec{I}_1$ flows across the PE in the solid phase along the x dimension (*i.e.,* across sandwich), and an ionic current density $\vec{I}_2$ flows similarly in the liquid phase. The sum of these two current densities is uniform across the PE, which means that any increase in $\vec{I}_2$ is compensated for by a decrease in $\vec{I}_1$. For the macroscopic model, this is expressed as:

$$\nabla \cdot \vec{I}_1 + \nabla \cdot \vec{I}_2 = 0 \qquad \text{(Eq. VI-1)}$$

By electroneutrality in the solution, a current balance relates the divergence of the ionic current density to the net cation flux leaving the macro-pore domain to enter the sub-pore domain:

$$\nabla \cdot \vec{I}_2 = A_{\mathrm{PA}} F (j_{3,+} - j_{3,-}) \qquad \text{(Eq. VI-2)}$$

in which A_{PA} ($\mathrm{m}^2_{\mathrm{PA}}/\mathrm{m}^3_{\mathrm{PE}}$) is the specific interfacial area between the PA and the liquid phase in macro-pore domain per unit volume of PE and F is the Faraday's constant. Given a spherical shape of the PA having a radius, R_{PA}, it is common in a macro-homogenous model that A_{PA} is estimated from the PA volume fraction, Ψ_{PA} ($\mathrm{m}^3_{\mathrm{PA}}/\mathrm{m}^3_{\mathrm{PE}}$), using the following equation:

$$A_{\mathrm{PA}} = \frac{3\Psi_{\mathrm{PA}}}{R_{\mathrm{PA}}} \qquad \text{(Eq. VI-3)}$$

The net cation flux $j_{3,+} - j_{3,-}$ ($\mathrm{mol}/\mathrm{m}^2_{\mathrm{PA}} \cdot \mathrm{s}$) relates to the amount of Li^+ consumed/produced by the electrochemical reactions occurring within the PA, at the interface between the AM particles and the sub-pores.

From Eq. VI-1, the electronic current balance in the solid phase is inferred:

$$\nabla \cdot \vec{I}_1 = -A_{\mathrm{PA}} F (j_{3,+} - j_{3,-}) \qquad \text{(Eq. VI-4)}$$

The electronic current density in solid phase $\vec{I}_1$ is simply described with Ohm's law, with Φ_1 the electric potential of the solid phase and σ_{eff} the effective electronic conductivity of the solid phase of the electrode.

$$\vec{I}_1 = -\sigma_{\mathrm{eff}} \nabla \Phi_1 \qquad \text{(Eq. VI-5)}$$

The ionic current density in liquid phase $\vec{I}_2$ is expressed using the Mac-Innes equation that derives from the concentrated solution theory and accounts for salt concentration gradients across the liquid phase.

$$\vec{I}_2 = -\kappa_{\text{eff},2}\nabla\Phi_2 + 2\kappa_{2,\text{eff}}\frac{RT}{F}(1-t_+^0)\alpha\nabla\ln c_2 \qquad \text{(Eq. VI-6)}$$

In this equation, R is the ideal gas constant, T is the absolute temperature, t_+^0 is the transference number of Li^+ in the electrolyte with respect to the solvent velocity, α is the thermodynamic factor, and $\kappa_{\text{eff},2}$ stands for the effective ionic conductivity the electrolyte within the macro-pore domain. The effective ionic conductivity can be calculated from the bulk ionic conductivity κ by:

$$\kappa_{\text{eff},2} = \frac{\Psi_2}{\tau_{\text{e},2}}\kappa \qquad \text{(Eq. VI-7)}$$

where Ψ_2 $(\text{m}_2^3/\text{m}_{\text{PE}}^3)$ is the volume fraction of the macro-pore domain, and $\tau_{\text{e},2}$ is the electrode tortuosity factor of the macro-pore domain.

It is noteworthy that E6 is strictly valid for a binary electrolyte, *i.e.*, a salt and a single solvent mixture. Newman and coworkers consider that solvent components commonly used in LiB are similar enough to be approximated as a single solvent component.[36]

In the separator domain, the charge is conserved, hence Eq. VI-2 reduces to:

$$\nabla\cdot\vec{I}_2 = 0 \qquad \text{(Eq. VI-8)}$$

The ionic current density is continuous at the interface between the separator and the PE.

Since only potential differences, and not absolute potentials, are measurable, Φ_2 has an arbitrary datum as a boundary condition. Here, we set the reference potential at the PE/current collector boundary:

$$\Phi_2 = 0 \qquad \text{(BC. VI-1)}$$

At the Li foil, a boundary condition specifies all the applied current is carried by the ionic current in the liquid phase:

$$\vec{I}_2\cdot\vec{n} = Fi_{\text{Li}}^0\left\{\exp\left(\frac{(1-\beta)F}{RT}(\Phi_{1,\text{Li}}-\Phi_2)\right)-\exp\left(-\frac{\beta F}{RT}(\Phi_{1,\text{Li}}-\Phi_2)\right)\right\} = -I_{\text{app}} \quad \text{(BC. VI-2)}$$

where, $i_{\text{Li}}^0 = Fk_{0,\text{Li}}c_2^{1-\beta}$ represents the exchange current density at the Li foil, where the reaction $\text{Li} \leftrightarrow \text{Li}^+ + \text{e}^-$occurs, I_{app} represents the discharge current density $(\text{A}/\text{m}_{\text{CC}}^2)$, which is negative for Li insertion in AM phase in convention.

At the current collector/PE boundary, the ionic current is set to be 0, as all applied current is carried by the electronic current in the solid phase:

$$\vec{I}_2\cdot\vec{n} = 0 \qquad \text{(BC. VI-3)}$$

For the solid phase, the electronic current density is assumed to be equal to the applied current

density at the current collector:

$$\vec{I}_1 \cdot \vec{n} = I_{\text{app}} \qquad \text{(BC. VI-4)}$$

At separator/PE boundary, the electronic current density is set to be 0, as the total current is carried by ions only:

$$\vec{I}_1 \cdot \vec{n} = 0 \qquad \text{(BC. VI-5)}$$

Since conventional Li intercalation process in LiB involves only the Li^+, the equations are made simpler later on if a mass balance on the anion of the salt (*e.g.*, PF_6^-) is used in order to solve for the salt concentration. By virtue of electroneutrality, the concentration of the anion is identical to that for the cation.

From porous electrode theory, the mass balance for the anion across the PE reads:

$$\Psi_2 \frac{\partial c_2}{\partial t} = -\nabla \cdot \vec{N}_{2,-} + A_{\text{PA}} j_{3,-} \qquad \text{(Eq. VI-9)}$$

where $A_{\text{PA}} j_{3,-}$ is the anion flux per unit volume of PE, that reciprocally flows between macro-pore domain in PE and sub-pore domain in PA.

The flux density of the anion is described by concentrated solution theory as:

$$\vec{N}_{2,-} = -\left(1 - \frac{d \ln c_{2,0}}{d \ln c_2}\right) D_{\text{eff},2} \nabla c_2 - (1 - t_+^0) \frac{\vec{I}_2}{F} + c_2 \vec{v}_0 \qquad \text{(Eq. VI-10)}$$

where $c_{2,0}$ is the solvent concentration, $\vec{v}_0$ is the solvent velocity, and $D_{\text{eff},2}$ represents the effective salt diffusion coefficient of the liquid phase in the macro-pore domain.

Similar to the effective conductivity, the effective diffusion coefficient can be calculated from the bulk diffusion coefficient D by:

$$D_{\text{eff},2} = \frac{\Psi_2}{\tau_{\text{e},2}} D \qquad \text{(Eq. VI-11)}$$

It is common in papers relying on Newman model that the convection term $c_2 \vec{v}_0$ in the anion flux expression is ignored, assuming that convection is negligible. Likewise, one generally assumes the term $\frac{d \ln c_{2,0}}{d \ln c_2}$ to be zero.

The flux density of the anion is zero at the current collector/PE boundary and at the Li foil surface, where all of the current is carried by ionic (Li^+) current:

$$\vec{N}_{2,-} \cdot \vec{n} = 0 \text{ at } x = 0 \text{ and } x = L_{\text{el}} + L_{\text{sep}} \qquad \text{(BC. VI-6) (BC. VI-7)}$$

The concentration and flux are continuous at the boundary between the separator and a porous electrode.

"Micro model"

The volume fraction of the sub-pore domain, Ψ_3 (m_3^3/m_{PE}^3) is expressed as:

$$\Psi_3 = \Psi - \Psi_2 = \xi_3 \Psi \qquad \text{(Eq. VI-12)}$$

where ξ_3 is the ratio of sub-pore domain among the total porosity of the PE, Ψ.

From Eq. VI-12, we can infer the volume fraction of the sub-pore domain at PA scale, ε_3 (m_3^3/m_{PA}^3), by:

$$\varepsilon_3 = \frac{\Psi_3}{\Psi_{PA}} \qquad \text{(Eq. VI-13)}$$

The mass transport in the electrolyte filling in the sub-pore domain is also described by concentrated solution theory. For the sake of simplicity, the mass balance for the anion is considered:

$$\varepsilon_3 \frac{\partial c_3}{\partial t} = -\nabla \cdot \vec{n}_{3,-} \qquad \text{(Eq. VI-14)}$$

where:

$$\vec{n}_{3,-} = -\left(1 - \frac{d \ln c_{3,0}}{d \ln c_3}\right) D_{\text{eff},3} \vec{\nabla} c_3 - (1 - t_+^0) \frac{\vec{\imath}_3}{F} \approx -D_{\text{eff},3} \vec{\nabla} c_3 - (1 - t_+^0) \frac{\vec{\imath}_3}{F} \qquad \text{(Eq. VI-15)}$$

where $D_{\text{eff},3} = \frac{\varepsilon_3}{\tau_{e,3}} D$ represents the effective diffusion coefficient of the liquid phase in the sub-pore domain. The electrode tortuosity factor of the sub-pores is $\tau_{e,3}$. $c_{3,0}$ is the solvent concentration. Similar to the macro-pore domain, the convection term $c_3 \vec{v}_0$ in the anion flux expression is also ignored and $\frac{d \ln c_{3,0}}{d \ln c_3}$ is assumed to be zero.

The flux density of anion is zero at the PA center by symmetry. At the PA surface, one has the continuity of the salt concentration between the sub-pore and macro-pore domain. As the result, we get:

$$\vec{n}_{3,-} \cdot \overrightarrow{r^*} = 0 \quad \text{at } r^* = 0 \qquad \text{(BC. VI-8)}$$

$$c_3 = c_2 \quad \text{at } r^* = R_{PA} \qquad \text{(BC. VI-9)}$$

Moreover, the continuity of the anion and cation fluxes at the PA surface holds:

$$\vec{n}_{3,-} \cdot \overrightarrow{r^*} = -D_{\text{eff},3} \frac{\partial c_3}{\partial r^*} - (1 - t_+^0) \frac{i_{3,r^*}}{F} = j_{3,-} \qquad \text{(Eq. VI-16)}$$

$$\vec{n}_{3,+} \cdot \overrightarrow{r^*} = -D_{\text{eff},3} \frac{\partial c_3}{\partial r^*} + t_+^0 \frac{i_{3,r^*}}{F} = j_{3,+} \qquad \text{(Eq. VI-17)}$$

These two extra equations are necessary to close the equation system (by solving for $j_{3,-}$ and $j_{3,+}$).

The current balance in electrolyte filling in the sub-pore domain reads:

$$\nabla \cdot \vec{i}_3 = a_{\text{AM}-3} F j_{\text{int},+} \quad \text{(Eq. VI-18)}$$

where $a_{\text{AM}-3}$ ($\text{m}^2_{\text{AM}-3}/\text{m}^3_{\text{PA}}$) the specific interfacial area between the AM and the liquid phase in the sub-pore domain and $j_{\text{int},+}$ the cation internal pore-wall flux. The internal pore-wall flux $j_{\text{int},+}$ corresponds to the rate of the electrochemical reaction for Li insertion/deinsertion, and is detailed in the following.

Since the particle surface is likely not fully exposed to the electrolyte in sub-pores due to the inter-connectivity between solid particles, we introduce a new variable, $f_{\text{AM}-3}$ representing the fraction of particle surface in contact with the electrolyte. Therefore, $a_{\text{AM}-3}$ is estimated using the following equation:

$$a_{\text{AM}-3} = \frac{3\varepsilon_{\text{AM}} f_{\text{AM}-3}}{r_{\text{P}}} \quad \text{(Eq. VI-19)}$$

where r_{P} is the radius of a NMC secondary particle.

The ionic current density in liquid phase $\vec{i}_3$ is expressed by means of Mac-Innes equation, according to:

$$\vec{i}_3 = -\kappa_{\text{eff},3} \nabla \Phi_3 + 2\kappa_{\text{eff},3} \frac{RT}{F} (1 - t_+^0) \alpha \nabla \ln c_3 \qquad \text{(Eq. VI-20)}$$

where $\kappa_{\text{eff},3} = \frac{\varepsilon_3}{\tau_{\text{e},3}} \kappa$ stands for the effective ionic conductivity of the electrolyte within the sub-pore domain.

Two boundary conditions are required for solving for Φ_3 by combining Eq. VI-18 and Eq. VI-20. The current density is equal to zero at the PA center by symmetry. At the PA surface, there is a continuity of the liquid phase potential between sub-pore and macro-pore domain.

$$\vec{i}_3 \cdot \overrightarrow{r^*} = 0 \quad \text{at } r^* = 0 \qquad \text{(BC. VI-10)}$$

$$\Phi_3 = \Phi_2 \text{ at } r^* = R_{\text{PA}} \qquad \text{(BC. VI-11)}$$

At the PA scale, an additional mass balance applied on inserted “neutral” Li in the AM phase is introduced, which considers the inter-particle solid diffusion through the AM/AM interface. It is an additional pathway for Li transport across the radial dimension of the PA, alongside with the

Li^+ transport across the sub-pores followed by electrochemical insertion in the AM. Based on the porous electrode theory applied to the PA scale, it reads:

$$\varepsilon_{\mathrm{AM}} \frac{d\bar{c}_{\mathrm{s}}}{dt} = -\nabla \cdot \vec{n}_{\mathrm{AM-AM}} - a_{\mathrm{AM-3}} j_{\mathrm{int,+}} \quad \text{(Eq. VI-21)}$$

With $\bar{c}_{\mathrm{s}}$ is the local volume-averaged solid Li concentration of AM phase within the PA; $\vec{n}_{\mathrm{AM-AM}} = -\frac{\varepsilon_{\mathrm{AM}}}{\tau_{\mathrm{AM}}} D_{\mathrm{s}} \vec{\nabla} \bar{c}_{\mathrm{s}}$ represents the Li flux diffusing between AM particles within the PA; τ_{AM} is the tortuosity factor of the AM phase.

At particle scale, the transport model is based on solid diffusion of "neutral" Li species, and reads:

$$\frac{dc_{\mathrm{s}}}{dt} = -\nabla \cdot \vec{n}_{\mathrm{s}} \quad \text{(Eq. VI-22)}$$

With $\vec{n}_{\mathrm{s}}$ the Li flux in the AM particle, which is zero at the particle center (by symmetry) and which is set equal to the total flux, j_{total} $(\mathrm{mol}/(\mathrm{m}^2_{\mathrm{AM}} \cdot \mathrm{s}))$ entering the particle at the surface.

$$\vec{n}_{\mathrm{s}} \cdot \vec{r} = 0 \quad \text{at } r = 0 \qquad \text{(BC. VI-12)}$$

$$\vec{n}_{\mathrm{s}} \cdot \vec{r} = j_{\mathrm{total}} \quad \text{at } r = r_{\mathrm{P}} \qquad \text{(BC. VI-13)}$$

The total flux entering the AM particle is set equal to the sum of the two contributions at the particle surface, which gives:

$$j_{\mathrm{total}} = f_{\mathrm{AM-3}} j_{\mathrm{int,+}} + (1 - f_{\mathrm{AM-3}}) j_{\mathrm{AM-AM}} \quad \text{(Eq. VI-23)}$$

where, $j_{\mathrm{AM-AM}}$ $(\mathrm{mol}/(\mathrm{m}^2_{\mathrm{AM-AM}} \cdot \mathrm{s}))$ is the rate of transfer of solid Li from the AM particle to another AM particle, and $(1 - f_{\mathrm{AM-3}})$ is the fraction of AM particle surface in contact with other AM particles (fraction covered with CBD is assumed to be negligible here).

To resolve the transport model at particle scale, the polynomial approximation is adopted, so that the particle dimension is dropped. The detail of the development of the polynomial approximation can be found in [30]. Here, only the three final equations are presented along with the three variables to be solved, namely $\bar{c}_{\mathrm{s}}$; the volume-averaged concentration flux $\bar{q}$; and the concentration at the surface of the AM particle, $c_{\mathrm{s,surf}}$.

$$\frac{d\bar{c}_{\mathrm{s}}}{dt} + 3\frac{j_{\mathrm{total}}}{r_{\mathrm{p}}} = 0 \qquad \text{(Eq. VI-24)}$$

$$\frac{d}{dt}\bar{q} + 30\frac{D_{\mathrm{s}}}{r_{\mathrm{p}}^2}\bar{q} + \frac{45}{2}\frac{j_{\mathrm{total}}}{r_{\mathrm{p}}^2} = 0 \qquad \text{(Eq. VI-25)}$$

$$35\frac{D_{\mathrm{s}}}{r_{\mathrm{p}}}\left[c_{\mathrm{s,surf}} - \bar{c}_{\mathrm{s}}\right] - 8D_{\mathrm{s}}\bar{q} = -j_{\mathrm{total}} \qquad \text{(Eq. VI-26)}$$

Notice that by combining Eq. VI-21 and Eq. VI-24, one gets:

$$\varepsilon_{\mathrm{AM}}(-3)\frac{j_{\mathrm{total}}}{r_{\mathrm{p}}} = -\nabla\cdot\vec{n}_{\mathrm{AM-AM}} - a_{\mathrm{AM-3}}j_{\mathrm{int,+}} \quad \text{(Eq. VI-27)}$$

Substitute $a_{\mathrm{AM-3}}$, $\vec{n}_{\mathrm{AM-AM}}$, and j_{total} gives:

$$\nabla\cdot\left(-\frac{\varepsilon_{\mathrm{AM}}}{\tau_{\mathrm{AM}}}D_{\mathrm{s}}\vec{\nabla}\bar{c}_{\mathrm{s}}\right) = \frac{3(1-f_{\mathrm{AM-3}})\varepsilon_{\mathrm{AM}}j_{\mathrm{AM-AM}}}{r_{\mathrm{p}}} \quad \text{(Eq. VI-28)}$$

where, $\frac{3(1-f_{\mathrm{AM-3}})\varepsilon_{\mathrm{AM}}}{r_{\mathrm{p}}}$ gives the specific interfacial area of AM in contact with other AM particles, so-called $a_{\mathrm{AM-AM}}$ ($\mathrm{m}^2_{\mathrm{AM-AM}}/\mathrm{m}^3_{\mathrm{PA}}$).

The two boundary conditions are required for solving Eq. VI-28. The Li^+ flux is equal to zero at the PA center by symmetry. At the PA surface, one makes the hypothesis of no charge transfer, hence the flux of lithium in the AM phase is zero

$$-\frac{\varepsilon_{\mathrm{AM}}}{\tau_{\mathrm{AM}}}D_{\mathrm{s}}\vec{\nabla}\bar{c}_{\mathrm{s}}\cdot\overrightarrow{r^*} = 0 \ \text{ at } r^* = R_{\mathrm{PA}} \quad \text{(BC. VI-14)}$$

$$-\frac{\varepsilon_{\mathrm{AM}}}{\tau_{\mathrm{AM}}}D_{\mathrm{s}}\vec{\nabla}\bar{c}_{\mathrm{s}}\cdot\overrightarrow{r^*} = 0 \ \text{ at } \ r^* = 0 \quad \text{(BC. VI-15)}$$

At $t = 0$, the volume-average concentration of Li in all the AM particles is taken as:

$$\bar{c}_{\mathrm{s}}(t=0) = 0.38 * c_{\mathrm{s,max}} \quad \text{(IC. VI-1)}$$

Reaction rate

The pore-wall flux $j_{\mathrm{int,+}}$ directly relates to the reaction rate occurring at the internal solid/liquid interface (*i.e.*, between the AM and sub-pore domain within the PA). Thus, an equation is needed to simulate the kinetics of the reaction, which depends on the local concentrations and phase-potential difference at the interface. Butler-Volmer kinetic equation is used to this end:

$$j_{\mathrm{int,+}} = i_{\mathrm{n}}^0\left\{\exp\left(\frac{(1-\beta)F}{RT}(\Phi_1-\Phi_3-U(c_{\mathrm{s,surf}}))\right) - \exp\left(-\frac{\beta F}{RT}(\Phi_1-\Phi_3-U(c_{\mathrm{s,surf}}))\right)\right\} \quad \text{(Eq. VI-29)}$$

where U represents the equilibrium potential of the AM that is a function of Li content; i_{n}^0 denotes the exchange current density.

For an insertion electrode involving the reaction $\mathrm{Li}\Theta \leftrightarrow \mathrm{Li}^+ + \Theta + \mathrm{e}^-$, where Θ represents the solid lattice, the exchange current density depends on the lithium concentration in the electrolyte c_3 that fills in the sub-pores , the lithium concentration in the solid lattice $c_{\mathrm{s,surf}}$ and the concentration of unoccupied sites in the lattice $c_{\mathrm{s,max}} - c_{\mathrm{s,surf}}$ according to:

$$i_{\mathrm{n}}^0 = Fk_0c_3^{1-\beta}(c_{\mathrm{s,max}} - c_{\mathrm{s,surf}})^{1-\beta}c_{\mathrm{s,surf}}^{\beta} \quad \text{(Eq. VI-30)}$$

where k_0 is the rate constant of the electrochemical reaction. The exchange current density tends to zero as the solid concentration approaches either 0 or $c_{\mathrm{s,max}}$.

Since the reaction-rate equation is algebraic, it requires no boundary condition.

Compared with the Newman P2D model, the PApa model has three additional parameters, representing the fraction of particle surface in contact with electrolyte in sub-pores ($f_{\mathrm{AM-3}}$), the PA radius (R_{PA}) and the volume fraction of the sub-pore domain (ξ_3).

Table VI-1. Summary of equations and boundary equations in PApa model.

Equations	Boundary Conditions
$\Psi_2 \frac{\partial c_2}{\partial t} = -\nabla \cdot \vec{N}_{2,-} + A_{\mathrm{PA}} j_{3,-}$	$\vec{N}_{2,-} \cdot \vec{n} = 0$ at $x = 0$ and $x = L_{\mathrm{el}} + L_{\mathrm{sep}}$
$\nabla \cdot \vec{I}_2 = A_{\mathrm{PA}} F (j_{3,+} - j_{3,-})$	$\vec{I}_2 \cdot \vec{n} = 0$ at $x = L_{\mathrm{el}} + L_{\mathrm{sep}}$ $\Phi_2 = 0$ at $x = L_{\mathrm{el}} + L_{\mathrm{sep}}$
$\nabla \cdot \vec{I}_1 = -A_{\mathrm{PA}} F (j_{3,+} - j_{3,-})$	$\vec{I}_1 \cdot \vec{n} = I_{\mathrm{app}}$ at $x = L_{\mathrm{el}} + L_{\mathrm{sep}}$ $\vec{I}_1 \cdot \vec{n} = 0$ at $x = L_{\mathrm{sep}}$
$\varepsilon_3 \frac{\partial c_3}{\partial t} = -\nabla \cdot \vec{n}_{3,-}$	$\vec{n}_{3,-} \cdot \overrightarrow{r^*} = 0$ at $r^* = 0$ $c_3 = c_2$ at $r^* = R_{\mathrm{PA}}$
$\nabla \cdot \vec{\imath}_3 = a_{\mathrm{AM-3}} F j_{\mathrm{int},+}$	$\vec{\imath}_3 \cdot \overrightarrow{r^*} = 0$ at $r^* = 0$ $\Phi_3 = \Phi_2$ at $r^* = R_{\mathrm{PA}}$
$\frac{d\bar{c}_{\mathrm{s}}}{dt} + 3\frac{j_{\mathrm{total}}}{r_{\mathrm{p}}} = 0$	
$\frac{d}{dt}\bar{q} + 30\frac{D_{\mathrm{s}}}{r_{\mathrm{p}}^2}\bar{q} + \frac{45}{2}\frac{j_{\mathrm{total}}}{r_{\mathrm{p}}^2} = 0$	

$35\frac{D_s}{r_p}\left[c_{s,surf}-\bar{c}_s\right]-8D_s\bar{q}=-j_{total}$	
$\nabla\cdot\left(-\frac{\varepsilon_{AM}}{\tau_{AM}}D_s\vec{\nabla}\bar{c}_s\right)=\frac{3(1-f_{AM-3})\varepsilon_{AM}j_{AM-AM}}{r_p}$	$-\frac{\varepsilon_{AM}}{\tau_{AM}}D_s\vec{\nabla}\bar{c}_s\cdot\overrightarrow{r^*}=0$ at $r^*=R_{PA}$ $-\frac{\varepsilon_{AM}}{\tau_{AM}}D_s\vec{\nabla}\bar{c}_s\cdot\overrightarrow{r^*}=0$ at $r^*=0$

VI.3 Experimental

NMC electrode preparation — Four different industry-grade positive electrodes are investigated in this work and labelled as MX-01, MX-02, MX-01b, and MX-02b. Each electrode is a mixture of $LiNi_{0.5}Mn_{0.3}Co_{0.2}O_2$ (NMC532) as AM, conductive carbon black and a mixture of polyvinylidene fluoride (PVdF) with a co-binder as additives with various compositions and loadings. They are all calendered to reach the targeted high density value. Their specifications from supplier's datasheet are shown in Table VI-2.

Table VI-2. Theoretical composition, porosity, thickness (without Al current collector), AM loading and density of NMC electrodes used in this work.

Sample	Content %w NMC/CB/Binder %v NMC/CB/ Binder	Porosity (Ψ) m^3_{2+3}/m^3_{PE}	Thickness µm	AM loading mg/cm²	Density g/cm³
MX-01	96.0/2.2/1.8 90.0/5.0/5.0	0.212	74.4	25	3.5
MX-02	96.0/2.2/1.8 90.0/5.0/5.0	0.280	48.8	15	3.2
MX-01b	94.2/3.2/2.6 86.0/7.0/7.0	0.191	74.4	25	3.5
MX-02b	94.2/3.2/2.6 86.0/7.0/7.0	0.191	44.6	15	3.5

Particle size distribution. — The particle size distribution (PaSD) of the raw NMC532 particles is determined with the laser diffraction method. PaSD is obtained from the angular variation in the intensity of light scattered as a laser beam passes through a dispersed particulate sample. Large particles scatter light at small angles relative to the laser beam and small particles scatter light at large angles. The angular scattering intensity data is then analyzed to calculate the size of the particles responsible for creating the scattering pattern, using the Mie theory of light scattering. As for output, laser diffraction will give a volume-weighted distribution of particle diameter, which is calculated with the volume-equivalent sphere diameter.

Thin Electrode fabrication. — The mixture of AM and carbon black is first pre-mixed for 12 hours before adding binder dispersed in NMP using a Polytron PT10-35 homogenizer. The slurry is cast on an 18 μm thick battery-grade aluminum foil. After being dried overnight in the dry room at room temperature, only uniform regions of the electrode are calendared using a rolling mill and their thickness is measured to an accuracy of 1 μm with the digital Palmer. The measured thicknesses are *ca.* 7 to 12 μm, ranging from two to four layers of NMC particles on the current collector (Figure VI-7).

Coin cell fabrication. — The electrodes are punched from the laminates to 1.3 cm diameter disks. The weight and thickness are measured for each electrode, so that electrode porosity and specific capacity is calculated for each coin cell. The electrodes are dried completely under vacuum at 120°C for 8-10 hours before coin-cell assembling. The coin cells are assembled inside an argon-filled glove box in standard 2032 coin cell hardware. A lithium metal disk with a diameter of 1.75 cm is used as the counter electrode. The counter electrode is pressed on a 0.5 mm stainless steel spacer. A Celgard 2500 monolayer polypropylene separator of 1.6 cm is placed on top of the Li foil. 100 μL of different electrolytes are then added to soak the separators. Three electrolytes are used in this work to unveil different limitations sources, as discussed later in the text. The LP30 1 M refers to the 1 mol/L solution of lithium hexafluorophosphate ($LiPF_6$) in ethylene carbonate (EC)/dimethyl carbonate (DMC) (1:1 w). The LP40 1 M refers to the 1 mol/L solution of lithium hexafluorophosphate ($LiPF_6$) in EC/diethyl carbonate (DEC) (1:1 w). Finally, the same mixture is used but with a lower concentration (0.5 M), hereafter referred to as "LP40" 0.5 M. Lastly, the cathode is placed on top of the separator. The cell is then crimped closed with a hydraulic crimping machine.

Electrochemical measurements. — All measurements are carried out in a controlled temperature chamber at 25°C. The cycling tests are performed with a multipotentiostat (Bio-logic, France). The potential window for the NMC materials in this work is between 2.5 and 4.3 V vs Li/Li^+.

All coin cells first undergo a formation process in which they are cycled five times with constant-current (CC) discharge/charge cycles at C/10 to form a stable passive layer at particle surfaces as well as for Li foil to further cycle on already cycled Li. A CV is held at the end of the discharge of the fifth cycle until the current gets down to C/50. This extra step before further charging is to ensure that the electrode discharge is complete (close to pristine state). Finally, a CCCV charge followed by a CC discharge is carried out, both at C/25, for capacity determination. The available capacity is determined at the end of the CC discharge.

The rate-capability experiments are conducted on two separate coin cells using the same electrode to ensure repeatable results. Upon both charge and discharge, a CCCV protocol is used, where the cells are cycled with different currents (C/25, C/10, C/5, C/2, 1C, 2C, and 3C). During the CV steps, the cell potential is held constant at both cutoff voltages until the current gets down to C/50. Between each change of current, cell is idled during 1 h to allow for some relaxation.

For the potentiostatic intermittent titration technique (PITT), the cell potential is stepped by 10 mV increments from 2.5 and 4.3 V and vice-versa. Each individual titration (at a potential step) is held until the current decreases to C/200 (in magnitude).

For the tortuosity determination, the symmetric cell method is used, which is reported by Landesfeind *et al.*[37] and Malifarge *et al.*[38]. The coin cells are assembled with identical cathodes at both sides of a separator, filled with a blocking electrolyte (10 mM of $TBAClO_4$ in EC:DMC (1:1 w) solvent). Two stainless-steel spacers of 1 mm instead of 0.5 mm are used to compensate for the lower thickness of the cathode compared to a Li foil, so that an appropriate pressure inside the cell is ensured. The impedance spectroscopy of the cells is measured using MTZ frequency analyzer from Bio-logic. The measurements are carried out at two different temperatures (25°C and 10°C). The change in temperature changes the ratio between the effective ionic and electronic conductivity of the liquid and solid phase respectively; as the ionic conductivity is more temperature-dependence than the electronic conductivity. It is a simple way to assess whether the electronic conductivity can be safely ignored from the determination of the electrode tortuosity factor. If the electrode tortuosity factor value is consistent at both temperatures, no electronic conductivity measurement is needed to analyze data from the symmetric cell. In addition, the experiments are conducted on two separate coin cells using the same electrode to ensure the results are reproducible.

For electronic conductivity determination, Electrochemical Impedance Spectroscopy (EIS) is performed using a 4-line configuration. This configuration ensures that measured conductivities are independent of the contact resistances between the probes and the sample, which are known to vary depending on the applied pressure of the probes onto the sample. The temperature is set to vary within a range [-20°C, 60°C], allowing to extract an activation energy for the electronic conductivity. The measurements are carried out using an ITS system and a MTZ (Bio-logic, France).

Besides, to access the local electronic conductivity, a direct current measurement is performed using the µ4-probe method.[39–41] When the 4 probes are aligned, the voltage drop ΔV between the two inner contacts is measured, while a current I is injected through the two outer contacts, so that the ratio $\frac{\Delta V}{I}$ is a measure of the sample resistance R. The 4 probes are fixed on µ-manipulators allowing independent movement of each probe. As a result, the distance between probes can be varied, then the measured scale also changes. Depending on the probing distance, the effective resistivity of the PE can be determined through equations in Table 1 in [37].

VI.4 Results & Discussion:

VI.4.1 Parametrization results

Electrolyte properties as a function of Li concentration are reported by Lundgren *et al.*[42] and Landesfeind *et al.*[43]. It is worth mentioning that in order to improve model prediction, we have

extrapolated the LP40 properties from [0.5–1.5] mol/L to [0–3] mol/L, just like it was done by Malifarge *et al.*[14]. For the LP30, the experimental data was already reported over the range [0-3] mol/L. Both electrolytes' properties are presented in Figure VI-3.

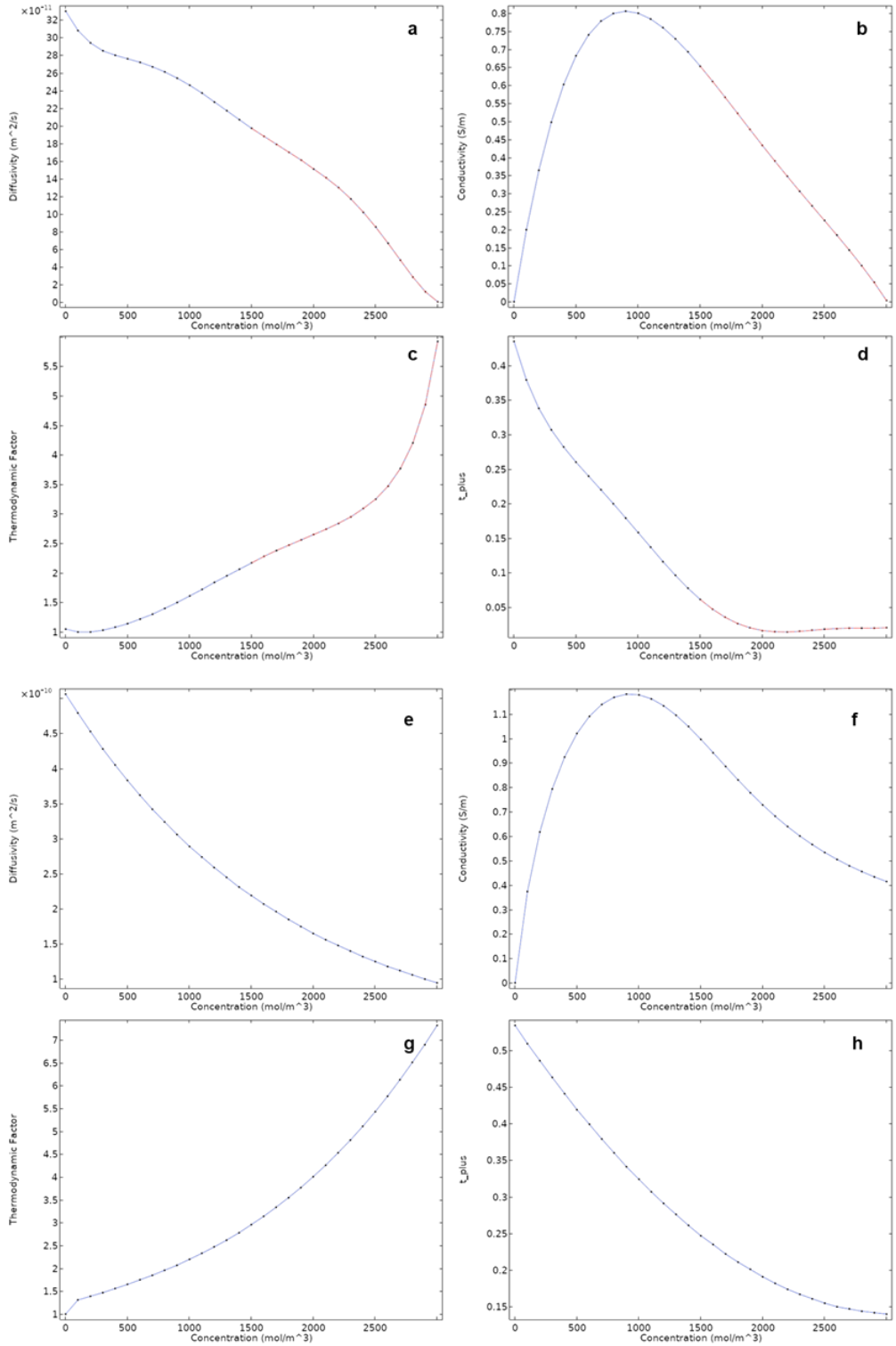

Figure VI-3. Summary of the electrolyte properties. a, b, c, d. for LP40 ($LiPF_6$ in EC:DEC (1:1wt)); the extrapolated data is colored in red. **e, f, g, h.** for LP30 ($LiPF_6$ in EC:DMC (1:1wt)).

Values for the separator thickness and porosity are taken from the Celgard datasheet. Its tortuosity factor is determined by measuring the effective electrolyte conductivity by EIS (more details in Figure VI-4).

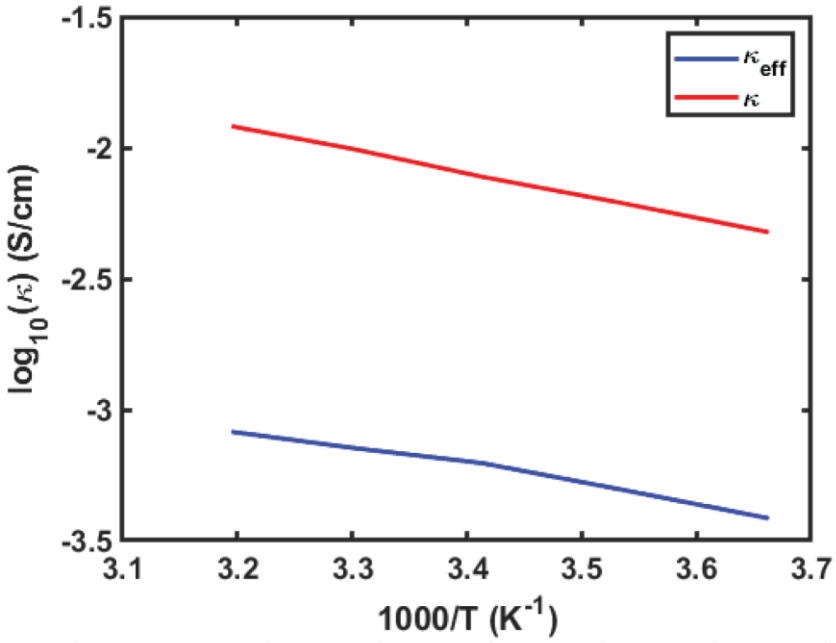

Temperature (°C)	0	10	20	30	40
Porosity	0.55	0.55	0.55	0.55	0.55
Tortuosity factor	6.8	6.83	6.81	7.61	8.07

Figure VI-4. The electrolyte bulk and effective ionic conductivity are presented. The tortuosity factor can be calculated.

The reaction-rate constant at the lithium foil was measured by Mastali *et al.*[44]. It is determined from data analysis of a lithium symmetric cell cycled at various current densities. Similar experiments carried out in house yielded a similar value at 25°C (not shown here).

Regarding the PE, a multi-modal approach combined with model analysis is required for complete characterization: transport properties (electronic/ ionic conductivity), AM intrinsic properties (solid diffusion coefficient, reaction-rate constant). For AM, the variation of the solid diffusion coefficient with Li concentration is significant, especially as to the material gets close to a full lithiation state.[45,46] Thus, a variable diffusion coefficient is considered in this work for higher simulation accuracy. This is also applied to the reaction-rate constant.[47]

Despite the authors' effort to build the model from the root, solid diffusion coefficient still needs to be taken from the work of Wu *et al.*[45], after it is slightly adjusted to validate the rate capability of the thin electrode. This will be discussed later in the paper.

The common parameters for the models in this work are summarized in Table VI-3.

Table VI-3. Common parameters for the models used in this work (a: assumed, m: measured, *: calculated)

Parameters	Values
$LiNi_{0.5}Mn_{0.3}Co_{0.2}O_2$	
Theoretical Capacity, Q_{th}	277 Ah/kg*
Density, ρ_{el}	4740 kg/m^{3*}
Initial stoichiometry, x_0	0.38[m]
Particle diameter, d_{50}	4.7 µm[m]
Charge transfer coefficient, β	0.5[a]
Li foil	
Li metal reaction rate, k_{Li}^{0}	6.6410^{-6} mol/[m^2 · s · (mol/m^3)$^{0.5}$][44]
Separator	
Porosity, $\varepsilon_{\mathrm{sep}}$	0.55[48]
Tortuosity factor, τ_{sep}	6.8[m]
Thickness, L_{sep}	25 µm[48]
Electrolyte	
$LiPF_6$ in EC:DEC (1:1 w)	Lundgren (2014)[42]
$LiPF_6$ in EC:DMC (1:1 w)	Landesfeind (2019)[43]

VI.4.1.1 Particle size distribution:

PaSD of AM measured by laser diffraction is presented as black line in Figure VI-5, which possess a d_{50} of 4.7 µm. The PaSD is divided into multiple intervals or bins (in this case, 12). The full PaSD (12 bins), as well as a binned PaSD (reduced to 5 bins) are used for simulations, and both show no substantial differences from simulation with one-particle size using the d_{50} value (Figure VI-6). As a result, for the simulation convenience (duration and convergence), one-particle size instead of multiple particle sizes is used for simulations.

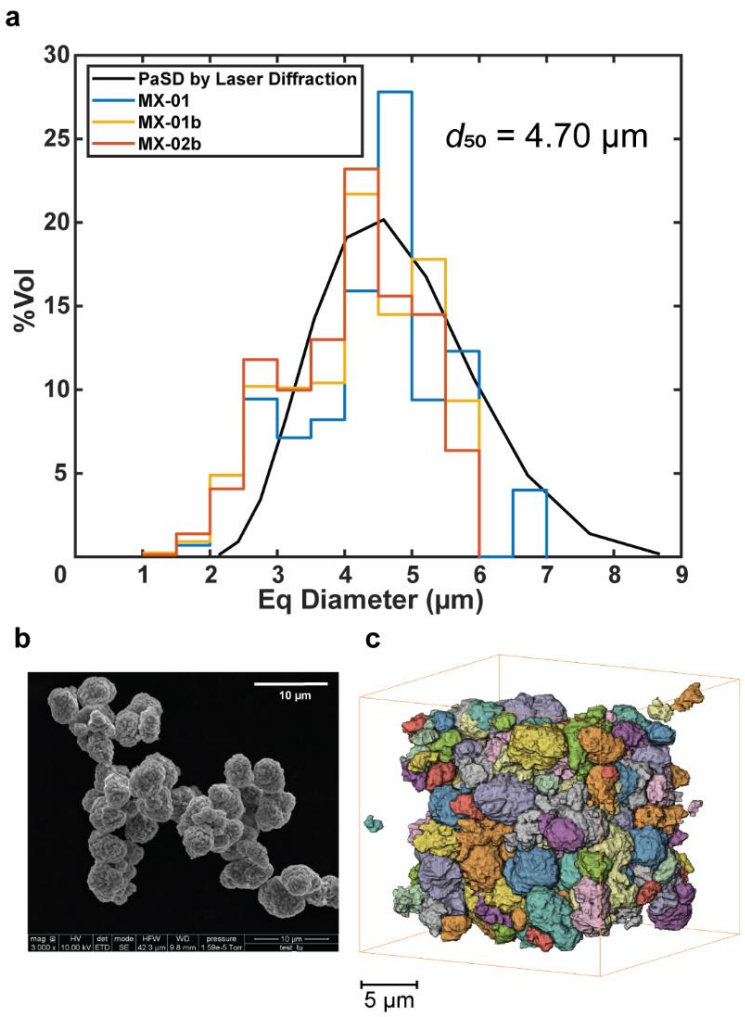

Figure VI-5. Morphology of the AM phase. **a.** PaSD of the NMC used as AM characterized by Laser diffraction and X-ray Holotomography. **b.** SEM photo of NMC powder. **c.** The NMC in an electrode captured by X-ray Holotomography is separated into individual particles that allow the statistical analysis of the microstructural properties by particles.

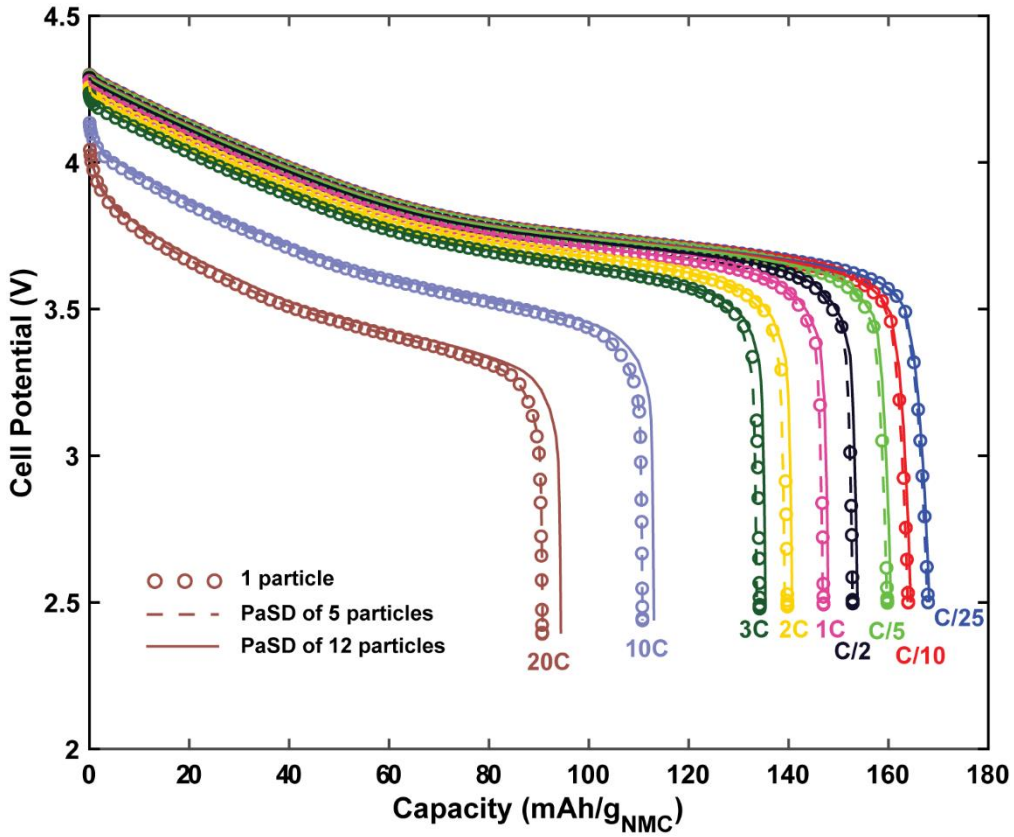

Figure VI-6. Rate capability simulated by DUM*BAT* using Newman P2D model with different number of particle sizes.

Besides, the PaSD using tomographic data of MX-01, MX-01b and MX-02b from our previous work[7] are also presented in Figure VI-5a, showing a good agreement with the laser diffraction experiment. The largest population of particles from three tomographic data correspond to the d_{50} from measurement, despite a slightly larger population of particles having a diameter less than 3 µm. Here, this can be due to the calendering process, which is known to cause fractures of AM particles under high mechanical pressure resulting in smaller particles. The cracked AM particles can be clearly observed from the tomographic data.[7]

It is worth noting that the particle size is calculated after separating the NMC continuum phase into individual particles. The analysis discards the possible agglomeration of particles, hence it does not contradict with the model based on particle agglomeration that is discussed in this work.

VI.4.1.2 Porous effects on thin electrodes

As mentioned above, thin electrodes are made in our laboratory using the same AM powder used in the industry-grade electrodes under investigation. Thin electrodes are well-suited to the determination of intrinsic properties of AM, because the porous-electrode effects are alleviated, thereby increasing the sensitivity to solid diffusion and charge transfer.

The minor effects of porous-electrode limitations are experimentally assessed by comparing

the rate capabilities of two thin electrodes with different compositions and porosity and that are filled with a different electrolyte (LP30 1 M or LP40 1 M). The geometric characteristics of the two electrodes are shown in the Table VI-4. Figure VI-7 shows a good agreement between the rate capabilities of the two electrodes, which confirms that porous-electrode effects are almost negligible. The thin electrodes are, therefore, appropriate for the determination of AM intrinsic properties, namely the reaction rate constant and the solid-diffusion coefficient.

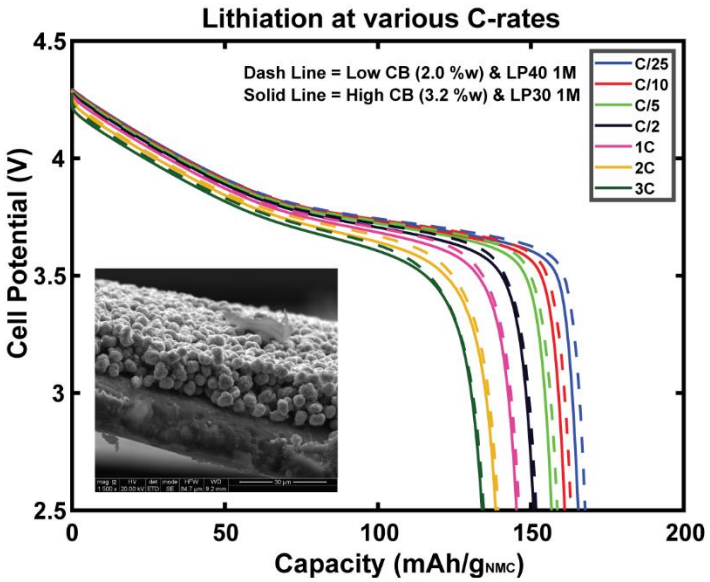

Figure VI-7. Rate capabilities of two thin electrodes. Both are made with different compositions (%w AM/CB/PVdF: 96/2/2 vs 94/3.2/2.8) and filled with different electrolytes (LP40 1 M vs LP30), respectively.

VI.4.1.3 Solid diffusion coefficient & Reaction rate constant

The NMC used in this work are intercalation compounds, the performance of which depends on the kinetics of charge transfer and the solid Li diffusion. These two processes are described in Newman-type models by two parameters, namely the reaction-rate constant k_0 and the solid diffusion coefficient D_s. Numerous experimental methods were developed to determine them, *e.g.*, PITT,[49–54] galvanostatic intermittent titration technique (GITT),[55,56] cyclic voltammetry (CV),[57] and electrochemical impedance spectroscopy (EIS).[58,59]

Here, the PITT is employed because it is well suited for a fine screening of composition ranges in which the AM experiences a steep change in equilibrium potential with composition. For NMC, it is the region close to the full lithiation state that is known to experience the largest variation of the diffusivity.

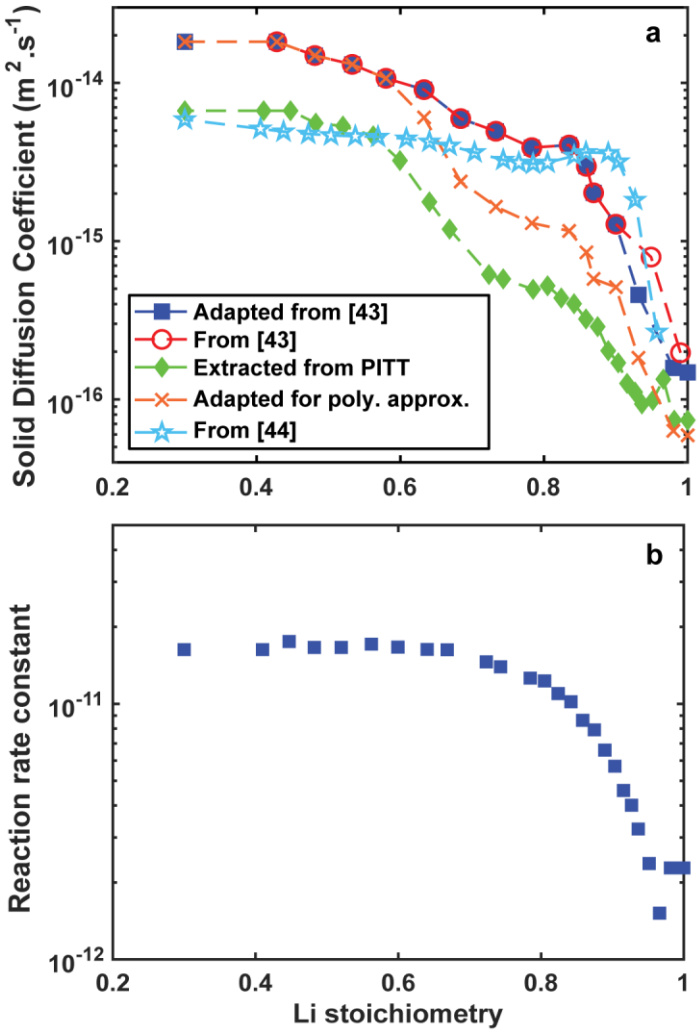

Figure VI-8. Intrinsic properties of the NMC used in this work. a. The solid-diffusion coefficient extracted from PITT experiment along with four others: the original values from Wu *et al.*[45] and Verma *et al.*[46], two set of adjusted values to fit the rate capability of thin electrode from this work using either the Newman model or the "baseline" model. **b.** The reaction rate constant extracted from PITT measurement.

In Figure VI-8, the two parameters are determined from the PITT experiment on thin electrodes by combining with Newman model analysis, as used in many works.[45,54,60] They are estimated by matching the simulated and experimental current response during potential steps at different lithiation states using a least-square regression method.

Nonetheless, as discussed later, the solid-diffusion coefficient determined in this work does not provide a good agreement between the simulated and experimental rate capability of the thin electrode, despite decent fits of the current response during potential steps in PITT (see Figure VI-9). Instead, we relied on the solid diffusion coefficient obtained from Figure 6 in [43] with slight adjustments so as to approach the experimental rate capability better. For comparison, D_s reported by Wu *et al.*[45] for NMC111, and by Verma *et al.*[46] for NMC532, along with the D_s extracted from PITT in this work and the "adjusted" D_s used for the Newman and the "baseline" models are

all presented in Figure VI-8a.

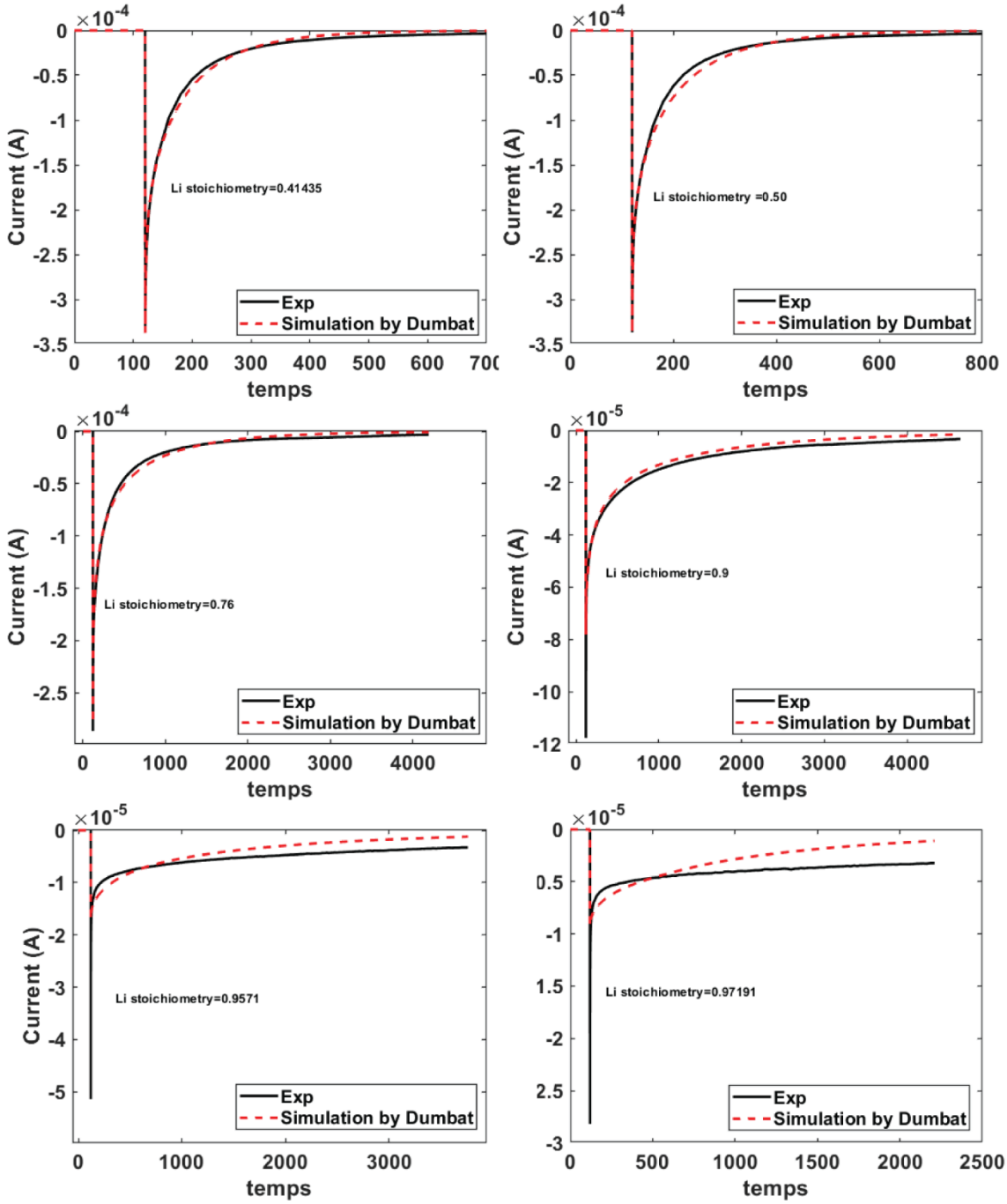

Figure VI-9. Current responses during the potential step in PITT experiment along with the simulated responses given by Newman P2D model using DUMBAT.

VI.4.1.4 Equilibrium potential

At the end of each potential step during the PITT experiments, the lithiation state within the NMC particles reaches quasi-equilibrium, as the current is lower than C/200. At that time, the cell potential is considered at equilibrium. Upon charge and discharge, two different equilibrium

potential curves due to a residual hysteresis are obtained. Thus, the final equilibrium potential is taken as the average of the two curves.

On the other hand, we also consider a low-rate discharge (C/50) to get the full lithiation state started from the initial stoichiometry $x_0 = 0.38$ (*i.e.*, $Li_{0.38}Ni_{0.5}Mn_{0.3}Co_{0.2}O_2$). This low-current potential profile, whenever used directly as input for the equilibrium potential, is more correctly labelled as a pseudo-equilibrium potential because the system is never at equilibrium.

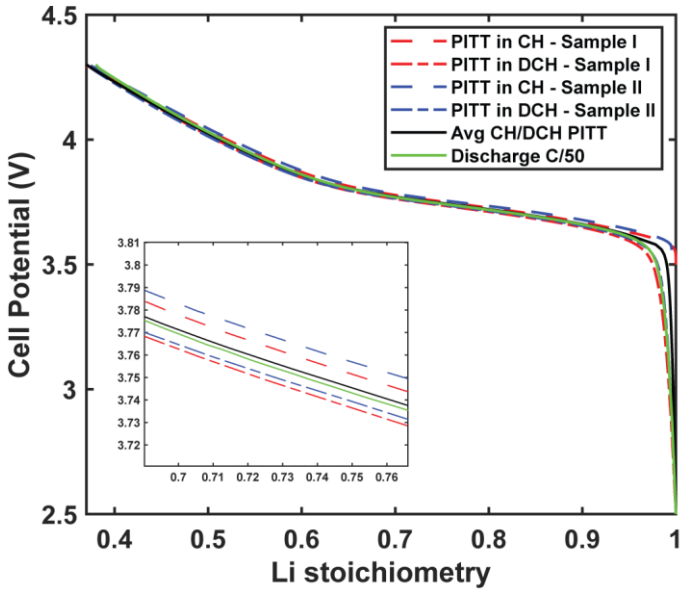

Figure VI-10. Equilibrium potential of the NMC used in this work. Different potential curves during the charge and discharge process extracted from PITT experiment along with the discharge curve at C/50 are presented for comparison.

Figure VI-10 compares the average equilibrium potential obtained from the PITT upon charge and discharge with the pseudo-equilibrium potential from the low-rate discharge at C/50. The discrepancy in terms of polarization between these two curves is minor. In other words, during a discharge at C/50, the system is very close to its thermodynamic stability. While the equilibrium potential averaged from PITT shows an abrupt drop toward the cut-off voltage at the EoD, referred to as the "kink" region, the PITT in discharge and the discharge curve at C/50 represent a more gradual potential decline at the EoD. Therefore, as we focus on the discharge behavior of the electrodes, the discharge curve at C/50 is rather considered hereafter as the equilibrium potential to better capture this behavior.

VI.4.1.5 Electrode Tortuosity factor

The electrode tortuosity factors are measured with the symmetric cell method,[37,38] which has been demonstrated through experimental[61,62] as well as a numerical approaches[63] to be appropriate for the determination of tortuosity applied to porous electrodes.

Figure VI-11 shows the electrode tortuosity factor determined from the symmetric-cell method

for the four industry-grade electrodes studied in this work. The results suggest negative effects of the CBD on the electrode in terms of tortuosity, as MX-01b and MX-02b both yield higher electrode tortuosity factor values than MX-01, despite having similar porosities.

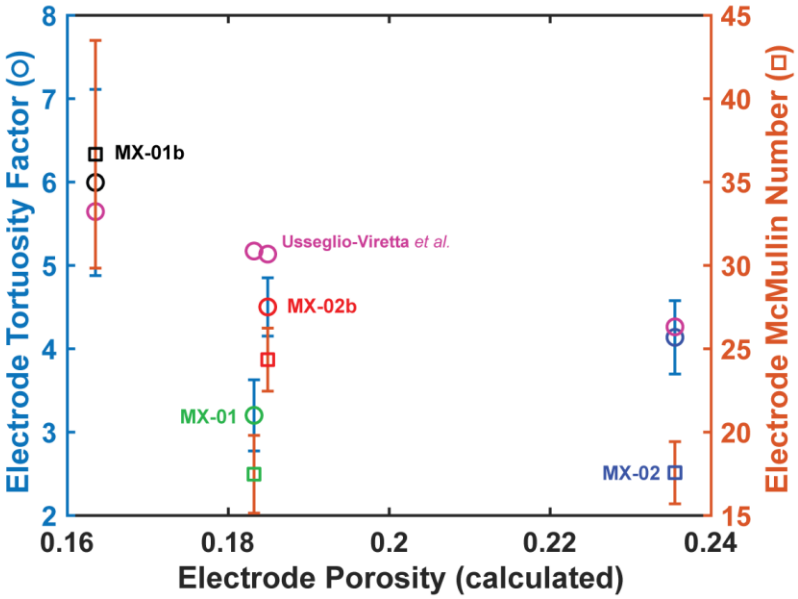

Figure VI-11. Electrode tortuosity factor and McMullin number. The electrode tortuosity factors of the 4 electrodes measured by the symmetric cell method are presented along with the McMullin number calculated for each electrode.

Notably, the results are in good agreement with the values calculated from the power-law reported by Usseglio-Viretta *et al.*[62] based on a fit of measured values using the same method for electrodes having similar NMC532 materials. Given that the porosity can slightly deviate (±3%) from theoretical value due to a non-optimized manufacturing process, the McMullin number for each electrode is also calculated (*i.e.*, it corresponds to an electrode tortuosity "normalized" by its porosity).

Furthermore, Malifarge *et al.*[38] measured the electrode tortuosity factors of different graphite electrodes using a similar method (except for the use of a conventional LP40 electrolyte instead of a blocking salt) and found really good agreement between simulated and experimental rate capability of the electrodes. For graphite electrodes with similar porosity, they found that the electrode tortuosity factors range from 7 to 10. Since the graphite particles have flake-like geometry, electrodes having graphite as AM are expected to be more tortuous than those with more spherical particles such as NMC. Therefore, the electrode tortuosity-factor values shown in Figure VI-11 seem to be reasonable for industry-grade electrodes in this work.

Moreover, the simulations by *TauFactor*[63,64] using the tomographic data also give the values within the experimental ranges for MX-01b and MX-02, as shown in Figure VI-12. The EIS responses of the four electrodes, along with the fit for tortuosity factor determination are shown in

Figure VI-13.

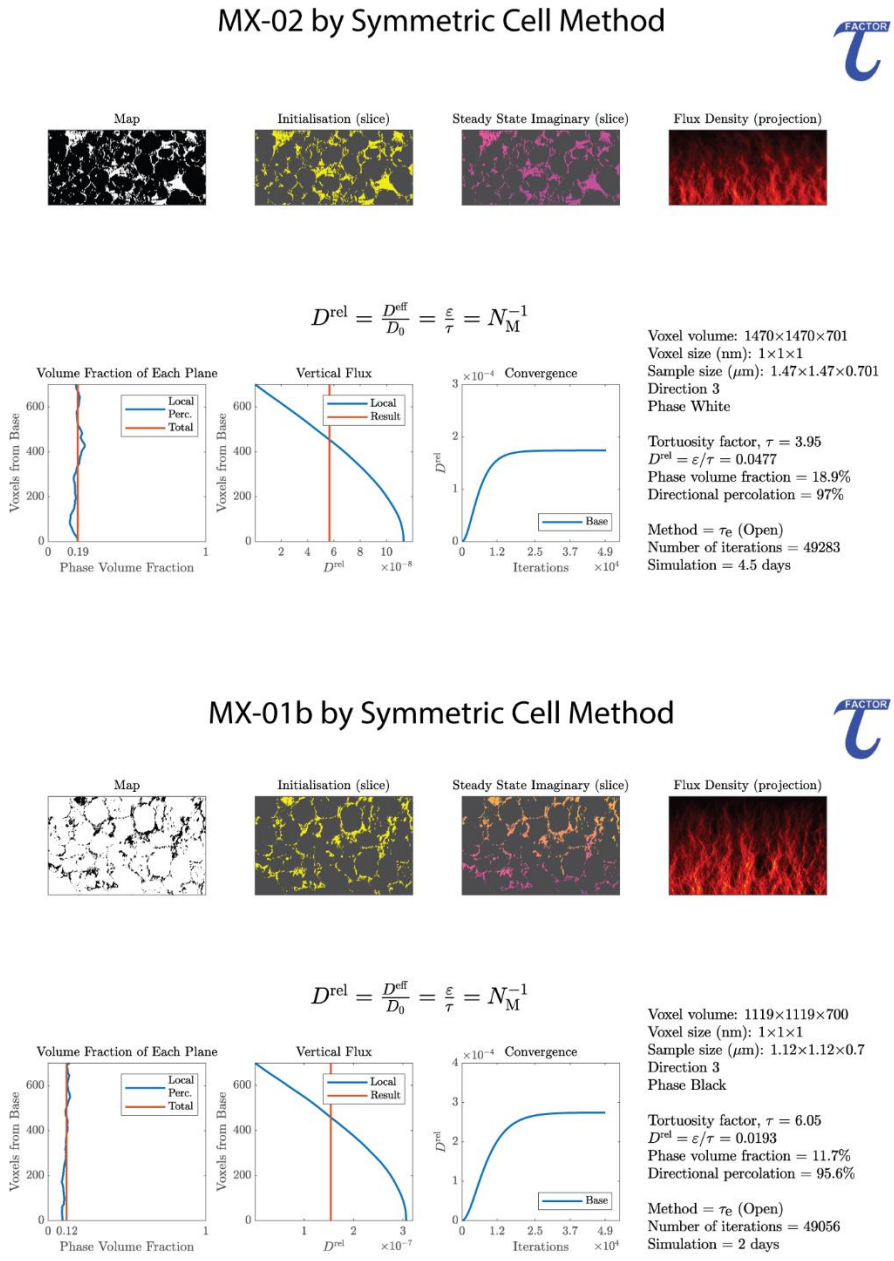

Figure VI-12. The electrode tortuosity factors are calculated by *TauFactor*[1,2] using X-ray tomographic data. a. MX-02. **b.** MX-01b.

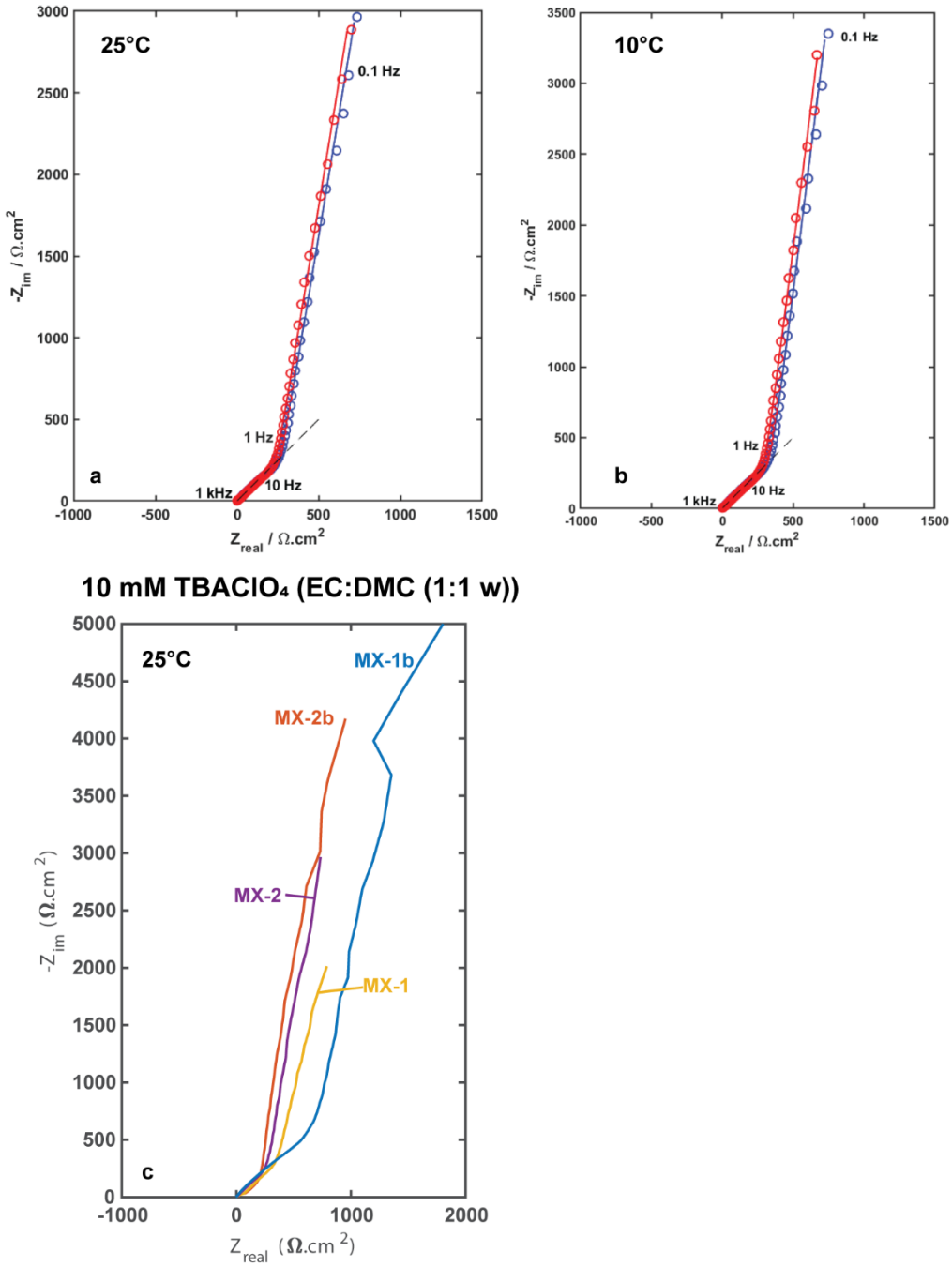

Figure VI-13. EIS response of symmetric cell measurements for tortuosity determination. a, b. MX-02b in 10mM of $TBAClO_4$ at different temperatures (25°C, 10°C) along with the fit proposed by Landesfeind *et al.*[37]. **c.** Summarize of EIS responses of the industry-grade electrodes used in this work.

VI.4.1.6 Electronic conductivity

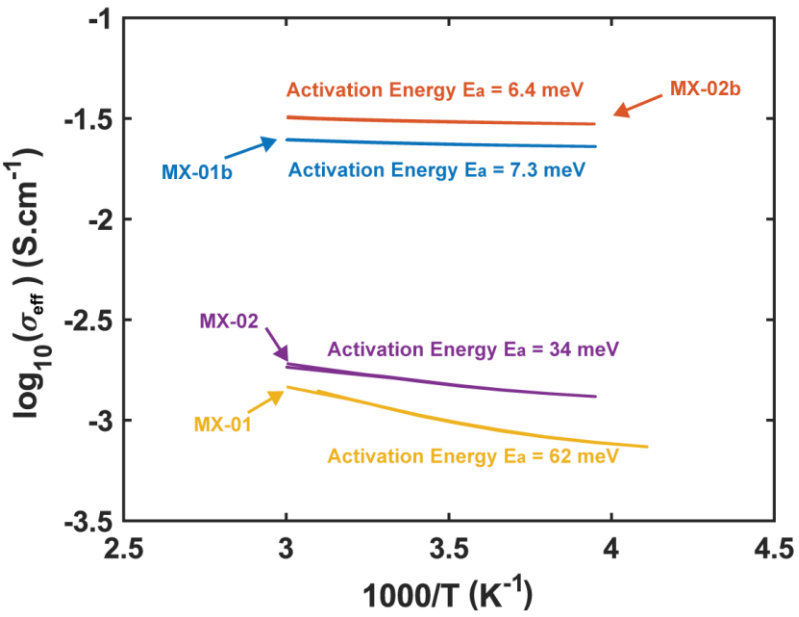

Figure VI-14. Electronic conductivities of the 4 industry-grade electrodes measured by the 4-line method as a function of the temperature.

For the electronic conductivity measurements, the 4-line method[65] is used instead of the 2-point method that highly depends on the compression pressure by the two probes, which cannot be controlled with our equipment. The effective conductivity in function of the temperature along with the activation energy for four electrodes is shown in Figure VI-14. The sensitivity of the conductivity measured by the 2-point method as a function of the compression pressure is shown in Figure VI-15.

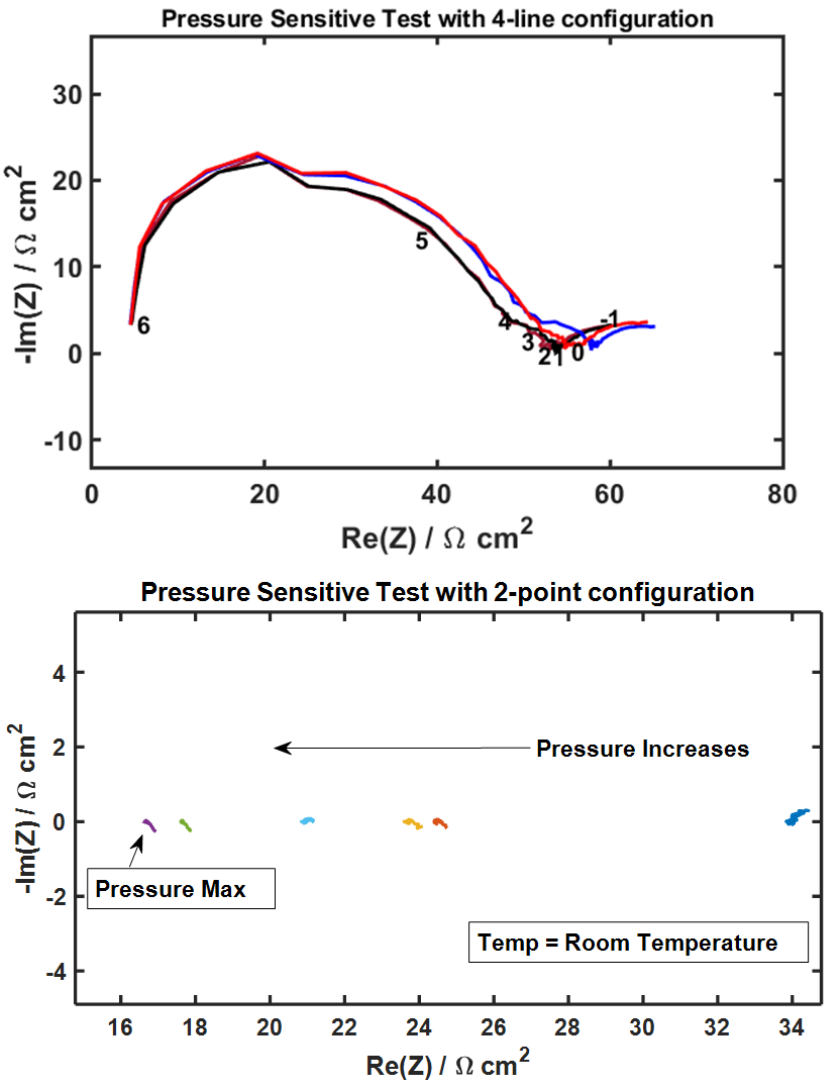

Figure VI-15. Pressure sensitivity investigation of 2-point & 4-line electronic conductivity measurement.

Besides, a µ-4probe method is also employed that allows probing the electronic conductivity at various scales, as the probing distance can be adjusted using µ-manipulators. This study enables the mapping of the electronic conductivity at different locations throughout the electrode surface. A correlation between the local electronic conductivity and the electrode microstructure, measured at identical locations, is a scope of future work. Several measurements were performed at different locations (without overlapping) to assess the microstructure heterogeneities, at each probing distance. The average/min/max σ_{eff} along with the 95% confidence intervals are presented in Figure VI-16. As expected, a higher dispersion, *i.e.* larger error bar, of σ_{eff} is observed, as we go to a lower scale, as it gets more sensitive to local microstructure. All values measured at the macro scale lie within the confidence intervals of the conductivity measured with the µ-4probe method at the lowest scale.

A higher amount of carbon additives (1%w) shows a big improvement (~x10) on the electronic conductivity of the electrode across multi-length scales. The effective electronic conductivities of the porous electrodes lie between the bulk values of the carbon binder mixture (250-300 S/m)[66] and the NMC materials at a pristine state (0.00136 S/m).[26,67] In a multi-phase porous structure, there might be a mix of transport properties, so that the carbon additives and the NMC materials both contribute to the electronic transport throughout the electrodes. Given that the NMC electronic conductivity varies with the Li concentration, the electronic conductivity of the porous electrode may vary as a function of the SoC. Nevertheless, we notice here that the electronic conductivity is not a dominant limitation of these electrodes as the higher CBD possess a lower electrochemical performance, as shown later. Therefore, throughout our work, it is assumed that the electronic conductivities of the electrodes during operation can be represented by the values measured at a pristine state.

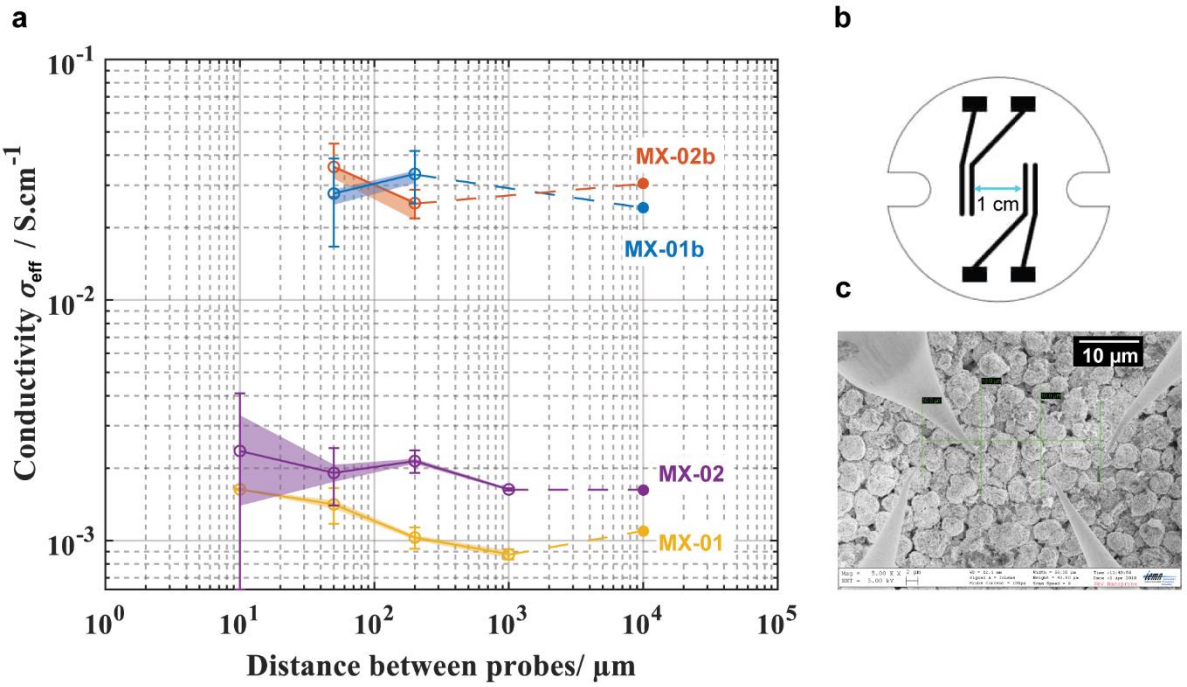

Figure VI-16. Multi-scale electronic conductivity. a. The electronic conductivities of the 4 electrodes measured by two methods (4-line and µ4-probe) at different length scales are presented. **b.** Schematics of the electrode used in the 4-line method from Bio-logic, in which the 4 probes are made by gold deposit on a plastic substrate. **c.** SEM photo of the 4 µ-probes made by tungsten in µ4-probe method.

VI.4.2 Model Validation against experimental results

In this section, the Newman model is first used to validate the AM properties: reaction rate constant (k_0) and solid diffusion coefficient (D_s), in the framework of the thin electrodes. Then, a model-based analysis of the rate capability of the four different industry-grade electrode designs with respect to their experimental results is detailed.

Simulations for which local salt concentration reaches 3 mol/L anywhere across the cell sandwich are interrupted. In this situation, simulated values of the cell overpotential may still serve for comparison with experiments, whereas values of the delivered capacity are irrelevant and discarded.

Besides, the reported electrolyte diffusion coefficients, for both LP40 and LP30, are a strong function of salt concentration and decrease by nearly one order of magnitude with every 1 M of increasing concentration. In model calculations, the small diffusion coefficient at high concentration results in a large potential drop near the lithium anode, which in turns lowers the potentials throughout the separator and electrode. Therefore, at high current density, the simulated discharge potential curve might show a fast drop and a much smaller EoD capacity than that observed in the experiments.

For some simulations, the cut-off voltage is set to 3.0 V to avoid convergence issues, as it causes only a minor difference on discharge capacity if it is set to 2.5 V instead.

VI.4.2.1 Validation on thin electrodes

Regarding the thin electrode characterization, its effective electronic conductivity cannot be measured properly with the 4-line method as for higher loading electrodes, since the aluminum foil cannot be removed without breaking the electrode due to its low loading. Also, the symmetric cell method is conducted first, so as to determine the electrode tortuosity factor. However, the EIS response does not agree well with theoretical expectations; a large semi-circle appears in the intermediate frequency range instead of a straight line with slope of *ca.* 45°.

Fortunately, as demonstrated above, porous electrode effects in the thin electrode are negligible. As a result, it is assumed that the thin electrode tortuosity factor follows Bruggeman's correlation, even though it is known to poorly predict electrode tortuosity factor for the other electrodes studied here. Also, the effective electronic conductivity of the thin electrode is set to a high value, so that there is no ohmic drop across the electrode thickness. Table VI-4 shows the set of parameters used for the Newman model of the thin electrodes.

Table VI-4. List of model parameters used for half-cell simulations at 25°C of rate capability of the thin electrode. a: assumed value, m: measured value, *: calculated from design.

Parameters	**Values**	
Electrode	**3.2 %w CB**	**2 %w CB**
Thickness, $\boldsymbol{L_{el}}$	6.44 µm[m]	7.57 µm[m]
Porosity, $\boldsymbol{\varepsilon}$	0.41*	0.19*
Tortuosity factor of the liquid phase (Bruggeman), $\boldsymbol{\tau_{Br}}$	$0.41^{-0.5}$[a]	$0.19^{-0.5}$[a]
Electronic conductivity, $\boldsymbol{\sigma_{eff}}$	1000 S/m[a]	1000 S/m[a]
%v AM, $\boldsymbol{\Psi_{AM}}$	0.51*	0.73*

The parameters (D_s, k_0) determined from PITT experiments on a thin electrode are integrated back to the Newman model to simulate its rate capability for validation. Even though the current response during potential steps simulated by the Newman model match pretty well with the PITT experiment albeit perhaps close to full AM lithiation (see Figure VI-9), Figure VI-17a shows that the simulated rate capability does not match experimental data correctly. Despite the significant discrepancies in EoD capacity, the polarizations of the electrode from simulations match well with the measurements (up to 3C in Figure VI-17b). Therefore, k_0 values from PITT are retained for the rest of the study. Conversely, the mismatch between simulated and experimental EoD capacity suggests values of D_s from PITT are not suitable for rate-capability simulations. The root cause of the disagreement remains unclear. Further investigations are needed to determine the origin of this inconsistency, but it is not addressed here.

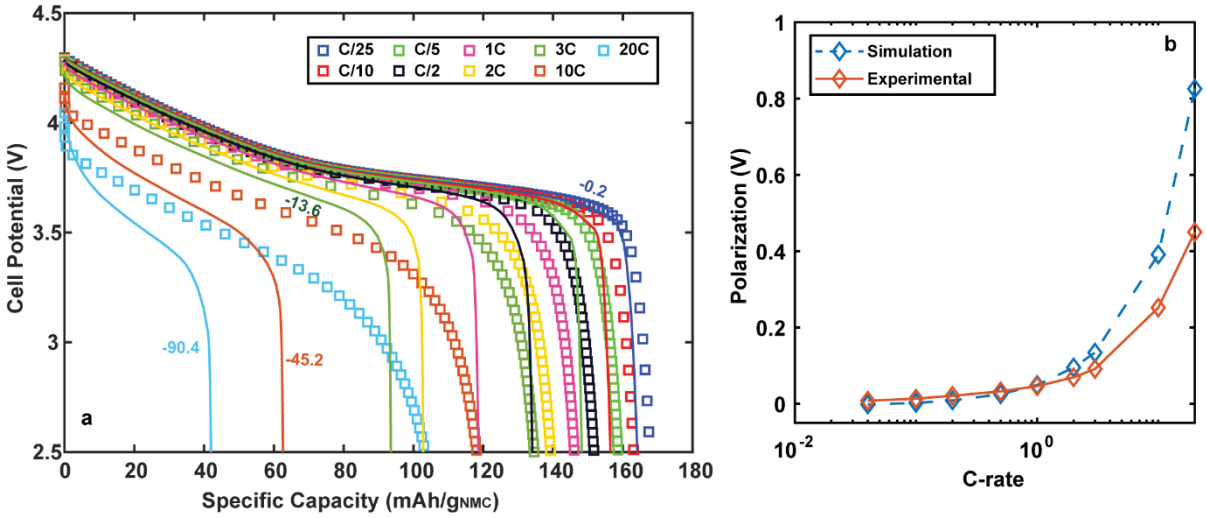

Figure VI-17. Validation of the experimental results. The simulation of the rate capability of the thin electrode (solid lines) is compared with the experimental results (square markers). AM intrinsic properties (D_s, k_0) derived from the PITT measurement are used as model inputs. The current densities are in A/m².

The solid-diffusion coefficient, D_s, determined by Wu *et al.* for NMC111 materials using another interrupted titration technique (namely GITT on a thin electrode combined with a model analysis), is used instead. To get a better match between simulations and experiments upon discharge rate capability, D_s is manually adjusted in the Li-rich composition range and turns out to decrease faster than that by Wu *et al.* for NMC111.

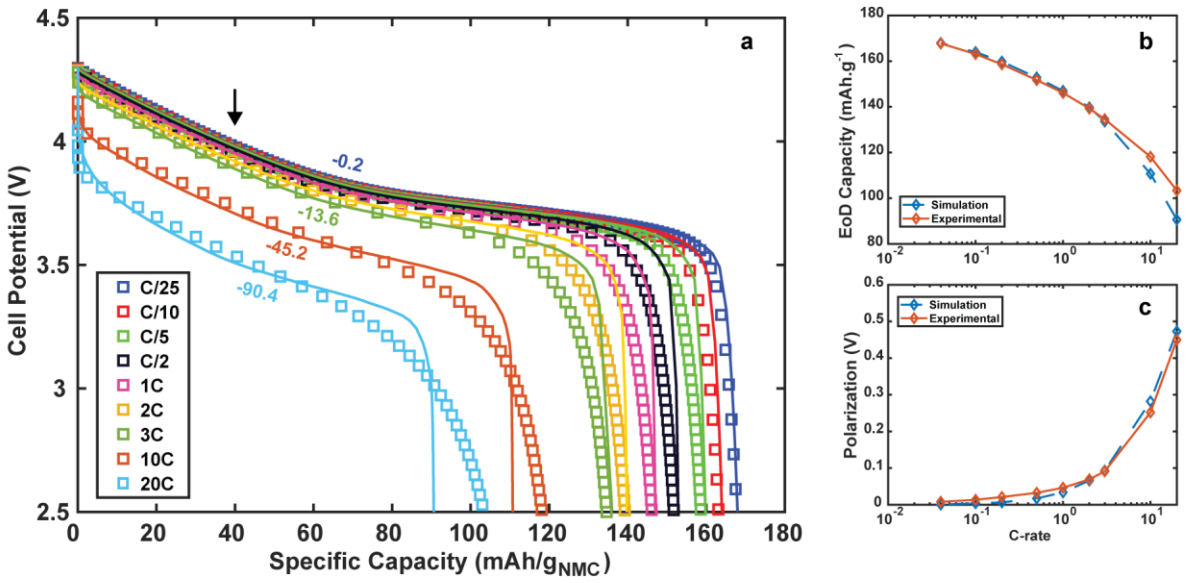

Figure VI-18. Validation rate capability on thin electrodes. a. Discharge curves of thin electrodes at different current densities. **b.** EoD capacity as a function of C-rate from experimental and simulation data. **c.** Overpotential at $Li_{0.77}Ni_{0.5}Mn_{0.3}Co_{0.2}O_2$ upon discharge from $Li_{0.38}Ni_{0.5}Mn_{0.3}Co_{0.2}O_2$ (indicated by the black arrow) in function of C-rates from experimental and simulation data. The current densities are in A/m².

Figure VI-18a shows a good agreement between the simulated discharge curves and the experimental data, regarding both EoD capacity (Figure VI-18b) and average polarization (Figure VI-18c), over the entire range of discharge C-rates. Thus, D_s and k_0 are then retained for modeling the industry-grade electrodes here below.

Nevertheless, the model cannot represent the gradual decline of cell potential toward the EoD, especially at high C-rates. Even with the use of the discharge curve at C/50 as an equilibrium potential rather than the averaging of PITT charge and discharge, the simulated potential drop near the EoD is much more sudden with the model than it is in the experimental data.

A possible reason for it is the distribution of the electronic resistance (*e.g.*, electronic contact resistance between AM/CBD, electronic resistance across the AM) that would account for a distribution of the resistance for electron transport from the conductive electrode matrix all the way to the reaction sites.[22] Furthermore, the NMC conductivity is reported to decrease substantially once the materials get close to full lithiation state.[35] Consequently, considering a constant effective electronic conductivity during the entire operation might not be accurate enough to properly address the cell potential decline toward the EoD. Here, the authors decide not to focus on this minor discrepancy, but acknowledge that electronic effects (distribution + stoichiometry dependence of AM conductivity) could be implemented to the mathematical model for a better model prediction capability in a future work.

As seen in Figure VI-19a-c, the simulated liquid-phase concentration profile across the electrode thickness does not show any Li depletion issue.

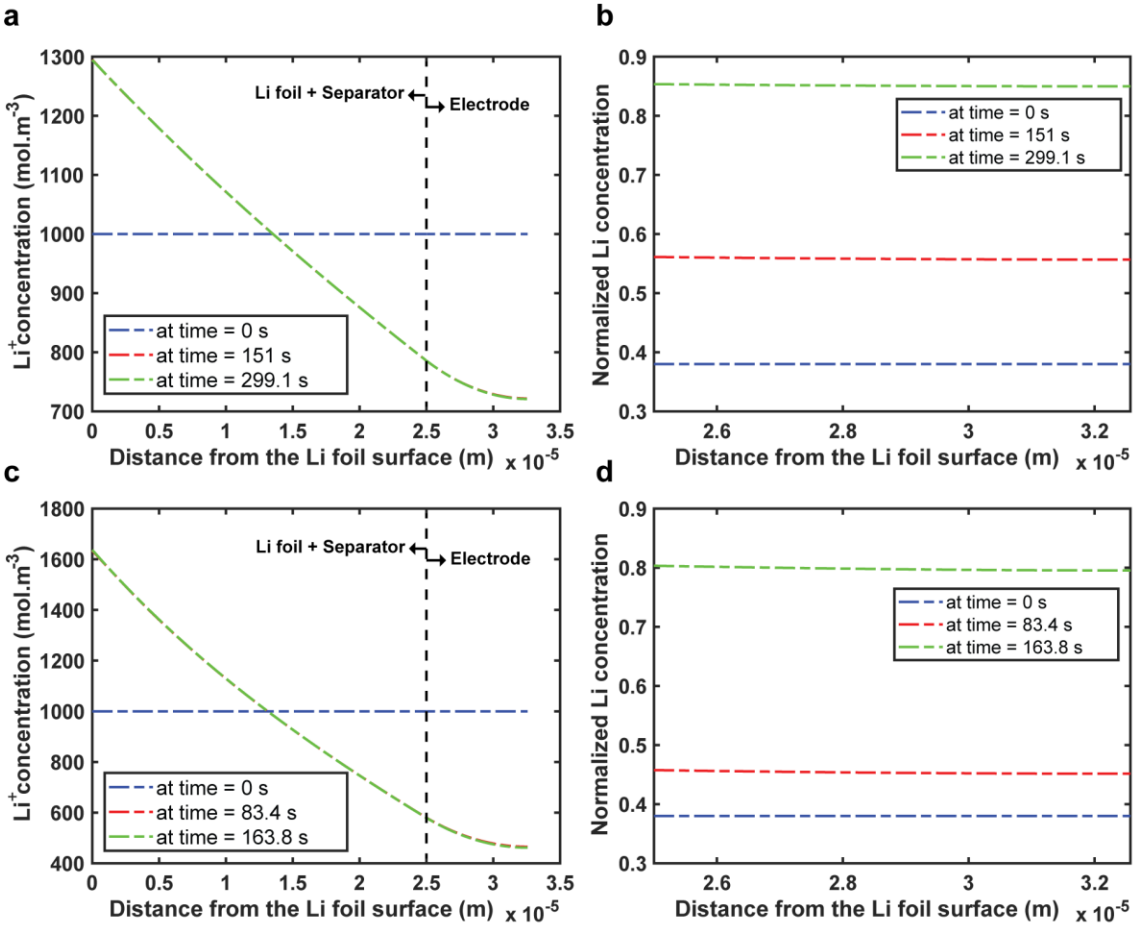

Figure VI-19. Simulated concentration profile across the thin electrode ("model" electrode). a, c. Concentration profile at different times across the separator + PE thickness at 10C and 20C, respectively. **b, d.** AM utilization profile at different times across the separator + PE thickness at 10C and 20C, respectively.

In addition, Figure VI-19b-d show the volume-average Li utilization within the particles across the thickness of the electrodes, which is nearly uniform, even for C-rates as high as 10C and 20C. This justifies that the Li intercalation occurs uniformly across the electrode thickness, as expected if porous-electrode effects are negligible. Increasing the tortuosity factor at values well above that estimated from Bruggeman correlation also yields no effect on the particle utilization.

Later in the paper, we develop a new model that uses the polynomial approximation[30] as an approximate solution to solve the solid diffusion in AM particles. Compared with the regular Newman P2D model, this approximation allows removing the additional dimension across the particle radius.

As mentioned above, the solid coefficient diffusion D_s is no longer taken as a function of c_s, but assumed to be a function of $\bar{c}_s$ whenever the polynomial approximation is used. Thus, D_s must

be re-adjusted to validate the thin electrode rate capability (orange curve in Figure VI-8a), given the slight differences due to this assumption (Figure VI-1).

Figure VI-20 represents the model/experiment comparison of the discharge rate capability of the thin electrode with the "baseline" model using the new "fitted" D_s. On the other hand, the polarization from simulations shows good agreement to the experimental for the entire range of C-rates. Therefore, k_0 is kept identical hereafter.

As a short conclusion, the validation step on the thin electrode without substantial porous-electrode effects, proves our set of parameter values to be relevant for representing the AM intrinsic properties.

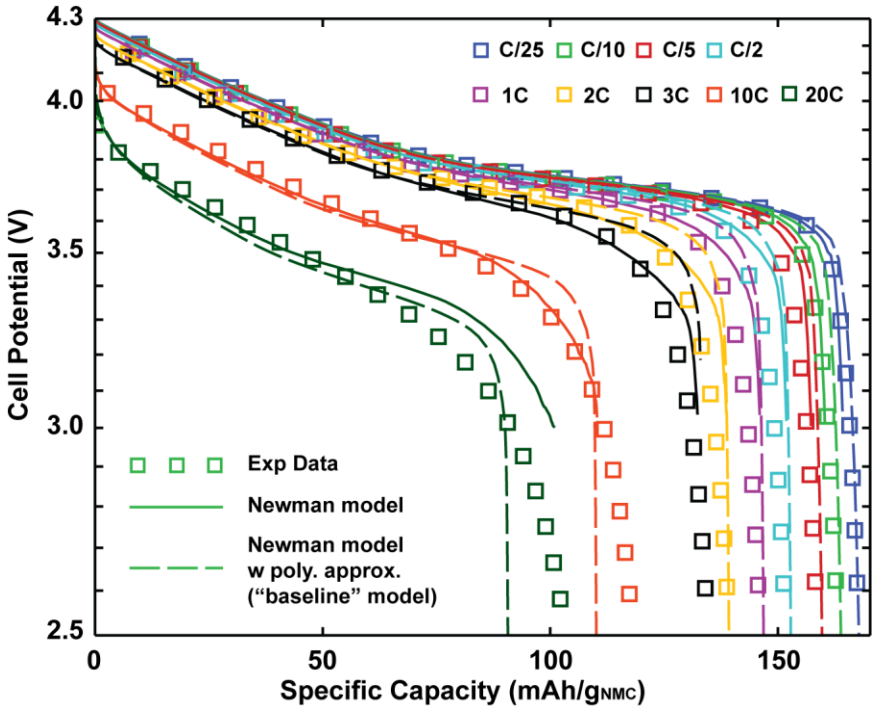

Figure VI-20. Validation on the thin electrode for polynomial approximation. The parameters for intrinsic properties of AM are validated again using the Newman model with polynomial approximation upon the rate capability of the thin electrode.

VI.4.2.2 Industry-grade-electrode validation

Here, we focus on how rate capability changes for different electrode designs to identify rate-limiting factors for each design. For this purpose, different electrolytes are used, resulting in different impacts on ionic transport. Using an electrolyte with low transport properties (LP40 1 M and 0.5 M) magnifies the discrepancy between electronic and ionic transport limitations. In contrast, ionic transport is improved with a high-performance electrolyte (LP30), so that it ionic transport limitations get closer to electronic ones. By changing the ratio between electronic and ionic transport, it can lead to either a more uniform reaction rate across the electrode (with LP30)

or conversely a narrow reaction zone that moves across the PE as discharge proceeds (with LP40).[18] This is expected to provide more insights for understanding the interplay between electrode design and its performance.

Table VI-5. List of model parameters used for discharge process simulations at 25°C.

Parameters	**Values**		
MX-01	**LP40 1 M**	**LP40 0.5 M**	**LP30 1 M**
Thickness, $\boldsymbol{L_{el}}$	73.55 µm	72.13 µm	72.95 µm
Porosity, $\boldsymbol{\Psi}$	0.24	0.24	0.25
McMullin number, $\boldsymbol{N_{M,e}}$	17.47		
Electronic conductivity, $\boldsymbol{\sigma_{eff}}$	0.11 S/m	0.11 S/m	0.11 S/m
%v AM, $\boldsymbol{\Psi_{AM}}$	0.68	0.68	0.66
MX-02	**LP40 1 M**	**LP40 0.5 M**	**LP30 1 M**
Thickness, $\boldsymbol{L_{el}}$	46.13 µm	46.40 µm	46.50 µm
Porosity, $\boldsymbol{\Psi}$	0.28	0.25	0.25
McMullin number, $\boldsymbol{N_{M,e}}$	17.56		
Electronic conductivity, $\boldsymbol{\sigma_{eff}}$	0.16 S/m	0.16 S/m	0.16 S/m
%v AM, $\boldsymbol{\Psi_{AM}}$	0.65	0.68	0.68
MX-01b	**LP40 1 M**	**LP40 0.5 M**	**LP30 1 M**
Thickness, $\boldsymbol{L_{el}}$	74.35 µm	73.75 µm	74.45 µm
Porosity, $\boldsymbol{\Psi}$	0.19	0.19	0.22
McMullin number, $\boldsymbol{N_{M,e}}$	36.67		
Electronic conductivity, $\boldsymbol{\sigma_{eff}}$	2.38 S/m	2.38 S/m	2.38 S/m
%v AM, $\boldsymbol{\Psi_{AM}}$	0.70	0.67	0.67
MX-02b	**LP40 1 M**	**LP40 0.5 M**	**LP30 1 M**
Thickness, $\boldsymbol{L_{el}}$	39.95 µm	39.95 µm	39.95 µm
Porosity, $\boldsymbol{\Psi}$	0.16	0.18	0.17
McMullin number, $\boldsymbol{N_{M,e}}$	24.35		
Electronic conductivity, $\boldsymbol{\sigma_{eff}}$	3.07 S/m	3.07 S/m	3.07 S/m
%v AM, $\boldsymbol{\Psi_{AM}}$	0.72	0.70	0.71

Figure VI-21a, c, e summarize the experimental rate capabilities of all industry-grade electrodes with three different electrolytes. Notably, all electrodes show very similar performances up to C/5 regardless of the type of electrolyte, which are also very close to those of the thin electrodes (Figure VI-18). This indicates that the limitations at low C-rates mainly come from the solid diffusion and charge transfer at particle scale, related to AM intrinsic properties rather than electrode design (PE scale).

As the discharge rate increases further (C/2 or more), the electrode performance starts to deviate from each other and from that of the thin electrode. This suggests a change in the electrode

limitation, as the thickness increases, which is commonly explained by the contribution from porous-electrode effects, *i.e.* ionic/electronic transport. The Newman model should be able to capture this behavior, since the electrode tortuosity and electronic conductivity were carefully determined using appropriate experiments, as detailed above.

Also, it is noteworthy that a lower performance is observed experimentally for electrodes with a higher CB/binder content, despite a higher electronic conductivity. This result, albeit surprising at first sight, does not contradict with other works in the literature.[26,67] It is explained by the fact that a higher content of CB/binder content leads to a higher electrode tortuosity factor, as the CBD tends to form clusters containing meso/nano-pores.[7,68] Moreover, a reduction of the active surface area can also occur as a larger AM particle surface is covered by the CBD, at the expense of the surface in contact with liquid electrolyte.

Furthermore, our previous work[7] demonstrated that the MX-01 electrode has a better dispersion of CBD than MX-01b and MX-02b based on tomographic data. This promotes better short-range contacts[13,69,70] for electronic transport. It was experimentally demonstrated to be essential for electrode performance rather than long-range electronic conductivity, as it allows to have a more uniform distribution of reactions throughout the PE.

Regarding the simulations, Figure VI-21b, d, f show the corresponding results simulated with the "baseline" model. The model operates with the set of parameters determined earlier (Table VI-5) without any fitting parameters. Unfortunately, there is a poor agreement between the model and the experimental results. Overall, the model tends to overestimate the performance in all cases, especially toward moderate to high-rate discharge curves (*ca.* C/5 or larger). This is seen in Figure VI-22a, in which the complete simulated and experimental discharge curves are compared for MX-01b in LP40 1 M. Similar to the thin electrode, the polarization of simulated curves is in agreement with the experimental curves at least at low C-rate (< C/5).

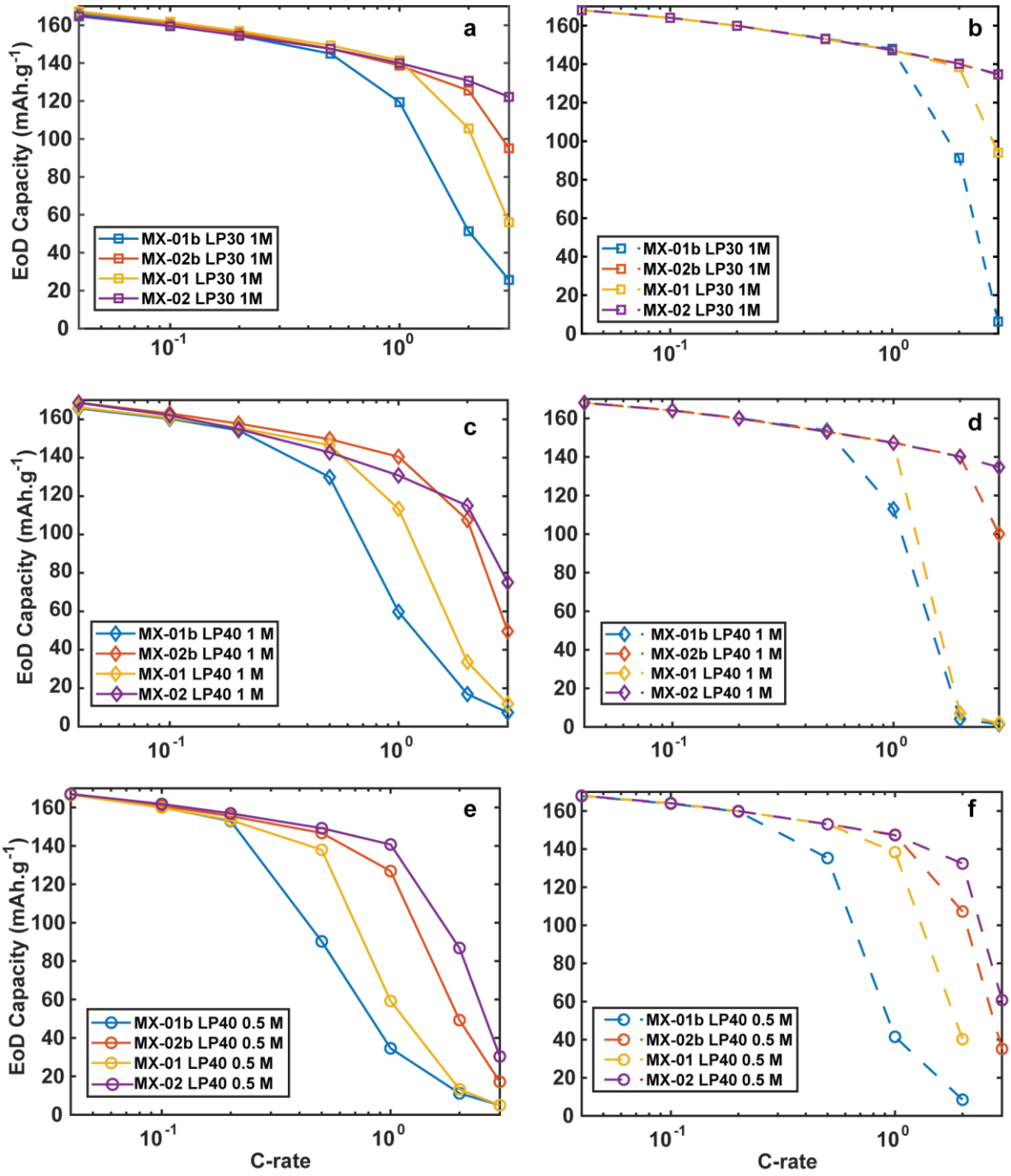

Figure VI-21. Validation on industry-graded electrodes with "baseline" model.

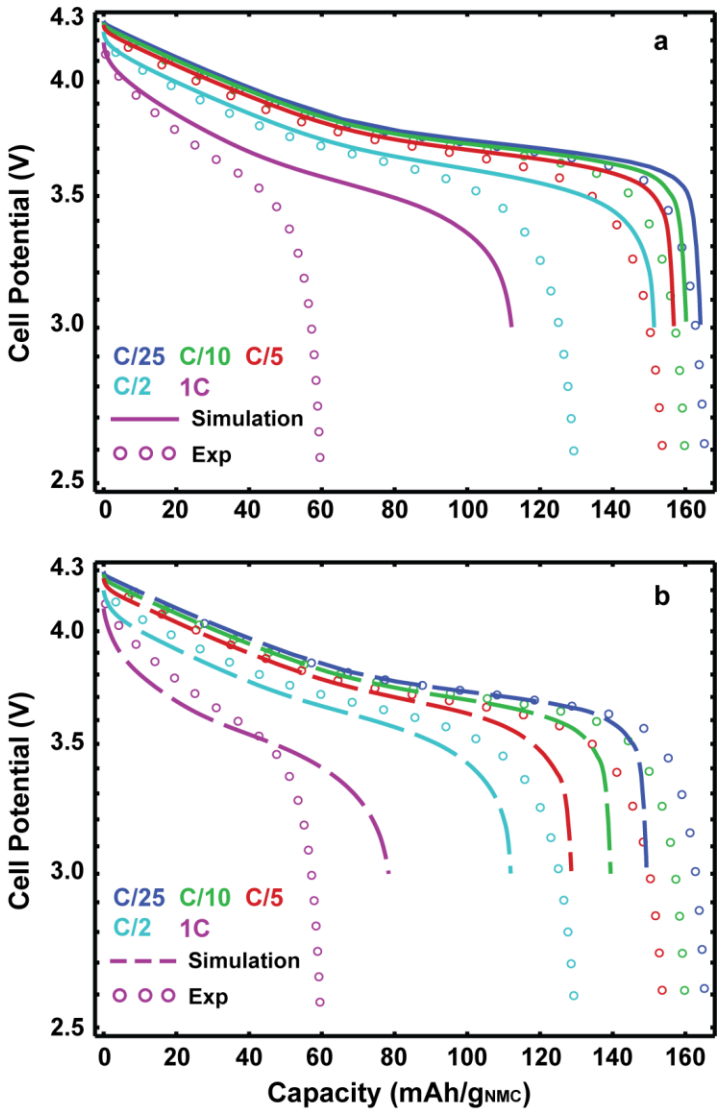

Figure VI-22. Study the effects of the particle size on the simulation results of MX-01b sample with LP40 1 M. a. Simulation results using "baseline" model with one particle size (2.35 µm diameter given by laser diffraction measurement). **b.** Simulation results using "baseline" model with a particle size of 10 µm diameter.

Although Malifarge *et al.*[14] demonstrated a good agreement between simulation and experimental results by measuring all the model parameters carefully in the case of graphite electrodes, the same approach on NMC positive electrodes do not seem to be as straightforward. Many literature works struggle to capture the correct discharge behavior at multiple C-rates using the Newman-based model for the family of NMC materials.[24,26–28]

It is worth mentioning that in most of these works, an overestimation of predicted capacities is observed in the discharge simulations. The dominant performance-limiting factor is attributed to the ionic transport related to the liquid phase within the electrode porosity. Hence, they explain the performance overestimation by either an underestimation of the electrode microstructural

parameters (*e.g.* τ_e) or an overestimation of the bulk electrolyte properties.

Among these works, Wu *et al.*[24] proposed a similar approach, in which they carefully validated the intrinsic properties of their AM through the use of a "model" electrode, just like we do in this work. However, the authors had to assume a large electrode tortuosity factor ($\tau_e = 26$) in order to match the experimental data. Tambio *et al.*[26] assumed EoD capacity is diffusion-limited by the liquid phase. Following this postulate, the authors relied on the empirical model developed by Gallagher *et al.*[71], which explicitly neglects other limitation sources, to validate the experimental measurements. However, the authors considered the geometric tortuosity factor, which is not the most appropriate to represent the tortuosity of a PE, as it suffers some key conceptual issues such as not accounting for "bottleneck" pores.[72] This explains why the tortuosity are quite low for their electrodes, albeit their high density, and also why the effective porosity is lower than given in order to compensate the underestimation of the tortuosity. Even when they demonstrated an increase of the electrode tortuosity factor values due to micro/nano-porosities, the values remain low ($1.2 < \tau_e < 2.9$). They do not significantly differ from the values estimated by the Bruggeman correlation, which is reported to frequently underestimate the tortuosity of the pore network.

Although electrode tortuosity-factor values seem to be reliable, as discussed above, attempts are made to adjust them for matching the experimental results and possibly verify assumptions on liquid-phase limitations. The case of MX-01b using LP30 1 M is considered (Figure VI-23a, b), in which MX-01b shows important capacity loss from rates above C/2 (*ca.* 1 mA/cm²). An electrode tortuosity factor larger than 11 is needed to capture this behavior. Though, it does not affect the discharge at C/2. Figure VI-23c, d show simulation results of MX-02 with LP40 1 M, with an electrode tortuosity factor that is increased by a factor of 2 ($\tau_{e,fit} = 8$), which shows a better agreement with experimental data at the high discharge rates (1C, 2C). However, similar to MX-01b, this value does not resolve the difference between simulations and experimental results at lower discharge rates (C/5, C/2).

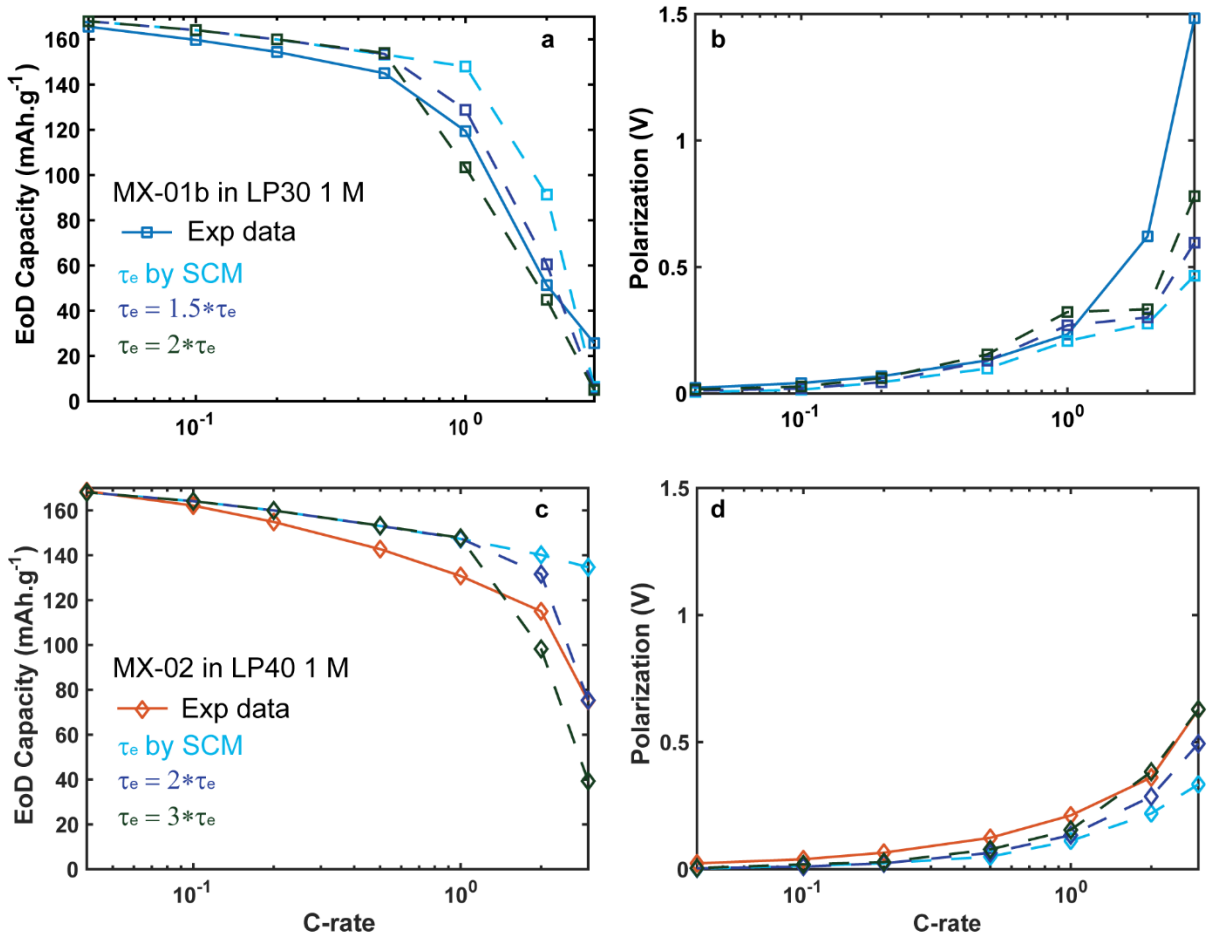

Figure VI-23. Study the effects of the electrode tortuosity factor on the simulation results. The electrode tortuosity factor was varied in two different cases to match the simulation results to the measurements. **a, c**. Comparison of EoD capacity between simulation and experiment for MX-01b and MX-02b, respectively. **b, d**. Comparison of polarization between simulation and experiment for MX-01b and MX-02b, respectively.

The analysis above has thus far suggested that the mass transport in liquid phase is likely not the solely limiting source of the electrode performance. Xu *et al.*[28] and Appiah *et al.*[27] tackle the issue differently, as they attribute the severe drop in capacity observed at high C-rate to the solid-state Li diffusion, which is a process occurring at the particle scale. However, using the Newman model, they need to exacerbate the limitation of this process through an empirical correlation of the solid-diffusion coefficient to either the electrode thickness or to the C-rate in order to fit the experimental data. Even though both correlations allow for matching the experimental data, the underlying physics accounting for these dependencies is not clearly unraveled.

Back to the electrodes studied in this work, the worst performance is observed for electrodes with a higher content CB, so it is unlikely that the lack of limitations at the higher discharge rates of the simulations cannot be addressed by additional electronic resistances, which can be referred to as contact resistance between either particles or between porous electrodes and current collector. Furthermore, the change of electronic resistances mainly impacts the polarization of the discharge

curves but has slight impacts upon the EoD capacity, unless a there is a large distribution of contact resistances, with a fraction of poorly-connected particles.

In this work, given that a good agreement between experimental and simulated rate-capability curves is obtained for thin electrodes up to very high C-rates (20C corresponding to a current density of ~8 mA/cm²), the parameters used for AM properties are expected to represent the AM behavior even in higher-loading electrodes correctly, as long as the assumptions at particle scale remain valid (isolated spherical particles).[18] Thus, the discrepancies indicate that the AM particle morphology in industry-grade electrodes might deviate from the "ideal" particle model used for the thin electrodes.

Fortunately, the analysis from tomographic data of the industry-grade electrodes can give more insights.[7] It shows a tendency of narrowing the gap between solid particles along the electrode thickness. In addition, a non-negligible extent of the inter-connectivity among AM particles is also quantified, which can reach up to 20% of the particle surface. Overall, the analysis implies a tendency of particle agglomeration (AM and CBD). This deviates from the assumption of isolated AM particles in Newman model, in which the Li diffusion between adjacent AM particles, referred to as inter-particle diffusion, is not accounted for.[73]

Recently, the inter-particle diffusion was numerically demonstrated by Ferraro *et al.*[74] to occur between particles in contact. Assuming that there is no resistance due to the inter-particle diffusion, then a group of particles in contact would behave as a large single particle. The solid diffusion length increases, as it now relies on the size of the large particle agglomerate. This makes solid diffusion more critical. Moreover, the formation of particle clusters tends to reduce the active surface area, as particles are no longer exposed completely to the liquid phase as in the physical representation of Newman model. This causes fewer reaction-sites dispersed over the particle surface, resulting in longer diffusive pathways for "neutral" Li to move in order to occupy all the solid lattice during the discharge process.

If the solid diffusion process is the primary rate-limiting factor, a simple increase of the apparent particle radius, *i.e.* diffusion length, may reproduce the detrimental effects on electrode performance at high C-rates that are seen experimentally. Figure VI-22b shows that in order to match the high C-rate region, the increase of diffusion length will also overestimate the limitation at the low C-rate region and vice-versa. Therefore, an apparent particle size that empirically varies as a function of the C-rate would be required in order to fit the entire rate capability.

To conclude this part, the Newman P2D model with a "micro" model that matches the AM behavior fails to predict the discharge rate capabilities of the industry-grade electrodes. Different hypotheses are investigated to understand the root cause of the non-agreement between simulations and experiments. Nevertheless, simply tuning an individual parameter to control either the liquid-phase transport (via τ_e) or the "micro" model behavior (via r_p) does not help reconcile simulations and experiments over the full range of C-rates. Thus, this discrepancy may arise from extra limitation(s) that are not built-in in the Newman model, but can be relevant for electrodes in this

study.

Given the high density of the industry-grade electrodes used in this work along with the analysis from tomographic data, the formation of particle agglomerates is likely to occur, which exacerbates the solid-diffusion limitations, as discussed above. However, we hypothesize that sub-pores can be located inside an agglomerate, making it a porous medium instead of a bulk nonporous agglomerate. In that case, the formation of agglomerates can also exacerbate the impacts from the ionic transport in the liquid phase. Since agglomerate formation reduces the available active surface area, which is also reduced by the CBD coverage, less reaction sites have to support a higher pore-wall flux under a same current density. This accelerates the Li^+ depletion in the liquid phase in the vicinity of the reaction-sites. Moreover, we assume that the pore network within the PA is formed by either the mesopores of the swollen CBD or the narrow gaps between solid particles due to the calendering process. Thus, the local size of the pores is another factor that would aggravate these local liquid-phase limitations.

Overall, the abovementioned combined effects (deterioration of solid diffusion, lowering of active surface area, and local Li^+ depletion) due to electrode calendering can be represented by a PA, in which solid particles are clustered together along with a low volume fraction of inter-connected sub-pores.

Figure VI-24 illustrates the geometric change from isolated-spherical particles to PA assumed to form on industry-grade electrodes. Within a highly dense agglomerate, as shown in Figure VI-24b, the inter-connectivity between solid particles is likely to occur, such that reduces the particle surface exposed to electrolyte (highlighted in red). It is worth noting that the interface particle/particle is not active for electrochemical reactions but allowing the inter-particle diffusive flux going through. As a result, a PA allows both inter-particle solid diffusion and ionic transport via sub-pores in order to reach the AM located at the inner of the PA. The CBD is assumed to be packed inside the PA and combines with AM particles to form the solid phase.

To numerically investigate this hypothesis, a new model, PApa model, is developed and used to simulate the performance of the electrodes. In this model, the PA is assumed to be spherical, which has a radius, R_{PA}; whereas ξ_3 represents the volume fraction of sub-pores among the total porosity. Since the AM particle surface is assumed to be covered by either the electrolyte in sub-pore domain or by other solid particles, a parameter representing the fraction of particle surface in contact with electrolyte in sub-pores, $f_{\mathrm{AM}-3}$ is also required.

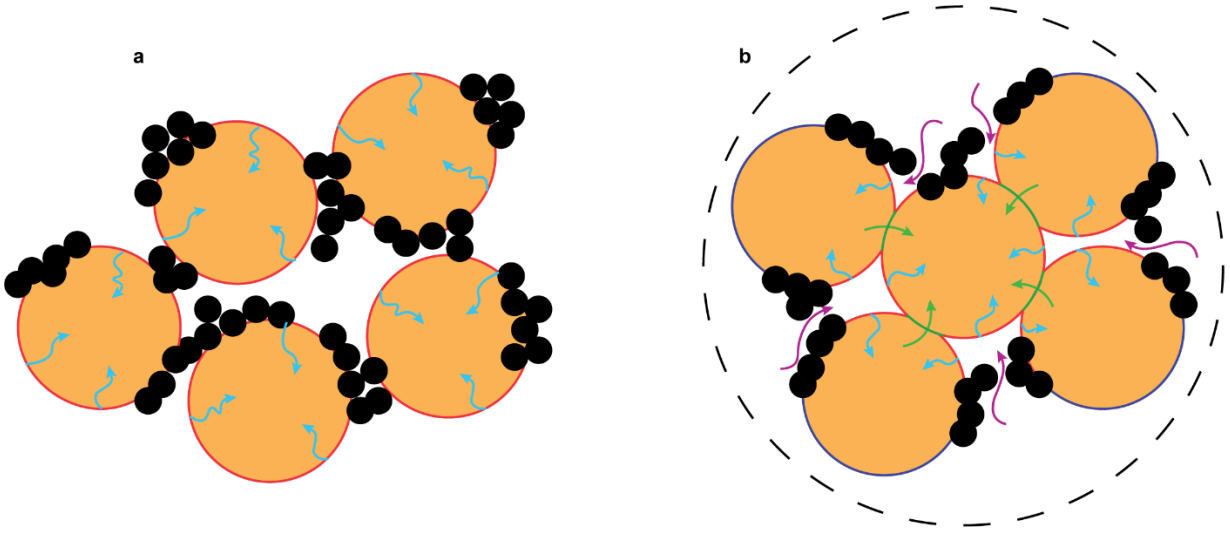

Figure VI-24. Our hypothesis of the formation of PA. Calendering process reduces the gap between solid particles (AM, CBD) leading to PA, in which a sub-pore domain contains some electrolyte. Within the PA, there are two mechanisms of transport where a Li^+ can diffuse through liquid phase in sub-pore domain or a bipolar <Li^+,e^-> can diffuse between secondary particles (interparticle solid diffusion). Ionic transport in sub-pore domain (magenta arrows), Inserted flux of Li^+ from electrolyte in sub-pores into individual AM particle (blue arrows), Inter-particle solid diffusion (green arrows). Active surface area is colored in red, Inter-connectivity between AM/AM is colored in green, Inactive surface area is colored in dark blue.

Regarding the parametrization for the model, most of the parameters remains unchanged compared to the "baseline" model or can be estimated by empirical laws from literature. For macro-pore domain, it is decided that the electrode tortuosity factor value remains equal to that determined by the symmetric cell method, since the volume fraction of sub-pores is eventually shown to be very small in the simulations below. For the sub-pore domain, the tortuosity is assumed to follow the power-law fit from Usseglio *et al.*,[62] since this law already demonstrated a somewhat good agreement for electrode tortuosity at PE scale in our work (Figure VI-11).

Commonly, since the entire surface of a spherical particle is assumed to be exposed to the electrolyte, the fraction of particle surface in contact with other phases is not resolved. Here, characterization based on advanced X-ray tomography techniques provides insights. In [7], the microstructure of the three samples MX-01, MX-01b and MX-02b were investigated using X-ray holotomography, where the three phases: AM, CBD and electrolyte were completely resolved. Furthermore, the AM phase was separated into more than 500 individual particles, allowing a statistical analysis of their inter-connectivity between different phases. Therefore, $f_{\mathrm{AM-3}}$ of these samples in this work is taken as the average value of the inter-connectivity AM/electrolyte obtained from the statistical analysis, as shown in Figure 5 in [7]. Also, in [7], we concluded that higher amount of CBD and higher density of the electrode reduce the interface AM/electrolyte. A highest fraction of particle surface exposed to electrolyte compared to the three others is, therefore, assumed for MX-02.

Since $f_{\mathrm{AM}-3}$ is determined from [7] except for the MX-02 that is assumed, (R_{PA}, ξ_3) are the only two additional parameters, which are not characterized. Therefore, they are set as fitting parameters to validate the experimental results. However, one must verify whether they can be fitted simultaneously. For that, they need to be independent of each other. Notably, these two parameters are connected through the characteristics time of the ionic transport within the sub-pore domain according to:

$$T_{\mathrm{elyte},3} = \frac{R_{\mathrm{PA}}^2}{D_{\mathrm{eff},3}} = \frac{1.4R_{\mathrm{PA}}^2}{\varepsilon_3^{1.77}D} \qquad \text{(Eq. VI-31)}$$

given $\tau_3 = 1.4\varepsilon^{-0.77}$ as assumed earlier.

If the two parameters are correlated, the simulations remain intact as long as the group $\frac{\varepsilon_3^{1.77}}{R_{\mathrm{PA}}^2}$ remains unchanged, even though ε_3 and R_{PA} are modified; in other words, simulations with $R_{\mathrm{PA}} = \gamma R_{\mathrm{PA},0}$, and $\varepsilon_3 = \gamma^{-1}\varepsilon_{3,0}$ ($R_{\mathrm{PA},0}$, $\varepsilon_{3,0}$ are set) are identical whatever the value of γ. As a result, only the group $\frac{\varepsilon_3^{1.77}}{R_{\mathrm{PA}}^2}$ can be fitted.

One shows that the Li transport through inter-particle diffusion should have minor effects if the transport through the electrolyte in sub-pores is dominated (*e.g.,* highly porous PA). Consequently, one cannot independently fit the two parameters. The case, where the inter-particle solid diffusion is disabled, is illustrated in Figure VI-25a.

Nevertheless, given the high density of PA, inter-particle solid diffusion can strongly contribute to the mass transport at the PA scale along with the regular ionic transport via the electrolyte. In this case, the R_{PA} will also impact the electrode performance via the inter-particle solid diffusion limitations, so that it will be decorrelated from the group in Eq. VI-31. A sensitivity analysis of R_{PA} is performed for two electrodes; for those the inter-particle solid diffusion effects are expected to be either the highest or lowest. In addition, only moderate to high C-rates are investigated, since low C-rates are mainly limited by the individual solid diffusion such that not sensitive to inter-particle diffusion.

Figure VI-25b, c show the sensitivity of the R_{PA} while the group $\frac{\varepsilon_3^{1.77}}{R_{\mathrm{PA}}^2}$ remains invariant. The effects from R_{PA} are clearly observed on the simulated curves. The larger PA size deteriorates the electrode performance, as the inter-particle solid diffusion turns more critical.

Following the sensitivity analysis, one can, therefore, consider (R_{PA}, ξ_3,) as two separated parameters to be fitted simultaneously. The tuning is manually performed by trial and error and assessing the qualitative agreement between experimental and simulations for each electrode in three electrolytes. These two parameters are tuned to achieve an overall good fit of all the cases, *i.e.* they allow fitting over the entire range of C-rates, while not having significant variation from one electrolyte to another instead of having a best fit for each electrolyte.

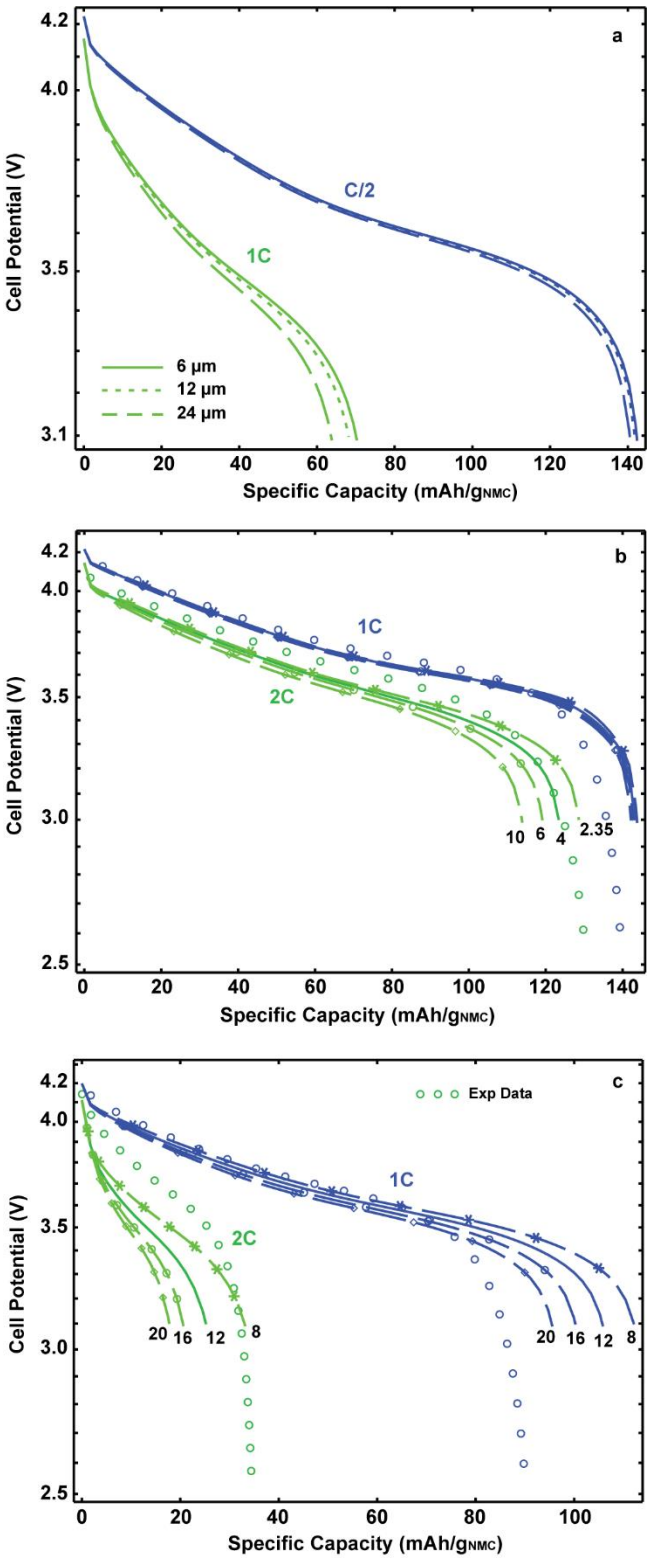

Figure VI-25. Sensitivity analysis of R_{PA} for MX-01b and MX-02. The corresponding values of R_{PA} (µm) are represented under each simulated curve. The experimental data are also plotted for the ease of comparison.

Regarding the model validation against experimental results, while the "baseline" model overestimates the rate performance for all the industry-grade electrodes studied here, the PApa model shows a very good agreement over a large range of C-rates for all these electrodes, even when different electrolytes are used (Figure VI-26, VI-27). In most cases, the model simulations match well in terms of both polarization and EoD capacities. For higher loading electrodes (MX-01, MX-01b), as current densities get above 1C (*ca.* 4 mA/cm²), a mismatch between experimental and simulated data starts appearing for the LP40 electrolyte. The mismatch can be due to the low LP40 bulk properties, that creates a large potential drop near the Li foil and much less EoD capacity as mentioned above. Still, a good agreement is achieved for electrolyte LP30 with better transport properties. This problem does not appear for lower loading electrodes (MX-02, MX-02b).

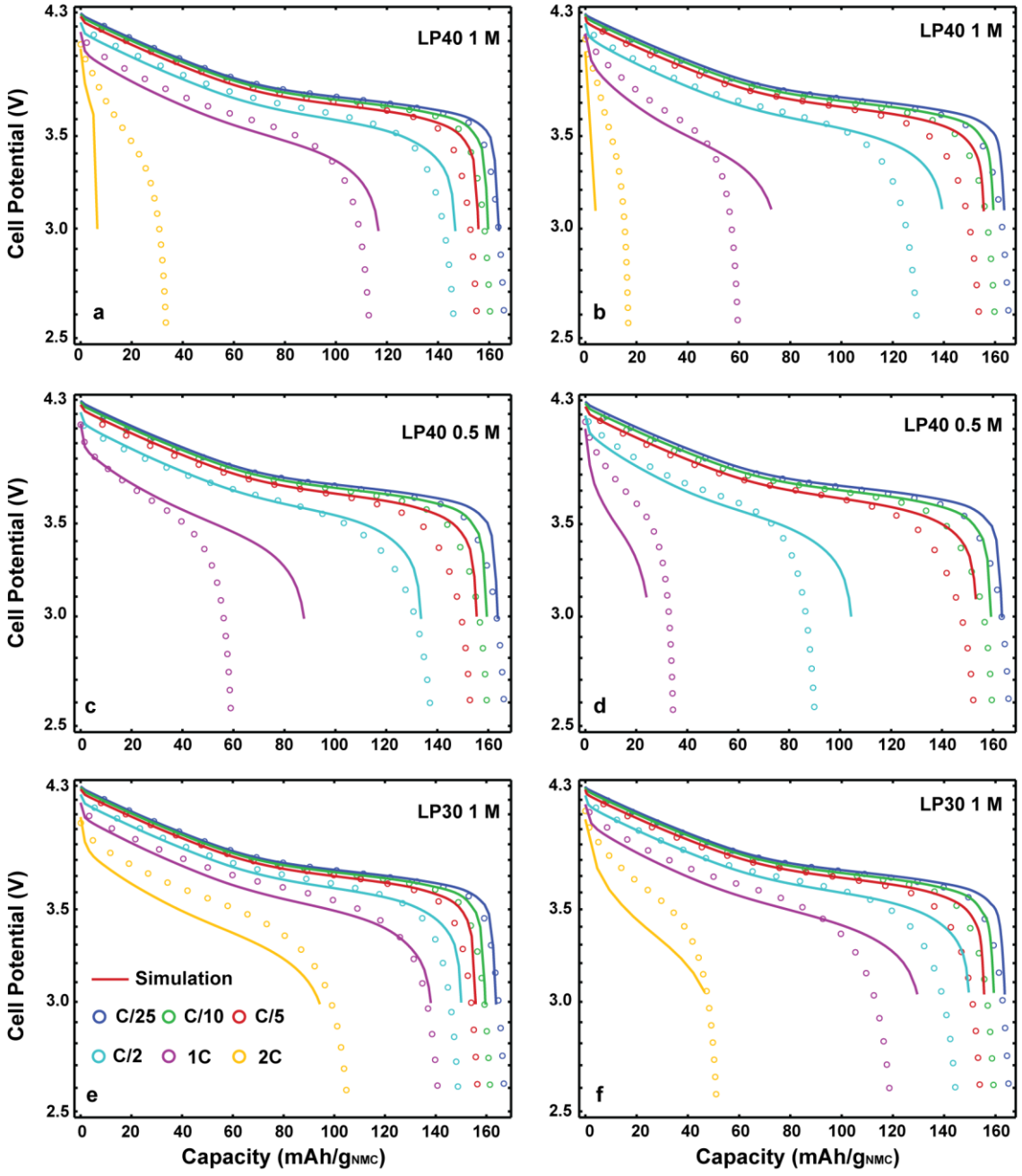

Figure VI-26. Validation of the PAPA model on electrodes with loading of 25 mg/cm^2. a, c, e. The discharge rate capabilities (C/25, C/10, C/5, C/2, 1C, 2C) using three different electrolytes (LP40 1 M, LP40 0.5 M, LP30 1 M) are shown for MX-01. **b, d, f.** The discharge rate capabilities (C/25, C/10, C/5, C/2, 1C, 2C) using three different electrolytes (LP40 1 M, LP40 0.5 M, LP30 1 M) are shown for MX-01b.

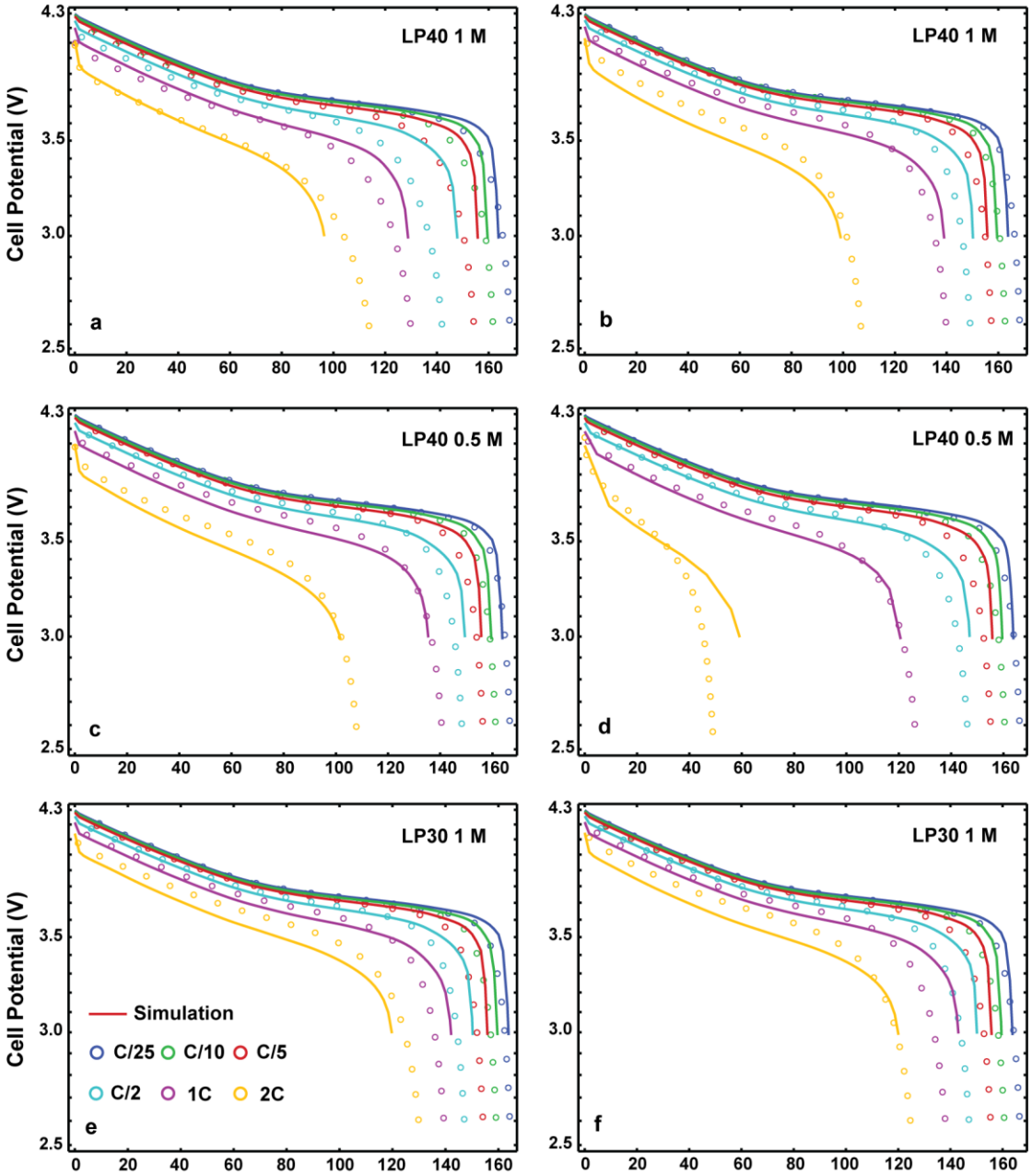

Figure VI-27. Validation of the PAPA model on electrodes with loading of 15 mg/cm^2. a, c, e. The discharge rate capabilities (C/25, C/10, C/5, C/2, 1C, 2C) using three different electrolytes (LP40 1 M, LP40 0.5 M, LP30 1 M) are shown for MX-02. **b, d, f.** The discharge rate capabilities (C/25, C/10, C/5, C/2, 1C, 2C) using three different electrolytes (LP40 1 M, LP40 0.5 M, LP30 1 M) are shown for MX-02b.

Figure VI-28a summarizes the two "fitted" parameters required to validate the experimental results for the set of electrodes, whereas the fraction of particle surface exposed to electrolyte and the group $\frac{\varepsilon_3^{1.77}}{R_{\mathrm{PA}}^2}$ are presented in Figure VI-28b. Since both "fitted" parameters are manually selected such that they remain persistent for all samples, even with different electrolytes, Figure VI-28a represents the values providing a qualitatively good fitting results in overall for each electrode.

As mentioned above, the limitations from inter-particle diffusion are mainly related to the PA radius when the PA is highly dense ($\varepsilon_{\mathrm{AM}} \to 1$). The size of the PAs shows clearly a strong correlation with the electrode loading, *i.e.* higher loading electrodes tend to have larger PA under the calendering effects. Thus, MX-01b is the most limited by the inter-particle diffusion among the electrodes. When MX-01b is compared against MX-02b, by reducing 40% of the electrode loading (from 25 to 15 mg/cm²), one reduces 50% of the PA size, which can significantly benefit for the power performance. As for MX-01 and MX-02, both the loading and the density are changed. Interestingly, the PA size is reduced by 60% overall, which is 10% higher than when only the loading is changed. The electrode density, therefore, shows less impacts on the PA size than the loading. This can also be observed for MX-02 and MX-02b, when 30% change of density (19% versus 28% of porosity) results in ~33% of change in PA size.

Moreover, a more significant fraction of pores that are sub-pores is observed for electrodes with a higher density and/or loading. As a consequence, the ionic transport across the sandwich is exacerbated as the macro-pore domain declines. The ionic transport in sub-pores can be evaluated via the group $\frac{\varepsilon_3^{1.77}}{R_{\mathrm{PA}}^2}$, which is directly related to the characteristic time $T_{\mathrm{elyte},3}$. Interestingly, it is worth noting that no large discrepancy is observed for the group $\frac{\varepsilon_3^{1.77}}{R_{\mathrm{PA}}^2}$ for all electrodes, which indicates that the extent of limitation from ionic transport in the sub-pore domain is tantamount for all electrodes. Electrode having a longer ionic conductive pathway to the PA center (*i.e.*, PA radius) is compensated with higher sub-porosity within the PA.

The inter-particle diffusion, therefore, remains the main limiting factor for mass transport at the PA scale. MX-01b and MX-02b have higher densities than their peers (MX-01 and MX-02), resulting in larger PA size, which undermines the inter-particle diffusion, albeit the PA is more porous (*i.e.*, lower ionic limitations). Higher porous and lower loading electrode under calendering process leads to smaller PA. Sample MX-02 with a lower loading and density has its porosity containing of mainly macro-pores along with smaller agglomerates provides the highest rate performance.

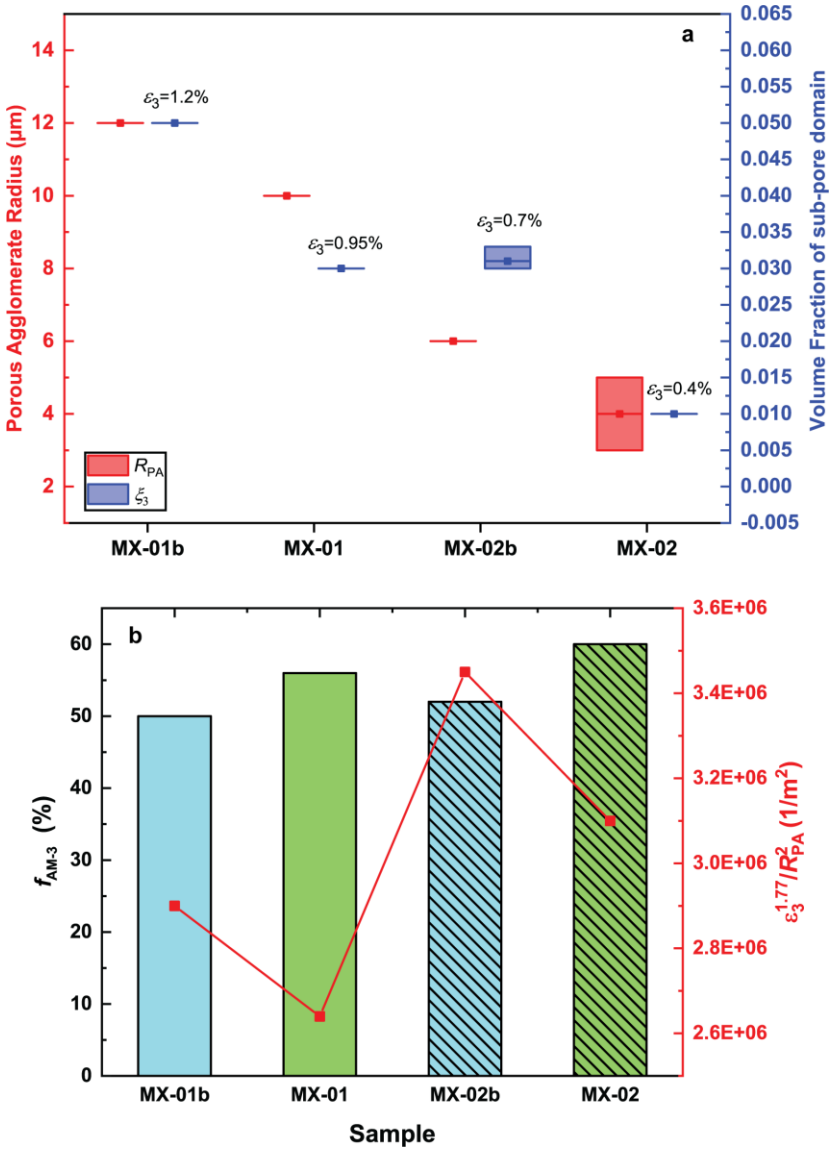

Figure VI-28. Summarize of the two additional parameters used for PApa model. a. For each sample, the mean values of the two parameters (R_{PA}, ξ_3) are presented along with the shaded area representing the max/min values. **b.** The fraction of particle surface exposed to the electrolyte, $f_{\mathrm{AM-3}}$ obtained from tomographic data and the group $\frac{\varepsilon_3^{1.77}}{R_{\mathrm{PA}}^2}$ are also presented for each sample.

For an easier interpretation of the simulation results with the PApa model, the "baseline" model simulations are used to compare low, moderate and high C-rates for MX-01b. This enables more insights about the effects of the presence of PAs compared to the case without.

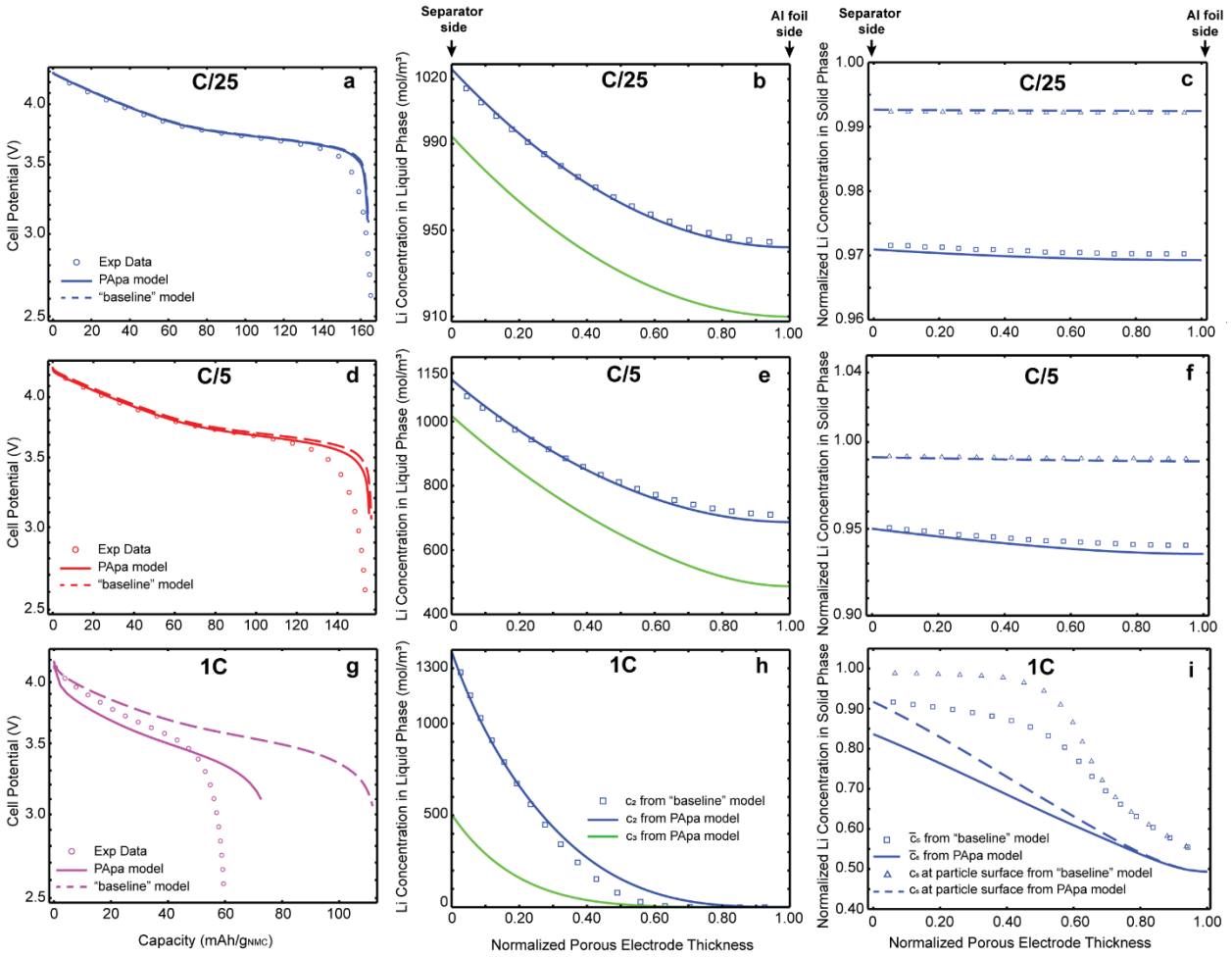

Figure VI-29. Comparison of concentration profiles in solid and liquid phases for MX-01b at EoD by "baseline" and PApa models. a, d, g. Comparison of the simulated discharge curves with the experimental data at C/25, C/5, 1C, respectively. **b, e, h.** The concentration profile of Li^+ in liquid phase across the PE at C/25, C/5 and 1C, respectively. **c, f, i.** The local volume-average AM utilization and the local AM utilization at the particle surface across the PE at C/25, C/5 and 1C are represented, respectively.

At low to moderate C-rates, a lower concentration in the sub-pore domain than in the macro-pore domain is observed in both cases, as expected. Nevertheless, the Li^+ concentration remains substantial (>0.4 mol/L) , so that no complete Li^+ depletion occurs during the full discharge process (see Figure VI-29a, c). Moreover, the concentration profile in the macro-pores of the PApa model does not show an important deviation from that in the liquid phase of the "baseline" model. This is because the sub-pore domain does not occupy a large volume fraction of the total porosity ($\xi_3 = 5\%$, which translates to a porosity for the PA of $\varepsilon_3 = 1.2\%$), so the macro-pore domain behaves similar as the total porosity under low-to-moderate current density (up to C/5 in Figure VI-29b). Besides, the AM utilization (Figure VI-29c, f) do not differ significantly between the two models, resulting in the same capacity at the end of the discharge (Figure VI-29a, d).

In contrast, at high C-rates, the concentration profile in the macro-pore domain starts deviate more substantially from the "baseline" model. The concentration in the sub-pore domain

significantly drops even in the vicinity of the separator/PE boundary (Figure VI-29h), resulting in local Li^+ depletion within this domain. Higher limitation from the solid diffusion can be observed as the concentration at the PA surface reaches higher extent than the "baseline" model. Also, the AM utilization is significantly lower in the PApa model than in the Newman model (Figure VI-29i), which results in a lower EoD capacity, thereby matching the experimental results.

In Figure VI-30, at PA scale, the total Li flux defined in Eq. VI-23 along with the inter-particle diffusive flux and the charge-transfer flux are scaled with the AM particle surface, the coverage fraction by AM and electrolyte in sub-pores, respectively. This allows to evaluate the main contribution of the inserted Li flux into the AM phase across the PA radius. At C/25, the ionic transport in sub-pores is not limited, so that the lithiation process is performed through electrochemical reactions. Consequently, the inter-particle diffusion flux is negligible. In contrast, at 1C, the inter-particle diffusion flux becomes important. A discrepancy between PA located at separator side and current collector side are also highlighted upon the 1C discharge. The PA at the current collector side is barely active, as the flux entering the AM phase is minor compared to that of the PA at the separator side.

Interestingly, near the PA center, the inter-particle diffusive flux dominates, because a local depletion of Li^+ in liquid phase prevents the charge-transfer to occur. In contrast, at the outer of the PA, the charge-transfer flux dominates the flux of Li^+ inserting to the AM particles, while there is an outward inter-particle diffusive flux leaving the particles at the outer to enter the particles at the inner. It is worth noting that the inter-particle diffusive flux is conserved over the PA volume, as any lithium leaving a particle of the agglomerate necessarily inserts into another particle. At 1C, at the current collector, the reactions mostly occur at the vicinity of the pore mouth of the sub-pore domain. The Li then diffuses toward the PA center solely through the inter-particle diffusion process.

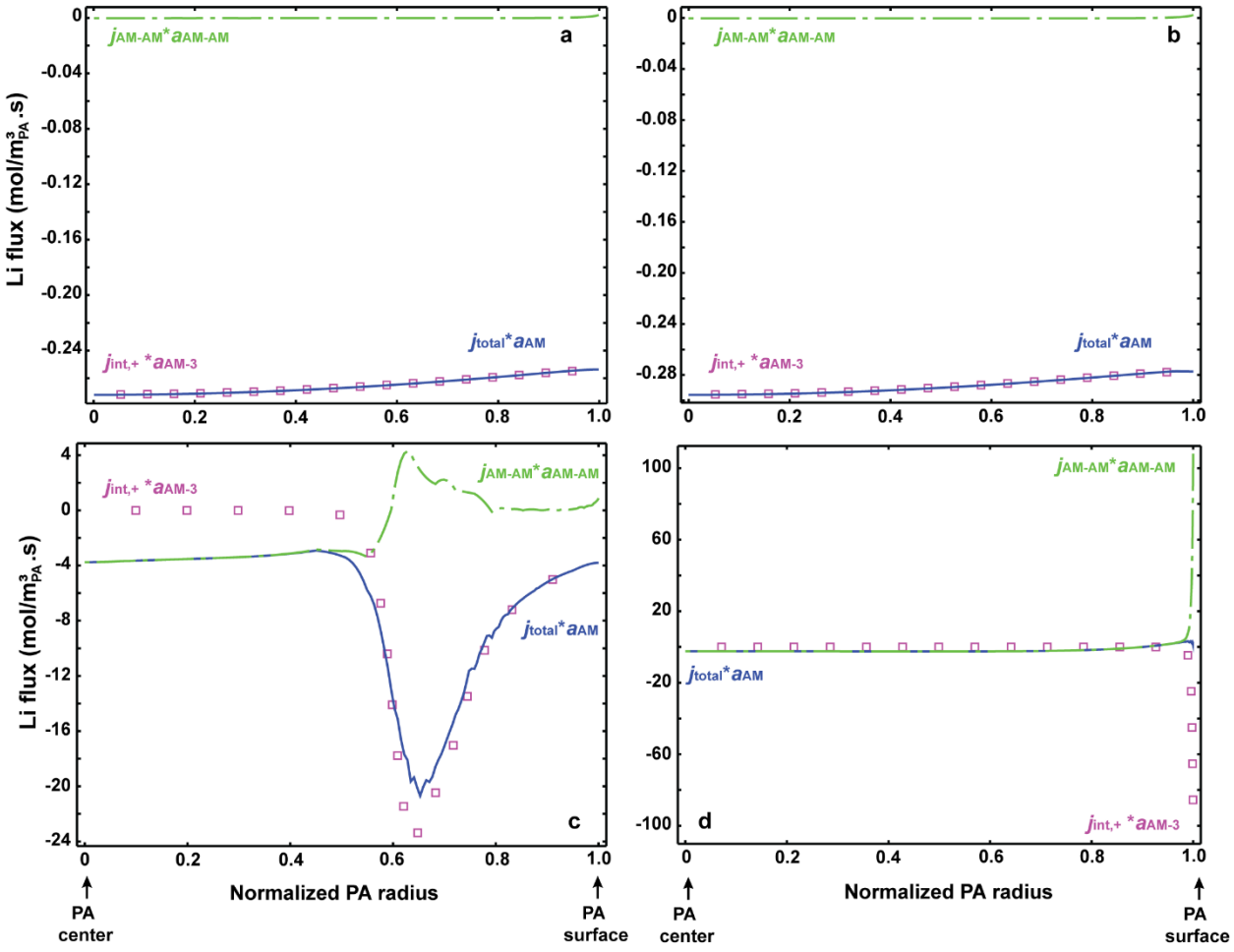

Figure VI-30. The Li flux flows within the PA at EoD. a, c. For PA located at separator side upon discharge at C/25 and 1C, respectively. **b, d.** For PA located at Al foil side upon discharge at C/25 and 1C, respectively.

VI.4.2.3 Model analysis

One of the unique strengths of battery modeling is its ability to predict the distributions of current, potential, and concentrations across the full cell during the operation of the battery. This often will provide information that is either difficult or impossible to determine experimentally, and improve our understanding of the phenomena occurring inside the cells.

After the validation of experimental results, the model can be used for an in-depth analysis of the electrode performance, which allows resolving the electrode overpotential into separated polarization sources and identifying performance limiting factors for each electrode design.

For this purpose, all the limitation sources are turned off sequentially. This means that parameter values are tuned so that limitations of corresponding physical phenomena are cancelled in the simulations. To this end, electrolyte conductivity, kinetic rate constant, and electrolyte/solid diffusion coefficient are set to high values. In addition, for electrolyte limitations shutdown, the

lithium transference number and thermodynamic factor are set to one. It is worth noting that the electrolyte limitations in the sub-pore domain are combined with the inter-particle diffusion into a so-called porous agglomerate effects, since they are parallel transport pathways and cannot be completely decorrelated. The electrolyte limitations in the sub-pore domain are, therefore, separately investigated from those in the macro-pore domain.

Here, we investigate samples MX-01b and MX-02, which provide us with the worst and the best performance among the four electrode designs, respectively. Figure VI-31 shows three cases with low, moderate and high current density for both samples. For both electrodes, at low C-rates, the performance is primarily limited by the solid diffusion within the secondary particles. This explains why the results simulated by the Newman baseline and PApa models are very similar at low current. As the current density increases, different contributions from other sources are involved as limitations of the electrode performance. For MX-01b, albeit the PE limitations still dominate as one moves to higher C-rates (1C, *ca.* 4 mA/cm^2), the effects from PA formation become significant. The rate capability of MX-01b can be considerably improved (up to 44% of EoD capacity at 1C) if we can avoid the negative effects from the PA.

For MX-02, given its high porosity and lower loading, limitations from liquid phase are minor compared to other sources even at 1C. The limitations are mainly at the PA and the particle scales, as the intra-particle solid diffusion is the most critical followed by the PA limitations. Without the presence of PAs, the rate capability of MX-02 can be improved up to 12% of EoD capacity at 1C.

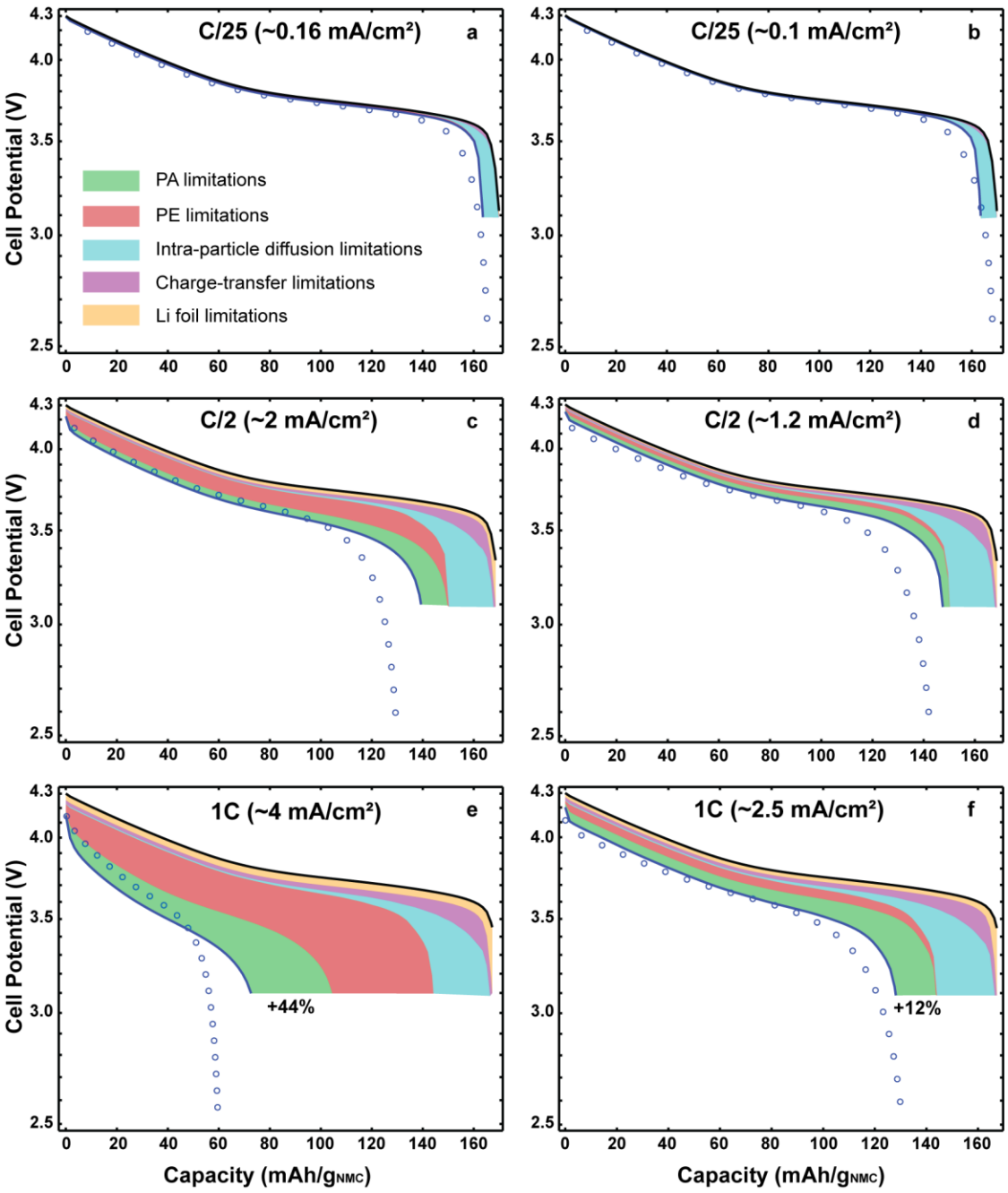

Figure VI-31. Decomposition of the potential curve. The potential curves along with experimental data (circles) at C/25, C/2 and 1C for MX-01b (**a**, **c**, **e**) and MX-02 (**b**, **d**, **f**) are resolved into different limitation sources. Starting from "as-is" simulations (blue line), porous agglomerate effects are first shutdown (light green), followed by porous electrode effects (light red), solid-phase diffusion intra-particles (cyan) and eventually the charge-transfer polarization (light purple). Lithium foil polarization (light orange) forms the last overpotential source up to the equilibrium potential represented as a solid black line.

VI.5 Conclusions

Industry-grade electrodes with high loading and density are capable of storing large amounts

of Li/energy, which is a requirement for battery packs to meet customer's expectation in terms of battery autonomy. However, the downside is that the power capability of such electrodes is limited. In this work, a combined experimental/modeling approach is carried out in order to shed light on the discharge performance limitations of these electrodes.

Thin electrodes, which have minor porous electrode effects are used to determine and validate intrinsic AM properties (D_s, k_0). Other electrode properties such as the electrode tortuosity factor and the effective electronic conductivity are determined through appropriate experiments.

Regarding the experimental results, three different electrolytes are used to gain more insights on the effects of liquid-phase limitations upon discharge. Electrodes with higher amounts of CBD are found to exhibit a worse performance than those with a lower amount of CBD, despite a higher electronic conductivity. Tomographic data from our previous work suggested that the dispersion of CBD might play a crucial role to improve the rate performance.

First, a classic Newman P2D model is used for validation of the experimental discharge rate capability of the four industry-grade electrodes at room temperature. Although this model on thin electrodes provides a strong agreement with the experimental data for the entire range of C-rates (up to 20C), its output only matches the experimental data at low C-rates, while diverges at higher C-rates for all the industry-grade electrodes. Different hypotheses from the literature are investigated, but none of these leads to adequate results.

Therefore, a new macroscale battery model, referred to as the PApa model, is constructed, taking into account the effects of possible porous agglomerates originating from the severe calendering process undergone by thick and dense electrodes. The new model has three additional parameters compared to regular Newman P2D model. Since X-ray tomography technique was used to quantify the fraction of particle surface exposed to the electrolyte, only two parameters (R_{PA}, ξ_3) were used as fitting parameters by which model output was tuned to match experimental results qualitatively for all electrode/electrolyte couples investigated here.

Compared to the Newman model, the PApa model showed a better agreement with the experimental results for all the industry-grade electrode up to 4 mA/cm² of current density. The values of fitting parameters (R_{PA}, ξ_3) are also consistent with the expectations. Higher-loading and higher-density electrodes result in a higher amount of pores that are sub-pores, and a larger apparent size of porous agglomerates. Both features exacerbate the limitations on the electrode performance.

For industry-grade electrodes used in this work, at low C-rates whenever the liquid-phase does not generate high limitations, solid-diffusion within individual NMC secondary particles is the performance-limiting factor. As one moves to higher C-rates, the PA effects turn a critical limitation source that deteriorates the rate performance of these electrodes. The model analysis suggests that a substantial gain in performance at high C-rate is expected if proper way rounds are figures to mitigate the agglomeration effects in these high-energy electrodes.

Nomenclature

A_{PA}	$\mathrm{m}_{\mathrm{PA}}^2/\mathrm{m}_{\mathrm{PE}}^3$	Specific interfacial area between the porous agglomerate and the liquid phase in macro-pore domain per unit volume of porous electrode
A_{CC}	$\mathrm{m}_{\mathrm{CC}}^2$	Current collector surface area
$a_{\mathrm{AM-3}}$	$\mathrm{m}_{\mathrm{AM-3}}^2/\mathrm{m}_{\mathrm{PA}}^3$	Specific interfacial area between the active materials and the liquid phase in the sub-pore domain at porous agglomerate scale
$a_{\mathrm{AM-AM}}$	$\mathrm{m}_{\mathrm{AM-AM}}^2/\mathrm{m}_{\mathrm{PA}}^3$	Specific interfacial area between the active materials particles at porous agglomerate scale
$\bar{c}_{\mathrm{s}}$	$\mathrm{mol}/\mathrm{m}_{\mathrm{AM}}^3$	Local volume-averaged of intercalated Li concentration in active materials phase within porous agglomerate
$c_{\mathrm{s,surf}}$	$\mathrm{mol}/\mathrm{m}_{\mathrm{AM}}^3$	Concentration of intercalated Li at the surface of the AM particle within porous agglomerate
$c_{\mathrm{s,max}}$	$\mathrm{mol}/\mathrm{m}_{\mathrm{AM}}^3$	Maximum concentration of intercalated Li in active materials particle
c_{s}	$\mathrm{mol}/\mathrm{m}_{\mathrm{AM}}^3$	Intercalated Li concentration within active materials particle
$c_{i,0}$	$\mathrm{mol}/\mathrm{m}^3$	Solvent concentration in phase i
c_i	$\mathrm{mol}/\mathrm{m}^3$	Salt concentration in a binary electrolyte in phase i
d_{50}	μm	Median diameter of active materials particles
D	m^2/s	Measured diffusion coefficient of a bulk binary electrolyte
$D_{\mathrm{eff},i}$	m^2/s	Effective salt diffusion coefficient of the liquid phase in phase i
D_{s}	m^2/s	Diffusion coefficient of Li in active materials particles
E_{a}	eV	Activation energy
F	C/mol	Faraday's constant
$f_{\mathrm{AM-3}}$		Fraction of particle surface in contact with the electrolyte in sub-pores

$f_{\pm}$		Mean molar activity coefficient of a binary electrolyte
$\vec{I}_1$	$\mathrm{A/m^2_{CC}}$	Electronic current density across porous electrode in the solid phase in the PApa model
$\vec{I}_2$	$\mathrm{A/m^2_{CC}}$	Ionic current density across porous electrode in the liquid phase in the PApa model
$\vec{\imath}_i$	$\mathrm{A/m^2_{CC}}$	Current density in phase i in the Newman P2D model or at porous agglomerate scale in the PApa model
i_{n}^0	$\mathrm{A/m^2_{ASA}}$	Exchange current density at the active surface area across porous electrode
i_{Li}^0	$\mathrm{A/m^2_{Li\ foil}}$	Exchange current density at the Li foil
I	A	Applied total current in the μ4-probe experiment
I_{app}	$\mathrm{A/m^2_{CC}}$	Discharge current density
$j_{\mathrm{int},+}$	$\mathrm{mol/(m^2_{AM-3} \cdot s)}$	Cation internal pore-wall flux within porous agglomerate
$j_{3,-}$	$\mathrm{mol/(m^2_{PA} \cdot s)}$	Net exchange anion flux between macro-pore domain in porous electrode and sub-pore domain within porous agglomerate
$j_{3,+}$	$\mathrm{mol/(m^2_{PA} \cdot s)}$	Net exchange cation flux between macro-pore domain in porous electrode and sub-pore domain within porous agglomerate
$j_{\mathrm{AM-AM}}$	$\mathrm{mol/(m^2_{AM-AM} \cdot s)}$	Rate of transfer of solid Li between active materials particles in contact
j_{n}	$\mathrm{mol/(m^2_{AM} \cdot s)}$	Pore-wall flux between active material particles and liquid phase in the Newman model
j_{total}	$\mathrm{mol/(m^2_{AM} \cdot s)}$	Total flux entering the active materials particle within porous agglomerate
k_0	$\mathrm{mol/[m^2 \cdot s \cdot (mol/m^3)^{1.5}]}$	Reaction rate constant of the active materials

$k_{0,\mathrm{Li}}$	$\mathrm{mol}/[\mathrm{m}^2 \cdot \mathrm{s} \cdot (\mathrm{mol}/\mathrm{m}^3)^{0.5}]$	Reaction rate constant of the Li foil
L_{PE}	μm	Porous electrode thickness
L_{sep}	μm	Separator thickness
L_{elyte}	m	Diffusion length in electrolyte
$\vec{n}$		Outward pointing unit normal to a plane or each voxel face
$\vec{N}_i$	$\mathrm{mol}/(\mathrm{m}^2 \cdot \mathrm{s})$	Flux density of species i in the Newman P2D model
$\vec{N}_{2,-}$	$\mathrm{mol}/(\mathrm{m}^2 \cdot \mathrm{s})$	Flux density of the anion in macro-pore domain at porous electrode scale in the PApa model
$\vec{n}_{3,-}$	$\mathrm{mol}/(\mathrm{m}^2 \cdot \mathrm{s})$	Flux density of the anion in sub-pore domain at porous agglomerate scale in the PApa model
$\vec{n}_{\mathrm{AM-AM}}$	$\mathrm{mol}/(\mathrm{m}^2 \cdot \mathrm{s})$	Li flux diffusing between active materials particles within porous agglomerate
$\vec{n}_{\mathrm{s}}$	$\mathrm{mol}/(\mathrm{m}^2 \cdot \mathrm{s})$	Li flux in the active materials particle
Q_{th}	Ah/kg	Electrode theoretical capacity
$\bar{q}$	$\mathrm{mol}/(\mathrm{m}^3 \cdot \mathrm{s})$	Volume-averaged concentration flux
R	$\mathrm{J}/(\mathrm{mol} \cdot \mathrm{K})$	Ideal gas constant
R	Ω	Sample resistance determined by the μ4-probe experiment
R_{PA}	μm	Porous agglomerate radius
r	m	Radial dimension along the active materials particle
r^*	m	Radial dimension of the porous agglomerate
r_{P}	μm	Radius of an active materials secondary particle
T	K	Absolute temperature
$T_{\mathrm{elyte},3}$	s	characteristic time of ionic transport in liquid phase

t_+^0		Transference number of Li^+ in the electrolyte with respect to the solvent velocity
U	V	Equilibrium potential of the AM vs Li
ΔV	V	Voltage drop between the two inner contacts in the µ4-probe experiment
V	V	Electrode or cell potential
$\vec{v}_0$	m/s	The solvent velocity
x	µm	Dimension across the sandwich
x_0		Initial Li stoichiometry

Greek symbols

α		Thermodynamic factor
β		Charge transfer coefficient
ε	m_{elyte}^3/m_{PE}^3	Porous electrode porosity
ε_{AM}	m_{AM}^3/m_{PA}^3	Volume fraction of the AM phase at porous agglomerate scale
ε_{sep}	m_{elyte}^3/m_{sep}^3	Separator porosity
ε_i	m_i^3/m_{PA}^3	Volume fraction of phase i at porous agglomerate scale
κ	S/m	Bulk ionic conductivity of the electrolyte
$\kappa_{eff,i}$	S/m	Effective ionic conductivity of the liquid phase in phase i
ρ_{el}	g/cm^3	Electrode density
σ_{eff}	S/m	Effective electronic conductivity of the solid phase of the electrode
τ_{AM}		Tortuosity factor of the active material phase
$\boldsymbol{\tau_{Br}}$		Tortuosity factor of the liquid phase by Bruggeman
$\tau_{e,i}$		Electrode tortuosity factor of phase i at porous agglomerate scale
τ_e		Electrode tortuosity factor

τ_{sep}		Separator tortuosity factor
ξ_3		Ratio of sub-pore domain among the total porosity of the porous electrode
$\Phi_{1,Li}$	V	Electric potential at Li foil
Φ_i	V	Electric potential of phase i
Ψ	m_{2+3}^3/m_{PE}^3	Total porosity of the porous electrode
Ψ_i	m_i^3/m_{PE}^3	Volume fraction of phase i at porous electrode scale
Ψ_{PA}	m_{PA}^3/m_{PE}^3	Porous agglomerate volume fraction at porous electrode scale

Subscripts

0	Solvent
1	Solid Matrix (Active Materials + Additives)
2	Liquid Phase (Electrolyte) in the pore space (Newman model) or in macro-pores (PApa model)
3	Liquid Phase (Electrolyte) in sub-pores (PApa model)
+	Cation of the Salt
−	Anion of the Salt
AM	Related to the Active Materials
eff	Effective properties
PE	Belong to the Porous Electrode

PA	Belong to the Porous Agglomerate

References

[1] J. Kim, H. Lee, H. Cha, M. Yoon, M. Park, J. Cho, *Adv. Energy Mater.* **2018**, *8*, 1702028.

[2] S. T. Myung, F. Maglia, K. J. Park, C. S. Yoon, P. Lamp, S. J. Kim, Y. K. Sun, *ACS Energy Lett.* **2017**, *2*, 196.

[3] A. Manthiram, B. Song, W. Li, *Energy Storage Mater.* **2017**, *6*, 125.

[4] W. Li, E. M. Erickson, A. Manthiram, *Nat. Energy* **2020**, *5*, 26.

[5] J. Li, A. R. Cameron, H. Li, S. Glazier, D. Xiong, M. Chatzidakis, J. Allen, G. A. Botton, J. R. Dahn, *J. Electrochem. Soc.* **2017**, *164*, A1534.

[6] X. Lu, A. Bertei, D. P. Finegan, C. Tan, S. R. Daemi, J. S. Weaving, K. B. O. Regan, T. M. M. Heenan, G. Hinds, E. Kendrick, D. J. L. Brett, P. R. Shearing, *Nat. Commun.* **2020**, *11*, 1.

[7] T. Nguyen, J. Villanova, Z. Su, R. Tucoulou, B. Fleutot, B. Delobel, C. Delacourt, A. Demortière, *Adv. Energy Mater.* **2021**, *11*, 2003529.

[8] M. M. Forouzan, B. A. Mazzeo, D. R. Wheeler, *J. Electrochem. Soc.* **2018**, *165*, DOI 10.1149/2.1281809jes.

[9] L. Almar, J. Joos, A. Weber, E. Ivers-Tiffée, *J. Power Sources* **2019**, *427*, 1.

[10] H. Zheng, L. Tan, G. Liu, X. Song, V. S. Battaglia, *J. Power Sources* **2012**, *208*, 52.

[11] R. Xu, Y. Yang, F. Yin, P. Liu, P. Cloetens, Y. Liu, F. Lin, K. Zhao, *J. Mech. Phys. Solids* **2019**, *129*, 160.

[12] D. E. Stephenson, B. C. Walker, C. B. Skelton, E. P. Gorzkowski, D. J. Rowenhorst, D. R. Wheeler, *J. Electrochem. Soc.* **2011**, *158*, A781.

[13] S. L. Morelly, N. J. Alvarez, M. H. Tang, *J. Power Sources* **2018**, *387*, 49.

[14] S. Malifarge, B. Delobel, C. Delacourt, *J. Electrochem. Soc.* **2018**, *165*, A1275.

[15] J. Newman, W. Tiedemann, *AIChE J.* **1975**, *21*, 25.

[16] T. F. Fuller, M. Doyle, J. Newman, *J. Electrochem. Soc.* **1994**, *141*, 982.

[17] J. Newman, K. E. Thomas, H. Hafezi, D. R. Wheeler, in *J. Power Sources*, Elsevier, **2003**, pp. 838–843.

[18] J. Newman, K. E. Thomas-Alyea, *Electrochemical Systems*, Wiley-Blackwell, **2012**.

[19] and D. U. S. Madeleine Ecker, Thi Kim Dung Tran, Philipp Dechent, Stefan Käbitz, Alexander Warnecke, *J. ofThe Electrochem. Soc.* **2015**, *162*, 1836.

[20] J. Schmalstieg, C. Rahe, M. Ecker, D. U. Sauer, *J. Electrochem. Soc.* **2018**, *165*, A3799.

[21] and E. K. Chang-Hui Chen, Ferran Brosa Planella, Kieran O'Regan, Dominika Gastol, W. Dhammika Widanage, *J. Electrochem. Soc.* **2020**, *167*, DOI 10.1149/1945-7111/ab9050.

[22] M. Doyle, J. Newman, A. S. Gozdz, C. N. Schmutz, J. Tarascon, *J. Electrochem. Soc.* **1996**, *143*, 1890.

[23] P. Albertus, J. Christensen, J. Newman, *J. Electrochem. Soc.* **2009**, *156*, A606.

[24] S.-L. Wu, D. Y. Parkinson, Y. Fu, S. Ferreira, V. Battaglia, V. Srinivasan, *J. Electrochem. Soc.* **2017**, *164*, 3473.

[25] A. M. Colclasure, A. R. Dunlop, S. E. Trask, B. J. Polzin, A. N. Jansen, K. Smith, *J. Electrochem. Soc.* **2019**, *166*, A1412.

[26] S. J. Tambio, F. Cadiou, E. Maire, N. Besnard, M. Deschamps, B. Lestriez, *J. Electrochem. Soc.* **2020**, *167*, 160509.

[27] W. A. Appiah, J. Park, S. Song, S. Byun, M. H. Ryou, Y. M. Lee, *J. Power Sources* **2016**, *319*, 147.

[28] M. Xu, B. Reichman, X. Wang, *Energy* **2019**, *186*, DOI 10.1016/j.energy.2019.115864.

[29] C. Delacourt, "DUMBAT," can be found under http://charles.delacourt.free.fr/dumbat, **n.d.**

[30] V. R. Subramanian, V. D. Diwakar, D. Tapriyal, *J. Electrochem. Soc.* **2005**, *152*, A2002.

[31] S. Dargaville, T. W. Farrell, *J. Electrochem. Soc.* **2010**, *157*, A830.

[32] S. Lueth, U. S. Sauter, W. G. Bessler, *J. Electrochem. Soc.* **2016**, *163*, A210.

[33] O. Birkholz, M. Kamlah, *Energy Technol.* **2021**, 2000910.

[34] W. L. Bin Wu, *J. ofThe Electrochem. Soc.* **2016**, *163*, 3131.

[35] R. Amin, Y.-M. Chiang, *J. Electrochem. Soc.* **2016**, *163*, A1512.

[36] S. G. Stewart, J. Newman, *J. Electrochem. Soc.* **2007**, *155*, F13.

[37] J. Landesfeind, J. Hattendorff, A. Ehrl, W. A. Wall, H. A. Gasteiger, *J. Electrochem. Soc.* **2016**, *163*, A1373.

[38] S. Malifarge, B. Delobel, C. Delacourt, *J. Electrochem. Soc.* **2017**, *164*, E3329.

[39] I. Shiraki, F. Tanabe, R. Hobara, T. Nagao, S. Hasegawa, *Surf. Sci.* **2001**, *493*, 633.

[40] I. Miccoli, F. Edler, H. Pfnür, C. Tegenkamp, *J. Phys. Condens. Matter* **2015**, *27*, 223201.

[41] B. Voigtländer, V. Cherepanov, S. Korte, A. Leis, D. Cuma, S. Just, F. Lüpke, B. Voigtï, F. L. ¨ Upke, *Rev. Sci. Instrum.* **2018**, *89*, 101101.

[42] H. Lundgren, M. Behm, G. Lindbergh, *J. Electrochem. Soc.* **2015**, *162*, A413.

[43] J. Landesfeind, H. A. Gasteiger, *J. Electrochem. Soc.* **2019**, *166*, A3079.

[44] M. Mastali, M. Farkhondeh, S. Farhad, R. A. Fraser, M. Fowler, *J. Electrochem. Soc.* **2016**, *163*, A2803.

[45] S.-L. Wu, W. Zhang, X. Song, A. K. Shukla, G. Liu, V. Battaglia, V. Srinivasan, *J. Electrochem. Soc.* **2012**, *159*, 438.

[46] A. Verma, K. Smith, S. Santhanagopalan, D. Abraham, K. P. Yao, P. P. Mukherjee, *J. Electrochem. Soc.* **2017**, *164*, A3380.

[47] J. Park, H. Zhao, S. D. Kang, K. Lim, C.-C. Chen, Y.-S. Yu, R. D. Braatz, D. A. Shapiro, J. Hong, M. F. Toney, M. Z. Bazant, W. C. Chueh, *Nat. Mater. 2021 207* **2021**, *20*, 991.

[48] "Celgard," can be found under https://www.celgard.com/, **n.d.**

[49] C. Delacourt, M. Ati, J. M. Tarascon, *J. Electrochem. Soc.* **2011**, *158*, A741.

[50] J. Li, F. Yang, X. Xiao, M. W. Verbrugge, Y. T. Cheng, *Electrochim. Acta* **2012**, *75*, 56.

[51] J. Li, X. Xiao, F. Yang, M. W. Verbrugge, Y. T. Cheng, *J. Phys. Chem. C* **2012**, *116*, 1472.

[52] M. D. Levi, D. Aurbach, *The Journal of Physical Chemistry B*, **1997**,*101*(23), 4641-4647.

[53] C. Montella, *Electrochim. Acta* **2006**, *51*, 3102.

[54] S. Malifarge, B. Delobel, C. Delacourt, *J. Electrochem. Soc.* **2017**, *164*, A3925.

[55] E. Markevich, M. D. Levi, D. Aurbach, *J. Electroanal. Chem.* **2005**, *580*, 231.

[56] D. R. Baker, M. W. Verbrugge, *J. Electrochem. Soc.* **2013**, *160*, A1319.

[57] R. S. Nicholson, I. Shain, *Anal. Chem.* **1964**, *36*, 706.

[58] Q. Guo, V. R. Subramanian, J. W. Weidner, R. E. White, *J. Electrochem. Soc.* **2002**, *149*,

A307.

[59] G. Sikha, R. E. White, *J. Electrochem. Soc.* **2007**, *154*, A43.

[60] I. V. Thorat, D. E. Stephenson, N. A. Zacharias, K. Zaghib, J. N. Harb, D. R. Wheeler, *J. Power Sources* **2009**, *188*, 592.

[61] F. Pouraghajan, H. Knight, M. Wray, B. Mazzeo, R. Subbaraman, J. Christensen, D. Wheeler, *J. Electrochem. Soc.* **2018**, *165*, 2644.

[62] K. S. F.L.E. Usseglio-Viretta, A. Colclasure, A.N. Mistry, K.P.Y. Claver, F. Pouraghajan, D.P. Finegan, T.M.M. Heenan, D. Abraham, P.P. Mukherjee, D. Wheeler, P. Shearing, S.J. Cooper, *J. Electrochem. Soc.* **2018**, *165*, A3403.

[63] T. T. Nguyen, A. Demortière, B. Fleutot, B. Delobel, C. Delacourt, S. J. Cooper, *npj Comput. Mater.* **2020**, *6*, 1.

[64] S. J. Cooper, A. Bertei, P. R. Shearing, J. A. Kilner, N. P. Brandon, *SoftwareX* **2016**, *5*, 203.

[65] S. W. Peterson, D. R. Wheeler, *J. Electrochem. Soc.* **2014**, *161*, A2175.

[66] H. Zheng, R. Yang, G. Liu, X. Song, V. S. Battaglia, *J. Phys. Chem. C* **2012**, *116*, 4875.

[67] F. Cadiou, T. Douillard, N. Besnard, B. Lestriez, E. Maire, J. Electrochem. Soc., **2020**, 167(10), 100521.

[68] J. Landesfeind, M. Ebner, A. Eldiven, V. Wood, H. A. Gasteiger, *J. Electrochem. Soc.* **2018**, *165*, A469.

[69] R. Tang, Q. Yun, W. Lv, Y. B. He, C. You, F. Su, L. Ke, B. Li, F. Kang, Q. H. Yang, *Carbon N. Y.* **2016**, *103*, 356.

[70] H. Bockholt, M. Indrikova, A. Netz, F. Golks, A. Kwade, *J. Power Sources* **2016**, *325*, 140.

[71] K. G. Gallagher, S. E. Trask, C. Bauer, T. Woehrle, S. F. Lux, M. Tschech, P. Lamp, B. J. Polzin, S. Ha, B. Long, Q. Wu, W. Lu, D. W. Dees, A. N. Jansen, *J. Electrochem. Soc.* **2016**, *163*, A138.

[72] N. Epstein, *Chem. Eng. Sci.* **1989**, *44*, 777.

[73] K. E. Thomas, J. Newman, R. M. Darling, *Advances in lithium-ion batteries*, **2002**.

[74] M. E. Ferraro, B. L. Trembacki, V. E. Brunini, D. R. Noble, S. A. Roberts, *J. Electrochem. Soc.* **2020**, *167*, 013543.

Chapter VII . Operando X-ray Computed Tomography coupled with XANES spectroscopy

VII.1 Introduction

One of the objectives of this work is to identify the microstructural heterogeneities and to understand their effects on the electrochemical performance, and eventually improve the electrode design.

For this purpose, a multimodal approach (electrochemical measurements combined with tomography techniques) has been used in the literature, despite significant efforts required for the setup preparation as well as the data post-processing. Our previous chapters are part of this multimodal approach as an attempt to learn more about the interplay between the microstructural and performance.

As we can see so far, while tomography techniques have been significantly developed and stand as a powerful tool to investigate the microstructural properties of the electrodes (Chapter II)[5–10], local electrochemical properties (*e.g.,* effective ionic conductivity, charge transfer impedance) are not trivial to measure by traditional electrochemical methods. Forouzan *et al.*[2] attempted to tackle this issue by considering an inverse correlation between the local electronic and ionic conductivities, as the mixture of additives, referred to as CBD, increases the electronic conductivity but also the tortuosity of the ionic conducting pathway with its nano-porosity. The local effective electronic conductivity was determined by a µ4-line system. The authors can, therefore, qualitatively correlate the microstructure of the electrode to its effective transport properties. A similar method, the µ4-probe was also adopted for the electronic conductivity mapping of the electrodes used in this work (chapter VI).

On the other hand, reaction distributions in composite battery electrodes can also be investigated using various techniques such as Raman microscopy,[11] X-ray diffraction (XRD),[12] or 2D XANES.[13–16] However, these methods have been restricted to 2D observation, because the obtained signal is usually spatially integrated along the depth direction. Hence, these methods, cannot accurately capture the 3D spatial distributions and can lead to a wrong interpretation of the mechanism caused by the difficulty of uniquely interpreting complex 3D structures based on projected images.[17] Recently, Finegan *et al.*[18] used *Operando* X-ray diffraction-computed tomography (XRD-CT) for characterizing, in 3D, the dynamic crystallographic structure between and within $LiMnO_2$ particles during operation. This technique facilitates identification of stoichiometric and phase heterogeneities within particles and/or in the bulk electrode, so that the reaction distribution can also be inferred. Nevertheless, the technique does not provide the access to other phases of the electrode such as CBD.

In this chapter, a method to capture the electrode microstructure during high-rate electrochemical operation is presented. The goal is to propose a more efficient approach to unveil the effects of the microstructural heterogeneities on the electrochemical performance.

Several authors have combined XANES and tomography to generate a rich data set that allows a direct correlation of the chemical information and the microstructure. Meirer *et al.* used 3D

XANES to probe the conversion of NiO to Ni metal in a partly reduced electrode. They found significant inhomogeneities in terms of chemical states across the particle that depended on its size, as well as evidence of fracturing caused by volume expansion during the reaction. More recently, Wang et al. collected a 46-point spectrum across the iron K-edge of a $LiFePO_4$ cathode particle and developed a run-out correction system to enable automated tomography. Nonetheless, the insight collected was noteworthy, with the advent of a clear core−shell structure.

Here, we perform XANES coupled with nano-XCT in *Operando* mode to investigate NMC532 electrodes. The ability to probe battery materials in *Operando*, provides significant advantages over ex situ approaches, as the battery stays functional during experiment. It holds the promise of characterizing the microstructure while capturing the electrochemical behavior (transport properties and reaction kinetics) at nanoscale resolution.

Nevertheless, *Operando* measurements create the most severe challenges to an imaging experiment when considering the three scales of resolution above, namely, spatial, chemical, and temporal. Many battery reactions span several hours, but the need to build a reaction pathway means that it is desirable to collect at least five data points during the reaction. This goal imposes restrictions on the time available to complete an image containing the desired chemical information, at the desired level of spatial resolution. Unfortunately, all modes of chemical contrast require collecting multiple frames for the same reaction state to reconstruct a map of the species present in the field view. Using XANES microscopy as an example, chemical resolution is achieved by collecting frames at a large number of energies, with the limit being set by the precision of the upstream optics. In practice, the most common choice is to minimize the number of points to obtain some level of chemical resolution in the individual frame-set, scanning energy (spectroscopy).

Moreover, most of the works on *in situ/Operando* whether 2D XANES or XANES-XCT worked with electrodes having very low loading of active material, and very low AM density (*ca.* %v AM = 20%).[13,19,20] This helps to avoid the overlapping issue when performing the 2D XANES experiment, *i.e.,* the information through the depth is lost as it is lumped into one projection, while allowing high X-ray transmission during the acquisition (to maximize signal-to-noise ratio). With the type of electrodes that has been used in the prior art, electrochemical performance is mainly limited to the solid diffusion in the AM particles rather than porous-electrode effects.

For the first time to the best of author's knowledge, there is an attempt to work with electrodes that are similar to real-life designs (%v AM > 60%) along with a high operating current density. As such, the system is more sensitive to the porous electrode effects rather than just the AM intrinsic properties.

VII.2 Results

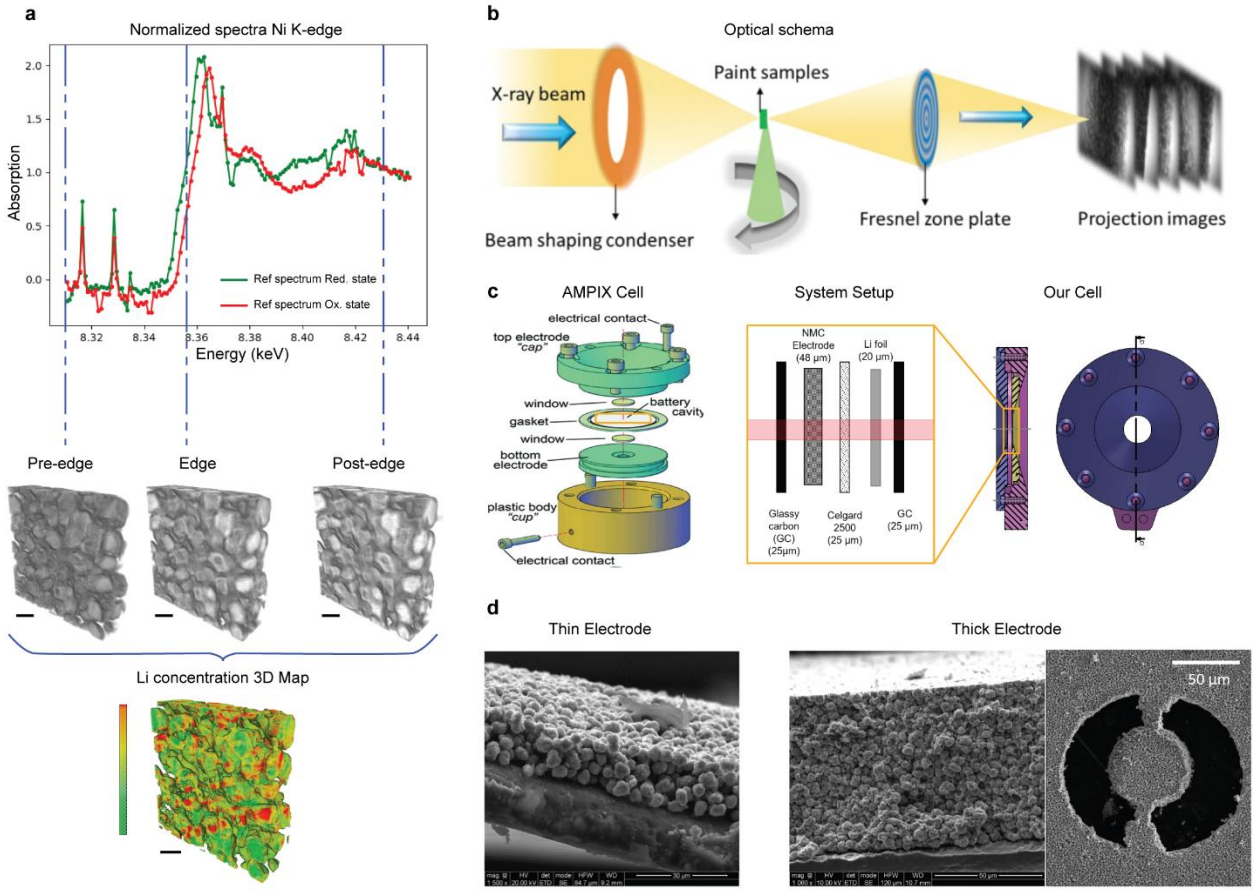

Figure VII-1. Illustration of the workflow used for this study. a. Two reference XANES were obtained at Ni K-edge for electrode at pristine (Li stoichiometry = 1) and delithiation state (*ca.* stoichiometry Li = 0.38). Three energy levels: pre-edge, edge, post-edge, were selected, at which three tomography datasets are obtained. The 3D map of Li concentration distribution can be extracted via the relative shift of the absorption edge, which reflects the shift of Ni oxidation state from NMC with Ni^{2+}/Ni^{3+} in a pristine state to NMC with Ni^{3+}/Ni^{4+} in a delithiation state (see details in Methods). **b.** Schematic representation of the hard X-ray nano-holotomography experimental setup. **c, d.** The two *Operando* electrochemical cells used in this work: AMPIX cell,[21,22] novel home-made cell, along with the low and high loading NMC electrodes that are used by each cell, respectively. The scale bar in **a** represent 10 µm.

Figure VII-1 illustrates the workflow used in this work, which highlights our approach for Li concentration mapping based on three energy levels (Figure VII-1a) and the use of two different electrodes that have similar AM density as real-life applications but have different AM loadings (Figure VII-1d). The thinner electrode, labelled as MX-A (AM loading = 3 mg/cm²), is made to facilitate the transmission of the X-ray through the sample without any further preparation steps as for higher AM loading electrode (AM loading = 15 mg/cm²), labelled as MX-B.

Within the cycling range between 2.5-4.3 V, Bak *et al.* reported that Ni is the predominant redox partner for lithium (de)intercalation in NMC, without any reactivities from Mn or Co have

been witnessed.[23] Hence, the Ni K-edge (Figure VII-1a) was selected to track the local Li content in the active material particles, as Ni edge is the most sensitive to the local electrochemical reactions (compared with Mn and Co).

Depending on the Ni oxidation state, the AM can exhibit a change in X-ray absorption coefficient at the K-edge leading to a change of voxels' intensity in the images. In spite of minor fluctuations at the pre-edge and post-edge energy, the AM keeps a stable interaction with the X-ray. This results in an invariance of intensity regardless the Ni oxidation state. Figures VII-1a shows the 3D volumes obtained at the X-ray energies of 8.30 keV (pre-edge), 8.35 keV (edge) and 8.43 keV (post-edge), respectively. As shown in these figures, an almost uniformly dark image was obtained when the X-ray energy was 8.30 keV. On the other hand, in the image obtained at 8.43 keV, the region where Ni was present showed a higher brightness. Edge absorption features (either edge position or peak top position) in the Ni K-edge have been shown in the literature to be approximately linearly correlated to Li content in NMC particles.[24,25] Thus, by following the relative change of the absorption coefficient at the edge level normalized by the absorption jump (gap between the pre-edge and post-edge's absorption coefficient), one can infer the local Li concentration at each voxel with a simple linear correlation. As a result, a 3D map of the Li distribution throughout the control volume can be derived.

It is worth to mention that two different electrochemical cells (Figure VII-1c) were used to carry out the *Operando* experiments in this work. The AMPIX cell,[21,22] developed by Argonne National Laboratory, allows *in situ* experiments including multiple synchrotron-based X-ray scattering and spectroscopy methodologies to be performed. However, it is not fully compatible with the setup for XCT experiment (*e.g.*, high thickness, low open-angle) leading to high dead-angle during the acquisition. To minimize the dead-angle that increases with the sample thickness, the AMPIX cell was only used for the thinner electrode, MX-A.

On the other hand, a new cell design has been developed that better satisfies requirements for XCT experiment giving high-quality tomographic data. Several features are optimized that allow the use of higher loading electrodes MX-B (loading AM = 15 mg/cm²) such as the cell thickness and the open-angle. The cell design is closely mirroring coin cell conditions, so that ensures good stack pressure as well as proper electrochemical functionality.

VII.2.1 Low loading Electrode MX-A

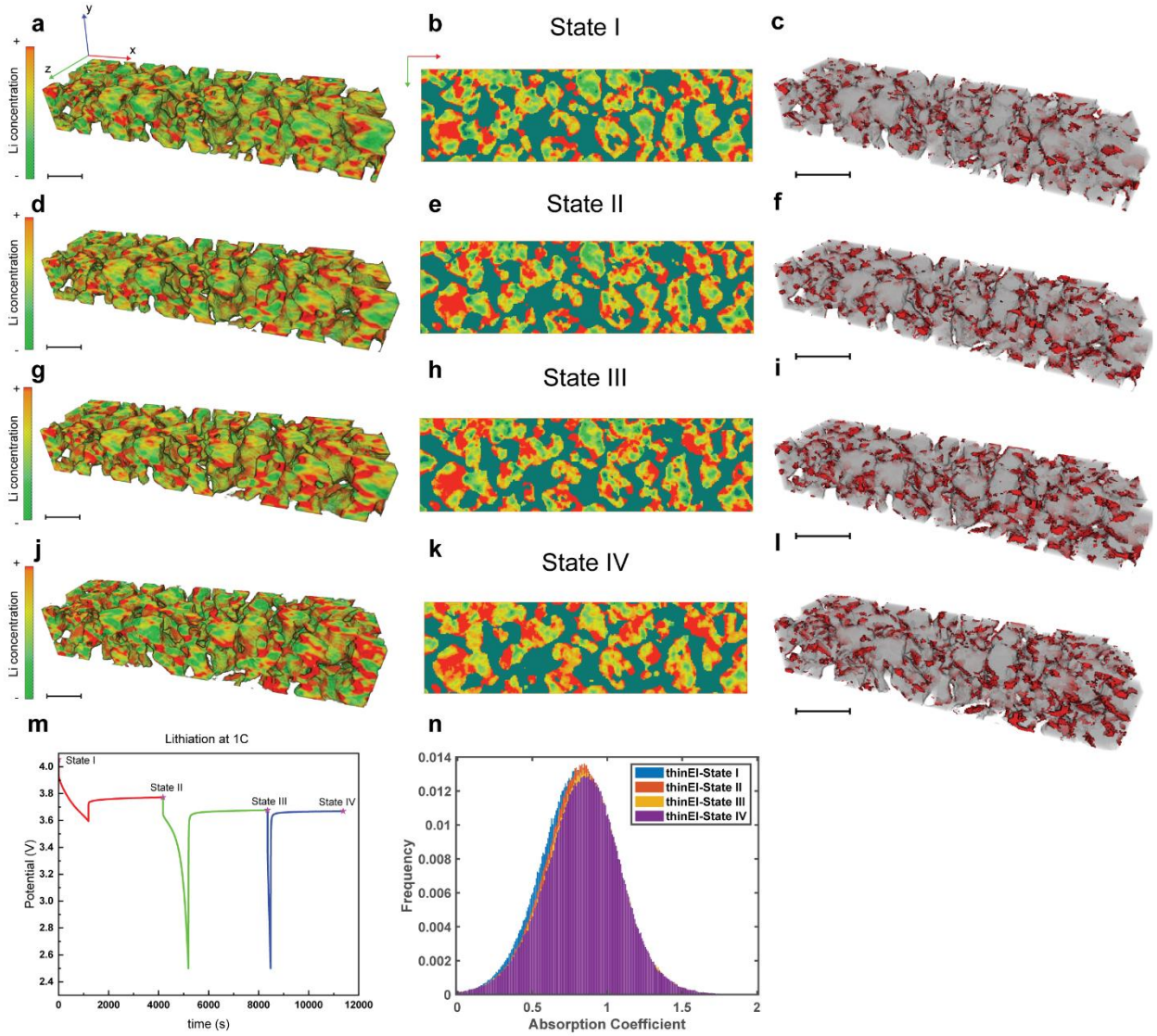

Figure VII-2. Results of thin electrodes MX-A using AMPIX cell. a, d , g, j. The 3D map of Li concentration extracted from the XANES-XCT performed at the end of the relaxation steps that correspond to state 1 to 4. **b, e ,h, k.** 2D slices of Li concentration distribution at the same electrode depth across different states of lithiation were shown for the ease of visualization. **c, f, i, l.** The repartition of Li-rich regions at each state are highlighted in red. **m.** The evolution of cell potential during the lithiation process. **n.** The distribution of voxel's absorption coefficient in each state. The Z-axis represents the direction of the electrode thickness. The scale bars represent 10 µm.

Given that the same region was monitored throughout the experiment, Figure VII-2a, d , g, j show the 3D Lithium concentration maps during the lithiation process with a current density of 2 mA/cm². The overall Li concentration increases, as the experiment goes from state 1 to 4, seen by the fact that the shading of each map turns reddish on average. Figure VII-2 c, f, i, l show an increase of the amount of Li-rich regions along the lithiation process, which are, however, not

well-dispersed throughout the volume (denser accumulation of Li-rich regions can be observed at the front-right corner of the electrode).

The 2D slices are also shown in Figure VII-2b, e ,h, k for the ease of the visualization. Overall, it can be seen that the core-shell structure is formed as the lithiation progresses. This result demonstrates that the Li intercalation starts first at the particle surface and moves toward the particle center as lithiation progresses, which is consistent with the results in [16]. However, it is worth noting that not all the particle surface area is active, as further discussed when zooming in individual AM particles (Figure VII-3).

The heterogeneity of Li spatial distribution can be investigated through the distribution of the absorption coefficient at each voxel, as it is directly related to the Li content at the voxel. A shift of the absorption coefficient to a higher value is found as the lithiation occurs, in agreement with the XANES theory (Figure VII-1a). However, one can see that the shift is minor in Figure VII-2n. Besides, one can notice a large polarization appearing during the lithiation process (green and blue curves in Figure VII-2m). It is possible that this large polarization stems from the use of AMPIX cell along with too low electrode thickness. According to the AMPIX design, an annular flat gasket is used as a means to accommodate battery stacks having a typical thickness of *ca.* 800 µm, which is significantly higher than the battery stack used with MX-A (*ca.* 400 µm for MX-A with Al current collector/Glassy fiber/Li foil). This can deteriorate the role of the 'spring' resistance necessary for controlling the application of stack pressure of the gasket, leading to higher polarization.

Figure VII-3a shows a zoom on the Li concentration evolution within the two particles as the lithiation proceeds. Notably, a heterogenous Li distribution is observed inside both particles as the Li front moves toward the particle center. This observation is consistent with other works using NMC as AM,[20,26] in which a heterogeneous Li distribution within the secondary particles was also witnessed.

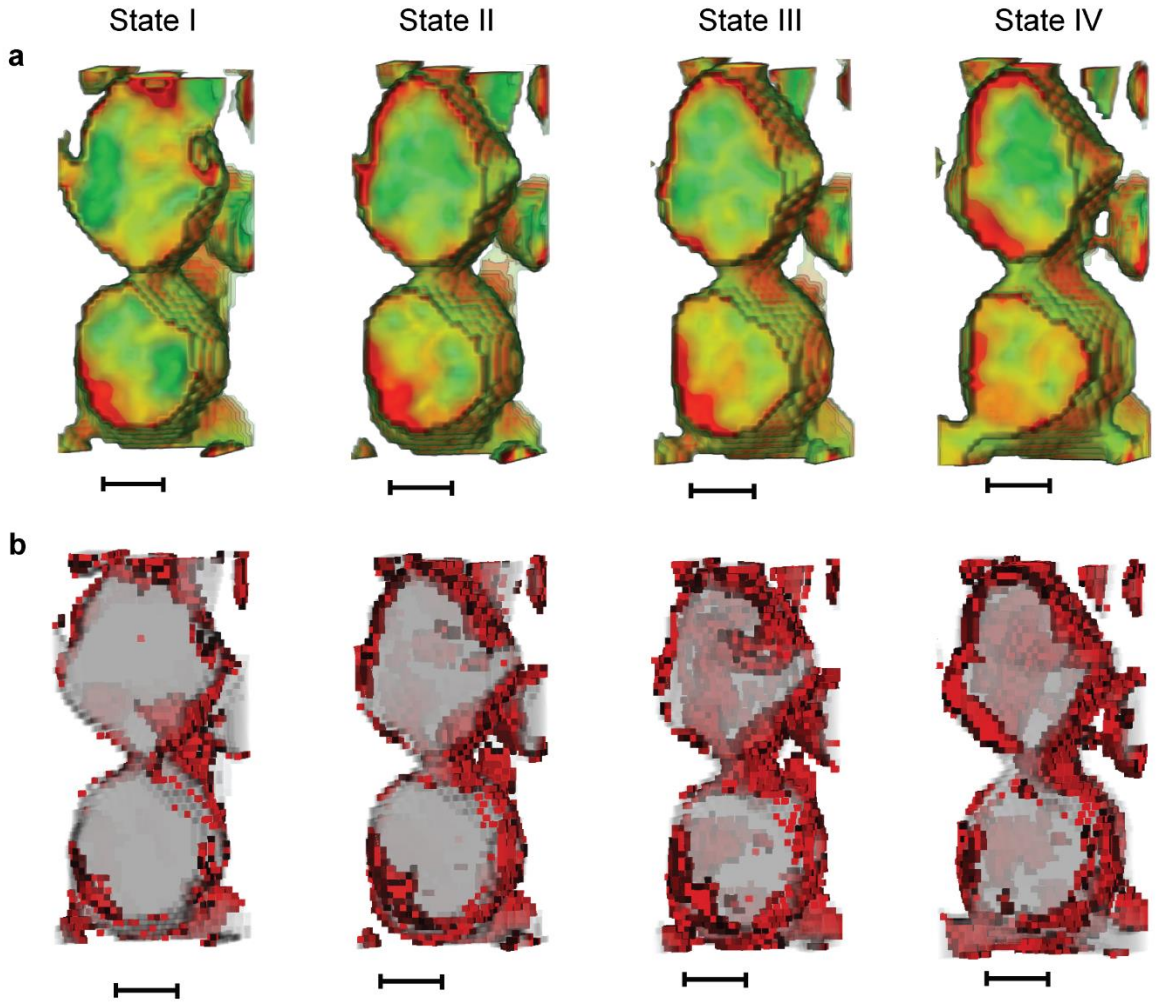

Figure VII-3. Zoom on the individual NMC secondary particles across the lithiation process. a. 3D map of Li concentration evolution as the lithiation proceeds. **b.** Repartition of the Li-rich regions (in red) at each state of lithiation (I-IV). The scale bars represent 2 µm.

Figure VII-3b highlights the Li-rich areas (in red), which mainly establish at the vicinity of the particle surface area during the lithiation process. These regions are not uniformly distributed over the particle surface area. Thus, Li intercalation is likely to occur at some preference sites. This might be attributed to the non-uniform distribution of phases such as the pore network or the CBD, which can impact the ionic/electronic transport to the reaction sites. Furthermore, the distribution of Li-rich regions at the AM particle surface might question the assumption used in macro-homogenous battery models that considers the entire particle surface area as available for reactions. Our next step will be to capture the presence of the CBD to understand further its role in the distribution of the reaction sites at the surface of the particles.

VII.2.2 High loading electrode MX-02

A industry-graded electrode with a substantial AM loading is subsequently investigated to reflect real-life scenarios better. Consequently, more limitations from the porous microstructures leading to higher non-uniformity of electrochemical behavior due to porous-electrode limitations are expected.

The electrode was charged by CCCV at *ca.* C/10 up to 4.3 V and relaxed (Figure VII-4a). Before the charge, the pristine electrode bears a uniform Li distribution throughout the volume (Figure VII-4b). Figure VII-4c shows the final Li concentration at delithiation state (state II) corresponding with the OCV that equals to 4.25 V at a different position than state I. Despite a moderate discharge rate following by a CV step, there still are regions having high Li concentration, *i.e.* electrochemical reactions might not take place at these regions. Still, we remarked a shift to more oxydation state of AM comapred to state I (majority is colored in green).

The discharge process is shown in Figure VII-5. It consists of two separate steps, starting from state II discharge to 50% DoD and from 50% DoD discharge to 2.5 V following by a CV step. We decided to reduce the number of acquistion points compared to the case of thin electrode, since we observed some important motion of the microstructure, *e.g.* detachment of the AM particles, during the acquistion. This makes the data processing cannot be ensured as the alignment would be challenging.

At 50% DoD, two different locations that went through the same lithiation process are shown in Figure VII-5b-c. Overall, the Li content at each state shows a good agreement with the expected values inferred from the electrochemical process. That is, a significant decrease of Li content at the end of the delithiation step (Figure VII-4b) then the Li concentration increases as we switch to the lithiation process (Figure VII-5b-c).

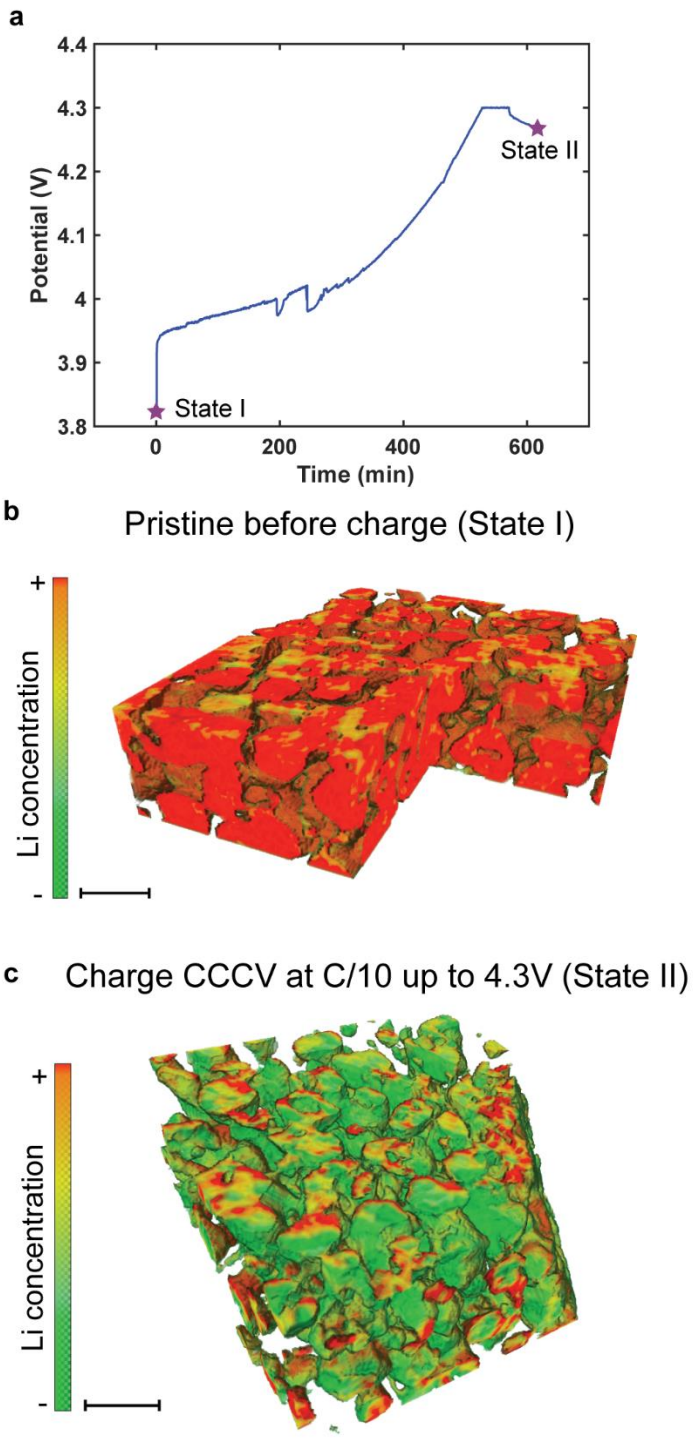

Figure VII-4. Results of thick electrode MX-B using our *Operando* cell during charge. a. The measured cell potential during the CCCV charge at C/10. The two XANES-XCT measurements are performed at points colored in purple. **b.** The 3D map of Li concentration at pristine state of the electrode before charging. **c.** The 3D map of Li concentration extracted from the XANES-XCT performed at the end of the relaxation step after reaching 4.3 V with a CCCV. The scale bars represent 8 µm.

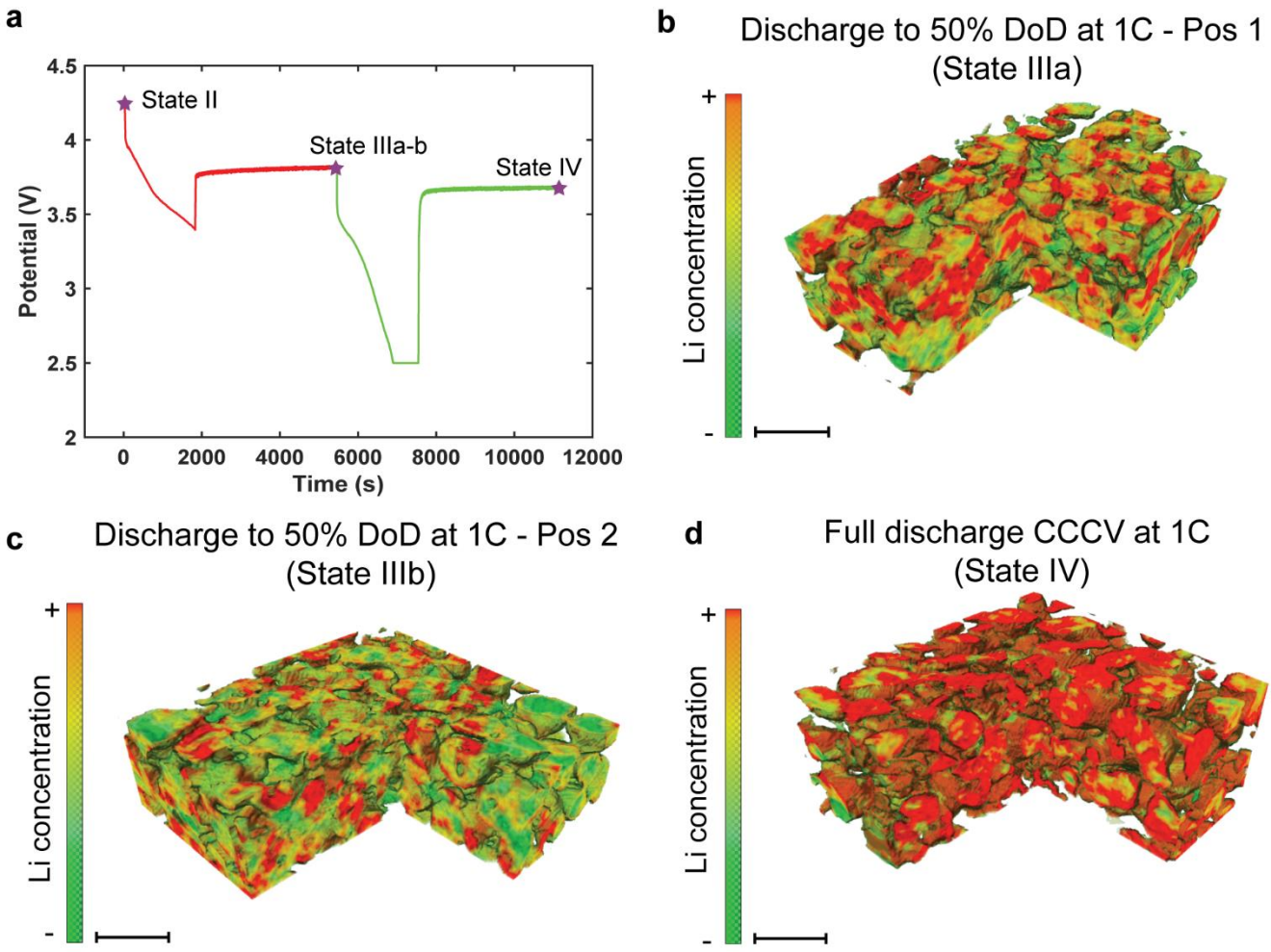

Figure VII-5. Results of thick electrode MX-02 using our *Operando* cell during discharge. a. The measured cell potential during the CC discharge at 1C. The three XANES-XCT measurements are performed at points colored in purple. **b-d.** The 3D map of Li concentration extracted from the XANES-XCT performed at the end of the relaxation steps that correspond to different states of lithiation. The scale bars represent 8 µm.

This is also confirmed in the bar graph, that compares the difference of Li content between different states (Figure VII-6a). It quantifies the volume fraction of three classes relying on their Li content: Li rich (where $0.9 \leq$ absorption coefficient), Li moderate (where $0.6 <$ absorption coefficient ≤ 0.9), and Li poor (where absorption coefficient ≤ 0.6), respectively. The bar graph unveils that the position in Figure VII-5b possesses a higher amount of Li than the position in Figure VII-5c, despite undergoing the same discharge process. This is evidence for electrochemical heterogeneity occurring across the electrode during the battery operation. Notably, the last step, after 1 hour of lithiation at 1C, shows a composition of Li concentration that is very close to the pristine electrode (Figure VII-5d).

Besides, the heterogeneity of Li content is also quantified, as shown in Figure VII-6b. The distribution of voxels' grey level is plotted, which is tantamount to the distribution of Li content

presented within the volume. The pristine electrode exhibits essentially uniform Li content, as the distribution represents a sharp peak. In contrast, at the end of the first charge, the electrode (Figure VII-4b) possesses a heterogenous Li concentration (broader distribution), where regions with high Li content still present. Interestingly, despite the good agreement of the overall Li concentration at the end of the lithiation process, the electrode (Figure VII-5e) bears a higher non-uniformity of the Li content when comparing to the pristine state.

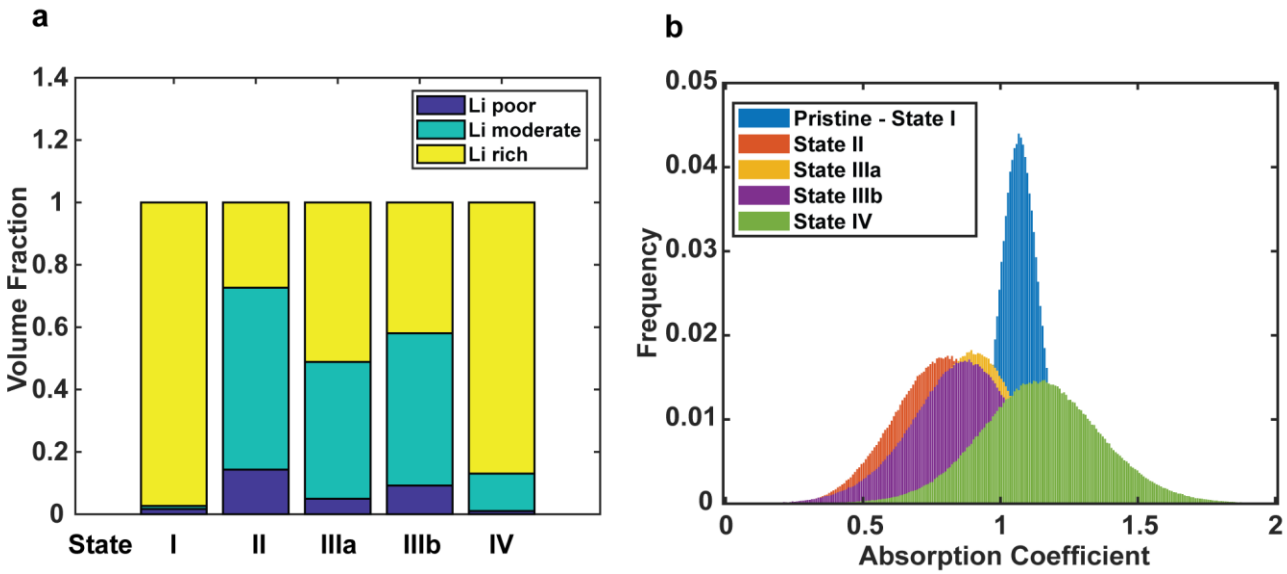

Figure VII-6. Summarize of the results. a. The bar graph represents the volume fraction of AM with different Li contents obtained from 3D quantitative analysis. **b.** The distribution of absorption coefficient at each voxel within the volume.

To quantitatively analyze the distribution of Li concentration in the thickness direction, we calculated the average Li content in each 2D slice in the through-plane direction (Z-axis) and plotted it as a function of distance in Z-axis (Figure VII-7). Pristine electrode (State I) shows an uniform high Li concentration across the thickness. Furthermore, position 2 also exhibits a higher uniformity of Li content than in position 1 after undergoing the same discharge condition. Overall, the average Li content was not significantly changed across the electrode thickness. The orientation of the thickness cannot be detected with our cell design. It should need further investigation in order to capture the electrochemical reaction evolving across the electrode thickness, which is crucial to investigate the effects of the porous electrode to the performance (*i.e.* transport in the liquid phase).

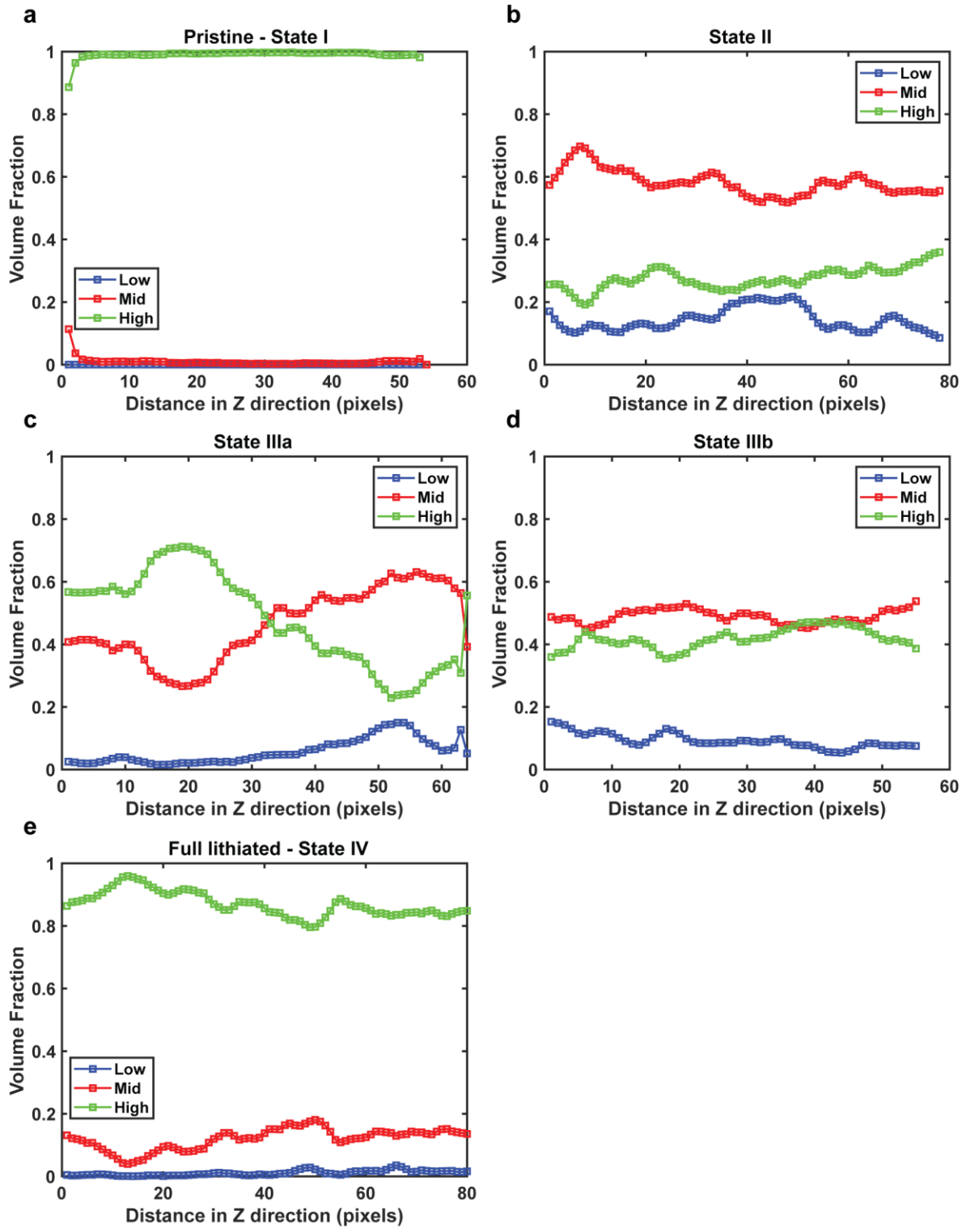

Figure VII-7. The volume fraction profiles along the Z-axis direction (through-plane) of the electrode. Each point was obtained by calculating the fraction of the phase in a 2D slice across the Z-axis. **a.** State I (Pristine electrode). **b.** State II (CCCV charge to 4.3 V). **c-d.** Discharge 1C to 50% DoD captured at position 1 and 2, respectively. **e.** State III (CCCV discharge to 2.5 V).

VII.3 Discussions

In this work, we demonstrate that *Operando* XANES-XCT nanoCT allows access to the Li distribution (local Li concentration) at nanoscale within the LiB electrodes during the operation. We also proposed a method that relies on just three energy levels located at pre-edge, edge, post-edge for minimization of radiation damage to the sample (see more details in Methods). Also, a specific electrochemical cell and a sample preparation process were introduced, which make the use of electrodes typical to those used in real-life applications possible. This is crucial for our study where our goal is to focus on the impact of the microstructure on the electrochemical performance at electrode scale rather than the composition distribution within an individual AM particle, as reported in previous works.

With the addition of three-dimensional capability, both microstructural and chemical properties are obtained for a given large control volume, avoiding an overlap of contributions to the attenuation and providing the opportunity to probe the sample at different locations throughout the electrode.

Our experimental results unveil the non-uniformity of the Li repartition throughout the LiB porous electrodes during operation. Besides the core-shell structure found within the AM particles arising from the solid diffusion, the heterogeneity mainly reflects the microstructural heterogeneity, that can locally impact the kinetics of the electrochemical reactions through a non-uniform distribution of whether ionic/electronic transport network or inter-connectivity between phases throughout the electrode. As a result, there are regions being more active than the others as well as preference spots on the particle surface where the reactions are more likely to occur.

The Li repartition across the electrode depth is adequately uniform, which indicates a negligible effect from porous electrode. It is worth noting that an electrolyte with high transport properties was used,[27] which can significantly reduce the effects from the porous electrode. Thus, the transport in electrolyte is not a rate limiting factor in this electrode under the applied cycling conditions.

However, without a knowledge of the CBD morphology in the microstructure, it is not possible to accurately address the correlation between the microstructure to the electrochemical heterogeneity, as the CBD can affect most of the microstructural properties (transport properties, active electrochemical surface area). Thus, our next step is to capture the CBD morphology, which would allow the determination of all the microstructural properties with their spatial distribution (*e.g.* electronic conductivity, ionic tortuosity factor, triple-phase boundary). The distribution of electrochemical performance can, therefore, be fully resolved.

In addition, some of the reconstructed slices also revealed that the lithiation process could also happen from internal pores of the AM particles. This observation also implies that the electrolyte along with the carbon conductive can penetrate into some internal pores through the AM grain boundaries and allow the (de)lithiation process to occur from the inside of the NMC secondary

particles. This observation is in line with our previous work, in which we observed the occasional presence of the CBD inside the internal pores as well as the work done by Miller *et al.*,[28] who revealed the penetration of electrolyte through the AM grain boundaries.

Finally, we expect that our analysis technique will provide a direct method to unveil the effects of the electrode microstructure on its electrochemical performance. This multiscale insight can shed light to the optimization of the electrode design to improve the electrode performance.

VII.4 Methods

VII.4.1 Materials

Two positive electrodes investigated are both a mixture of NMC532 as AM, conductive carbon black and a mixture of PVdF with the same composition (96%w AM, 2%w carbon black and 2%w PVdF) but different AM loading. Electrode labelled as MX-A is made in our laboratory having a very low loading (*c.a.* 3mg/cm²) with 30% of porosity after calendaring. The second electrode labelled as MX-B is a commercial electrode with a loading of 15mg/cm² and 28% of porosity after calendaring.

VII.4.2 Sample preparation

Our setup requires the X-ray to go through at least the entire thickness of the electrode, as the travel pathway increases as the rotation angles move between [-150°,150°] (assuming that the glassy carbon windows, the Celgard 2500 and the Li foil are mostly transparent). Since it is a transmission technique, it is necessary to have enough X-rays going out of the sample to have enough signal on the detector. For the two electrodes used in this work, the MX-B will cause an issue with its considerable thickness. Without the preparation step, the rotation angle is limited to only [-75°, 75°] for MX-B. Hence, the sample preparation for the MX-B is a crucial step to get a high-quality result and to limit the dead-angle during the acquisition.

Regarding the sample preparation, a “free-standing” electrode was first required, which was obtained by simply peeling the porous electrode material off the current collector foil. A ZEISS laser dissection was used to precisely cut a specific pattern from the bulk electrode (see Figure VII-1d). The pattern along with the void around allows reducing the pathway travelling by the X-ray over a wide rotation angle [-120°, 120°]. As a result, it reduces the dead angle from 75° to 30°. Smaller dead-angles allow the use of the thicker sample (MX-B) for the experiment. It is worth mentioning that to avoid any damage of the laser beam on the region of interest, the pulse mode was used for laser beam instead of permanent mode.

VII.4.3 Experiment process

Assembly of compact electrochemical cells

The assembly of the Operando cell was carried out in an argon-filled glovebox . The electrode was first introduced in the cell at the center, just above the glassy carbon window. For the MX-B, one may want to keep the patterns cut by laser beam near to the center of the windows for the ease of locating them during acquisition. Li foil and 1.2M $LiPF_6$ (dissolved in a solvent consisting of 50% EC and 50% DMC by weight) were used as the counter electrode and the electrolyte along with Celgard 2500 as the separator.

Our *Operando* cell was designed to minimize the dead angle as much as possible during the acquisition (see Figure VII-1c). The cells was verified to be stable for electrochemical cycling with constant current. This cell design is also compatible with other *Operando* experiments such as X-ray diffraction in transmission.

Electrochemical cycling

All cycling test were performed with a multipotentiostat from Biologic (France) and Maccor. The operational range for the NMC materials in this work is chosen between 2.5 and 4.3 V vs Li/Li^+.

Delithiation of NMC will be galvanostatically carried out under a C/10 current from pristine state to 4.3 V following by a CV step to get a stoichiometry as much uniform as possible. Then a high C-rate (1C) current will be used for the lithiation of NMC in order to enhance the limitation from porous electrode and to maximize the presence of heterogeneities. At the chosen state of lithiation, a relaxation step will be proceeded for 1 hour, and XANES-XCT data set will be collected at the end of this step. During the acquisition, 3 different energy level scans which are defined earlier, will take place.

Operando XANES tomographic data collection

The assembled cell was imaged using XCT at beamline 32-ID-C, Advanced Photon Source (APS). First, two reference spectra were collected from both pristine state and delithiation state (up to 4.3V vs Li/Li^+) with energy scan ranges from 8.30 keV to 8.43 keV with 150 energy steps in between. From those two reference spectra, we identified three energy levels that locate at pre-edge (8.33 keV), edge (8.58 keV), and post-edge (8.43 keV) respectively (Figure VII-1a). Here, in our approach, only 3 energy levels were recorded, which does not allow for the identification of all the Ni K-edge features during the operation as what proposed by Nowack *et al.*[13] using 12 energy levels. However, our approach can significantly reduce the exposure time to X-ray of the sample as well as the duration per scan.

At the end of each relaxation step, three XCT datasets at three energy levels defined earlier were collected using 721 projections over an angular range [-120°,120°] with a field of view of 50x50 μm^2.

VII.4.4 Data processing

It is worth stating that the voxel size of the XANES-XCT measurements with our experimental setup was *ca.* 30 nm. However, to reduce the noise and the artefacts of the tomographic data in order to facilitate registration of volumes, which is crucial for the mapping of Li content, we binned the voxels of the tomographic data. Thus, the spatial resolution of the 3D volumes became lower than the single voxel size. Kimura et al. has investigated the effect of binning on the data processing, and they reported that there was no large difference in the magnitude of noise for the number of binned voxels more than 6×6×6. In this work, each of 7x7x7 voxels was binned, resulting in a voxel size of 210 nm. Considering the average particle size of the NMC particles ($d_{50} = 4.7$ µm), this spatial resolution is thought to be high enough to discuss the mesoscopic charging state distribution.

Registration of 2D slices between energies

In order to process the quantification of the Li concentration based on the change of the absorption coefficient at the Ni K-edge, the three XCT datasets at the three energy levels have to be spatially aligned. Image registration was performed using the *elastix* software. Following an initial rigid transformation, a nonrigid b-spline-transform is applied.

Li concentration mapping

Both the edge and peak absorption features in the Ni K edge have been shown in the literature to be approximately linearly correlated to lithiation state in NMC. Therefore, our approach was relied on the relative shift of the absorption coefficient at the Ni K-edge (at 8.35 keV). The relative shift is obtained by normalizing the 3D volume captured at the K-edge to the absorption jump calculated as a difference of the absorption coefficient at the pre-edge and the post-edge.

$$\mathrm{MAP} = \frac{\mathrm{Vol}_{\mathrm{edge}} - \mathrm{Vol}_{\mathrm{pre-edge}}}{\mathrm{Vol}_{\mathrm{pre-edge}} - \mathrm{Vol}_{\mathrm{post\_edge}}} \qquad \text{(Eq. VII-1)}$$

where $\mathrm{Vol}_{\mathrm{edge}}$, $\mathrm{Vol}_{\mathrm{pre-edge}}$, $\mathrm{Vol}_{\mathrm{post-edge}}$ are the 3D volumes obtained at the edge, pre-edge and post-edge of the Ni K-edge respectively.

As a result, we obtained the 3D volume that has voxels' grey level reflecting the Li concentration within the NMC particles. By combining the obtained data of NMC distribution and the Li content at corresponding voxels, we acquired the 3D charging state (Li content) map. By repeating above procedure as lithiation proceeds, 3D lithium distribution evolution as a function of Li content in the AM can be rendered, as shown in Figure VII-1a.

References

[1] R. Xu, Y. Yang, F. Yin, P. Liu, P. Cloetens, Y. Liu, F. Lin, K. Zhao, *J. Mech. Phys. Solids* **2019**, *129*, 160.

[2] M. M. Forouzan, B. A. Mazzeo, D. R. Wheeler, *J. Electrochem. Soc.* **2018**, *165*, DOI 10.1149/2.1281809jes.

[3] Y. Yang, R. Xu, K. Zhang, S. Lee, L. Mu, P. Liu, C. K. Waters, S. Spence, Z. Xu, C. Wei, D. J. Kautz, Q. Yuan, Y. Dong, Y. Yu, X. Xiao, H. Lee, P. Pianetta, P. Cloetens, J. Lee, K. Zhao, F. Lin, Y. Liu, *Adv. Energy Mater.* **2019**, *9*, 1900674.

[4] X. Lu, A. Bertei, D. P. Finegan, C. Tan, S. R. Daemi, J. S. Weaving, K. B. O. Regan, T. M. M. Heenan, G. Hinds, E. Kendrick, D. J. L. Brett, P. R. Shearing, *Nat. Commun.* **2020**, *11*, 1.

[5] P. Pietsch, V. Wood, *Annu. Rev. Mater. Res.* **2017**, *47*, 451.

[6] V. Wood, *Nat. Rev. Mater.* **2018**, *3*, 293.

[7] C. Cao, M. F. Toney, T. K. Sham, R. Harder, P. R. Shearing, X. Xiao, J. Wang, *Mater. Today* **2020**, *34*, 132.

[8] P. R. Shearing, D. S. Eastwood, R. S. Bradley, J. Gelb, S. J. Cooper, F. Tariq, D. J. L. Brett, N. P. Brandon, P. J. Withers, P. D. Lee, *Microsc. Anal*, **2013**, 27(2), 19-22

[9] S. R. Daemi, C. Tan, T. Volkenandt, S. J. Cooper, A. Palacios-Padros, J. Cookson, D. J. L. Brett, P. R. Shearing, **2018**, DOI 10.1021/acsaem.8b00501.

[10] L. Almar, J. Joos, A. Weber, E. Ivers-Tiffée, *J. Power Sources* **2019**, *427*, 1.

[11] J. Nanda, J. Remillard, A. O'Neill, D. Bernardi, T. Ro, K. E. Nietering, J.-Y. Go, T. J. Miller, *Adv. Funct. Mater.* **2011**, *21*, 3282.

[12] J. Liu, M. Kunz, K. Chen, N. Tamura, T. J. Richardson, *J. Phys. Chem. Lett.* **2010**, *1*, 2120.

[13] L. Nowack, D. Grolimund, V. Samson, F. Marone, V. Wood, *Nat. Publ. Gr.* **2016**, DOI 10.1038/srep21479.

[14] G. Ouvrard, M. Zerrouki, P. Soudan, B. Lestriez, C. Masquelier, M. Morcrette, S. Hamelet, S. Belin, A. M. Flank, F. Baudelet, *J. Power Sources* **2013**, *229*, 16.

[15] T. Nakamura, K. Chiba, M. Fakkao, Y. Kimura, K. Nitta, Y. Terada, Y. Uchimoto, K. Amezawa, *Batter. Supercaps* **2019**, *2*, 688.

[16] K. Chen, S. Shinjo, A. Sakuda, K. Yamamoto, T. Uchiyama, K. Kuratani, T. Takeuchi, Y. Orikasa, A. Hayashi, M. Tatsumisago, Y. Kimura, T. Nakamura, K. Amezawa, Y. Uchimoto, *J. Phys. Chem. C* **2019**, *123*, 3292.

[17] J. Wang, Y.-C. K. Chen-Wiegart, C. Eng, Q. Shen, J. Wang, *Nat. Commun.* **2016**, *7*, DOI 10.1038/ncomms12372.

[18] D. P. Finegan, A. Vamvakeros, C. Tan, T. M. M. Heenan, S. R. Daemi, N. Seitzman, M. Di Michiel, S. Jacques, A. M. Beale, D. J. L. Brett, P. R. Shearing, K. Smith, *Nat. Commun.* **2020**, DOI 10.1038/s41467-020-14467-x.

[19] Y. S. Yu, M. Farmand, C. Kim, Y. Liu, C. P. Grey, F. C. Strobridge, T. Tyliszczak, R. Celestre, P. Denes, J. Joseph, H. Krishnan, F. R. N. C. Maia, A. L. D. Kilcoyne, S. Marchesini, T. P. C. Leite, T. Warwick, H. Padmore, J. Cabana, D. A. Shapiro, *Nat. Commun.* **2018**, DOI 10.1038/s41467-018-03401-x.

[20] W. E. Gent, Y. Li, S. Ahn, J. Lim, Y. Liu, A. M. Wise, C. B. Gopal, D. N. Mueller, R. Davis, J. N. Weker, J.-H. Park, S.-K. Doo, W. C. Chueh, *Adv. Mater.* **2016**, *28*, 6631.
[21] O. J. Borkiewicz, K. M. Wiaderek, P. J. Chupas, K. W. Chapman, **2015**, DOI 10.1021/ACS.JPCLETT.5B00891.
[22] O. J. Borkiewicz, B. Shyam, K. M. Wiaderek, C. Kurtz, P. J. Chupas, K. W. Chapman, *J. Appl. Crystallogr.* **2012**, *45*, 1261.
[23] S.-M. Bak, E. Hu, Y. Zhou, X. Yu, S. D. Senanayake, S.-J. Cho, K.-B. Kim, K. Y. Chung, X.-Q. Yang, K.-W. Nam, *ACS Appl. Mater. Interfaces* **2014**, *6*, 22594.
[24] W. S. Yoon, M. Balasubramanian, K. Y. Chung, X. Q. Yang, J. McBreen, C. P. Grey, D. A. Fischer, *J. Am. Chem. Soc.* **2005**, *127*, 17479.
[25] A. Deb, U. Bergmann, S. P. Cramer, E. J. Cairns, *J. Appl. Phys.* **2005**, *97*, 113523.
[26] Z. Jiang, J. Li, Y. Yang, L. Mu, C. Wei, X. Yu, P. Pianetta, K. Zhao, P. Cloetens, F. Lin, Y. Liu, *Nat. Commun.* **2020**, *11*, 1.
[27] J. Landesfeind, H. A. Gasteiger, *J. Electrochem. Soc.* **2019**, *166*, A3079.
[28] D. J. Miller, C. Proff, J. G. Wen, D. P. Abraham, J. Bareño, *Adv. Energy Mater.* **2013**, *3*, 1098.

Chapter VIII . Concluding Remarks & Perspectives

VIII.1 General conclusion

This thesis is in the continuity of the partnership with Renault car manufacturer that aims to improve the performance of the LiB through the electrode design. For this purpose, this work investigated the interplay between the microstructures of four industry-grade NMC electrodes: MX-01 (25 mg/cm² / 3.5 g/cm^3 / 2.2%w of CB), MX-02 (15 mg/cm² / 3.2 g/cm^3 / 2.2%w of CB), MX-01b (25 mg/cm² / 3.5 g/cm^3 / 3.2%w of CB), MX-01b (15 mg/cm² / 3.5 g/cm^3 / 3.2%w of CB); and their electrochemical performance.

Given the complexity of the LiB system's behavior, a numerical approach based on physics-based battery models was adopted, where the models allowed the identification of different sources of performance limitation, which can be quantitatively correlated to the microstructure.

Prior to that, since one understand the crucial role of reliable model parameters, a large part of this work focused on the characterization of the microstructural and electrochemical properties of the electrodes. Both image-based methods and electrochemical measurements were carried out to get as many properties as possible, such that they can either be used as input parameters for physics-based battery models or provide insights for better understanding about the system.

As a starting point, we revisited the concept of the tortuosity factor for porous electrodes. Using a numerical approach, based on simulations performed on synthetic microstructural image data (2D and 3D), we unveiled several key issues with the conventional tortuosity factor when used to characterize electrodes. As a result, we introduced a new concept called the "electrode tortuosity factor", which captures the transport processes relevant to porous electrodes better than conventional ones. We demonstrated that the symmetric cell method is appropriate for accurately determining the tortuosity factor for battery porous electrodes. This method was then used for the tortuosity determination of the electrodes studied in this work. Beyond the scope of this work, this is an important result for optimizing electrode design that electrochemical modelers should consider. This simulation tool is provided as an open-source MATLAB application and is freely available online as part of the *TauFactor* platform.

Since this work dealt with NMC materials that possess a better contrast against the additives and voids than materials such as Graphite, X-ray tomography works well in capturing the electrode 3D microstructure. Thus, an image-based approach relying on a quantitative phase-contrast imaging technique, so-called hard X-ray nano-holotomography, was carried out. This technique provides a large reconstructed volume, where the carbon binder domain can be resolved along with the active materials and the pore space. A complete quantitative analysis of the microstructures of three electrodes (MX-01, MX-01b, MX-02b), including the characterization of each phase separately along with the statistical quantification of their inter-connectivity at particle scale, is performed. This work suggests the negative impacts of an excess of carbon binder domain on the electrode performance at high C-rates. Those results are valid for industry-grade electrodes, and are ascribed to a decrease of the electrochemical active surface area. In addition, electrodes with a higher amount of additives exhibit a higher level of microstructural heterogeneities, which might

also deteriorate the overall performance.

Through the work on X-ray nano-holotomography, we noticed a marked uncertainty source related to the segmentation process. To resolve this uncertainty , a machine learning approach was applied to image segmentation. Although it has been changing dramatically the way one segmentate images, a labelling step required for network training might lead to significant user-to-user variation, as it strongly depends on the human perception of the images. Thus, it prevents the quantification of reliable properties using image-based methods. Consequently, having a consistent human perception for the same image regardless of the operator is essential to get reliable results from image data. Usually, one has to go through an image pre-processing step (*e.g.* denoise, contrast enhancement) for quality enhancement. However, this step frequently involves human observers that also results in user-to-user dispersion and uncertainties. We introduced a method with no observer-dependence in this work to tackle this challenge, which utilizes convolutional neural networks for tomographic image quality assessment. Our method requires fewer image labels to train the neuronal network and is more appropriate to assess the quality of X-ray tomographic images that need to be segmented than most existing data-driven methods. The evaluation results from this work demonstrate that our method can be a direct tool that guides the enhancement process and leads to reliable segmentation results regarding subjective human opinion. As a result, image processing can turn into a very robust, observer-independent process.

As mentioned above, the main goal of this work is to use physics-based models to decipher the effects of the electrode microstructure on their performance. For this purpose, we selected the Newman P2D model as a baseline model because it offers the best compromise between computation speed and physical significance among battery models. Most of these model inputs come from experimental measurements that have been done in this work, and then model simulations were run “as is”, *i.e.* without fitting any parameter. The model was validated against the discharge rate capabilities of the four industry-grade electrodes at 25°C. However, a careful analysis demonstrated that the Newman P2D model was not appropriate to represent the electrode rate capabilities. Considering the outcomes from tomographic data analysis, we suggested an additional limitation coming from the agglomeration of AM and a reduction of the available active surface area along with additional transport limitations for ions in the sub-pores within the porous agglomerates. A new physics-based model, the so-called PApa model, was developed to address this specific mechanism. The polynomial approximation was adopted for the solid diffusion within AM particles for the model to be pseudo 2D and not pseudo 3D.

Moreover, inter-particle solid diffusion is also considered in the model. The new model provided a very good agreement between simulation and experimental results on the set of four electrodes with three different electrolytes. This model is a sophistication of Newman model that may be relevant for dense porous electrodes, wherein active particles are agglomerated to some degree.

Finally, we investigated an approach that directly correlates the microstructure and

electrochemical performance at multi-scale through the *Operando* XANES combined with the nano-XCT experiment. An *Operando* electrochemical cell was purposely developed for this work, exhibiting good stability for electrochemical tests and small dead-angles for high-quality data. The results from this work demonstrated a high level of non-uniformity in state-of-charge within the porous electrodes during the operation.

VIII.2 Future work

All parts of this work can be continued based on several considerations. In what follows, we described some potential future modeling and experimental work.

VIII.2.2 Numerical Modeling

The charging behavior of NMC electrodes should also be investigated because it is critical for fast charging applications. With this regard, we have observed the asymmetric behavior between the charge & discharge process on the set of electrodes used in this work. Unfortunately, the root cause is still out of sight. Recently, Chueh *et al.*[1] addressed this asymmetric behavior by attributing it to the kinetic limitations from the NMC materials during fast delithiation. They have found the reaction rate constant that increases as the lithiation progresses, which is consistent with the result from this work. Upon fast charge, this behavior exacerbates the non-uniformity between high and low Li concentration particles, which leads to "fictive" phase-separation. A group of particles with a distribution of different properties such as electronic conductivity, particle size, and contact resistance with the CB matrix might be required to introduce this mechanism into the model.

Once the half-cell model for the NMC electrode is fully validated, a reliable full cell model can be built up from the two experimental-consistent half-cell models: Graphite anode (Malifarge's PhD thesis 2017) and the NMC cathode (this work). This model would allow engineers to improve the cell design for automotive applications and predict battery degradation phenomena such as Li plating during the fast charging process.

We can imagine such a full-cell model connected to the downstream of a numerical manufacturing model, which provides a digital twin of the cell fabricated in a real factory. The digital twin allows the identification of manufacturing parameters that are critical for battery performance. In addition, an optimization process that considers the cost model, the manufacturing yield can also be coupled to the cell performance given by the model to find the optimal compromise for the production.

Furthermore, access to the spatial distribution of different properties via electrochemical measurement (*e.g.* µ4probes) or tomography can be used as inputs of a (3D-1D) macroscopic model. Heterogeneities can, therefore, be directly taken into account in this model. As a result, the model can be used to investigate the effects of the heterogeneities at the electrode scale on the macroscopic performance and the degradation mode of the LiB system. For instance, the

interaction between heterogenous regions within the same electrode or the possible effects of the heterogeneities on the opposite electrode could be addressed. We have built this model based on the Newman P2D model using COMSOL Multi-physics, however, the investigation using this model is beyond the scope of the PhD work.

VIII.2.3 Experiments

Investigation of the performance of a larger set of electrodes covering a wider range of densities and or loadings can be carried out to gain more insights into the interplay between the electrode microstructure and its performance. In particular, it allows validating the assumption on the formation of porous agglomerates. Tomography with large FoV such as µ-XCT can be interesting to gain more evidence of the presence of porous agglomerates, as we only need to capture the AM phase.

Regarding the materials, NMC electrodes with single-crystalline particles can be used to compare with the behavior obtained from the polycrystalline particles in this work. Single crystalline particles have been demonstrated to prevent cracking during the calendering process.[2][3][4] This improvement can change the way the solid particles behave within the electrode and possibly the porous agglomerate effects.

Also, a full-cell (NMC/Graphite) rate capability could be performed to validate the corresponding full-cell model and investigate the fast-charging applications.

Operando XANES experiment has a large room for improvement. Once one can resolve the CBD morphology and better track a specific region, the complete picture of the correlation of microstructure and performance can be unveiled. A smaller *Operando* cell was designed and machined in order to fit more easily to different beamline configurations (*e.g.* SOLEIL and APS synchrotrons).

With a better strategy of coupling different methods, we can perform the electronic conductivity measurements and the tomography experiment on the same location. This would provide more insights into the interplay between transport and microstructural properties.

More data might be required to improve the accuracy of our algorithm for the image quality assessment. An online platform can be built where people can go and get guidelines for image processing in order to get image data that possess the most robust human perception, minimizing the uncertainty of the output.

References

[1] J. Park, H. Zhao, S. D. Kang, K. Lim, C.-C. Chen, Y.-S. Yu, R. D. Braatz, D. A. Shapiro, J. Hong, M. F. Toney, M. Z. Bazant, W. C. Chueh, *Nat. Mater.*, **2021**, *207*, *20*, 991.

[2] X. Fan, G. Hu, B. Zhang, X. Ou, J. Zhang, W. Zhao, H. Jia,L. Zou, P. Li and Y. Yang,Nano Energy, **2020**,70, 104450

[3] S. Klein, P. Bärmann, O. Fromm, K. Borzutzki, J. Reiter, Q. Fan, J. Kasnatscheew, *J. Mater. Chem. A*, **2021**, 9, 7546-7555.

[4] Y. Liu, J. Harlow, J. Dahn, *J. Electrochem. Soc.*, **2020**, 167(2), 020512.

Abstract

Although the use of Li-ion batteries has made the growth of the electric vehicle market possible, range is still a limiting point for many users. In order to improve this, a lot of research has been carried out to develop new positive electrode materials and negative electrode materials. However, the maturity of these different materials still does not allow considering their use in batteries for automotive applications. A simple alternative to increasing the energy density with the active materials currently in use is to decrease the amount of inactive material within the cell by increasing the amount of material deposited on the current collectors. However, this increase has the direct impact of increasing the thickness of the electrodes and their resistance. In addition, a side effect is to increase the inhomogeneities within the electrodes. To avoid excessive degradation linked to the use of this type of electrode, a detailed study (tomography, measurements of electrical and ionic transport) of various types of positive electrode, coupled with electrochemical modeling will bring us an improvement of understanding the limitations of this type of electrode. The first part of this work focuses on the complete characterization of porous electrodes, comprising both electrochemical performance and microstructural properties. The second part relies on the numerical approach to further understand the underlying physics of the electrode during operation

Keywords: Li-ion battery, electrode microstructure, electrochemical performance, tomography, mathematical modeling.

Résumé

Bien que l'utilisation des batteries Li-ion ait rendu possible la croissance du marché des véhicules électriques, l'autonomie est toujours un point limitant pour beaucoup d'utilisateurs. Afin d'améliorer cela, de nombreuses recherches ont été menées pour développer de nouveaux matériaux d'électrode positive et des matériaux d'électrode négative. Cependant, la maturité de ces différents matériaux ne permet toujours pas d'envisager leur utilisation au sein de batteries pour des applications automobiles. Une alternative simple pour augmenter la densité d'énergie avec les matériaux actifs actuellement utilisés est de diminuer la quantité de matière inactive au sein de la cellule en augmentant la quantité de matière déposée sur les collecteurs de courant. Cependant, cette augmentation a pour impact direct d'augmenter l'épaisseur des électrodes et leur résistance. De plus, un effet collatéral est d'augmenter les inhomogénéités au sein des électrodes. Pour éviter une dégradation trop importante liée à l'utilisation de ce type d'électrode, une étude détaillée (tomographie, mesures de transport électrique et ionique) de divers types d'électrode positive, couplée à de la modélisation électrochimique nous apportera une amélioration de la compréhension des limitations de ce type d'électrodes. La première partie de ce travail se concentre sur la caractérisation complète des électrodes poreuses, comprenant les performances électrochimiques et les propriétés de la microstructure. La deuxième partie s'appuie sur l'approche numérique pour mieux comprendre la physique liée au comportement de l'électrode pendant son fonctionnement.

Mots-clés : Batterie Li-ion, microstructure d'électrode, performance électrochimique, tomographie, modélisation mathématique.